



FACULTY OF SCIENCES

Electromagnetic production of pseudoscalar mesons

Tom Vrancx

PROMOTOR: Prof. dr. Jan Ryckebusch

Proefschrift ingediend tot het behalen van de academische graad van
DOCTOR IN DE WETENSCHAPPEN: FYSICA

Universiteit Gent
Faculteit Wetenschappen
Vakgroep Fysica en Sterrenkunde

RECTOR: Prof. dr. Anne De Paepe
DECAAN: Prof. dr. Herwig Dejonghe
VOORZITTER: Prof. dr. Dirk Ryckbosch

Academiejaar 2013–2014

*It is our choices that show what we truly are,
far more than our abilities,*

A. Dumbledore.

Jan,

Bedankt voor het vertrouwen, de kansen, en de vrijheid die je me gegeven hebt. Tevens bedankt voor de continue sturing en advies bij het publiceren; het is een vruchtbare samenwerking geweest.

Pa,

Bedankt voor de steun en je geloof in mij. Je hebt altijd interesse getoond en me steeds mijn eigen gang laten gaan.
Bedankt om er altijd te zijn.

Ma,

Bedankt om destijds alles te geven wat je kon en steeds het beste met me voor te hebben. De laatste jaren heb je het me niet bepaald gemakkelijk gemaakt, maar daar ben ik net een sterker en rationeler mens van geworden.

Peter en Sofie,

Ik zal altijd klaarstaan voor jullie en wens jullie enkel het beste toe. Bedankt om in mij te geloven. Jullie zijn een geweldige steun en toeverlaat.

The gang,

Zonder jullie zou ik zeker en vast niet geworden zijn wie ik vandaag ben. Bedankt om er te zijn en voor de zalige tijd. Dat er nog vele jaren mogen volgen.

Yasmine,

Jij bent zonder twijfel mijn belangrijkste 'ontdekking' in deze voorbije vier jaar. Bedankt om er steeds voor mij te zijn en om me zó graag te zien. Je bent fantastisch.

Contents

1	Introduction	1
2	The Regge-plus-resonance framework	7
2.1	Kinematics	7
2.2	Observables	8
2.2.1	Photoproduction	8
2.2.2	Electroproduction	10
2.3	Formalism	11
2.3.1	Tree-level approach	11
2.3.2	Form factors	12
2.3.3	Exchange of Regge trajectories	12
2.3.4	Interaction Lagrangians	14
2.3.5	Transition operators	17
2.4	The Regge-plus-resonance-2007 model for $p(\gamma, K^+)\Lambda$	19
2.4.1	Background and resonance contributions	19
2.4.2	Performance	19
3	Consistent interactions for high-spin fermion fields	21
3.1	Introduction	23
3.2	Consistent interactions	23
3.2.1	The massive spin-5/2 field	23
3.2.2	Massive fermion fields with arbitrary spin	27
3.3	Consistent interactions in hadron physics	30
3.3.1	Inconsistency of standard hadronic form factors	30
3.3.2	The multi-dipole-Gauss form factor	33
3.4	Conclusions	34
	Appendix A: The projection operators for the spin-5/2 theory	35

Appendix B: The spin- $(n + 1/2)$ projection operator	35
Appendix C: The modified decay width for the multi-dipole-Gauss form factor	37
4 The Regge-plus-resonance-2011 model	39
4.1 Introduction	41
4.2 Consistent interactions: RPR-2007 versus RPR-2011	42
4.3 Bayesian inference of the RPR-2011 resonance content	43
5 Incompleteness of complete $N(\gamma, M)B$ data sets	47
5.1 Introduction	49
5.2 Observables for pseudoscalar-meson photoproduction	50
5.2.1 Reaction amplitudes	50
5.2.2 Observables in the transversity basis	50
5.3 Inferring the transversity amplitudes from the asymmetries	52
5.3.1 The moduli	52
5.3.2 The relative phases	53
5.3.3 Introducing experimental error	53
5.4 Results	54
5.4.1 The angular and energy dependence of the transversity amplitudes	54
5.4.2 The merits of the transversity basis	54
5.4.3 Extracting the transversity amplitudes from RPR-2011 simulations	56
5.5 Conclusions	60
Appendix: Other representations of the asymmetries	61
1 Helicity representation	61
2 CGLN representation	61
6 Charged-pion electroproduction above the resonance region	63
6.1 Introduction	65
6.2 Kaskulov-Mosel model	66
6.2.1 Gauged pion exchange	66
6.2.2 Nucleon resonances	66
6.2.3 Additional Regge exchanges and model parameters	67
6.3 Transition form factor	67
6.3.1 On-shell limit of Kaskulov-Mosel transition form factor	67
6.3.2 Alternate transition form factor	67
6.3.3 Pion coupling strengths	68
6.4 Results	68
6.4.1 Proton cutoff energy	68
6.4.2 Low $-t$ regime	69
6.4.3 High $-t$ regime	70
6.5 Conclusion and outlook	72
7 $K^+\Lambda$ electroproduction above the resonance region	75
7.1 Introduction	77
7.2 Transition currents	77
7.3 High-energy $K^+\Lambda$ photoproduction	78
7.3.1 A third Regge trajectory	78
7.3.2 Parameter constraints	79
7.3.3 Results	80
7.4 High-energy $K^+\Lambda$ electroproduction	80
7.4.1 Form factors	80

7.4.2 Results	81
7.5 Conclusion and outlook	83
Appendix: Observables	84
1 Photoproduction	84
2 Electroproduction	84
8 Conclusions	87
Appendix	91
Summary	93
Samenvatting	97
Bibliography	103
Publications	107
Nomenclature	111

Fundamental particles and interactions

By the end of the 19th century, it was established that all matter is composed of atoms. The plethora of known chemical elements and their periodically recurring properties, however, indicated that atoms are not the fundamental building blocks of matter, but have an internal structure instead. At the beginning of the 20th century, Rutherford discovered that atoms consist of a very small, positively charged core that is surrounded by a vast, negatively charged electron cloud. The atomic core, or “nucleus”, is not indivisible either. With the discovery of the neutron in 1932, it was revealed that the constituents of nuclei, called “nucleons”, are protons and neutrons. Since electrons are much lighter than nucleons (about 1840 times), the atomic mass is essentially given by the nuclear mass. As a result, the nucleons account for practically all of the visible mass in the universe (more than 99.9%).

Unlike electrons, nucleons are not elementary particles. According to the Standard Model of particle physics, the constituents of matter are leptons and quarks, which are both spin-1/2 fermions. Table 1.1 shows the different types of elementary matter particles, known in the Standard Model. Nucleons are classified as “hadrons”, which is the common name for particles made up of quarks, and more specifically as “baryons”, being hadrons with three quarks. The quark content of the proton and neutron is given by $\{uud\}$ and $\{udd\}$. On the other side of the hadron class, one distinguishes “mesons”, which consist of two quarks: a quark and an antiquark. Examples of mesons are pions (e.g. π^+ : $\{u\bar{d}\}$) and kaons (e.g. K^+ : $\{u\bar{s}\}$).

The leptons and quarks interact with one another through the exchange of fundamental force carriers, known as the “gauge bosons”. The four known fundamental interactions are listed in Table 1.2 along with the corresponding gauge bosons. The neutrinos only interact weakly, but possibly also gravitationally. The charged leptons are affected by all interactions but the strong one. The quarks are subject to all four interactions. From the listed relative strengths of the four interactions, it is clear that gravity is irrelevant in nuclear physics. The weak interaction is only substantial in nuclear processes for which the strong and electromagnetic interactions do not

Table 1.1: Flavor, approximate mass (m), and electric charge (Q) of the elementary matter particles in the Standard Model of particle physics. These properties were collected from the Review of Particle Physics (RPP) [1].

Leptons				Quarks			
Flavor		m (MeV)	Q	Flavor		m (GeV)	Q
ν_e	electron neutrino	$< 2 \times 10^{-6}$	0	u	up	0.0023	+2/3
e	electron	0.511	-1	d	down	0.0048	-1/3
ν_μ	muon neutrino	< 0.19	0	c	charm	1.28	+2/3
μ	muon	106	-1	s	strange	0.095	-1/3
ν_τ	tau neutrino	< 18.2	0	t	top	173	+2/3
τ	muon	1770	-1	b	bottom	4.78	-1/3

Table 1.2: Gauge bosons, range, and relative strength of the four fundamental interactions [1]. The strength is relative to the strong interaction and applies for two u quarks at a mutual distance of approximately 0.01 fm.

Interaction	Gauge boson(s)	m (GeV)	J^P	Range (fm)	Relative strength
Gravitational	G graviton	0	2	∞	10^{-43}
Weak	W^\pm	80.4	1	0.01	10^{-6}
	Z weak bosons	91.2	1		
Electromagnetic	γ photon	0	1^-	∞	10^{-2}
Strong	g gluons (8 in total)	0	1^-	1	1

interfere, for example in neutrino-induced reactions. At smaller scales (below 0.01 fm), the weak interaction gains strength compared to the strong and electromagnetic ones. The limited range of the weak interaction is attributed to the finite mass of its gauge bosons. The electromagnetic interactions, for example, has an infinite range since its gauge bosons, i.e. photons, are massless. The fact that the weak interaction is so ‘weak’, is due to the relatively heavy masses of the W^\pm and Z bosons. The predominance of the strong interaction at the nuclear scale and its finite range, despite the gluons being massless, has to do with the fact that gluons do not only interact with quarks, but are also self-interacting.

Electromagnetic and strong interactions at the subatomic scale

In Table 1.1, it is seen that all fundamental particles, except for neutrinos, have a finite electric charge. This charge corresponds to the one experienced by an electromagnetic probe at infinitely large distances, or equivalently at vanishing momentum transfers. According to renormalization group theory, the bare electric charge of a fundamental particle is infinitely large however. The fact that a finite charge is observed, is attributed to the ‘screening’ of the bare charge by vacuum fluctuations of charged particle-antiparticle pairs. As a charged particle is probed at smaller distances, the screening becomes less and less effective and the observed electric charge increases. The rate at which the electric charge grows with momentum transfer, is extremely small though. The coupling strength of the electromagnetic interaction is described by the fine-structure constant $\alpha_e = e^2/4\pi \approx 1/137$, with e being the charge of an anti-electron or positron. Since α_e is a small parameter (compared to 1), and its running with momentum transfer can be ignored in practice, subatomic electromagnetic interactions can be described perturbatively in the framework of Feyn-

man diagrams. Indeed, as the number of electromagnetic vertices factorizes with the fine-structure constant, higher-order Feynman diagrams become increasingly less important.

Since gluons carry strong or “color” charge, and hence mutually interact, there is no screening in the strong interaction, like in the electromagnetic case. Instead, color charges are antiscreened by vacuum fluctuations. The antiscreening effect brings about a strong coupling constant that decreases with increasing momentum transfer, with a rate that is much faster compared to the running of the fine-structure constant. The antiscreening of the strong interaction implies that the energy required to separate two quarks increases with the mutual distance. As a result, quarks can never manifest themselves as free particles, as an infinite amount of energy is required to isolate them from hadrons. This effect is known as “confinement”. When a single quark gets knocked out of a hadron, by a high-energy photon for example, the interquark potential becomes so strong at a certain distance, that a real quark-antiquark pair will emerge from the vacuum and subsequently hadronize with the separated quark states. For decreasing distances, the interquark strong bond becomes weaker and weaker, and at infinitely small separations quarks are no longer affected by the strong interaction. This property is called “asymptotic freedom”.

One of the most astonishing results of the antiscreening of the strong interaction is the mass origin of hadrons. According to its quark content and Table 1.1, the proton, for example, should have a mass of approximately 9.4 MeV. In reality, however, the proton is 100 times heavier. This means that 99% of the proton mass is generated dynamically by the self-interaction of the gluons which bind the quarks. In a simplified picture, the proton can be conceived as a bound state of three so-called “constituent quarks” which have a mass of roughly one third the proton mass. A constituent quark is a quark that is “dressed” by a cloud of virtual gluons and quarks, from which it acquires its effective mass. For the electromagnetic interaction, the situation is opposite. An electromagnetically bound system has a total mass that is less than the combined mass of its constituents. The mass deficit is attributed to the electromagnetic binding energy of the system.

Explaining masses and resonance spectra of hadrons

At the typical energy scale of hadrons, the strong coupling constant is simply too large to allow for a perturbative description of the mutual quark interactions. Only at much higher energies, the strong interaction becomes sufficiently weak and a perturbative approach becomes feasible. In order to explain the properties of hadrons, such as their masses and resonance spectra for example, a different theoretical approach is needed. One such approach is lattice QCD, where “QCD” is short for quantum chromodynamics, being the quantum field theory for the strong interaction. In lattice QCD, the strong interaction theory is formulated on discretized space-time and treated numerically [1, 2]. Lattice calculations require an enormous amount of computing power, leaving no wonder as to why lattice QCD has only started to play a significant role in the past few years, even though its original conception dates back to the mid-1970s. Ever since, the predictions have become more accurate and experimentally testable, but most of the results are limited to the ground states of hadrons [3]. An example of a recent important achievement is the explanation of the observed masses of the ρ and K^* and of the unflavored and strange baryons, starting from the pion, kaon, and Σ masses [4].

The observed excitation spectra of hadrons can be most easily comprehended within the constituent quark and quark-diquark frameworks, although lattice QCD is also making progress in this area, e.g. Ref. [5]. In constituent quarks models, hadrons are treated as composite objects where the valence quarks are replaced by constituent quarks. Constituent quarks are ‘dressed’ by a virtual cloud of gluons and quark-antiquark pairs, causing their mass to depend on the four-momentum carried. Within this framework, excited states of hadrons emerge from different arrangements of the constituent quarks in an effective quark potential. Constituent quark models are able to explain the observed nucleon and Δ resonance spectrum, for example, but also predict a number of excited

states that are not observed experimentally, the so-called “missing resonances” [6, 7].

Quark-diquark models also regard the valence quarks of baryons as effective degrees of freedom, but the three quarks are not treated on equal grounds. In these models, the internal baryon dynamics are described by a single constituent quark, joined by a tightly bound constituent quark pair. This significantly reduces the number of degrees of freedom, leading to fewer excited states in the baryon spectra [8, 9]. Not all missing resonances are cleared out by these models though. In the higher parts of the excitation spectra, quark-diquark models also predict resonances that are not observed [10].

Modeling hadron reactions

Although lattice QCD and constituent quark models can account for most of the properties of hadrons, they are not able to describe scattering reactions involving hadrons. At low energies, an effective way of modeling hadron physics is to treat the hadrons as the relevant degrees of freedom, rather than the quarks. In such an approach, the hadrons are considered as massive point particles that have a well-defined set of quantum numbers and are described by a quantum field with the appropriate spin, for example a Klein-Gordon field for a spin-0 hadron, a Dirac field for a spin-1/2 hadron, etc. The mutual and electromagnetic interactions of hadrons are modeled by effective Lagrangians that conserve the relevant quantum numbers. These Lagrangians feature effective coupling constants of an a priori unknown strength, unlike the electromagnetic and strong coupling constants which have a definite size.

The use of hadronic degrees of freedom implies that the strong hadronic interactions are mediated by the exchange of virtual hadrons. Since hadrons are massive, higher-order reaction diagrams are suppressed by the number of hadron propagators involved. It is therefore an acceptable approximation to limit the description to the lowest-order or tree-level diagrams only, the so-called “isobar” approach. In the isobar theory, intermediate hadron states that are unstable are modeled by a modified propagator that accounts for the mean lifetime of the considered hadron.

From threshold energy up to a few GeV, the isobar theory proves very useful to describe a plethora of hadronic reactions. At higher energies, the substructure of hadrons becomes increasingly more manifest and the use of hadronic degrees of freedom is no longer sustainable. Consequently, it is to be expected that isobar models will experience difficulty in describing hadronic reactions at higher energies.

Electromagnetic pseudoscalar-meson production off the nucleon

The importance of the nucleon can hardly be underestimated, as it constitutes a vital building block of everyday matter. Since the electromagnetic interaction is better comprehended and more easily described than the strong interaction, it is theoretically appealing to study the nucleon and its excitation spectrum with an electromagnetic probe, such as photons or electrons. The most “elementary” final state in inelastic photon-nucleon or electron-nucleon scattering comprises a pseudoscalar meson ($J^P = 0^-$) and a $J^P = (1/2)^+$ baryon, represented by ‘ M ’ and ‘ B ’ respectively. In this process, the photon causes a virtual quark-antiquark pair to combine with the quarks of nucleon so as to form two new hadrons, being the meson M and baryon B . Since the electromagnetic interaction only conserves the third component of the strong isospin, both isospin-1/2 and isospin-3/2 final states are possible, whereas the initial $\gamma^{(*)}N$ state has isospin 1/2.

The “Theoretical Nuclear Physics and Statistical Physics” research group at Ghent University focuses on so-called “open strangeness” or KY final states, with K being a kaon and Y a hyperon. The $K^+\Lambda$ final state has been studied the most thoroughly [11–23], and to less extent the $K^+\Sigma^0$ and $K^0\Sigma^+$ [13, 18–20, 23–25], and $K^+\Sigma^-$ final states [23, 25, 26], for which far less data is available.

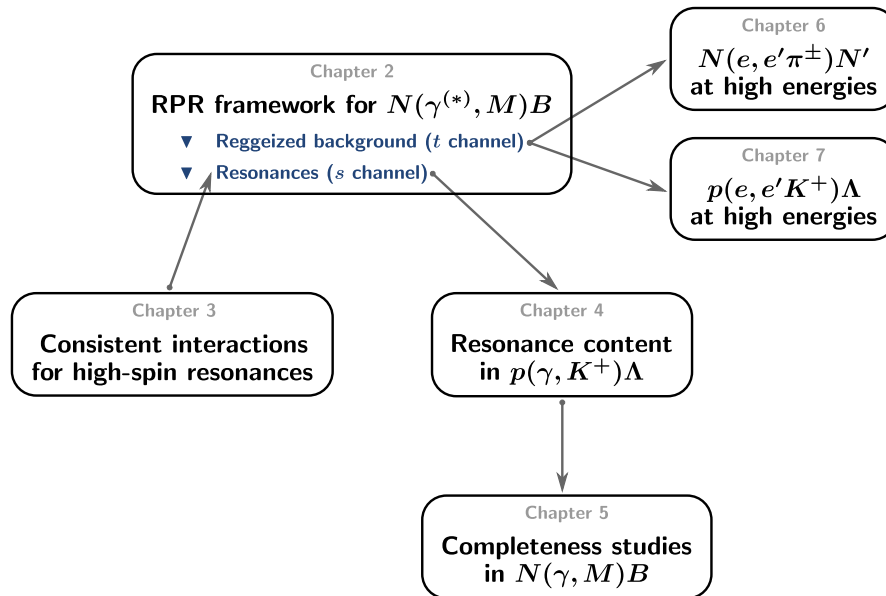


Figure 1.1: Flowchart for the hierarchy of the different chapters of this work. The RPR framework of Chapter 2 plays the central role. The consistent interactions of Chapter 3 give rise to an improved description of high-spin resonances within the central framework. The improved framework is subsequently employed in Chapter 4 to determine the resonance content of $p(\gamma, K^+)\Lambda$, giving rise to a new RPR model. The new RPR model is used in Chapter 5 to study complete sets of observables under simulated experimental conditions. Chapters 6 and 7 deal solely with the background component of the RPR framework and aim at describing $\pi^\pm N'$ and $K^+\Lambda$ electroproduction at high energies (above the resonance region).

For the description of these reactions, the group developed a unique model called the “Regge-plus-resonance” (RPR) model, which will be introduced in the following chapter. By construction, the RPR model has a wide applicability range in terms of energies. Over the years, the RPR model has been continuously improved and extended, and is now regarded as an important tool for interpreting and predicting $N(\gamma^{(*)}, K)Y$ data.

Outline

The outline of this work is schematically represented in Fig. 1.1 and is as follows:

- In Chapter 2, the kinematics and observables for the $N(\gamma^{(*)}, M)B$ reaction will be discussed and the RPR formalism will be presented. The following chapters, will be the subject of different topics within electromagnetic pseudoscalar-meson production. Each of these chapters will start off with a brief background discussion and subsequent outline, followed by the scientific publication that covers the topic in question.
- In Chapter 3, the off-shell interactions of high-spin fermions (fermions with a spin higher than $1/2$) and their application in hadron physics form the subject. These interactions are, for example, important to model propagating baryon resonances in the $N(\gamma^{(*)}, M)B$ reaction within the isobar approach.
- In Chapter 4, the strategy behind the development of the most recent version of the RPR model for the $p(\gamma, K^+)\Lambda$ reaction will be laid out. The realization of this model was enabled by the theoretical formalism, developed in Chapter 3.
- In Chapter 5, the solving potential of theoretically complete sets of $N(\gamma, M)B$ observables will be investigated in circumstances of limited experimental resolution. In particular, this will be

studied for the $p(\gamma, K^+)\Lambda$ reaction from simulated data by the RPR model of Chapter 4.

- In Chapters 6 and 7, a unified formalism will be presented for the description of the charged-pion and K^+ electroproduction reactions $N(\gamma^*, \pi^\pm)N'$ and $p(\gamma^*, K^+)\Lambda$ at high energies, building on the framework developed by Kaskulov and Mosel in Ref. [27]. The resulting model will be used to predict the outcome of experiments planned with the 12 GeV upgrade at the Thomas Jefferson National Accelerator Facility (JLab).
- In Chapter 8, the conclusions of this work will be listed and in the [Appendix](#), the employed notations and conventions will be discussed.

The Regge-plus-resonance framework

2.1 Kinematics

The four-momenta of the particles involved in the $N(e, e'M)B$ reaction are defined as in Fig. 2.1, and are given by

$$\begin{aligned} p_e &= (E_e, \mathbf{p}_e), & q &= (\omega, \mathbf{q}), & k' &= (E_M, \mathbf{k}'), \\ p_{e'} &= (E_{e'}, \mathbf{p}_{e'}), & p &= (E_N, -\mathbf{q}), & p' &= (E_B, -\mathbf{k}'). \end{aligned} \quad (2.1)$$

Here, the electron kinematics are given in the laboratory frame, and the photon and hadron kinematics in the center-of-mass frame. For the sake of notational simplicity, the laboratory and center-of-mass tags ‘lab’ and ‘c.m.’ are omitted, as well as the contravariant Lorentz index ‘ μ ’. Conservation of four-momentum leads to the relations

$$(p_e - p_{e'})^2 = -Q^2, \quad (2.2)$$

and

$$\omega + E_N = E_M + E_B. \quad (2.3)$$

The photon virtuality Q^2 is defined as $Q^2 = -q^2$. In photoproduction, the photon is not virtual and hence $Q^2 = 0$. The Mandelstam variables s , t , and u are defined in the standard way:

$$s = (q + p)^2, \quad t = (q - k')^2, \quad u = (q - p')^2, \quad (2.4)$$

and are connected by the relation

$$s + t + u + Q^2 = m_N^2 + m_M^2 + m_B^2. \quad (2.5)$$

The invariant mass W is given by $W = \sqrt{s}$. In the laboratory frame, the target nucleon N is stationary and hence has no three-momentum. Therefore, the total energy squared in the $N(e, e'M)B$ reaction therefore reads

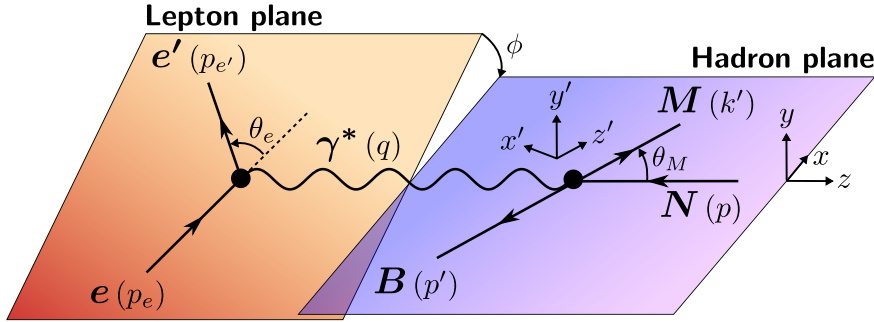


Figure 2.1: Kinematics for the $N(e, e'M)B$ reaction. The lepton plane is defined by the three-momenta of the initial and final electrons in the laboratory frame. Likewise, the hadron plane contains the three-momenta of the initial and final hadrons in the center-of-mass frame. The lepton and hadron plane are inclined by an angle ϕ .

$$s = (E_e - E_{e'} + m_N, \mathbf{p}_e - \mathbf{p}_{e'})^2. \quad (2.6)$$

By combining relations (2.2) and (2.6), the energy of the scattered electron can be expressed by

$$E_{e'} = E_e - \frac{s + Q^2 - m_N^2}{2m_N}. \quad (2.7)$$

2.2 Observables

2.2.1 Photoproduction

The unpolarized differential cross section for the $N(\gamma, M)B$ reaction is calculated as [19]

$$\frac{d\sigma}{d\Omega_M} = \frac{\alpha_e m_N m_B \sqrt{(s + m_M^2 - m_B^2)^2 - 4m_M^2 s}}{32\pi(s - m_N^2)s} \sum_{\lambda, \lambda_N, \lambda_B} |\mathcal{M}_{\lambda_N, \lambda_B}^\lambda|^2, \quad (2.8)$$

with α_e being the fine-structure constant and λ , λ_N , and λ_B the polarizations of the photon, the initial nucleon, and the final baryon. The matrix elements $\mathcal{M}_{\lambda_N, \lambda_B}^\lambda$ are given by

$$\mathcal{M}_{\lambda_N, \lambda_B}^\lambda = \epsilon_\mu^\lambda J_{\lambda_N, \lambda_B}^\mu, \quad (2.9)$$

with $(\epsilon^\lambda)^\mu$ being the polarization four-vector of the photon and $J_{\lambda_N, \lambda_B}^\mu$ the transition current. In photoproduction, the photon is real and can only have transverse polarization components. Three types of photon polarizations are given in Table 2.1: linear, circular, and oblique. The transition

Table 2.1: Definition of the linear, circular, and oblique photon polarizations in photoproduction. These are defined with respect to the xyz -frame, shown in Fig. 2.1. The given components are the contravariant ones.

Linear	Circular	Oblique
$\epsilon^x = (0, 1, 0, 0)$	$\epsilon^+ = -\frac{1}{\sqrt{2}}(0, 1, i, 0)$	$\epsilon^{+\pi/4} = \frac{1}{\sqrt{2}}(0, 1, 1, 0)$
$\epsilon^y = (0, 0, 1, 0)$	$\epsilon^- = \frac{1}{\sqrt{2}}(0, 1, -i, 0)$	$\epsilon^{-\pi/4} = \frac{1}{\sqrt{2}}(0, 1, -1, 0)$

Table 2.2: The definitions of the three single-polarization and twelve double-polarization asymmetries with regard to Eq. (2.11). The convention for the beam-target asymmetry E is adopted from Ref. [28] instead of Ref. [29].

Type	Asymmetry	$(\lambda, \lambda_N, \lambda_B)$	$(\lambda', \lambda'_N, \lambda'_B)$
single	Σ	$(+y, 0, 0)$	$(+x, 0, 0)$
	T	$(0, +y, 0)$	$(0, -y, 0)$
	P	$(0, 0, +y)$	$(0, 0, -y)$
beam-recoil	$C_{x'}$	$(+, 0, +x')$	$(+, 0, -x')$
	$C_{z'}$	$(+, 0, +z')$	$(+, 0, -z')$
	$O_{x'}$	$(+\frac{\pi}{4}, 0, +x')$	$(+\frac{\pi}{4}, 0, -x')$
	$O_{z'}$	$(+\frac{\pi}{4}, 0, +z')$	$(+\frac{\pi}{4}, 0, -z')$
beam-target	E	$(+, -z, 0)$	$(+, +z, 0)$
	F	$(+, +x, 0)$	$(+, -x, 0)$
	G	$(+\frac{\pi}{4}, +z, 0)$	$(+\frac{\pi}{4}, -z, 0)$
	H	$(+\frac{\pi}{4}, +x, 0)$	$(+\frac{\pi}{4}, -x, 0)$
target-recoil	$T_{x'}$	$(0, +x, +x')$	$(0, +x, -x')$
	$T_{z'}$	$(0, +x, +z')$	$(0, +x, -z')$
	$L_{x'}$	$(0, +z, +x')$	$(0, +z, -x')$
	$L_{z'}$	$(0, +z, +z')$	$(0, +z, -z')$

current reads

$$J_{\lambda_N, \lambda_B}^\mu = i \bar{u}_{\lambda_B} T^\mu u_{\lambda_N}, \quad (2.10)$$

with u_{λ_N} and \bar{u}_{λ_B} being the spinors of the initial nucleon and the final baryon in the Bjorken-Drell convention (see Appendix), and T^μ representing the transition operator. These quantities are all defined in the center-of-mass frame. Note that the inclusion of the factor ‘ i ’ in the definition of $J_{\lambda_N, \lambda_B}^\mu$ is a convention, and does not affect the calculated observables.

A polarization asymmetry A can generally be expressed as

$$A = \frac{\sum_{\{\lambda_i=0\}} |\mathcal{M}_{\lambda_N, \lambda_B}^\lambda|^2 - \sum_{\{\lambda'_i=0\}} |\mathcal{M}_{\lambda'_N, \lambda'_B}^{\lambda'}|^2}{\sum_{\{\lambda_i=0\}} |\mathcal{M}_{\lambda_N, \lambda_B}^\lambda|^2 + \sum_{\{\lambda'_i=0\}} |\mathcal{M}_{\lambda'_N, \lambda'_B}^{\lambda'}|^2}. \quad (2.11)$$

An unpolarized state is denoted by “ $\lambda_i = 0$ ”. The notation “ $\{\lambda_i = 0\}$ ” in Eq. (2.11) points to the fact that the summation only runs over unpolarized states. There are fifteen polarization asymmetries to be distinguished: three single-polarization and twelve double-polarization asymmetries. The latter can be subdivided into three types: beam-recoil, beam-target, and target-recoil asymmetries. The definitions of all the polarization asymmetries, with regard to Eq. (2.11), are listed in Table 2.2. In some cases the recoil polarization is specified in the xyz -frame, instead of the $x'y'z'$ -frame, and an alternative set of beam-recoil and target-recoil asymmetries is used. This alternative set is related to the corresponding “primed” one through

$$\begin{aligned} A_x &= A_{x'} \cos \theta_M + A_{z'} \sin \theta_M, \\ A_z &= -A_{x'} \sin \theta_M + A_{z'} \cos \theta_M, \end{aligned} \quad (2.12)$$

with $A_{x,z} \in \{C_{x,z}, O_{x,z}, T_{x,z}, L_{x,z}\}$.

2.2.2 Electroproduction

In electroproduction, the photon is virtual ($Q^2 > 0$) and a longitudinal polarization component is allowed:

$$\epsilon^0 = \frac{1}{\sqrt{Q^2}}(\sqrt{\nu^2 + Q^2}, 0, 0, \nu), \quad (2.13)$$

with $\nu = E_e - E_{e'}$. The $N(e, e'M)B$ differential cross section for a polarized electron beam and unpolarized target and recoils, reads [19]

$$\begin{aligned} \frac{d\sigma}{d\nu dQ^2 d\phi dt} = \frac{\Phi}{2\pi} & \left(\frac{d\sigma_T}{dt} + \varepsilon \frac{d\sigma_L}{dt} + \varepsilon \cos(2\phi) \frac{d\sigma_{TT}}{dt} \right. \\ & \left. + \sqrt{\varepsilon(1+\varepsilon)} \cos\phi \frac{d\sigma_{LT}}{dt} + h\sqrt{\varepsilon(1-\varepsilon)} \sin\phi \frac{d\sigma_{LT'}}{dt} \right), \end{aligned} \quad (2.14)$$

with the virtual-photon flux Φ given by

$$\Phi = \frac{\alpha_e(s - m_N^2)}{4\pi m_N(1 - \varepsilon)E_e^2 Q^2}, \quad (2.15)$$

and the longitudinal-to-transverse ratio ε by

$$\varepsilon = \frac{4E_e E_{e'} - Q^2}{2(E_e^2 + E_{e'}^2) + Q^2}. \quad (2.16)$$

Further, ϕ is the angle between the lepton and hadron plane (see Fig. 2.1) and $h = \pm 1$ is the helicity of the incident electron. For an unpolarized electron beam, the last term of Eq. (2.14) does not contribute to the cross section. The longitudinal, transverse, and interference structure functions in expression (2.14) are defined as

$$\begin{aligned} \frac{d\sigma_L}{dt} &= 2\kappa \mathcal{H}_{0,0}, & \frac{d\sigma_{LT}}{dt} &= -\kappa(\mathcal{H}_{+,0} + \mathcal{H}_{0,+} - \mathcal{H}_{0,-} - \mathcal{H}_{-,0}), \\ \frac{d\sigma_T}{dt} &= \kappa(\mathcal{H}_{+,+} + \mathcal{H}_{-,-}), & \frac{d\sigma_{TT}}{dt} &= -\kappa(\mathcal{H}_{+,-} + \mathcal{H}_{-,+}), \\ & & \frac{d\sigma_{LT'}}{dt} &= -\kappa(\mathcal{H}_{+,0} - \mathcal{H}_{0,+} + \mathcal{H}_{0,-} - \mathcal{H}_{-,0}), \end{aligned} \quad (2.17)$$

where

$$\mathcal{H}_{\lambda,\lambda'} = \sum_{\lambda_p, \lambda_\Lambda} \mathcal{M}_{\lambda_p, \lambda_\Lambda}^\lambda \left(\mathcal{M}_{\lambda_p, \lambda_\Lambda}^{\lambda'} \right)^*. \quad (2.18)$$

The matrix elements $\mathcal{M}_{\lambda_p, \lambda_\Lambda}^\lambda$ are defined in Eq. (2.9). The normalization factor κ is defined as

$$\kappa = \frac{\alpha_e m_N m_B}{2(s - m_N^2) \sqrt{(m_p^2 - s + Q^2)^2 + 4Q^2 s}}. \quad (2.19)$$

The transition from t -differentiated to Ω_M -differentiated cross sections can be carried out through the relation

$$\frac{d\Omega_M}{dt} = \frac{4\pi s}{\sqrt{\left((s + m_M^2 - m_B^2)^2 - 4m_M^2 s \right) \left((m_p^2 - s + Q^2)^2 + 4Q^2 s \right)}}. \quad (2.20)$$

Note that the differential dt , which has been used so far, is actually $-dt$. By convention, however, the former notation is used.

2.3 Formalism

2.3.1 Tree-level approach

Following the isobar approach, the contributions to the RPR transition operator are restricted to tree-level Feynman diagrams. The three possible types of tree-level diagrams are the s , t , and u channels, which are shown in Fig. 2.2. When the electromagnetic vertex features identical hadrons (apart from the photon), the diagram is called a ‘‘Born diagram’’. Otherwise, the diagram is of the ‘‘non-Born’’ type. There is only one Born diagram for each channel.

The pole structure of the tree-level diagrams is determined by the Feynman propagator of the intermediate particles. This propagator is proportional to either $(s - m_s^2)^{-1}$, $(t - m_t^2)^{-1}$, or $(u - m_u^2)^{-1}$, with $m_{s,t,u}$ being the mass of the intermediate particle in the corresponding channel. The t and u channels are referred to as ‘‘background channels’’ since the intermediate particles in these diagrams can never reach their poles ($t = m_t^2$ or $u = m_u^2$). Indeed, conservation of four-momentum dictates that both $t < 0$ and $u < 0$. Only in the s channel, the intermediate particle can go through its pole ($s = m_s^2$), as $s > 0$.

The mass pole in the s channel is only relevant for intermediate nucleon and Delta resonances since $\sqrt{s} \geq m_M + m_B > m_N$ and $m_{N^*, \Delta^*} > m_N$. When s equals the squared mass of such a resonance, however, the s -channel diagram diverges. This would correspond with a zero decay width for the resonance in question, which would appear as an infinitely large spike in the calculated cross section. In other words, the resonance would not be allowed to decay. In principle, a renormalization procedure, which involves contributions from higher-order Feynman diagrams, can remove the concerned divergence in the s channel, resulting in a natural decay width for the resonance. In a tree-level framework, one commonly adopts a phenomenological viewpoint and introduces the ‘measured’ decay width for the resonance, represented by Γ_s , into the s -channel propagator:

$$\frac{1}{s - m_s^2} \rightarrow \frac{1}{s - m_s^2 + im_s \Gamma_s}. \quad (2.21)$$

This procedure effectively counters the divergence: the decay width is inserted such that the propagator’s pole is shifted to the complex plane and cannot be reached in physical processes. In the expression for the cross section, the transition amplitude is multiplied by its complex conjugate and the structure (2.21) gives rise to a Breit-Wigner shape for the resonance in question:

$$\frac{1}{(s - m_s^2)^2 + m_s^2 \Gamma_s^2}. \quad (2.22)$$

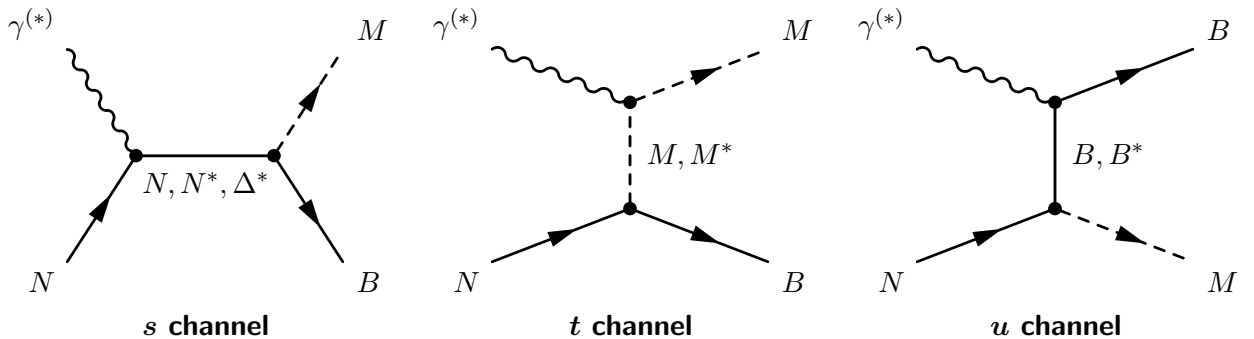


Figure 2.2: The three tree-level Feynman diagrams for the $N(\gamma^{(*)}, M)B$ reaction: the s , t , and u channels. In these diagrams, the squared four-momentum carried by the intermediate particle is respectively s , t , and u . The asterisk denoting the photon’s virtuality should not be confused with the asterisks featuring in N^* , Δ^* , M^* , and B^* , which denote nucleon, Delta, meson, and baryon resonances.

Note that the experimental value for Γ_s is actually the result of a Breit-Wigner fit to the observed resonant structure. Extracting those quantities Γ_s from data is, however, far from trivial (see Refs. [30,31] for example).

2.3.2 Form factors

So far, the hadrons have been treated as point particles. In reality, however, hadrons are composed of quarks and have an internal structure. In effective field theories, the spatial extension of hadrons is commonly modeled by the introduction of form factors. Since quarks carry both color and electromagnetic charge, they interact through the exchange of gluons, as well as photons. While the photon has no electromagnetic charge and hence cannot couple to other photons, gluons can mutually interact since they are color-charged. As a consequence, the color and electromagnetic charge have different space-time distributions and both strong and electromagnetic form factors are to be distinguished.

Commonly used forms for the strong form factor are a monopole for mesons:

$$F_x^S(x) = \left(1 + \frac{|x - m_x^2|}{(\Lambda_x^S)^2}\right)^{-1}, \quad (2.23)$$

and a dipole for baryons:

$$F_x^S(x) = \left(1 + \frac{(x - m_x^2)^2}{(\Lambda_x^S)^4}\right)^{-1}. \quad (2.24)$$

Here, x , m_x , and Λ_x^S represent the squared four-momentum, the mass, and the strong cutoff energy of the intermediate hadron. Roughly stated, the strong form factor restricts the diagram contribution to a symmetric range around m_x , proportional to Λ_x^S . Another form that can be adopted for the baryon strong form factor is a Gauss form:

$$F_x^S(x) = \exp\left(-\frac{(x - m_x^2)^2}{(\Lambda_x^S)^4}\right). \quad (2.25)$$

For the meson and baryon electromagnetic form factors, monopole ($a = 1$) and dipole ($a = 2$) forms are also employed:

$$F^{\text{EM}}(Q^2) = \left(1 + \frac{Q^2}{(\Lambda^{\text{EM}})^2}\right)^{-a}, \quad (2.26)$$

with Λ^{EM} being the electromagnetic cutoff energy. For elastic scattering, Λ^{EM} is inversely proportional to the root-mean-square radius of the electromagnetic charge distribution of the probed hadron. Note that, apart from the mass term, the functional structure of the dipole form of Eq. (2.26) differs from the one in expression (2.24).

The tree-level diagrams of Fig. 2.2 each have both an electromagnetic vertex (the initial one) and a strong vertex (the final one). The electromagnetic and strong form factors are to be introduced in the appropriate vertices. As such, the vertex coupling strengths vary with the squared four-momentum carried by the probing intermediate particle. In photoproduction, only the strong hadronic form factor is of relevance since $Q^2 = 0$.

2.3.3 Exchange of Regge trajectories

In an isobar framework, there are both background contributions from the t and the u channel. From the definitions of t and u in Sec. 2.1, it can be shown that $-t$ is small at forward and large at backward meson-scattering angles θ_M , and vice-versa for $-u$. This implies that the background amplitude

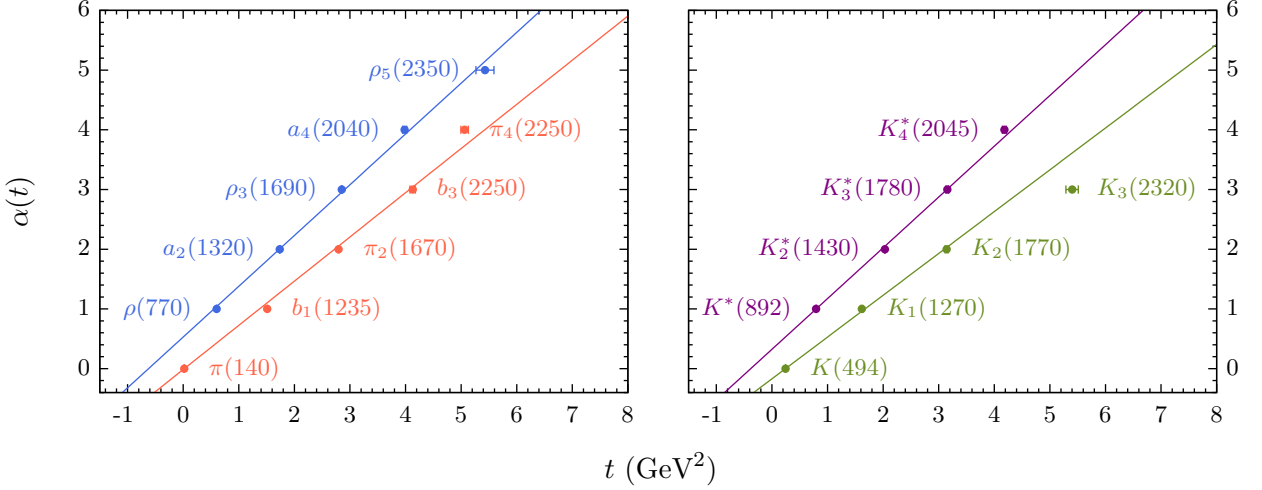


Figure 2.3: Regge trajectories for the two lightest, charged mesons in both the unflavored (left) and the strange (right) meson sector. The properties of the shown meson spectra were extracted from the RPP [1].

is dominated by t -channel contributions at forward scattering and by u -channel contributions at backward scattering, given the pole structures $(t - m_t^2)^{-1}$ and $(u - m_u^2)^{-1}$ of the t - and u -channel propagators. The pole structure also implies that the exchange of less massive particles is dominant over the exchange of heavier particles. Given that on average heavier particles are exchanged in the u channel (baryons), compared to the t channel (mesons), it can be anticipated that the t channel dominates and that the $N(\gamma^{(*)}, M)B$ cross section is forward-peaked.

The RPR framework restricts the background to t -channel contributions only, which is supported by the above reasoning. The fact that the RPR model was originally designed to describe the $N(\gamma^{(*)}, K)Y$ reaction specifically at forward scattering, even further justifies the t -channel restriction. In the RPR framework, the t -channel background is not modeled by the exchange of individual mesons but of families of mesons, which share certain quantum numbers. Such a family of mesons is characterized by a linear relation between the squared mass and the spin of the individual family members. This linear relation is known as the ‘‘Regge trajectory’’ of the family. As an example, the Regge trajectories for the charged π , ρ , K , and K^* mesons are shown in Fig. 2.3, which are quantified by the following relations [19, 27]:

$$\begin{aligned} \alpha_\pi(t) &= \alpha'_\pi(t - m_\pi^2), & \alpha_K(t) &= \alpha'_K(t - m_K^2), \\ \alpha_\rho(t) &= 0.53 + \alpha'_\rho t, & \alpha_{K^*}(t) &= 1 + \alpha'_{K^*}(t - m_{K^*}^2), \end{aligned} \quad (2.27)$$

with $\alpha'_\pi = 0.74 \text{ GeV}^{-2}$, $\alpha'_\rho = 0.85 \text{ GeV}^{-2}$, $\alpha'_K = 0.70 \text{ GeV}^{-2}$, and $\alpha'_{K^*} = 0.85 \text{ GeV}^{-2}$, being the corresponding Regge slopes. Exchanging Regge trajectories, instead of individual particles, has the advantage of not having to introduce a strong hadronic form factor in the background diagrams which, after all, is an artificial procedure to account for the internal structure of hadrons. The exchange of a single Regge trajectory accounts for the contributions of an infinite number of background diagrams, in which the members of the Regge family constitute the intermediate states. This aspect of the Regge theory leads to a natural ‘damping’ of the background amplitude for $s \rightarrow \infty$ [19]. This makes the introduction of phenomenological strong form factors in the t channel unnecessary and is a great asset to the proposed framework.

The exchange of a Regge trajectory is accomplished by replacing the pole of the propagator of the intermediate meson M , which is the first materialization of the Regge trajectory, by the corresponding Regge propagator:

$$\frac{1}{t - m_M^2} \rightarrow \mathcal{P}_M(t, s). \quad (2.28)$$

The expression for the Regge propagator $\mathcal{P}_M(t, s)$ reads [19]

$$\mathcal{P}_M(t, s) = -\alpha'_M \varphi(\alpha_M(t) - J_M) \Gamma(J_M - \alpha_M(t)) \left(\frac{s}{s_0} \right)^{\alpha_M(t) - J_M}, \quad (2.29)$$

with J_M being the spin of the meson M , s_0 a scale factor, Γ the Gamma function, and φ the phase of the Regge trajectory. Note that, in principle, this expression for the Regge propagator is only valid at high s and low $-t$. The phase for a non-degenerate Regge trajectory is given by

$$\varphi(\alpha_M(t) - J_M) = \frac{1 + e^{-i\pi(\alpha_M(t) - J_M)}}{2}, \quad \text{non-degenerate.} \quad (2.30)$$

In a non-degenerate trajectory, the Regge members have either natural, i.e. $(-1)^{J_M}$, or unnatural parity, i.e. $-(-1)^{J_M}$. This means that the members of a non-degenerate trajectory have either even or odd spin. The trajectories shown in Fig. 2.3 all have a degenerate nature. A degenerate Regge trajectory comprises both a natural- and an unnatural-parity trajectory, which are both described by the same $\alpha(t)$ relation (to a good approximation). For these trajectories, the Regge phase can either be constant or rotating:

$$\varphi(\alpha_M(t) - J_M) = \begin{cases} 1 & \text{constant,} \\ e^{-i\pi(\alpha_M(t) - J_M)} & \text{rotating,} \end{cases} \quad (2.31)$$

depending on the specific combination (addition or subtraction) of the non-degenerate phases of the natural- and unnatural-parity trajectories. In some cases, the nature of the degenerate Regge phase can be constrained by theory; in other cases this has to be extracted from experiment. Note that, since $\Gamma(x) \rightarrow x^{-1}$ for $x \rightarrow 0$, it is readily seen that the Regge propagator reduces to the pole of the Feynman propagator in the on-shell limit for M :

$$\mathcal{P}_M(t, s) \rightarrow \frac{1}{t - m_M^2}, \quad \text{for } t \rightarrow m_M^2. \quad (2.32)$$

This justifies the substitution (2.28), which allows to incorporate the Regge phenomenology into the framework of Feynman diagrams.

2.3.4 Interaction Lagrangians

The dynamics at a specific interaction vertex is described by the corresponding interaction Lagrangian. Below, the electromagnetic and strong interaction Lagrangians are listed for the tree-level diagrams shown in Fig. 2.2. More specifically, the s -, t -, and u -channel Born diagrams and the s - and t -channel non-Born diagrams will be discussed. In the t channel, the exchange of pseudoscalar, vector, and axial-vector mesons will be considered. In the s channel, spin-1/2 and spin-3/2 resonance exchanges are considered. Note that the given Lagrangians are specific to the interaction vertices for the initial γN and final MB states. The complete interaction theory requires the addition of the Hermitian conjugate of the Lagrangian, which describes the time-reversed interaction vertex.

Born terms

The interaction Lagrangians at the electromagnetic vertices of the s -, t -, and u -channel Born diagrams of Fig. 2.2 read [19]

$$\begin{aligned} \mathcal{L}_{\gamma^* N \bar{N}} &= -Q_N F_N^e(Q^2) \bar{N} \gamma_\mu N A^\mu + F_N^m(Q^2) \frac{\kappa_N}{4m_N} \bar{N} \sigma_{\mu\nu} F^{\mu\nu} N, \\ \mathcal{L}_{\gamma^* M M^\dagger} &= -iQ_M F_{\gamma MM}(Q^2) (M^\dagger \partial_\mu M - M \partial_\mu M^\dagger) A^\mu, \\ \mathcal{L}_{\gamma^* B \bar{B}} &= -Q_B F_B^e(Q^2) \bar{B} \gamma_\mu B A^\mu + F_B^m(Q^2) \frac{\kappa_B}{4m_N} \bar{B} \sigma_{\mu\nu} F^{\mu\nu} B. \end{aligned} \quad (2.33)$$

Here, A^μ represents the Proca field for the photon, N and B the Dirac fields for the nucleon and baryon, and M the Klein-Gordon field for the pseudoscalar meson M . Further, $\sigma^{\mu\nu}$ is defined as

$$\sigma^{\mu\nu} = \frac{i}{2}[\gamma^\mu, \gamma^\nu], \quad (2.34)$$

and the antisymmetric photon tensor $F^{\mu\nu}$ is given by

$$F^{\mu\nu} = \partial^\nu A^\mu - \partial^\mu A^\nu. \quad (2.35)$$

The electric charges of the nucleon, meson, and baryon (in units of the elementary charge) are represented by Q_N , Q_M , and Q_B , with $Q_N = Q_M + Q_B$. The electromagnetic form factors $F_{N,B}^e(Q^2)$ and $F_{N,B}^m(Q^2)$ are the electric (or Dirac) and magnetic (or Pauli) form factors of the nucleon and baryon, and $F_{\gamma MM}(Q^2)$ is the pseudoscalar-meson electromagnetic form factor. The $\kappa_{N,B}$ are the nucleon and baryon anomalous magnetic moments. Note that the elementary charge unit, which is usually featured by the electric Lagrangians of Eq. (2.33), is contained in the normalization factors for the photo- and electroproduction cross sections (more specifically in the fine-structure constant), which are defined in Secs. 2.2.1 and 2.2.2. At the strong MBN vertex, the interaction Lagrangian is given by [19]

$$\mathcal{L}_{NM^\dagger\bar{B}} = -iI_{MBN}g_{MBN}M^\dagger\bar{B}\gamma_5N. \quad (2.36)$$

The strong MBN coupling constant is given by g_{MBN} and I_{MBN} is an SU(2)-symmetry factor. Note that SU(2)-symmetry factors are only relevant for unflavored final states (e.g. $MB = \pi N'$).

Exchange of vector and axial-vector mesons

The exchange of vector mesons M_V ($J^P = 1^-$) and axial-vector mesons M_A ($J^P = 1^+$) in the t channel is described by the Lagrangians

$$\begin{aligned} \mathcal{L}_{\gamma^*M_V M^\dagger} &= F_{\gamma M_V M}(Q^2) \frac{G_{\gamma^*M_V M}}{2} \varepsilon_{\mu\nu\sigma\tau} F^{\mu\nu} (\partial^\tau M_V^\sigma) M^\dagger, \\ \mathcal{L}_{\gamma^*M_A M^\dagger} &= iF_{\gamma M_A M}(Q^2) G_{\gamma^*M_A M} F_{\mu\nu} (\partial^\nu M_A^\mu) M^\dagger, \end{aligned} \quad (2.37)$$

at the electromagnetic vertex and by

$$\mathcal{L}_{NM_V^\dagger\bar{B}} = -I_{M_V,ABN} \left(G_{M_V,ABN}^v \bar{B} \gamma_\mu M_{V,A}^{\dagger\mu} \Gamma N + \frac{G_{M_V,ABN}^t}{m_N + m_B} \bar{B} \sigma_{\mu\nu} (\partial^\mu M_{V,A}^{\dagger\nu}) \Gamma N \right), \quad (2.38)$$

at the strong vertex [19]. Here, $M_{V,A}^\mu$ represent the Proca fields for the vector and axial-vector mesons. The $G_{\gamma^*M_V,AM}$ are the electromagnetic coupling constants (in GeV^{-1}), and $G_{M_V,ABN}^v$ and $G_{M_V,ABN}^t$ are the strong vector and tensor coupling constants (dimensionless). The vector- and axial-vector-meson electromagnetic form factors are given by $F_{\gamma M_V,AM}(Q^2)$. Further in Eq. (2.38), $\Gamma = \gamma_5$ (1) for axial-vector (vector) mesons and $I_{M_V,ABN}$ is the SU(2)-symmetry factor. The strong Lagrangian of Eq. (2.38) is often defined in terms of the standard vector and anomalous tensor coupling constants $G_{M_V,ABN}$ and $\kappa_{M_V,ABN}$, instead of $G_{M_V,ABN}^v$ and $G_{M_V,ABN}^t$. The former are related to the latter through

$$\begin{aligned} G_{M_V BN} &= -G_{M_V BN}^v + \left(\frac{m_N - m_B}{m_N + m_B} \right) G_{M_V BN}^t, \\ \kappa_{M_V BN} &= \frac{2m_N G_{M_V BN}^t}{(m_N + m_B) G_{M_V BN}^v + (m_B - m_N) G_{M_V BN}^t}, \end{aligned} \quad (2.39)$$

and

$$G_{MABN} = -G_{MABN}^v + \left(\frac{3m_N - m_B}{m_N + m_B} \right) G_{MABN}^t, \\ \kappa_{MABN} = \frac{2m_N G_{MABN}^t}{(m_N + m_B) G_{MABN}^v + (m_B - 3m_N) G_{MABN}^t}, \quad (2.40)$$

for the vector and axial-vector mesons, respectively. Note that for unflavored mesons, the Lagrangians of Eqs. (2.37) and (2.38) are only valid for vector and axial-vector mesons with a positive and negative G -parity, respectively.

Exchange of spin-1/2 resonances

The electromagnetic interaction of a spin-1/2 resonance with a photon and a nucleon is described by the Lagrangian [19]

$$\mathcal{L}_{\gamma^* N \bar{R}} = F_{\gamma RN}^m(Q^2) \frac{G_{\gamma RN}^m}{4m_N} \bar{R} \sigma_{\mu\nu} F^{\mu\nu} \Gamma' N. \quad (2.41)$$

The spin-1/2 resonance is described by the Dirac field R . The magnetic coupling constant for the $\gamma N \rightarrow R$ transition is given by $G_{\gamma RN}^m$ (dimensionless) and $F_{\gamma RN}^m(Q^2)$ represents the magnetic form factor for the $\gamma^* N \rightarrow R$ transition. As for the vector and axial-vector mesons, $\Gamma = \gamma_5(1)$ and $\Gamma' = 1(\gamma_5)$ for positive (negative) parity resonances. The Lagrangian modeling the strong MBR vertex is given by [19]

$$\mathcal{L}_{RM^\dagger \bar{B}} = -i I_{MBR} G_{MBR} M^\dagger \bar{B} \Gamma R, \quad (2.42)$$

with G_{MBR} the strong coupling constant and I_{MBR} the SU(2)-symmetry factor.

Exchange of spin-3/2 resonances

The interaction Lagrangians for the electromagnetic and strong interaction with spin-3/2 resonances read

$$\mathcal{L}_{\gamma^* N \bar{R}} = i F_{\gamma RN}^{(1)}(Q^2) \frac{G_{\gamma RN}^{(1)}}{2m_N} \bar{R}^\mu \Theta_{\mu\nu}(z_{\gamma RN}^{(1)}) \Gamma \gamma_\sigma F^{\sigma\nu} N \\ - F_{\gamma RN}^{(2)}(Q^2) \frac{G_{\gamma RN}^{(2)}}{4m_N^2} \bar{R}^\mu \Theta_{\mu\nu}(z_{\gamma RN}^{(2)}) \Gamma F^{\nu\sigma} (\partial_\sigma N), \quad (2.43)$$

and

$$\mathcal{L}_{RM^\dagger \bar{B}} = I_{MBR} \frac{G_{MBR}}{m_M} \bar{R}^\mu \Theta_{\mu\nu}(z_{MBR}) \Gamma' (\partial^\nu M) B, \quad (2.44)$$

[19]. The spin-3/2 resonance is described by the Rarita-Schwinger field R^μ . The electromagnetic coupling constants for the $\gamma N \rightarrow R$ transition is given by $G_{\gamma RN}^{(1,2)}$ (dimensionless) and $F_{\gamma RN}^{(1,2)}(Q^2)$ represent the electromagnetic form factors for the $\gamma^* N \rightarrow R$ transition. The tensor $\Theta_{\mu\nu}(z)$ is given by

$$\Theta_{\mu\nu}(z) = g_{\mu\nu} - \left(z + \frac{1}{2} \right) \gamma_\mu \gamma_\nu, \quad (2.45)$$

and is referred to as an ‘‘off-shell tensor’’, and $z_{\gamma RN}^{(1)}$, $z_{\gamma RN}^{(2)}$, and z_{MBR} are the electromagnetic and strong ‘‘off-shell parameters’’.

2.3.5 Transition operators

From the interaction Lagrangians presented in the previous section, the transition operator for each background and resonant diagram can now be derived. In the t channel, the effective propagators for an intermediate scalar meson M and an intermediate vector or axial-vector meson $M_{V,A}$ are given by

$$\begin{aligned} P_M(t, s) &= i\mathcal{P}_M(t, s), \\ P_{M_{V,A}}^{\mu;\nu}(t, s) &= -ig_{\mu\nu}\mathcal{P}_{M_{V,A}}(t, s). \end{aligned} \quad (2.46)$$

In these expressions for the effective propagators, the pole structure is replaced by the Regge propagator (see Eq. (2.28)) and the inclusion of the imaginary unit is a matter of convention. The effective propagators for the exchange of spin-1/2 and spin-3/2 particles with four-momentum q'^μ read

$$\begin{aligned} P_R(q') &= \frac{i(q' + m_R)}{q'^2 - m_R^2 + im_R\Gamma_R}, \\ P_R^{\mu;\nu}(q') &= \frac{i(q' + m_R)}{q'^2 - m_R^2 + im_R\Gamma_R} \left(g^{\mu\nu} - \frac{1}{3}\gamma^\mu\gamma^\nu - \frac{2}{3m_R^2}q'^\mu q'^\nu + \frac{1}{3m_R}(q'^\mu\gamma^\nu - q'^\nu\gamma^\mu) \right), \end{aligned} \quad (2.47)$$

with m_R and Γ_R the mass and decay width of the resonance R . In order to calculate the transition operator for each diagram contributing to the total transition amplitude, the interaction vertices have to be derived from the interaction Lagrangians of Sec. 2.3.4. This is accomplished by means of a transformation from configuration space to momentum space:

$$\begin{aligned} \partial^\mu\Psi &\rightarrow -ip^\mu\Psi, \\ \partial^\mu\Psi^\dagger &\rightarrow ip^\mu\Psi^\dagger, \end{aligned} \quad (2.48)$$

with p^μ being the four-momentum of the incoming (Ψ) or outgoing (Ψ^\dagger) field, and subsequently extracting the fields from the interaction Lagrangian. Upon multiplying the resulting expression by a factor i , the interaction vertex is obtained. The transition operator for each diagram D contributing to the total transition amplitude is then calculated as

$$T_D^\mu = \Gamma_S^{\nu_1\dots\nu_n} P_{\nu_1\dots\nu_n;\sigma_1\dots\sigma_n} \Gamma_{EM}^{\sigma_1\dots\sigma_n,\mu}, \quad (2.49)$$

with $\Gamma_S^{\nu_1\dots\nu_n}$ and $\Gamma_{EM}^{\sigma_1\dots\sigma_n,\mu}$ being the strong and electromagnetic interaction vertices of diagram D , $P_{\nu_1\dots\nu_n;\sigma_1\dots\sigma_n}$ being the intermediate-particle propagator of diagram D , and μ being the Lorentz index of the photon field. The total transition operator, featuring in expression (2.10) for the total transition current, is the sum of all the transition operators of the individual diagrams D_i :

$$T^\mu = \sum_i T_{D_i}^\mu. \quad (2.50)$$

Below, the calculated transition operators for the considered diagrams are listed.

Gauged exchange of a t -channel pseudoscalar meson

At the electromagnetic vertex, the exchange of M is described by the second Lagrangian of Eq. (2.33). This Lagrangian, however, is not symmetric under electromagnetic-gauge transformations $A^\mu \rightarrow A^\mu + \partial^\mu\xi$, with ξ an arbitrary, space-time dependent scalar field. Consequently, the resulting transition operator is also not gauge-invariant. For the transition operator, gauge invariance is translated as

$$q_\mu T_D^\mu = 0, \quad (2.51)$$

with q^μ being the four-momentum of the photon. The electromagnetic Lagrangians that feature the antisymmetric photon tensor $F^{\mu\nu}$, are invariant under the electromagnetic gauge by construction. In the Born t -channel, a gauge-fixing term is required in order to assure the electromagnetic-gauge symmetry. This term is provided by the electric term of the Born s - or u -channel, depending on whether the initial nucleon is a proton ($N = p$) or a neutron ($N = n$). The $N = p$ transition operator for the gauged exchange of a Reggeized pseudoscalar meson M reads

$$T_M^\mu = I_{MBN}g_{MBN}\gamma_5 \left(Q_M F_{\gamma MM}(Q^2) \mathcal{P}_M(t, s)(2k' - q)^\mu + Q_N F_N^e(Q^2) \mathcal{P}_M(t, s) \frac{t - m_M^2}{s - m_N^2} (\not{p} + \not{q} + m_N) \gamma^\mu \right). \quad (2.52)$$

For $N = n$, the gauged Regge- M exchange is described by

$$T_M^\mu = I_{MBN}g_{MBN} \left(Q_M F_{\gamma MM}(Q^2) \mathcal{P}_M(t, s)(2k' - q)^\mu + Q_B F_B^e(Q^2) \mathcal{P}_M(t, s) \frac{t - m_M^2}{u - m_B^2} \gamma^\mu (\not{p}' - \not{q} + m_B) \right) \gamma_5. \quad (2.53)$$

Note that the an additional term should be added to each of the above transition operators in order to satisfy the relation (2.51). In the Lorentz gauge, however, these terms vanish upon contraction with the photon-polarization four-vector $(\epsilon^\lambda)^\mu$, which is why they are omitted.

Exchange of t -channel vector and axial-vector mesons

The transition operator for the exchange of a Reggeized vector meson M_V in the t channel is

$$T_{M_V}^\mu = -i I_{M_V BN} F_{\gamma M_V M}(Q^2) G_{\gamma^* M_V M} \epsilon^{\mu\nu\sigma\tau} q_\nu (k' - q)_\sigma \times \mathcal{P}_{M_V}(t, s) \left(G_{M_V BN}^v \gamma_\tau + \frac{i G_{M_V BN}^t}{m_N + m_B} \sigma_{\tau\rho} (q - k')^\rho \right). \quad (2.54)$$

For a Reggeized axial-vector meson M_A , the transition operator reads

$$T_{M_A}^\mu = I_{M_A BN} F_{\gamma M_A M}(Q^2) G_{\gamma^* M_A M} \left(q^\nu (k' - q)^\mu - g^{\mu\nu} q_\sigma (k' - q)^\sigma \right) \times \mathcal{P}_{M_A}(t, s) \left(G_{M_A BN}^v \gamma_\nu + \frac{i G_{M_A BN}^t}{m_N + m_B} \sigma_{\nu\tau} (q - k')^\tau \right). \quad (2.55)$$

Exchange of s -channel spin-1/2 resonances

The exchange of a spin-1/2 resonance R in the s channel is described by the transition operator

$$T_R^\mu = \frac{i I_{MBR}}{2m_N} F_{\gamma RN}^m(Q^2) G_{MBR} G_{\gamma RN}^m \Gamma P_R(p + q) \sigma^{\mu\nu} q_\nu \Gamma'. \quad (2.56)$$

Exchange of s -channel spin-3/2 resonances

The transition operator describing the exchange of a spin-3/2 resonance R in the s channel is given by

$$T_R^\mu = \frac{I_{MBR}}{2m_N m_M} G_{MBR} (k' - q)^\nu \Gamma' \Theta_{\nu\sigma}(z_{MBR}) P_R^{\sigma;\tau}(p + q) \times \left(F_{\gamma RN}^{(1)}(Q^2) G_{\gamma RN}^{(1)} \Theta_{\tau\rho}(z_{\gamma RN}^{(1)}) \gamma_\eta - F_{\gamma RN}^{(2)}(Q^2) \frac{G_{\gamma RN}^{(2)}}{2m_N} \Theta_{\tau\rho}(z_{\gamma RN}^{(2)}) p_\eta \right) (q^\rho g^{\eta\mu} - q^\eta g^{\rho\mu}) \Gamma. \quad (2.57)$$

2.4 The Regge-plus-resonance-2007 model for $p(\gamma, K^+)\Lambda$

The RPR formalism conjoins a t -channel Regge-background amplitude with the exchange of resonances in the s channel, and hence has the potential to describe $N(\gamma^{(*)}, M)B$ reactions over a wide energy range. To this day, the RPR formalism has exclusively been applied to model electromagnetic kaon production off the nucleon, or $N(\gamma^{(*)}, K)Y$. In particular, the most extensively studied reaction within the RPR framework is $K^+\Lambda$ photoproduction off the proton. The original $p(\gamma, K^+)\Lambda$ model is described in detail in Refs. [19, 24], and is dubbed the ‘‘RPR-2007 model’’. The forthcoming section will provide a brief summary of the key ingredients and global performance of the RPR-2007 model.

2.4.1 Background and resonance contributions

The RPR-2007 model features the exchange of a rotating K and a rotating K^* Regge trajectory in the t channel (see Sec. 2.3.3), and a specific set of nucleon resonances in the s channel. The included nucleon resonances are listed in Table 2.3. The K and K^* diagrams in the t channel and the nucleon-resonance diagrams in the s channel are described by the transition operators given in Sec. 2.3.5. Each s -channel diagram of the RPR-2007 model is confined by a Gaussian hadronic form factor (see Eq. (2.25)) with a cutoff energy of approximately 1650 MeV. Mathematically, this is realized by multiplying each s -channel transition operator with the hadronic form factor. In the t channel, the natural s -dependence of the Regge amplitude does not require the introduction of a hadronic cutoff.

The specific setting for the RPR-2007 model, mentioned above, is the result of a comparative analysis of different model variants, with varying Regge phases and nucleon-resonance sets, to the forward-scattering $p(\gamma, K^+)\Lambda$ data that was available at that time. The restriction in the angular range of the analyzed data was adopted back then since the RPR framework was originally set up to describe the $p(\gamma, K^+)\Lambda$ reaction at forward scattering. As discussed in Sec. 2.3.3, however, such a constraint does not necessarily have to be imposed.

2.4.2 Performance

The RPR-2007 model provides a good description of the forward-scattering data, against which it was optimized. This is for example observed in Fig. 2.4, which shows a comparison of the RPR-2007 predictions with the $p(\gamma, K^+)\Lambda$ differential cross section data from the CLAS Collaboration at forward, intermediate, and backward scattering. The forward-angle part of these data, more specifically the data for $\cos \theta_K > 0.35$, was employed in the model analysis.

Table 2.3: The spin-parity, mass, and decay width of the nucleon resonances featured by the RPR-2007 model. All except for the $D_{13}(1900)$ are established resonances that are listed in the RPP [1]. The $D_{13}(1900)$ is a so-called ‘‘missing resonance’’ and is predicted by the Capstick-Roberts constituent-quark model [32]. The listed values for the $P_{13}(1720)$ and $P_{13}(1900)$ decay widths correspond with those employed in the RPR-2007 model and deviate from the ones mentioned in the RPP (250 MeV for both).

N^*	$J_{N^*}^P$	m_{N^*} (MeV)	Γ_{N^*} (MeV)
$S_{11}(1650)$	$(1/2)^-$	1655	150
$P_{11}(1710)$	$(1/2)^+$	1710	100
$P_{13}(1720)$	$(3/2)^+$	1720	150
$D_{13}(1900)$	$(3/2)^-$	1895	200
$P_{13}(1900)$	$(3/2)^+$	1900	500

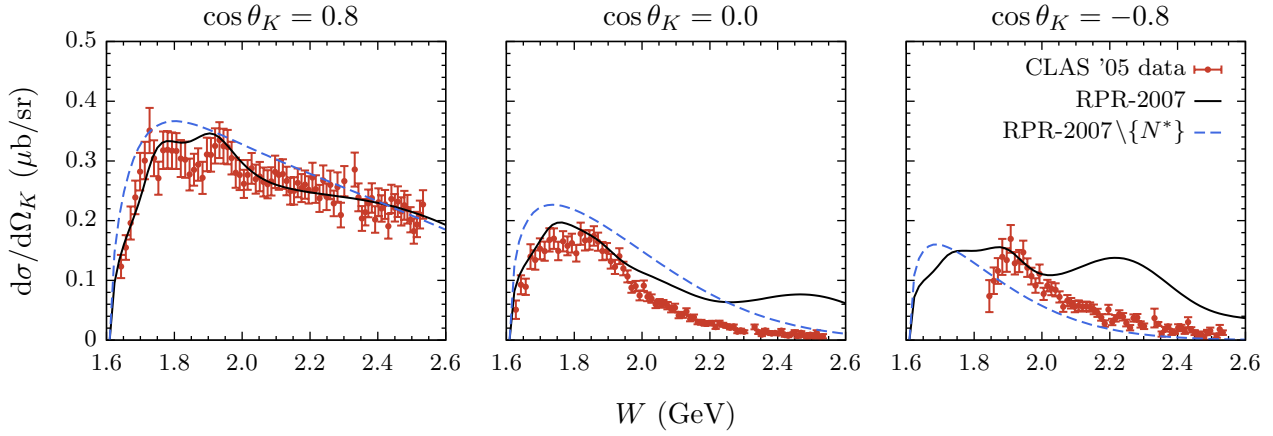


Figure 2.4: The W dependence of the $p(\gamma, K^+)\Lambda$ differential cross section $d\sigma/d\Omega_K$ at forward (left), intermediate (center), and backward (right) kaon-scattering angles. Predictions from the RPR-2007 model with (full curves) and without (dashed curves) nucleon-resonance contributions are shown. The data are from Ref. [33].

Figure 2.4 also shows that RPR-2007 performs gradually worse at increasing kaon-scattering angles. By comparing the full with the dashed curves, which respectively show the RPR-2007 predictions with and without resonance contributions, it becomes clear that this can be mainly attributed to the resonance contributions. The fact that the backward-angle data was not used in the analysis and optimization procedure, on the other hand, is also partly responsible for the observed discrepancy. The level of disagreement with the backward-angle data, however, implies that the specific model assumptions do not suffice to provide a unified description of the data at forward and backward scattering.

Consistent interactions for high-spin fermion fields

Background and outline

The RPR-2007 model, which was introduced in the previous chapter, receives contributions from both spin-1/2 and spin-3/2 nucleon resonances in the s channel. By comparing the transition operators of Eqs. (2.56) and (2.57), it can be inferred that the field-theoretic description of resonances with a higher spin becomes increasingly more complicated. This is one of the major reasons why the RPR-2007 model was originally limited to spin-1/2 and spin-3/2 resonances. The nucleon-resonance spectrum, however, features two spin-5/2 states, namely the $D_{15}(1675)$ and $F_{15}(1680)$, with masses of less than 100 MeV above the $K^+\Lambda$ -production threshold [1]. Hence, it can be inferred that these states might contribute significantly to the $p(\gamma, K^+)\Lambda$ observables. In addition, more massive spin-5/2 (and even higher-spin) states are found in the nucleon-resonance spectrum that could possibly affect the reaction dynamics of $p(\gamma, K^+)\Lambda$. Consequently, extension of the RPR model to include higher-spin resonances is in order.

In quantum field theory, free spin-1/2 particles are described by Dirac fields. A Dirac field consists of a plane wave, multiplied by a Dirac spinor which has four components. These components correspond with the two spin states of both the particle and the antiparticle. Fermions with a higher spin are commonly described by the Rarita-Schwinger (RS) theory [34]. In the RS theory, a free spin- $(n + 1/2)$ particle with mass m is represented by the RS field $\psi^{\mu_1 \dots \mu_n}$ which obeys the RS equations:

$$\begin{aligned} (i\partial - m)\psi^{\mu_1 \dots \mu_n} &= 0, \\ \gamma_{\mu_1} \psi^{\mu_1 \dots \mu_n} &= 0. \end{aligned}$$

The RS field $\psi^{\mu_1 \dots \mu_n}$ is totally symmetric in its Lorentz indices and, as the RS equations imply, each of its components has a spinor index. By construction, the RS fields have too many degrees

of freedom, which can be associated with unphysical lower-spin components. For on-shell RS fields, these unphysical degrees of freedom are removed by the so-called “RS constraints”, $\gamma_{\mu_1} \psi^{\mu_1 \dots \mu_n} = 0$. When the RS field is off its mass shell, however, the unphysical components do not longer decouple. The latter are contained in the RS propagator and for a general interaction vertex these do not cancel upon contracting both tensors. The interaction vertex must be constructed so that only the physical components of the RS propagator participate in the interaction. An interaction that features this property will be referred to as a “consistent interaction”.

The spin-3/2 resonances of the RPR-2007 model are described by RS fields. The transition operator of Eq. (2.57), describing the s -channel exchange of these resonances, receives contributions from the unphysical components of the spin-3/2 RS propagator of Eq. (2.47). In fact, the three off-shell parameters featured by this transition operator, allow for an arbitrary coupling strength to the unphysical states of the RS propagator. In this chapter, a consistent-interaction formalism will be developed for massive, off-shell RS fields of arbitrary spin. With regard to the RPR framework, such a formalism will allow for the consistent description of high-spin resonance interactions. In addition, the application of consistent interactions within isobar frameworks will be examined.

PHYSICAL REVIEW C **84**, 045201 (2011)**Consistent interactions for high-spin fermion fields**

Tom Vrancx,* Lesley De Cruz, Jan Ryckebusch, and Pieter Vanraeyveld

Department of Physics and Astronomy, Ghent University, Proeftuinstraat 86, B-9000 Ghent, Belgium

(Received 26 May 2011; published 3 October 2011)

We address the issue of consistent interactions for off-shell fermion fields of arbitrary spin. These interactions play a crucial role in the quantum hydrodynamical description of high-spin baryon resonances in hadronic processes. The Rarita-Schwinger (R-S) description of high-spin fermion fields involves unphysical degrees of freedom associated with their lower-spin content. These enter the interaction if not eliminated outright. The invariance condition of the interaction under the unconstrained R-S gauge removes the lower-spin content of the fermion propagator and leads to a consistent description of the interaction. We develop the most general consistent interaction structure for high-spin fermions. We find that the power of the momentum dependence of a consistent interaction rises with the spin of the fermion field. This leads to unphysical structures in the energy dependence of the computed tree-level cross sections when the short-distance physics is cut off with standard hadronic form factors. A spin-dependent hadronic form factor is proposed that suppresses the unphysical artifacts.

DOI: [10.1103/PhysRevC.84.045201](https://doi.org/10.1103/PhysRevC.84.045201)

PACS number(s): 11.15.-q, 13.60.Le, 13.75.-n, 14.20.Gk

I. INTRODUCTION

In 1941, Rarita and Schwinger proposed a quantum-field theory for particles with an arbitrary half-integral spin s [1]. Today, 70 years later, this theory is commonly used to describe phenomena that involve relativistic high-spin ($s \geq 3/2$) fermions. In the Rarita-Schwinger (R-S) theory, a relativistic spin- s fermion, with $s = n + 1/2$ and $n \in \mathbb{N}^*$, is described by the totally symmetric spin- $(n + 1/2)$ field $\psi_{\mu_1 \dots \mu_n}$, which obeys the so-called R-S equations,

$$(i\cancel{\partial} - m)\psi_{\mu_1 \dots \mu_n} = 0, \quad (1a)$$

$$\gamma^{\mu_1} \psi_{\mu_1 \mu_2 \dots \mu_n} = 0. \quad (1b)$$

These equations comprise the equations of motion (1a), which are akin to those of the Dirac theory, and the R-S constraints (1b). By construction, R-S fields have redundant degrees of freedom (dof), which are associated with unphysical lower-spin fields. Massive R-S fields have $\frac{4(n+3)!}{3!n!}$ dof, whereas, the required number is $4(n+1)$. The R-S constraints (1b) eliminate the redundant dof of noninteracting R-S fields [1]. Massless R-S fields, however, can have only 4 dof to guarantee consistency with the special theory of relativity. Therefore, the massless R-S theory should be invariant under the spin- $(n + 1/2)$ R-S gauge (R-S $_{n+1/2}$) [2],

$$\psi_{\mu_1 \dots \mu_n} \rightarrow \psi_{\mu_1 \dots \mu_n} + \frac{i}{n(n-1)!} \sum_{P(\mu)} \partial_{\mu_1} \xi_{\mu_2 \dots \mu_n}, \quad (2)$$

$$\gamma^{\mu_1} \xi_{\mu_1 \mu_2 \dots \mu_{n-1}} = 0.$$

The notation $\sum_{P(\mu)}$ denotes the summing over all the permutations of the μ_i indices. Further, $\xi_{\mu_1 \dots \mu_{n-1}}$ represents a totally symmetric space-time-dependent rank- $(n-1)$ tensor-spinor field. The inclusion of the factor i in Eq. (2) is a convention. If $\psi_{\mu_1 \dots \mu_n}$ is a real field, then the field $\xi_{\mu_1 \dots \mu_{n-1}}$ has to be defined as an imaginary field.

The interacting case is more convoluted. If the R-S field is off its mass shell (off shell), the unphysical R-S components might participate in the interaction if not eliminated in a controlled way. Such an interaction is dubbed inconsistent since it is not mediated purely by the physical component of the R-S field. Several physically unacceptable problems are associated with these inconsistent interactions, the most famous of which are the Johnson-Sudarshan and Velo-Zwanzinger problems [3,4].

In 1998, Pascalutsa succeeded in formulating a consistent interaction theory for massive spin-3/2 fields [5]. The consistency is provided by the invariance of the spin-3/2 interaction under the local $U(1)$ gauge. In Sec. II A of this paper, Pascalutsa's theory is extended, and a consistent interaction theory for massive spin-5/2 fields is developed. In Sec. II B, the most general consistent interaction structure for massive spin- $(n + 1/2)$ fields is derived, based on a generalization of the results obtained for the spin-5/2 theory in Sec. II A. Then, consistent couplings for the $(\phi \psi \psi_{\mu_1 \dots \mu_n}^*)$ and $(A_\mu \psi \psi_{\mu_1 \dots \mu_n}^*)$ theories are constructed. Here, the fields ϕ , ψ , and A_μ represent a spin-0 field, a spin-1/2 field, and a spin-1 field. Section III illustrates the application of the consistent $(\phi \psi \psi_{\mu_1 \dots \mu_n}^*)$ and $(A_\mu \psi \psi_{\mu_1 \dots \mu_n}^*)$ couplings in hadron physics. In Sec. III A, the problems that arise when combining consistent high-spin interactions with standard hadronic form factors are discussed. An alternative hadronic form factor is proposed in Sec. III B, which remedies the issues mentioned in Sec. III A. Finally, Sec. IV states the conclusions of this paper.

II. CONSISTENT INTERACTIONS**A. The massive spin-5/2 field****1. Gauge invariance as a requirement for a consistent interaction theory**

A general interaction theory for a massive off-shell spin-5/2 field $\psi_{\mu\nu}$ and an on-shell source $J_{\mu\nu}$ can be constructed from

*tom.vrancx@ugent.be

VRANCX, DE CRUZ, RYCKEBUSCH, AND VANCRAEYVELD

PHYSICAL REVIEW C **84**, 045201 (2011)

a Lagrangian of the type,

$$\mathcal{L}_I = \bar{\psi}_{\mu\nu} J^{\mu\nu} + \bar{J}_{\mu\nu} \psi^{\mu\nu}, \quad (3)$$

where the subscript I stands for interaction. To obtain a consistent spin-5/2 interaction theory, \mathcal{L}_I has to be constructed in such a way that only the physical $\mathcal{P}_{\mu\nu;\lambda\rho}^{5/2}(\partial)\psi^{\lambda\rho}$ component of $\psi_{\mu\nu}$ mediates the interaction, i.e.,

$$\begin{aligned} \bar{\Gamma}_f^{\mu\nu}(\{p_f\})P_{\mu\nu;\lambda\rho}(p)\Gamma_i^{\lambda\rho}(\{p_i\}) \\ = \bar{\Gamma}_f^{\mu\nu}(\{p_f\})\frac{\not{p} + m}{p^2 - m^2}\mathcal{P}_{\mu\nu;\lambda\rho}^{5/2}(p)\Gamma_i^{\lambda\rho}(\{p_i\}), \end{aligned} \quad (4)$$

with m as the mass of $\psi_{\mu\nu}$, $\Gamma_{i,f}^{\mu\nu}(\{p_{i,f}\})$ as the initial-final interaction vertex, which is derived from the source $J_{i,f}^{\mu\nu}$, $P_{\mu\nu;\lambda\rho}(p)$ as the spin-5/2 propagator, and $\mathcal{P}_{\mu\nu;\lambda\rho}^{5/2}(p)$ as the spin-5/2 projection operator. Furthermore, p represents the four-momentum of $\psi_{\mu\nu}$, and $\{p_{i,f}\}$ denotes the collection of four-momenta of the fields that are contained in $J_{i,f}^{\mu\nu}$. The explicit expressions for the spin-5/2 projection operator and the spin-3/2 and spin-1/2 projection operators, which project the field $\psi_{\mu\nu}$ onto its unphysical spin-3/2 and spin-1/2 components, are given in Appendix A.

The propagator $P_{\mu\nu;\lambda\rho}(p)$ can be projected onto the spin-5/2, the spin-3/2, and the spin-1/2 projection operators, which span the complete spin-5/2 space in the R-S representation. As seen from Eqs. (A1)–(A3), the spin-projection operators contain terms that are proportional to p^{-2} and p^{-4} . However, to describe a massive off-shell spin-5/2 field in a physically meaningful way, $P_{\mu\nu;\lambda\rho}(p)$ has to be regular for $p^2 \rightarrow 0$. So, in the expression for $P_{\mu\nu;\lambda\rho}(p)$, the singular terms, which stem from the spin-projection operators, have to cancel each other out.

In a consistent spin-5/2 interaction, only the physical spin-5/2 component of $P_{\mu\nu;\lambda\rho}(p)$ remains, as expressed through Eq. (4). Since the left-hand side of Eq. (4) is regular for $p^2 \rightarrow 0$, the right-hand side of this equation has to be regular for $p^2 \rightarrow 0$ as well. So, for Eq. (4) to hold, the singular terms of the spin-5/2 projection operator have to be removed by the interaction vertices $\Gamma_{i,f}^{\mu\nu}(\{p_{i,f}\})$. This implies that the interaction vertices cannot be completely arbitrary. Instead, they have to be constrained by a certain local symmetry. This local symmetry can readily be found. Indeed, all of the singular terms of $\mathcal{P}_{\mu\nu;\lambda\rho}^{5/2}(p)$, at least, are linear in p_μ , p_ν , p_λ , or p_ρ . It is straightforward to show that the right-hand side of Eq. (4) is

only regular for $p^2 \rightarrow 0$ when the interaction vertices satisfy the following transversality conditions:

$$p_\mu \Gamma_I^{\mu\nu} = 0, \quad p_\nu \Gamma_I^{\mu\nu} = 0. \quad (5)$$

This requirement is equivalent to the invariance of \mathcal{L}_I under the unconstrained spin-5/2 R-S (uR-S_{5/2}) gauge,

$$\psi_{\mu\nu} \rightarrow \psi_{\mu\nu} + \frac{i}{2}(\partial_\mu \chi_\nu + \partial_\nu \chi_\mu), \quad (6)$$

where χ_μ represents an arbitrary space-time-dependent rank-1 tensor-spinor field. The invariance of interaction theories under the uR-S_{5/2} gauge of Eq. (6) is the required local symmetry that guarantees the consistency of massive off-shell spin-5/2 interactions.

To construct interaction vertices (which are derived from the sources) that satisfy conditions (5) is not a trivial task. However, by using a field construction that is invariant under the uR-S_{5/2} gauge (6), the problem of finding conserved sources can be circumvented.

2. The gauge-invariant field

Inspired by the gauge-invariant field,

$$G_{\mu,\nu} = i(\partial_\mu \psi_\nu - \partial_\nu \psi_\mu), \quad (7)$$

which was introduced by Pascalutsa in Ref. [5] to set up consistent interaction theories for spin-3/2 particles, a gauge-invariant spin-5/2 field can be constructed. The field $G_{\mu,\nu}$ can be rewritten as

$$G_{\mu,\nu} = i(\partial_\mu g_{\nu\lambda} - \partial_\nu g_{\mu\lambda})\psi^\lambda = O_{(\mu,\nu)\lambda}^{3/2}(\partial)\psi^\lambda, \quad (8)$$

which reveals the interaction operator $O_{(\mu,\nu)\lambda}^{3/2}(\partial) = -O_{(\nu,\mu)\lambda}^{3/2}(\partial)$. This operator has the following property:

$$\partial^\lambda O_{(\mu,\nu)\lambda}^{3/2}(\partial) = O_{(\mu,\nu)\lambda}^{3/2}(\partial)\partial^\lambda = 0, \quad (9)$$

which ensures the invariance of $G_{\mu,\nu}$ under the uR-S_{5/2} gauge. The notation $(\mu, \nu)\lambda$, for the tensor indices of the spin-3/2 interaction operator, is used to separate the actual Lorentz indices of the gauge-invariant field, i.e., μ and ν , from the Lorentz index that is contracted with the spin-3/2 field, i.e., λ . The corresponding spin-5/2 interaction operator, i.e., $O_{(\mu\nu,\lambda\rho)\sigma\tau}^{5/2}(\partial)$, is constructed from the direct product of two spin-3/2 interaction operators,

$$\begin{aligned} O_{(\mu\nu,\lambda\rho)\sigma\tau}^{5/2}(\partial) &= \frac{1}{4}[O_{(\mu,\lambda)\sigma}^{3/2}(\partial)O_{(\nu,\rho)\tau}^{3/2}(\partial) + O_{(\mu,\rho)\sigma}^{3/2}(\partial)O_{(\nu,\lambda)\tau}^{3/2}(\partial) + O_{(\mu,\lambda)\tau}^{3/2}(\partial)O_{(\nu,\rho)\sigma}^{3/2}(\partial) + O_{(\mu,\rho)\tau}^{3/2}(\partial)O_{(\nu,\lambda)\sigma}^{3/2}(\partial)] \\ &= -\frac{1}{2}\partial_\mu\partial_\nu(g_{\lambda\sigma}g_{\rho\tau} + g_{\lambda\tau}g_{\rho\sigma}) - \frac{1}{2}\partial_\lambda\partial_\rho(g_{\mu\sigma}g_{\nu\tau} + g_{\mu\tau}g_{\nu\sigma}) + \frac{1}{4}\partial_\mu\partial_\lambda(g_{\nu\sigma}g_{\rho\tau} + g_{\nu\tau}g_{\rho\sigma}) + \frac{1}{4}\partial_\mu\partial_\rho(g_{\nu\sigma}g_{\lambda\tau} + g_{\nu\tau}g_{\lambda\sigma}) \\ &\quad + \frac{1}{4}\partial_\nu\partial_\lambda(g_{\mu\sigma}g_{\rho\tau} + g_{\mu\tau}g_{\rho\sigma}) + \frac{1}{4}\partial_\nu\partial_\rho(g_{\mu\sigma}g_{\lambda\tau} + g_{\mu\tau}g_{\lambda\sigma}). \end{aligned} \quad (10)$$

The corresponding gauge-invariant field for the spin-5/2 theory reads

$$\begin{aligned} G_{\mu\nu,\lambda\rho} &= O_{(\mu\nu,\lambda\rho)\sigma\tau}^{5/2}(\partial)\psi^{\sigma\tau} \\ &= -\partial_\mu\partial_\nu\psi_{\lambda\rho} - \partial_\lambda\partial_\rho\psi_{\mu\nu} \\ &\quad + \frac{1}{2}(\partial_\mu\partial_\lambda\psi_{\nu\rho} + \partial_\mu\partial_\rho\psi_{\nu\lambda} + \partial_\nu\partial_\lambda\psi_{\mu\rho} + \partial_\nu\partial_\rho\psi_{\mu\lambda}), \end{aligned} \quad (11)$$

where the symmetry of the spin-5/2 field, i.e., $\psi_{\mu\nu} = \psi_{\nu\mu}$, has been applied. This field is invariant under the uR-S_{5/2} gauge (6) since

$$\begin{aligned} \partial^\sigma O_{(\mu\nu,\lambda\rho)\sigma\tau}^{5/2}(\partial) &= O_{(\mu\nu,\lambda\rho)\sigma\tau}^{5/2}(\partial)\partial^\sigma = 0, \\ \partial^\tau O_{(\mu\nu,\lambda\rho)\sigma\tau}^{5/2}(\partial) &= O_{(\mu\nu,\lambda\rho)\sigma\tau}^{5/2}(\partial)\partial^\tau = 0. \end{aligned} \quad (12)$$

The specific definition (10) for the spin-5/2 interaction operator is chosen so as to symmetrize $G_{\mu\nu,\lambda\rho}$, i.e.,

$$\begin{aligned} G_{\mu\nu,\lambda\rho} &= G_{\nu\mu,\lambda\rho} = G_{\mu\nu,\rho\lambda} = G_{\nu\mu,\rho\lambda}, \\ G_{\mu\nu,\lambda\rho} &= G_{\lambda\rho,\mu\nu}. \end{aligned} \quad (13)$$

An interaction theory constructed from $G_{\mu\nu,\lambda\rho}$ and a source $T_{\mu\nu\lambda\rho}$, i.e.,

$$\mathcal{L}_I = \bar{G}_{\mu\nu,\lambda\rho} T^{\mu\nu\lambda\rho} + \bar{T}_{\mu\nu\lambda\rho} G^{\mu\nu,\lambda\rho}, \quad (14)$$

consequently, generates interaction vertices that obey the transversality conditions of Eq. (5).

3. The propagator and the consistent interaction structure

Apart from the interaction vertices, the Feynman propagator is another key element in the quantum-field theory of an interaction. The Lagrangian \mathcal{L}_I , defined in Eq. (14), gives rise to the following interaction structure:

$$O_{(\mu\nu,\lambda\rho)\sigma\tau}^{5/2}(p) P^{\sigma\tau;\sigma'\tau'}(p) O_{(\mu'\nu',\lambda'\rho')\sigma'\tau'}^{5/2}(p), \quad (15)$$

in the transition amplitude. In Ref. [6], Shklyar *et al.* derived an explicit form for the spin-5/2 propagator $P_{\mu\nu,\lambda\rho}(p)$. This propagator form, however, is not suitable for the current analysis because it does not lead to the consistent interaction structure of Eq. (4). In other words, with the propagator of Ref. [6], the imposed condition of invariance of the interaction theory under the uR-S_{5/2} gauge (6) is not sufficient to remove the unphysical interactions from the Feynman amplitude. Indeed, using properties (12) in momentum space and the explicit definitions of the lower-spin projection operators (A2) and (A3), it is easy to show that

$$\begin{aligned} O_{(\mu\nu,\lambda\rho)\sigma\tau}^{5/2}(p) \mathcal{P}_{ij}^{3/2,\sigma\tau;\sigma'\tau'}(p) O_{(\mu'\nu',\lambda'\rho')\sigma'\tau'}^{5/2}(p) &= 0, \\ i, j &= 1, 2, \\ ij &\neq 22, \end{aligned} \quad (16)$$

and

$$\begin{aligned} O_{(\mu\nu,\lambda\rho)\sigma\tau}^{5/2}(p) \mathcal{P}_{kl}^{1/2,\sigma\tau;\sigma'\tau'}(p) O_{(\mu'\nu',\lambda'\rho')\sigma'\tau'}^{5/2}(p) &= 0, \\ k, l &= 1, 2, 3, \\ kl &\neq 22. \end{aligned} \quad (17)$$

This implies that all the lower-spin components of $\psi_{\mu\nu}$, except for $\mathcal{P}_{22,\mu\nu;\lambda\rho}^{1/2}(\partial)\psi^{\lambda\rho}$ and $\mathcal{P}_{22,\mu\nu;\lambda\rho}^{3/2}(\partial)\psi^{\lambda\rho}$, decouple from a gauge-invariant spin-5/2 interaction. The propagator from Ref. [6], however, contains these projection operators for arbitrary values of its two free parameters. For a specific choice of one of the parameters, $\mathcal{P}_{22,\mu\nu;\lambda\rho}^{3/2}(p)$ can be removed from the propagator. However, this is not the case for the spin-1/2 sector, and the interaction always receives contributions from the propagating $\mathcal{P}_{22,\mu\nu;\lambda\rho}^{1/2}(\partial)\psi^{\lambda\rho}$ component. This peculiarity is intimately related to the infamous discontinuity in the R-S description of spin-5/2 fields, which was found by Berends *et al.* in Ref. [7]: The zero-mass limit of the massive theory does not coincide with the massless theory, which is invariant under the R-S_{5/2} gauge (2). The conclusion is that a gauge-invariant spin-5/2 propagator, i.e., without terms proportional to $\mathcal{P}_{22,\mu\nu;\lambda\rho}^{1/2}(p)$ and $\mathcal{P}_{22,\mu\nu;\lambda\rho}^{3/2}(p)$, cannot be derived from the massive spin-5/2 theory. It is clear that, to construct a consistent interaction from a gauge-invariant theory, a different approach should be adopted.

The commonly used spin-3/2 propagator reads [8]

$$\begin{aligned} P_{\mu;\nu}(p) &= \frac{\not{p} + m}{p^2 - m^2} \left(g_{\mu\nu} - \frac{1}{3} \gamma_\mu \gamma_\nu - \frac{1}{3m} (\gamma_\mu p_\nu - \gamma_\nu p_\mu) \right. \\ &\quad \left. - \frac{2}{3m^2} p_\mu p_\nu \right). \end{aligned} \quad (18)$$

It is important to note that this propagator results from a massive theory that is invariant under the R-S_{3/2} gauge in the zero-mass limit [5]. The projection operator that projects the spin-3/2 field ψ_μ onto the physical spin-3/2 component $\mathcal{P}_{\mu\nu}^{3/2}(\partial)\psi^\nu$ is given by [8]

$$\begin{aligned} \mathcal{P}_{\mu;\nu}^{3/2}(p) &= \left(g_{\mu\nu} - \frac{1}{3} \gamma_\mu \gamma_\nu - \frac{\not{p}}{3p^2} (\gamma_\mu p_\nu - \gamma_\nu p_\mu) \right. \\ &\quad \left. - \frac{2}{3p^2} p_\mu p_\nu \right). \end{aligned} \quad (19)$$

A closer inspection shows that the gauge-invariant spin-3/2 propagator (18) can be obtained from the spin-3/2 projection operator (19) by means of the following substitutions:

$$\not{p} \rightarrow m, \quad p^2 \rightarrow m^2, \quad (20)$$

and subsequently, by multiplying it with $(\not{p} - m)^{-1}$. Since $[\not{p}, \gamma_\mu] \neq 0$, the substitution $\not{p} \rightarrow m$ of Eq. (20) only holds when all the \not{p} 's are moved to the left from the Dirac matrices, which is the case in expression (19). Equivalently, when all the \not{p} 's are moved to the right from the Dirac matrices, the substitution $\not{p} \rightarrow -m$ should be carried out. By applying the prescription of Eq. (20) to the spin-5/2 projection operator (A1), the following expression for the spin-5/2 propagator is

obtained:

$$\begin{aligned}
P_{\mu\nu;\lambda\rho}(p) = & \frac{\not{p} + m}{p^2 - m^2} \left[\frac{1}{2}(g_{\mu\lambda}g_{\nu\rho} + g_{\mu\rho}g_{\nu\lambda}) - \frac{1}{5}g_{\mu\nu}g_{\lambda\rho} - \frac{1}{10}(g_{\mu\lambda}\gamma_\nu\gamma_\rho + g_{\mu\rho}\gamma_\nu\gamma_\lambda + g_{\nu\lambda}\gamma_\mu\gamma_\rho + g_{\nu\rho}\gamma_\mu\gamma_\lambda) \right. \\
& + \frac{1}{10m}(g_{\mu\lambda}(p_\nu\gamma_\rho - p_\rho\gamma_\nu) + g_{\mu\rho}(p_\nu\gamma_\lambda - p_\lambda\gamma_\nu) + g_{\nu\lambda}(p_\mu\gamma_\rho - p_\rho\gamma_\mu) + g_{\nu\rho}(p_\mu\gamma_\lambda - p_\lambda\gamma_\mu)) \\
& + \frac{1}{5m^2}(g_{\mu\nu}p_\nu p_\rho + g_{\lambda\rho}p_\mu p_\nu) - \frac{2}{5m^2}(g_{\mu\lambda}p_\nu p_\rho + g_{\mu\rho}p_\nu p_\lambda + g_{\nu\lambda}p_\mu p_\rho + g_{\nu\rho}p_\mu p_\lambda) \\
& + \frac{1}{10m^2}(\gamma_\mu\gamma_\lambda p_\nu p_\rho + \gamma_\mu\gamma_\rho p_\nu p_\lambda + \gamma_\nu\gamma_\lambda p_\mu p_\rho + \gamma_\nu\gamma_\rho p_\mu p_\lambda) + \frac{1}{5m^3}(\gamma_\mu p_\nu p_\lambda p_\rho + \gamma_\nu p_\mu p_\lambda p_\rho \\
& \left. - \gamma_\lambda p_\mu p_\nu p_\rho - \gamma_\rho p_\mu p_\nu p_\lambda) + \frac{2}{5m^4}p_\mu p_\nu p_\lambda p_\rho \right]. \quad (21)
\end{aligned}$$

The expansion of $P_{\mu\nu;\lambda\rho}(p)$ in terms of the projection operators defined in Eqs. (A1)–(A3) reads:

$$\begin{aligned}
P_{\mu\nu;\lambda\rho}(p) = & \left[\frac{\not{p} + m}{p^2 - m^2} \mathcal{P}^{5/2} - \frac{4}{5m^2}(\not{p} + m)\mathcal{P}_{11}^{3/2} + \frac{1}{\sqrt{5}m}(\mathcal{P}_{12}^{3/2} + \mathcal{P}_{21}^{3/2}) + \frac{2}{5m^4}(\not{p} + m)(p^2 - m^2)\mathcal{P}_{11}^{1/2} - \frac{1}{5m^2}(\not{p} + m)\mathcal{P}_{33}^{1/2} \right. \\
& \left. + \frac{\sqrt{3}}{5m^2}(\not{p} + m)(\mathcal{P}_{12}^{1/2} + \mathcal{P}_{21}^{1/2}) - \frac{\sqrt{6}}{5m^3}(p^2 - m^2)(\mathcal{P}_{13}^{1/2} + \mathcal{P}_{31}^{1/2}) - \frac{\sqrt{2}}{5m}(\mathcal{P}_{32}^{3/2} + \mathcal{P}_{23}^{3/2}) \right]_{\mu\nu;\lambda\rho} (p). \quad (22)
\end{aligned}$$

This propagator is a Hermitian operator,

$$P_{\mu\nu;\lambda\rho}^\dagger(p) = \gamma_0 P_{\lambda\rho;\mu\nu}(p) \gamma_0, \quad (23)$$

and has the following symmetry properties:

$$P_{\mu\nu;\lambda\rho}(p) = P_{\nu\mu;\lambda\rho}(p) = P_{\mu\nu;\rho\lambda}(p) = P_{\nu\mu;\rho\lambda}(p). \quad (24)$$

Moreover, this propagator does not receive contributions from $\mathcal{P}_{22,\mu\nu;\lambda\rho}^{1/2}(p)$ and $\mathcal{P}_{22,\mu\nu;\lambda\rho}^{3/2}(p)$. As a result, it generates consistent couplings from gauge-invariant interaction theories,

$$\begin{aligned}
O_{(\mu\nu,\lambda\rho)\sigma\tau}^{5/2}(p) P^{\sigma\tau;\sigma'\tau'}(p) O_{(\mu'\nu',\lambda'\rho')\sigma'\tau'}^{5/2}(p) \\
= \frac{\not{p} + m}{p^2 - m^2} O_{(\mu\nu,\lambda\rho)\sigma\tau}^{5/2}(p) \mathcal{P}^{5/2,\sigma\tau;\sigma'\tau'}(p) O_{(\mu'\nu',\lambda'\rho')\sigma'\tau'}^{5/2}(p), \quad (25)
\end{aligned}$$

which is precisely of the form proposed in Eq. (4). As a result, the unphysical components in the propagator completely decouple from the interaction, which is fully mediated by the physical spin-5/2 component $\mathcal{P}_{\mu\nu;\lambda\rho}^{5/2}(\partial)\psi^{\lambda\rho}$. By combining Eqs. (12) and (21), the consistent interaction structure (25) can be reduced to

$$\begin{aligned}
O_{(\mu\nu,\lambda\rho)\sigma\tau}^{5/2}(p) P^{\sigma\tau;\sigma'\tau'}(p) O_{(\mu'\nu',\lambda'\rho')\sigma'\tau'}^{5/2}(p) \\
= \frac{\not{p} + m}{p^2 - m^2} O_{(\mu\nu,\lambda\rho)\sigma\tau}^{5/2}(p) O_{(\mu'\nu',\lambda'\rho')\sigma'\tau'}^{5/2}(p) \\
\times \left[\frac{1}{2}(g^{\sigma\sigma'}g^{\tau\tau'} + g^{\sigma\tau'}g^{\tau\sigma'}) - \frac{1}{5}g^{\sigma\tau}g^{\sigma'\tau'} \right. \\
\left. - \frac{1}{10}(g^{\sigma\sigma'}\gamma^\tau\gamma^{\tau'} + g^{\sigma\tau'}\gamma^\tau\gamma^{\sigma'}) \right. \\
\left. + g^{\tau\sigma'}\gamma^\sigma\gamma^{\tau'} + g^{\tau\tau'}\gamma^\sigma\gamma^{\sigma'} \right]. \quad (26)
\end{aligned}$$

From Eq. (26), it becomes clear why relation (25) holds without resorting to the decomposition (22) of the propagator.

The propagator was obtained from the spin-5/2 projection operator by means of the substitutions (20). These only affect the terms that, at least, are linear in p_μ , which all vanish upon contraction with the interaction operator since relations (12) hold. As a result, only the physical component of the propagator remains present in Eq. (25).

The above-mentioned method for deriving $P_{\mu\nu;\lambda\rho}(p)$ raises some issues. As a matter of fact, there is an infinite number of propagators that satisfy conditions (23) and (24) and concurrently lead to consistent interactions. However, it is confirmed by Huang *et al.*, in their paper on the Feynman propagator for a particle with arbitrary spin [9], that expression (21) is indeed the appropriate one for the spin-5/2 propagator apart from a series of noncovariant terms. As emphasized by Weinberg in Ref. [10], the noncovariant terms should be removed from the Feynman propagator to guarantee that the S matrix remains invariant under proper orthochronous Lorentz transformations. The derivation of the Feynman propagator by Huang *et al.* does not rely on the expression for the free R-S Lagrangian. Instead, the propagator is derived from its definition: the vacuum expectation value of the time-ordered product of the free R-S field and its adjoint. For the spin-5/2 theory, this definition gives rise to the following propagator:

$$\begin{aligned}
\Delta_F^{\mu\nu;\lambda\rho}(x - x') = & \langle 0 | \mathcal{T} \{ \psi^{\mu\nu}(x) \bar{\psi}^{\lambda\rho}(x') \} | 0 \rangle, \\
= & \theta(t - t') \langle 0 | \psi^{\mu\nu}(x) \bar{\psi}^{\lambda\rho}(x') | 0 \rangle \\
& - \theta(t' - t) \langle 0 | \bar{\psi}^{\lambda\rho}(x') \psi^{\mu\nu}(x) | 0 \rangle. \quad (27)
\end{aligned}$$

The calculation of the Feynman propagator by Huang *et al.* is based on the solutions to the R-S Eqs. (1). Therefore, this method does not suffer from the mentioned discontinuity between the massive and the massless spin-5/2 theory.

In Ref. [11], Shklyar *et al.* obtained a consistent spin-5/2 interaction by the explicit replacement,

$$P'_{\mu\nu;\lambda\rho}(p) \rightarrow \frac{p^4}{m^4} \frac{\not{p} + m}{p^2 - m^2} \mathcal{P}_{\mu\nu;\lambda\rho}^{5/2}(p), \quad (28)$$

in the expression for the spin-5/2 interaction structure. They use the following expression for $P'_{\mu\nu;\lambda\rho}(p)$:

$$\begin{aligned} P'_{\mu\nu;\lambda\rho}(p) = & \frac{\not{p} + m}{p^2 - m^2} \left(\frac{1}{2} (S_{\mu\lambda} S_{\nu\rho} + S_{\mu\rho} S_{\nu\lambda}) - \frac{1}{5} S_{\mu\nu} S_{\lambda\rho} \right. \\ & + \frac{1}{10} (\not{\delta}_{\mu} \not{\delta}_{\lambda} S_{\nu\rho} + \not{\delta}_{\mu} \not{\delta}_{\rho} S_{\nu\lambda} \\ & \left. + \not{\delta}_{\nu} \not{\delta}_{\lambda} S_{\mu\rho} + \not{\delta}_{\nu} \not{\delta}_{\rho} S_{\mu\lambda}) \right), \quad (29) \end{aligned}$$

with

$$\begin{aligned} S_{\mu\nu}(p) &= -g_{\mu\nu} + \frac{1}{m^2} p_{\mu} p_{\nu}, \\ \not{\delta}_{\mu}(p) &= \gamma^{\nu} S_{\mu\nu}(p) \\ &= -\gamma_{\mu} + \frac{\not{p}}{m^2} p_{\mu}. \quad (30) \end{aligned}$$

Note that $P'_{\mu\nu;\lambda\rho}(p)$ does not coincide with $P_{\mu\nu;\lambda\rho}(p)$ of Eq. (21). In Ref. [11], Shklyar *et al.* assume that a uR-S_{5/2} gauge-invariant interaction leads to the substitution (28) in the spin-5/2 interaction structure. However, they do not prove this statement. Furthermore, $P'_{\mu\nu;\lambda\rho}(p)$ is not a spin-5/2 propagator, it is a regular spin-5/2 projection operator that is multiplied with $(\not{p} - m)^{-1}$. By regular, we mean that the singular p^{-2} and p^{-4} factors of the spin-5/2 projection operator are replaced with the factors m^{-2} and m^{-4} , respectively.

B. Massive fermion fields with arbitrary spin

1. The general consistent interaction structure

In the previous section, it was demonstrated how consistent interaction structures can be constructed for off-shell spin-5/2 fields. These results will now be generalized for off-shell spin- s fermions with $s = n + 1/2$ and $n \in \mathbb{N}^*$.

The generalized interaction operator is defined as

$$\begin{aligned} & O_{(\mu_1 \dots \mu_n, \nu_1 \dots \nu_n) \lambda_1 \dots \lambda_n}^{n+1/2}(\partial) \\ &= \frac{1}{(n!)^2} \sum_{P(v)} \sum_{P(\lambda)} O_{(\mu_1, \nu_1) \lambda_1}^{3/2}(\partial) \dots O_{(\mu_n, \nu_n) \lambda_n}^{3/2}(\partial). \quad (31) \end{aligned}$$

Note that

$$\begin{aligned} & \tilde{O}_{(\mu_1 \dots \mu_n, \nu_1 \dots \nu_n) \lambda_1 \dots \lambda_n}^{n+1/2}(\partial) \\ &= \frac{1}{(n!)^3} \sum_{P(\mu)} \sum_{P(v)} \sum_{P(\lambda)} O_{(\mu_1, \nu_1) \lambda_1}^{3/2}(\partial) \dots O_{(\mu_n, \nu_n) \lambda_n}^{3/2}(\partial) \\ &= 0, \quad (32) \end{aligned}$$

since this operator is symmetric under $\mu_i \leftrightarrow \nu_j$ and $O_{(\mu, \nu) \lambda}^{3/2} = -O_{(\nu, \mu) \lambda}^{3/2}$. The associated gauge-invariant field for the spin- $(n + 1/2)$ theory is given by

$$G_{\mu_1 \dots \mu_n, \nu_1 \dots \nu_n} = O_{(\mu_1 \dots \mu_n, \nu_1 \dots \nu_n) \lambda_1 \dots \lambda_n}^{n+1/2}(\partial) \psi^{\lambda_1 \dots \lambda_n}, \quad (33)$$

where $\psi_{\mu_1 \dots \mu_n}$ represents the spin- $(n + 1/2)$ R-S field. By considering the expression for $O_{(\mu_1 \dots \mu_n, \nu_1 \dots \nu_n) \lambda_1 \dots \lambda_n}^{n+1/2}(\partial)$ of Eq. (31) and the total symmetry of $\psi_{\mu_1 \dots \mu_n}$ in its Lorentz indices, the expression for $G_{\mu_1 \dots \mu_n, \nu_1 \dots \nu_n}$ of Eq. (33) is reduced to

$$G_{\mu_1 \dots \mu_n, \nu_1 \dots \nu_n} = \frac{1}{n!} \sum_{P(v)} O_{(\mu_1, \nu_1) \lambda_1}^{3/2}(\partial) \dots O_{(\mu_n, \nu_n) \lambda_n}^{3/2}(\partial) \psi^{\lambda_1 \dots \lambda_n}. \quad (34)$$

This expression for $G_{\mu_1 \dots \mu_n, \nu_1 \dots \nu_n}$ can be reformulated as

$$\begin{aligned} G_{\mu_1 \dots \mu_n, \nu_1 \dots \nu_n} &= \sum_{P(\mu)} \sum_{P(v)} \sum_{k=0}^n \mathcal{G}_k^n \partial_{\nu_1} \dots \partial_{\nu_k} \\ &\quad \times \partial_{\mu_{k+1}} \dots \partial_{\mu_n} \psi_{\mu_1 \dots \mu_k \nu_{k+1} \dots \nu_n}, \quad (35) \end{aligned}$$

with

$$\mathcal{G}_k^n = \frac{i^n (-1)^k}{n! k! (n-k)!}. \quad (36)$$

The field $G_{\mu_1 \dots \mu_n, \nu_1 \dots \nu_n}$ is totally symmetric in its μ_i and ν_j indices and has the following property:

$$G_{\mu_1 \dots \mu_n, \nu_1 \dots \nu_n} = (-1)^n G_{\nu_1 \dots \nu_n, \mu_1 \dots \mu_n}. \quad (37)$$

Furthermore, it is invariant under the uR-S _{$n+1/2$} gauge,

$$\psi_{\mu_1 \dots \mu_n} \rightarrow \psi_{\mu_1 \dots \mu_n} + \frac{i}{n(n-1)!} \sum_{P(\mu)} \partial_{\mu_1} \chi_{\mu_2 \dots \mu_n}, \quad (38)$$

with $\chi_{\mu_1 \dots \mu_{n-1}}$ as an arbitrary totally symmetric space-time-dependent rank- $(n-1)$ tensor-spinor field. The invariance of $G_{\mu_1 \dots \mu_n, \nu_1 \dots \nu_n}$ under the uR-S _{$n+1/2$} gauge (38) is assured by the following properties of the interaction operator:

$$\begin{aligned} & \partial^{\lambda k} O_{(\mu_1 \dots \mu_n, \nu_1 \dots \nu_n) \lambda_1 \dots \lambda_n}^{n+1/2}(\partial) \\ &= O_{(\mu_1 \dots \mu_n, \nu_1 \dots \nu_n) \lambda_1 \dots \lambda_n}^{n+1/2}(\partial) \partial^{\lambda k} \\ &= 0, \quad (39) \end{aligned}$$

where k runs from 1 to n . The interaction theory,

$$\begin{aligned} \mathcal{L}_I &= \overline{G}_{\mu_1 \dots \mu_n, \nu_1 \dots \nu_n} T^{\mu_1 \dots \mu_n \nu_1 \dots \nu_n} \\ &\quad + \overline{T}_{\mu_1 \dots \mu_n \nu_1 \dots \nu_n} G^{\mu_1 \dots \mu_n, \nu_1 \dots \nu_n}, \quad (40) \end{aligned}$$

which couples the gauge-invariant field $G_{\mu_1 \dots \mu_n, \nu_1 \dots \nu_n}$ to the external source $T_{\mu_1 \dots \mu_n \nu_1 \dots \nu_n}$, generates transverse interaction vertices, i.e.,

$$p_{\mu k} \Gamma_I^{\mu_1 \dots \mu_n} = 0, \quad (41)$$

where k runs from 1 to n , p_{μ} represents the four-momentum of $\psi_{\mu_1 \dots \mu_n}$, and $\Gamma_I^{\lambda_1 \dots \lambda_n}$ represents the interaction vertex derived from $O_{(\mu_1 \dots \mu_n, \nu_1 \dots \nu_n) \lambda_1 \dots \lambda_n}^{n+1/2}(\partial) T^{\mu_1 \dots \mu_n \nu_1 \dots \nu_n}$.

The next step consists of defining the spin- $(n + 1/2)$ projection operators. The general expressions for the spin-projection operators for bosons and fermions were first derived by Behrends and Fronsdal in Ref. [12]. The spin- $(n + 1/2)$ projection operator is defined as

$$\mathcal{P}_{\mu_1 \dots \mu_n, \nu_1 \dots \nu_n}^{n+1/2}(p) = \frac{n+1}{2n+3} \gamma^{\mu} \mathcal{P}_{\mu \mu_1 \dots \mu_n, \nu_1 \dots \nu_n}^{n+1}(p) \gamma^{\nu}, \quad (42)$$

and depends on the spin- $(n+1)$ projection operator. The expression for the spin- n projection operator reads

$$\mathcal{P}_{\mu_1 \dots \mu_n; v_1 \dots v_n}^n(p) = \frac{1}{n!^2} \sum_{P(\mu)} \sum_{P(v)} \sum_{k=0}^{k_{\max}} A_k^n \mathcal{P}_{\mu_1 \mu_2} \mathcal{P}_{v_1 v_2} \dots \mathcal{P}_{\mu_{2k-1} \mu_{2k}} \mathcal{P}_{v_{2k-1} v_{2k}} \prod_{i=2k+1}^n \mathcal{P}_{\mu_i v_i}, \quad (43)$$

with

$$k_{\max} = \begin{cases} \frac{n}{2}, & n \text{ even,} \\ \frac{n-1}{2}, & n \text{ odd,} \end{cases} \quad (44)$$

$$\mathcal{P}_{\mu_1 \dots \mu_n; v_1 \dots v_n}^{n+1/2}(p) = \sum_{P(\mu)} \sum_{P(v)} \left(\sum_{k=0}^{k_{\max,1}} \mathcal{A}_k^n \mathcal{P}_{\mu_1 \mu_2} \mathcal{P}_{v_1 v_2} \dots \mathcal{P}_{\mu_{2k-1} \mu_{2k}} \mathcal{P}_{v_{2k-1} v_{2k}} \prod_{i=2k+1}^n \mathcal{P}_{\mu_i v_i} + \mathcal{P}_{\mu_1} \mathcal{P}_{v_1} \sum_{k=0}^{k_{\max,2}} \mathcal{B}_k^n \mathcal{P}_{\mu_2 \mu_3} \mathcal{P}_{v_2 v_3} \dots \mathcal{P}_{\mu_{2k} \mu_{2k+1}} \mathcal{P}_{v_{2k} v_{2k+1}} \prod_{i=2k+2}^n \mathcal{P}_{\mu_i v_i} \right), \quad (47)$$

with

$$k_{\max,1} = \begin{cases} \frac{n}{2}, & n \text{ even,} \\ \frac{n-1}{2}, & n \text{ odd,} \end{cases} \quad (48)$$

$$k_{\max,2} = \begin{cases} \frac{n-2}{2}, & n \text{ even,} \\ \frac{n-1}{2}, & n \text{ odd.} \end{cases}$$

The coefficients \mathcal{A}_k^n and \mathcal{B}_k^n read

$$\mathcal{A}_k^n = \frac{1}{(-2)^k} \frac{1}{n!k!(n-2k)!} \frac{(2n-2k+1)!!}{(2n+1)!!}, \quad (49a)$$

$$\mathcal{B}_k^n = -\frac{1}{(-2)^k} \frac{1}{n!k!(n-2k-1)!} \frac{(2n-2k-1)!!}{(2n+1)!!}. \quad (49b)$$

The spin- $(n+1/2)$ projection operator is totally symmetric in its μ_i indices as well as in its v_j indices and satisfies the R-S constraints,

$$\gamma^{\mu_1} \mathcal{P}_{\mu_1 \dots \mu_n; v_1 \dots v_n}^{n+1/2}(p) = \mathcal{P}_{\mu_1 \dots \mu_n; v_1 \dots v_n}^{n+1/2}(p) \gamma^{v_1} = 0, \quad (50)$$

$$p^{\mu_1} \mathcal{P}_{\mu_1 \dots \mu_n; v_1 \dots v_n}^{n+1/2}(p) = \mathcal{P}_{\mu_1 \dots \mu_n; v_1 \dots v_n}^{n+1/2}(p) p^{v_1} = 0.$$

The general expression for the spin- $(n+1/2)$ propagator, which was derived by Huang *et al.* in Ref. [9], consists of a covariant part and a noncovariant part. The covariant part of the propagator is given as

$$P_{\mu_1 \dots \mu_n; v_1 \dots v_n}(p) = \frac{\not{p} + m}{p^2 - m^2} \tilde{\mathcal{P}}_{\mu_1 \dots \mu_n; v_1 \dots v_n}^{n+1/2}(p). \quad (51)$$

The on-shell spin-projection operator $\tilde{\mathcal{P}}_{\mu_1 \dots \mu_n; v_1 \dots v_n}^{n+1/2}(p)$ is obtained from the off-shell spin-projection operator

and $\mathcal{P}_{\mu\nu}$,

$$\mathcal{P}_{\mu\nu} = g_{\mu\nu} - \frac{1}{p^2} p_\mu p_\nu. \quad (45)$$

The coefficients A_k^n are given as

$$A_k^n = \frac{1}{(-2)^k} \frac{n!}{k!(n-2k)!} \frac{(2n-2k-1)!!}{(2n-1)!!}. \quad (46)$$

However, expression (42), for the spin- $(n+1/2)$ projection operator, can be elaborated further by explicitly carrying out the contractions with the Dirac matrices. This leads to a more convenient expression for the projection operator. Through a series of tedious calculations, which is the subject of Appendix B, the definition of the spin- $(n+1/2)$ projection operator is reformulated as

$\mathcal{P}_{\mu_1 \dots \mu_n; v_1 \dots v_n}^{n+1/2}(p)$ through the substitutions,

$$\mathcal{P}_{\mu\nu}(p) = g_{\mu\nu} - \frac{1}{p^2} p_\mu p_\nu$$

$$\rightarrow g_{\mu\nu} - \frac{1}{m^2} p_\mu p_\nu, \quad (52a)$$

and

$$\mathcal{P}_\mu(p) \mathcal{P}_\nu(p) = \gamma_\mu \gamma_\nu + \frac{\not{p}}{p^2} (\gamma_\mu p_\nu - \gamma_\nu p_\mu) - \frac{1}{p^2} p_\mu p_\nu$$

$$\rightarrow \gamma_\mu \gamma_\nu + \frac{1}{m} (\gamma_\mu p_\nu - \gamma_\nu p_\mu) - \frac{1}{m^2} p_\mu p_\nu. \quad (52b)$$

These are equivalent to the substitutions (20) carried out for the spin-5/2 theory. Obviously, the noncovariant part of the propagator should be ignored to preserve the Lorentz invariance of the transition amplitude as required by the special theory of relativity.

The consistency of gauge-invariant interactions, which are described by the interaction Lagrangian (40), can now be proven. As becomes clear from substitutions (52), the spin- $(n+1/2)$ propagator $P_{\mu_1 \dots \mu_n; v_1 \dots v_n}(p)$ differs from the spin- $(n+1/2)$ projection operator $\tilde{\mathcal{P}}_{\mu_1 \dots \mu_n; v_1 \dots v_n}^{n+1/2}(p)$ in the momentum-dependent terms. However, by considering the properties of Eq. (39), the momentum-dependent terms of the propagator drop out from the interaction structure. As a consequence, the general interaction structure is invariant under substitutions of the type (52), and the propagator can be replaced by

$$P_{\mu_1 \dots \mu_n; v_1 \dots v_n}(p) \rightarrow \frac{\not{p} + m}{p^2 - m^2} \tilde{\mathcal{P}}_{\mu_1 \dots \mu_n; v_1 \dots v_n}^{n+1/2}(p). \quad (53)$$

This proves the consistency of gauge-invariant interactions. The latter property follows directly from the fact that the physical spin- $(n + 1/2)$ component $\mathcal{P}_{\mu_1 \dots \mu_n; v_1 \dots v_n}^{n+1/2}(\partial) \psi^{v_1 \dots v_n}$ of $\psi_{\mu_1 \dots \mu_n}$ mediates the interaction.

The expression for the most general consistent interaction structure is reduced to

$$\begin{aligned} & \mathcal{O}_{(\mu_1 \dots \mu_n, v_1 \dots v_n) \sigma_1 \dots \sigma_n}^{n+1/2}(p) P^{\sigma_1 \dots \sigma_n; \tau_1 \dots \tau_n}(p) \mathcal{O}_{(\lambda_1 \dots \lambda_n, \rho_1 \dots \rho_n) \tau_1 \dots \tau_n}^{n+1/2}(p) \\ &= \frac{\not{p} + m}{p^2 - m^2} \mathcal{O}_{(\mu_1 \dots \mu_n, v_1 \dots v_n) \sigma_1 \dots \sigma_n}^{n+1/2}(p) \mathcal{O}_{(\lambda_1 \dots \lambda_n, \rho_1 \dots \rho_n) \tau_1 \dots \tau_n}^{n+1/2}(p) \sum_{P(\sigma)} \sum_{P(\tau)} \left(\sum_{k=0}^{k_{\max,1}} \mathcal{A}_k^n g^{\sigma_1 \sigma_2} g^{\tau_1 \tau_2} \dots g^{\sigma_{2k-1} \sigma_{2k}} g^{\tau_{2k-1} \tau_{2k}} \prod_{i=2k+1}^n g^{\sigma_i \tau_i} \right. \\ & \quad \left. + \gamma^{\sigma_1} \gamma^{\tau_1} \sum_{k=0}^{k_{\max,2}} \mathcal{B}_k^n g^{\sigma_2 \sigma_3} g^{\tau_2 \tau_3} \dots g^{\sigma_{2k} \sigma_{2k+1}} g^{\tau_{2k} \tau_{2k+1}} \prod_{i=2k+2}^n g^{\sigma_i \tau_i} \right), \end{aligned} \quad (54)$$

owing to relations (39). From Eq. (54), it can be concluded that the power of the momentum dependence of the consistent interaction structure rises with the spin of the R-S field. This is a direct consequence of the gauge invariance of the interaction. Indeed, the spin-specific momentum dependence of the consistent interaction structure is provided by the two interaction operators of Eq. (54), and the interaction operator consists of products of n four-momenta as can be derived from the definition of $\mathcal{O}_{(\mu_1 \dots \mu_n, v_1 \dots v_n) \sigma_1 \dots \sigma_n}^{n+1/2}(p)$ in Eq. (31).

2. Consistent couplings for the $(\phi \psi \psi_{\mu_1 \dots \mu_n}^*)$ and $(A_\mu \psi \psi_{\mu_1 \dots \mu_n}^*)$ theories

Consistent interaction theories for off-shell spin- $(n + 1/2)$ fields can be constructed from the gauge-invariant field $G_{\mu_1 \dots \mu_n, v_1 \dots v_n}$, which is defined as

$$\begin{aligned} G_{\mu_1 \dots \mu_n, v_1 \dots v_n} &= \sum_{P(\mu)} \sum_{P(v)} \sum_{k=0}^n \mathcal{G}_k^n \partial_{v_1} \dots \partial_{v_k} \\ & \quad \times \partial_{\mu_{k+1}} \dots \partial_{\mu_n} \psi_{\mu_1 \dots \mu_k v_{k+1} \dots v_n}. \end{aligned} \quad (55)$$

From $G_{\mu_1 \dots \mu_n, v_1 \dots v_n}$, a much more convenient gauge-invariant field can be derived by considering the fact that $G_{\mu_1 \dots \mu_n, v_1 \dots v_n}$ possesses twice as many Lorentz indices as the original field $\psi_{\mu_1 \dots \mu_n}$. This field is defined as

$$\begin{aligned} \Psi_{\mu_1 \dots \mu_n} &= \gamma^{v_1} \dots \gamma^{v_n} G_{\mu_1 \dots \mu_n, v_1 \dots v_n} \\ &= \sum_{P(\mu)} \sum_{k=0}^n n! \mathcal{G}_k^n \not{p}^k \partial_{\mu_{k+1}} \dots \partial_{\mu_n} \\ & \quad \times \gamma^{v_{k+1}} \dots \gamma^{v_n} \psi_{\mu_1 \dots \mu_k v_{k+1} \dots v_n}, \end{aligned} \quad (56)$$

and shares the properties of $\psi_{\mu_1 \dots \mu_n}$. Indeed, it has the same number of Lorentz indices, it is a totally symmetric field, and it obeys the R-S constraints,

$$\partial^{\mu_1} \Psi_{\mu_1 \dots \mu_n} \rightarrow 0, \quad (57a)$$

$$\gamma^{\mu_1} \Psi_{\mu_1 \dots \mu_n} \rightarrow 0. \quad (57b)$$

That is, the field combinations in Eqs. (57) result in a zero transition amplitude, as will be clarified shortly. The corresponding interaction operator for the field $\Psi_{\mu_1 \dots \mu_n}$

reads

$$\begin{aligned} \mathcal{O}_{(\mu_1 \dots \mu_n) \lambda_1 \dots \lambda_n}^{n+1/2}(\partial) &= \gamma^{v_1} \dots \gamma^{v_n} \mathcal{O}_{(\mu_1 \dots \mu_n, v_1 \dots v_n) \lambda_1 \dots \lambda_n}^{n+1/2}(\partial) \\ &= \frac{1}{n!} \sum_{P(\lambda)} \mathcal{O}_{(\mu_1) \lambda_1}^{3/2}(\partial) \dots \mathcal{O}_{(\mu_n) \lambda_n}^{3/2}(\partial), \end{aligned} \quad (58)$$

with

$$\mathcal{O}_{(\mu) \lambda}^{3/2}(\partial) = \gamma^v \mathcal{O}_{(\mu, v) \lambda}^{3/2}(\partial) = i(\partial_\mu \gamma_\lambda - \not{p} g_{\mu \lambda}). \quad (59)$$

The advantage of using $\Psi_{\mu_1 \dots \mu_n}$ instead of $G_{\mu_1 \dots \mu_n, v_1 \dots v_n}$ should be clear: The reduction in the number of Lorentz indices along with the R-S constraints (57), lowers the number of possible interaction theories. The interaction structure associated with $\Psi_{\mu_1 \dots \mu_n}$ is found to be

$$\begin{aligned} & \mathcal{O}_{(\mu_1 \dots \mu_n) \lambda_1 \dots \lambda_n}^{n+1/2}(p) P^{\lambda_1 \dots \lambda_n; \rho_1 \dots \rho_n}(p) \mathcal{O}_{(v_1 \dots v_n) \rho_1 \dots \rho_n}^{n+1/2}(p) \\ &= p^{2n} \frac{\not{p} + m}{p^2 - m^2} \mathcal{P}_{\mu_1 \dots \mu_n; v_1 \dots v_n}^{n+1/2}(p). \end{aligned} \quad (60)$$

Indeed, only the term $(-\not{p})^n g_{\mu_1 \lambda_1} \dots g_{\mu_n \lambda_n}$ of the interaction operator, which corresponds to the term $(-i \not{p})^n \psi_{\mu_1 \dots \mu_n}$ of $\Psi_{\mu_1 \dots \mu_n}$, contributes to the interaction structure. All other terms of the interaction operator contain at least one γ_{λ_i} and, subsequently, vanish because of the first of properties (50). Since the interaction structure associated with $\Psi_{\mu_1 \dots \mu_n}$ is proportional to the spin- $(n + 1/2)$ projection operator $\mathcal{P}_{\mu_1 \dots \mu_n; v_1 \dots v_n}^{n+1/2}(p)$, relations (57) follow immediately from properties (50). Equation (60) is just how a consistent local interaction structure would be constructed in an intuitive way. It is proportional to the spin- $(n + 1/2)$ projection operator, which ensures the consistency of the interaction, and the nonlocalities of the latter are exactly canceled through the p^{2n} factor.

To construct consistent couplings for the $(\phi \psi \psi_{\mu_1 \dots \mu_n}^*)$ and $(A_\mu \psi \psi_{\mu_1 \dots \mu_n}^*)$ theories, the spin-3/2 theory is considered first, since this is the most simple and, hence, the most studied R-S theory. Popular choices for the $(\phi \psi \psi_\mu^*)$ and $(A_\mu \psi \psi_\mu^*)$ couplings read [13]

$$\mathcal{L}'_{\phi \psi \psi_\mu^*} = \frac{i g_0}{m_\phi} \bar{\psi}^\mu \Theta_{\mu\nu}(z_0) \Gamma \psi \partial^\nu \phi + \text{H.c.}, \quad (61)$$

VRANCX, DE CRUZ, RYCKEBUSCH, AND VANCRAEYVELD

PHYSICAL REVIEW C **84**, 045201 (2011)

and

$$\begin{aligned}\mathcal{L}_{A_\mu\psi\psi_\mu^*}^{(1)} &= \frac{ig_1}{2m_\psi}\bar{\psi}^\mu\Theta_{\mu\nu}(z_1)\Gamma\gamma_\lambda\psi F^{\lambda\nu} + \text{H.c.}, \\ \mathcal{L}_{A_\mu\psi\psi_\mu^*}^{(2)} &= -\frac{g_2}{4m_\psi^2}\bar{\psi}^\mu\Theta_{\mu\nu}(z_2)\Gamma\partial_\lambda\psi F^{\lambda\nu} + \text{H.c.}, \\ \mathcal{L}_{A_\mu\psi\psi_\mu^*}^{(3)} &= -\frac{g_3}{4m_\psi^2}\bar{\psi}^\mu\Theta_{\mu\nu}(z_3)\Gamma\psi\partial_\lambda F^{\lambda\nu} + \text{H.c.}\end{aligned}\quad (62)$$

Here, the g_i 's are coupling constants, the z_i 's are so-called off-shell parameters, $\Theta_{\mu\nu}(z) = g_{\mu\nu} - (z + \frac{1}{2})\gamma_\mu\gamma_\nu$ is the off-shell tensor, and $F_{\mu\nu} = \partial_\mu A_\nu - \partial_\nu A_\mu$. Furthermore, $\Gamma = 1$ if the parities of the outgoing state and the incoming state are equal, and $\Gamma = \gamma_5$ in the opposite situation. The Lagrangians of Eqs. (61) and (62) are inconsistent since they involve unphysical interactions that are mediated by the spin-1/2 component of ψ_μ . This comes as no surprise since these couplings are not gauge invariant. However, the inconsistent off-shell interactions can be turned into consistent interactions by means of the substitution,

$$\Theta_{\mu\nu}(z_i)\psi^\nu \rightarrow \frac{1}{m}\Psi_\mu, \quad (63)$$

where m represents the mass of ϕ or twice the mass of ψ . The new consistent $(\phi\psi\psi_\mu^*)$ and $(A_\mu\psi\psi_\mu^*)$ couplings read

$$\mathcal{L}_{\phi\psi\psi_\mu^*} = \frac{ig_0}{m_\phi^2}\bar{\Psi}_\mu\Gamma\psi\partial^\mu\phi + \text{H.c.}, \quad (64)$$

and

$$\begin{aligned}\mathcal{L}_{A_\mu\psi\psi_\mu^*}^{(1)} &= \frac{ig_1}{4m_\psi^2}\bar{\Psi}_\mu\Gamma\gamma_\nu\psi F^{\nu\mu} + \text{H.c.}, \\ \mathcal{L}_{A_\mu\psi\psi_\mu^*}^{(2)} &= -\frac{g_2}{8m_\psi^3}\bar{\Psi}_\mu\Gamma\partial_\nu\psi F^{\nu\mu} + \text{H.c.}, \\ \mathcal{L}_{A_\mu\psi\psi_\mu^*}^{(3)} &= -\frac{g_3}{8m_\psi^3}\bar{\Psi}_\mu\Gamma\psi\partial_\nu F^{\nu\mu} + \text{H.c.}\end{aligned}\quad (65)$$

The consistency of these interactions is guaranteed by the explicitly gauge-invariant field $\Psi_\mu = i\partial_\mu\gamma^\nu\psi_\nu - \not{\partial}\psi_\mu$. Note that the derivative, which acts on ϕ in Lagrangian (64), cannot be replaced by a Dirac matrix because of property (57a). The interaction Lagrangian with the derivative, which acts on ψ , i.e.,

$$\mathcal{L}_{\phi\psi\psi_\mu^*} = \frac{ig_0}{m_\phi^2}\bar{\Psi}_\mu\Gamma\partial^\mu\psi\phi + \text{H.c.} \quad (66)$$

is equivalent to Eq. (64), aside from a minus sign, as seen from partial integration and property (57b).

The consistent interaction Lagrangians for the spin-3/2 theory, i.e., Eqs. (64) and (65), can be generalized for the spin- $(n+1/2)$ theory. The consistent $(\phi\psi\psi_{\mu_1\cdots\mu_n}^*)$ and $(A_\mu\psi\psi_{\mu_1\cdots\mu_n}^*)$ couplings read

$$\mathcal{L}_{\phi\psi\psi_{\mu_1\cdots\mu_n}^*} = \frac{i^n g_0}{m_\phi^{2n}}\bar{\Psi}_{\mu_1\cdots\mu_n}\Gamma\psi\partial^{\mu_1}\cdots\partial^{\mu_n}\phi + \text{H.c.}, \quad (67)$$

and

$$\begin{aligned}\mathcal{L}_{A_\mu\psi\psi_{\mu_1\cdots\mu_n}^*}^{(1)} &= \frac{i^n g_1}{(2m_\psi)^{2n}}\bar{\Psi}_{\mu_1\cdots\mu_{n-1}\mu_n}\Gamma\gamma_\nu\partial^{\mu_1} \\ &\quad \cdots\partial^{\mu_{n-1}}\psi F^{\nu\mu_n} + \text{H.c.},\end{aligned}$$

$$\begin{aligned}\mathcal{L}_{A_\mu\psi\psi_{\mu_1\cdots\mu_n}^*}^{(2)} &= \frac{i^{n+1}g_2}{(2m_\psi)^{2n+1}}\bar{\Psi}_{\mu_1\cdots\mu_{n-1}\mu_n}\Gamma\partial_\nu\partial^{\mu_1} \\ &\quad \cdots\partial^{\mu_{n-1}}\psi F^{\nu\mu_n} + \text{H.c.}, \\ \mathcal{L}_{A_\mu\psi\psi_{\mu_1\cdots\mu_n}^*}^{(3)} &= \frac{i^{n+1}g_3}{(2m_\psi)^{2n+1}}\bar{\Psi}_{\mu_1\cdots\mu_{n-1}\mu_n}\Gamma\partial^{\mu_1} \\ &\quad \cdots\partial^{\mu_{n-1}}\psi\partial_\nu F^{\nu\mu_n} + \text{H.c.}\end{aligned}\quad (68)$$

Indeed, the joining $(n-1)$ Lorentz indices of $\Psi_{\mu_1\cdots\mu_n}$, as compared to Ψ_μ , can only be contracted by derivatives that do not act on $\Psi_{\mu_1\cdots\mu_n}$ since properties (57) hold.

III. CONSISTENT INTERACTIONS IN HADRON PHYSICS

The nucleon has various excited states, which are commonly dubbed nucleon resonances. They are identified with their different masses, spins, and decay widths, which reflect the specific internal structure of the resonance. The quantitative information on the excited nucleon states is gathered by the Particle Data Group (PDG) from various partial-wave analyses, which aims at describing pion- and photon-induced meson production processes [14]. Alternatively, these processes can be described by isobar models. An extensive overview of the various partial-wave and isobar models is found in Ref. [15]. To describe nucleon excitation processes in a consistent way, isobar models require a consistent high-spin interaction theory. Such a theory was developed in Sec. II B2. The following sections illustrate how this interaction theory can be implemented in the study of processes that are of key importance in hadron physics. To this end, the $K^+\Lambda$ photoproduction process from the proton is selected

$$\gamma p \rightarrow K^+\Lambda. \quad (69)$$

It is worth stressing that all discussions of the following sections apply equally well to other hadronic processes that involve off-shell high-spin interactions.

A. Inconsistency of standard hadronic form factors

The threshold energy W_0 for $K^+\Lambda$ production is given by [14]

$$W_0 = m_{K^+} + m_\Lambda \approx 1610 \text{ MeV}. \quad (70)$$

In an effective-field framework, the $p(\gamma, K^+)\Lambda$ reaction is modeled with hadrons as the basic degrees of freedom, i.e., the hadrons are represented by effective quantum fields. The expression for the differential $p(\gamma, K^+)\Lambda$ cross section in the center-of-mass frame is given by [16]

$$\frac{d\sigma}{d\Omega_K} = \frac{1}{64\pi^2} \frac{1}{W^2} \frac{|\vec{p}_K|}{E_\gamma^{\text{lab}}} \sum_{\lambda, \lambda_p, \lambda_\Lambda} |\mathcal{M}_{\lambda, \lambda_p, \lambda_\Lambda}|^2. \quad (71)$$

Here, W is the invariant mass, E_γ^{lab} is the photon energy in the laboratory frame, \vec{p}_K is the three-momentum, and θ_K is the scattering angle of the kaon in the center-of-mass frame. Furthermore, λ , λ_p , and λ_Λ are the photon, proton, and hyperon polarizations. The notation $\sum_{\lambda, \lambda_p, \lambda_\Lambda}$ denotes appropriate summing and/or averaging over the polarizations

CONSISTENT INTERACTIONS FOR HIGH-SPIN FERMION ...

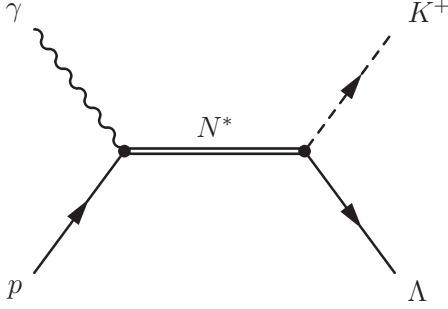
 PHYSICAL REVIEW C **84**, 045201 (2011)


FIG. 1. The tree-level Feynman diagram for the resonant s -channel contribution to the $p(\gamma, K^+)\Lambda$ reaction in an effective-field theoretical framework.

of initial- and final-state particles. Finally, $\mathcal{M}_{\lambda, \lambda_p, \lambda_\Lambda}$ is the total transition amplitude. Its squared absolute value is calculated as

$$|\mathcal{M}_{\lambda, \lambda_p, \lambda_\Lambda}|^2 = |\bar{u}_\Lambda^{\lambda_\Lambda} T^\mu \varepsilon_\mu^\lambda u_p^{\lambda_p}|^2, \quad (72)$$

with $u_p^{\lambda_p}$ and $u_\Lambda^{\lambda_\Lambda}$ as the proton and hyperon spinors, ε_μ^λ as the polarization four-vector of the photon, and T_μ as the truncated interaction current.

Figure 1 depicts the tree-level Feynman diagram for the resonant s -channel contribution to the $p(\gamma, K^+)\Lambda$ reaction. In this channel, the photon excites the proton to form a nucleon resonance, which is labeled N^* . In the N^* 's rest frame, the spin of N^* can be determined by the photon-proton relative orbital angular momentum. The nucleon resonance subsequently decays into a K^+ and a Λ . To account for the finite lifetime of N^* , the following substitution in the expression for the N^* propagator is required:

$$\frac{\not{p}_R + m_R}{p_R^2 - m_R^2} \rightarrow \frac{\not{p}_R + m_R}{p_R^2 - m_R^2 + im_R \Gamma_R}. \quad (73)$$

In the tree-level approximation of Fig. 1, the propagator remains undressed. As a consequence, the decay width of the unstable particle, i.e., the resonance, is not generated dynamically. Then, the finite lifetime of the resonance can be implemented by means of the substitution of Eq. (73).

From expression (71), the unpolarized total cross section,

$$\sigma(W) = \int \frac{d\Omega_K}{4\pi} \frac{1}{W^2} \frac{|\vec{p}_K|}{E_\gamma^{\text{lab}}} \frac{1}{2} \sum_{\lambda, \lambda_p, \lambda_\Lambda} |\mathcal{M}_{\lambda, \lambda_p, \lambda_\Lambda}|^2 \quad (74)$$

can be calculated. In the presented calculations, the coupling constants of Eqs. (67) and (68) are chosen to be equal, i.e., $g_0 = g_1 = g_2 = g$. The coupling constant g is determined from the requirement that $\sigma_{\text{max}} = 0.10 \mu\text{b}$, which is the typical order of magnitude for the reaction $\gamma p \rightarrow K^+ \Lambda$. In Fig. 2, σ is plotted for three artificial resonances with $m_R = 1700 \text{ MeV}$, $\Gamma_R = 50 \text{ MeV}$, and spins $J_R^P = 1/2^+, 3/2^+, 5/2^+$. The coupling constant g for each of the three resonances is denoted by $g_{1/2}$, $g_{3/2}$, and $g_{5/2}$. The explicit expressions for the spin- $1/2^+$, the spin- $3/2^+$, and the spin- $5/2^+$ truncated currents are

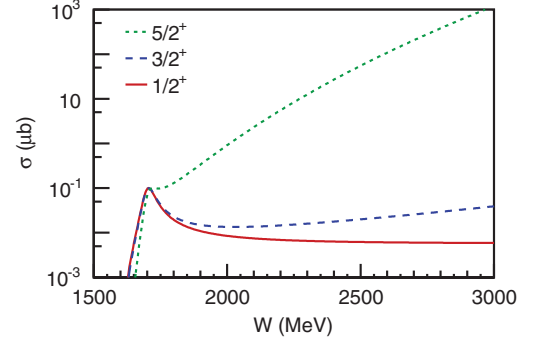


FIG. 2. (Color online) The energy dependence of the $\gamma p \rightarrow N^* \rightarrow K^+ \Lambda$ cross section. N^* is a mock resonance with $m_R = 1700 \text{ MeV}$, $\Gamma_R = 50 \text{ MeV}$, and $J_R^P = 1/2^+$ (solid curve), $3/2^+$ (dashed curve), $5/2^+$ (dotted curve). The coupling constants are $g_{1/2} = 1.7$, $g_{3/2} = 0.75$, and $g_{5/2} = 3.2$.

given by

$$T_\mu^{1/2^+} = (g_0 \gamma_5) \left(\frac{\not{p}_R + m_R}{p_R^2 - m_R^2 + im_R \Gamma_R} \right) \times \left[\frac{ieg_1}{2m_p} (k_\mu - k\gamma_\mu) \right], \quad (75)$$

$$T_\mu^{3/2^+} = \left(\frac{ig_0}{m_{K^+}^2} p_{K^+}^{\mu_1} \right) \left(p_R^2 \frac{\not{p}_R + m_R}{p_R^2 - m_R^2 + im_R \Gamma_R} \mathcal{P}_{\mu_1; \nu_1}^{3/2}(p_R) \right) \times \left[\frac{ieg_1}{4m_p^2} \gamma_5 (\not{k} g_\mu^{\nu_1} - k^{\nu_1} \gamma_\mu) + \frac{ieg_2}{8m_p^3} \gamma_5 ((kp) g_\mu^{\nu_1} - k^{\nu_1} p_\mu) \right], \quad (76)$$

$$T_\mu^{5/2^+} = \left(\frac{ig_0}{m_{K^+}^4} \gamma_5 p_{K^+}^{\mu_1} p_{K^+}^{\mu_2} \right) \times \left(p_R^4 \frac{\not{p}_R + m_R}{p_R^2 - m_R^2 + im_R \Gamma_R} \mathcal{P}_{\mu_1 \mu_2; \nu_1 \nu_2}^{5/2}(p_R) \right) \times \left[\frac{ieg_1}{16m_p^4} p^{\nu_1} (\not{k} g_\mu^{\nu_2} - k^{\nu_2} \gamma_\mu) + \frac{ieg_2}{32m_p^5} p^{\nu_1} ((kp) g_\mu^{\nu_2} - k^{\nu_2} p_\mu) \right], \quad (77)$$

and the corresponding cross sections are denoted as $\sigma_{1/2^+}$, $\sigma_{3/2^+}$, and $\sigma_{5/2^+}$. In the above expressions, e represents the charge of the proton, k_μ , p_μ , $p_{K^+, \mu}$, and $p_{R, \mu} = k_\mu + p_\mu$ represent the four-momenta of the photon, the proton, the kaon, and N^* . Furthermore, m_p and m_{K^+} are the masses of the proton and the kaon. Note that $p_R^2 = W^2$. The expression for $T_\mu^{1/2^+}$ was obtained from Ref. [17]. The expressions for $T_\mu^{3/2^+}$ and $T_\mu^{5/2^+}$ were derived from the consistent interaction Lagrangians (67) and (68) and the consistent interaction structure (60). Since the equations of motion for the real photon field are

VRANCX, DE CRUZ, RYCKEBUSCH, AND VANCRAEYVELD

PHYSICAL REVIEW C **84**, 045201 (2011)

given by

$$\partial_\mu F^{\mu\nu} = 0, \quad (78)$$

the truncated currents $T_\mu^{3/2+}$ and $T_\mu^{5/2+}$ do not receive contributions from the third Lagrangian of Eq. (68).

By inspecting Fig. 2, it is observed that $\sigma_{1/2+}$ decreases asymptotically with W , whereas, $\sigma_{3/2+}$ and $\sigma_{5/2+}$ grow indefinitely with W . The higher the spin of the resonance, the faster σ rises with W . This clearly is an unphysical and an unacceptable behavior. To remedy this, one commonly introduces a hadronic form factor, which cuts the transition amplitude $\mathcal{M}_{\lambda,\lambda_p,\lambda_\Lambda}$ beyond a certain energy scale. Hadronic form factors that are commonly used in the literature are of the dipole form [18]

$$F_d(s; m_R, \Lambda_R) = \frac{\Lambda_R^4}{(s - m_R^2)^2 + \Lambda_R^4}, \quad (79)$$

or the Gaussian form [19]

$$F_G(s; m_R, \Lambda_R) = \exp\left(-\frac{(s - m_R^2)^2}{\Lambda_R^4}\right), \quad (80)$$

with $s = W^2$ and Λ_R as the cutoff energy.

For the remainder of this discussion, the following resonant s -channel contribution to the $p(\gamma, K^+)\Lambda$ reaction will be investigated in detail,

$$\gamma p \rightarrow N(1680) F_{15} \rightarrow K^+ \Lambda. \quad (81)$$

The nucleon resonance $N(1680) F_{15}$ is an established $J_R^P = 5/2^+$ resonance with a four-star rating in the Review of Particle Physics of the PDG [14]. It has a mass $m_R = 1685$ MeV and a decay width $\Gamma_R = 130$ MeV. The computed cross section that uses a Gaussian form factor to cut off the transition amplitude at high energies is denoted as σ_G . The value of the cutoff energy is fixed at a typical value of $\Lambda_R = 1500$ MeV. The result of the calculation of σ_G is shown in Fig. 3(a). A seemingly resonant structure is observed. This structure, however, is not associated with the resonant structure of the $N(1680) F_{15}$. Indeed, σ_G has $W_{\max} \approx 2250$ MeV and FWHM ≈ 450 MeV, with W_{\max} as the invariant mass that corresponds to the maximum value of the cross section and FWHM as the full width at half maximum. Clearly, the computed energy dependence of σ_G displays little resemblance to the expected behavior of a resonance with $m_R = 1685$ MeV and $\Gamma_R = 130$ MeV. Figure 3(b), which provides a closer look at σ_G in the threshold-energy region, reveals that any sign of a resonant structure at $W \approx m_R$ is missing.

The observed energy dependence of σ_G , which can be conceived as unphysical, is generated by the combination of the opposite high-energy behavior of σ and F_G . In the high-energy limit, σ rises with the energy as observed in Fig. 2. This feature is characteristic for off-shell high-spin interactions. On the other hand, F_G decreases for growing $W > m_R$. For a particular value of the invariant mass, denoted by W_{\max} , the decrease in F_G becomes strong enough so as to prevent σ_G from growing indefinitely. As a result, the maximum value of σ_G is reached at W_{\max} , and an artificial structure is created. The fact that the resonant structure at $W \approx m_R$ is not observed in the computed energy dependence

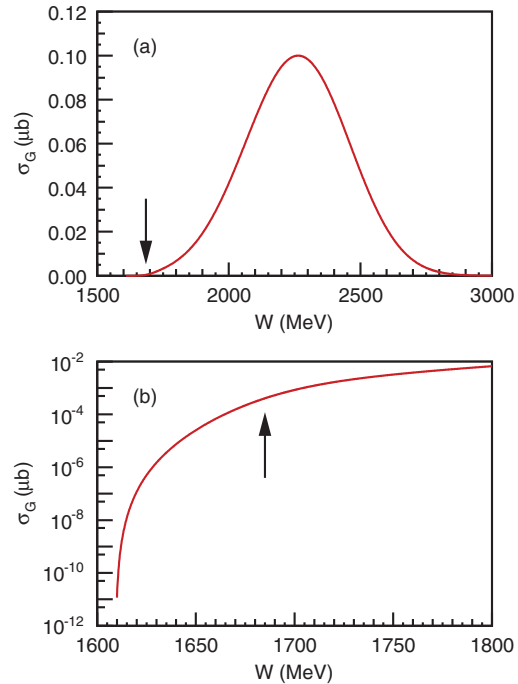


FIG. 3. (Color online) (a) The energy dependence of the $\gamma p \rightarrow N(1680) F_{15} \rightarrow K^+ \Lambda$ cross section. A Gaussian form factor was used with $\Lambda_R = 1500$ MeV and $g = 1.7$. (b) A semilogarithmic view of the cross section in the threshold-energy region. The arrows indicate the position of the mass of the $N(1680) F_{15}$.

of σ_G can be attributed to the relatively large decay width of the $N(1680) F_{15}$ in combination with the fast increase in σ with growing W .

Clearly, the computed cross section σ_G of Fig. 3(a) lacks any obvious physical meaning. Indeed, the resonant structure at $W \approx m_R$ is erased, and an unphysical bump dominates σ_G for $m_R \lesssim W \lesssim 3000$ MeV. A clear-cut remedy consists in cutting off the physics at smaller energies, i.e., lowering Λ_R . Figure 4(a) illustrates the energy dependence of σ_G for a range of cutoff energies. Indeed, it is observed that lowering Λ_R results in a mere shift in the unphysical bump toward the threshold energy W_0 . The peak position and width of the bump in the energy dependence of σ_G appear to be a function of Λ_R . The unphysical bump persistently dominates σ_G . In Fig. 4(b), the decay width of the $N(1680) F_{15}$ was artificially lowered to $\Gamma'_R = 20$ MeV so that the $N(1680) F_{15}$'s resonance peak is dominant at $W \approx m_R$. In this case, lowering Λ_R is indeed an effective remedy. However, it is not *a priori* clear what value that should be assigned to Λ_R . Furthermore, most of the established nucleon resonances, if not all, have a relatively large decay width [14]. As such, lowering Λ_R does not really provide a physically acceptable solution. Similar problems occur for spin-3/2 resonances and higher-spin resonances. This is a feature that is inherent to the consistent description of high-spin interactions within the R-S framework. The conclusion is that the unphysical structure in σ_G cannot be removed in a consistent way by lowering the value of the form factor's cutoff energy.

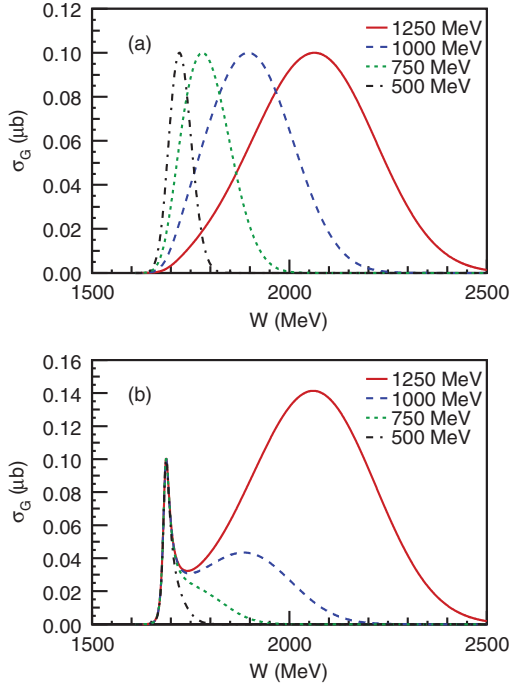


FIG. 4. (Color online) The energy dependence of the $\gamma p \rightarrow N(1680) F_{15} \rightarrow K^+ \Lambda$ cross section for various values of the cut-off energy of the Gaussian form factor. In (a), the real decay width of the $N(1680) F_{15}$ was used, i.e., $\Gamma_R = 130$ MeV, and $g = 2.4, 3.3, 4.2, 5.3$ for $\Lambda_R = 1250, 1000, 750, 500$ MeV. In (b), the decay width of the $N(1680) F_{15}$ was set to $\Gamma'_R = 20$ MeV and $g = 2.6$.

It is important to stress that, with the dipole form factor of Eq. (79), things get even worse. Indeed, the dipole form factor does not fall fast enough with energy, and σ_d keeps on growing in the high-energy limit. This is obviously an unsatisfactory situation.

In Ref. [6], consistent spin-5/2 interactions are constructed from the gauge-invariant field $\Psi'_{\mu\nu}$, defined as

$$\Psi'_{\mu\nu} = \frac{\square^2}{m^4} \mathcal{P}_{\mu\nu;\lambda\rho}^{5/2}(\partial) \psi^{\lambda\rho}, \quad (82)$$

with m as an arbitrary mass. The gauge-invariant field $\Psi'_{\mu\nu}$ is restricted to a pure spin-5/2 component. This restriction is indispensable since the spin-5/2 propagator of Ref. [6] does not generate consistent couplings from interaction theories that are only required to be invariant under the uR-S_{5/2} (6) as clarified in Sec. II A 3. The gauge-invariant field $\Psi'_{\mu\nu}$ gives rise to the following truncated current for the tree-level $p(\gamma, K^+) \Lambda$ amplitude:

$$T'_\mu = \left(-\frac{p_R^2}{m_{K^+}^2} \right) T_\mu \left(-\frac{p_R^2}{4m_p^2} \right) = \frac{W^4}{4m_p^2 m_{K^+}^2} T_\mu, \quad (83)$$

with T_μ defined in Eq. (77). Since it features additional powers of W , the corresponding cross section grows even stronger with W in the high-energy limit than by applying the consistent

interaction theory of Sec. II B 2. It is clear that its unphysical behavior is even more problematic.

B. The multi-dipole-Gauss form factor

In Sec. III A, it was pointed out that the unphysical behavior of σ_G is caused by the divergent high-energy behavior of σ in the tree-level approximation. This feature is characteristic for consistent high-spin interactions. To restore the physical resonance peak, the high-energy behavior of σ needs to be regulated. The angular dependence of σ , which reflects the quantum numbers of the exchanged particles, should be left unaltered by such an operation.

In the expression for the consistent interaction structure (60), the prefactor $(p_R^2)^{n_R} = s^{n_R}$, with $n_R = J_R - \frac{1}{2}$, combined with the $2n_R$ four-momenta that are to be contracted with the spin- J_R projection operator, give rise to a factor $s^{2n_R} = (s^2)^{J_R-1/2}$ for $s \gg m_R^2$. It is exactly this factor that causes the unphysical behavior of σ_G . To resolve these problems, the $(s^2)^{J_R-1/2}$ factor needs to be included in the denominator of the hadronic form factor. This can be achieved by multiplying $J_R - \frac{1}{2}$ dipole form factors (79) with the Gaussian form factor (80). The following explicit form for the modified hadronic form factor is suggested:

$$F_{mG}(s; m_R, \Lambda_R, \Gamma_R, J_R) = \left(\frac{m_R^2 \tilde{\Gamma}_R^2(J_R)}{(s - m_R^2)^2 + m_R^2 \tilde{\Gamma}_R^2(J_R)} \right)^{J_R-1/2} \times \exp\left(-\frac{(s - m_R^2)^2}{\Lambda_R^4} \right), \quad (84)$$

and is dubbed a multi-dipole-Gauss form factor. To preserve the interpretation of the decay width of the resonance as the FWHM of the resonance peak, a modified decay width $\tilde{\Gamma}_R$ is required. The explicit expression for the modified decay width depends on the spin of the resonance and reads

$$\tilde{\Gamma}_R(J_R) = \frac{\Gamma_R}{\sqrt{2^{1/(2J_R)} - 1}}. \quad (85)$$

The details of the derivation of the expression for $\tilde{\Gamma}_R(J_R)$ have been diverted to Appendix C. The above choice for F_{mG} is inspired by the expression for the squared absolute value of the propagator denominator, i.e.,

$$(p_R^2 - m_R^2 + im_R \tilde{\Gamma}_R)^{-1} (p_R^2 - m_R^2 - im_R \tilde{\Gamma}_R)^{-1} = [(s - m_R^2)^2 + m_R^2 \tilde{\Gamma}_R^2]^{-1}, \quad (86)$$

where $p_R^2 = s$ has been substituted. In this way, the multi-dipole-Gauss form factor raises the multiplicity of the propagator pole at the resonance mass.

Figure 5(a) compares a multi-dipole-Gauss form factor with $\Lambda_R = 1500$ MeV to a Gaussian form factor with the same FWHM. Despite the fact that the two form factors shown in Fig. 5(a) appear similar, their effect on σ is vastly different. This is illustrated in Fig. 5(b), which depicts the computed cross sections that adopt both form factors. As explained before, the energy dependence of σ_G should be interpreted as artificial. The peak position and width of the observed structure

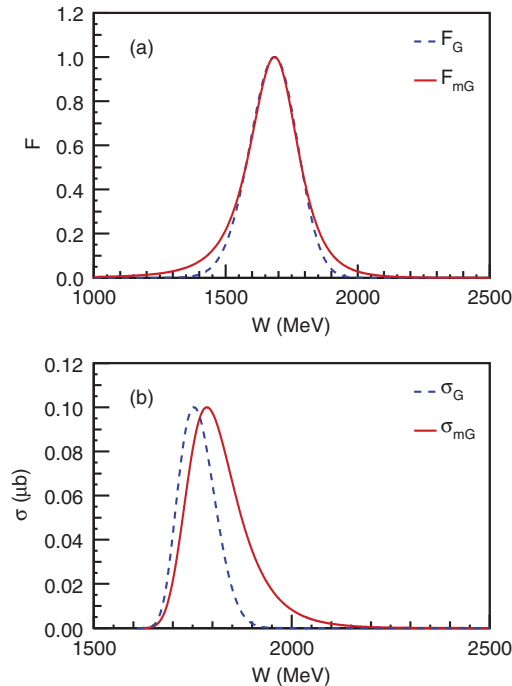


FIG. 5. (Color online) (a) The multi-dipole-Gauss form factor with $\Lambda_R = 1500$ MeV (solid curve) and the Gaussian form factor with $\Lambda_R \approx 655$ MeV (dashed curve) for the $N(1680) F_{15}$ as a function of the invariant mass W . The cutoff energy of the Gaussian form factor was calculated so as to obtain the same FWHM. (b) The energy dependence of the corresponding $\gamma p \rightarrow N(1680) F_{15} \rightarrow K^+ \Lambda$ cross section with $g = 6.2$ (solid curve) and $g = 4.6$ (dashed curve).

in σ_G are determined by the value of the cutoff energy. The multi-dipole-Gauss form factor has a larger impact on the high-energy behavior of σ and prevents the formation of an artificial bump. The form factor F_{mG} augments the effect of the $N(1680) F_{15}$'s propagator, and this makes sure that, in the computed σ_{mG} , the resonance peak occurs at $W \approx m_R$. Yet, it appears as though the mass of the $N(1680) F_{15}$ is shifted by approximately 100 MeV. This mass shift is a threshold effect and is caused by the fact that $m_R - \frac{\Gamma_R}{2} \approx W_0$ and $\sigma(W_0) = 0$. The mass shift decreases with increasing resonance mass and decreasing resonance decay width.

In Fig. 6, the cross sections of Fig. 4 are replotted by employing a multi-dipole-Gauss form factor. The minor shift in the resonance peak in Fig. 6(a) does not have the same origin as the artificial bump of Fig. 4(a). Here, the shift is caused by the comparable magnitudes of Λ_R and Γ_R . As a consequence, the resonance peak gets increasingly narrowed by the form factor, and this results in a reduction in the mass shift, which was explained in the previous paragraph. In Fig. 4(b), the decay width of the $N(1680) F_{15}$ was artificially lowered to $\Gamma'_R = 20$ MeV. Here, it is apparent that the energy dependence of σ_{mG} is indeed the same for all cutoff energies. Figure 4(b) also confirms the fact that the mass shift decreases with decreasing decay width: The mass shift amounts to approximately 3.5 MeV.

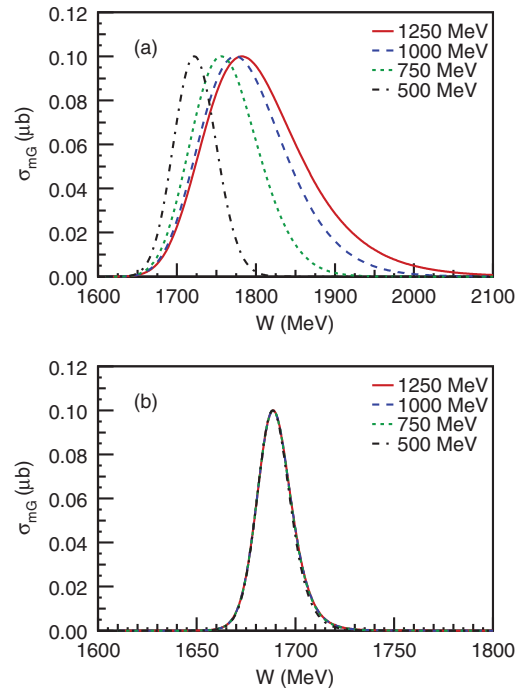


FIG. 6. (Color online) The energy dependence of the $\gamma p \rightarrow N(1680) F_{15} \rightarrow K^+ \Lambda$ cross section for various values of the cutoff energy of the multi-dipole-Gauss form factor. In (a), the real decay width of the $N(1680) F_{15}$ was used, i.e., $\Gamma_R = 130$ MeV, and $g = 6.3, 6.5, 7.0, 8.5$ for $\Lambda_R = 1250, 1000, 750, 500$ MeV. In (b), the decay width of the $N(1680) F_{15}$ was set to $\Gamma'_R = 20$ MeV and $g = 4.2$.

IV. CONCLUSIONS

In this paper, a theory of consistent interactions for massive high-spin fermions was developed. It was proven that gauge symmetry was the necessary and sufficient condition to assure the consistency of high-spin interactions. From this gauge symmetry, the most general consistent interaction structure was constructed for off-shell high-spin fermions. In addition, consistent couplings for the $(\phi \psi \psi^*_{\mu_1 \dots \mu_n})$ and $(A_\mu \psi \psi^*_{\mu_1 \dots \mu_n})$ theories were derived.

It turns out that the power of the momentum dependence of consistent couplings rises with the spin of the R-S field. This gives rise to unphysical behavior in the computed tree-level cross sections if the reaction is cut off by a standard hadronic form factor. A persuasive solution was proposed in terms of an alternative phenomenological hadronic form factor, namely, the multi-dipole-Gauss form factor. We deem that this form factor, in conjunction with the consistent interaction Lagrangians developed in Sec. II B2, provides a proper framework to implement the exchange of high-spin resonances in hadrodynamical analyses.

ACKNOWLEDGMENTS

This work was supported by the Fund for Scientific Research Flanders and the Research Council of Ghent University.

APPENDIX A: THE PROJECTION OPERATORS FOR THE SPIN-5/2 THEORY

The projection operators for the spin-5/2 theory read [6]

$$\mathcal{P}_{\mu\nu;\lambda\rho}^{5/2}(p) = \frac{1}{2}(\mathcal{P}_{\mu\lambda}\mathcal{P}_{\nu\rho} + \mathcal{P}_{\mu\rho}\mathcal{P}_{\nu\lambda}) - \frac{1}{5}\mathcal{P}_{\mu\nu}\mathcal{P}_{\lambda\rho} - \frac{1}{10}(\mathcal{P}_{\mu}\mathcal{P}_{\lambda}\mathcal{P}_{\nu\rho} + \mathcal{P}_{\mu}\mathcal{P}_{\rho}\mathcal{P}_{\nu\lambda} + \mathcal{P}_{\nu}\mathcal{P}_{\lambda}\mathcal{P}_{\mu\rho} + \mathcal{P}_{\nu}\mathcal{P}_{\rho}\mathcal{P}_{\mu\lambda}), \quad (\text{A1})$$

$$\mathcal{P}_{11,\mu\nu;\lambda\rho}^{3/2}(p) = \frac{1}{2}(\mathcal{P}_{\mu\lambda}\mathcal{Q}_{\nu\rho} + \mathcal{P}_{\nu\lambda}\mathcal{Q}_{\mu\rho} + \mathcal{P}_{\mu\rho}\mathcal{Q}_{\nu\lambda} + \mathcal{P}_{\nu\rho}\mathcal{Q}_{\mu\lambda}) - \frac{1}{6p^2}\mathcal{R}_{\mu\nu}\mathcal{R}_{\lambda\rho},$$

$$\mathcal{P}_{22,\mu\nu;\lambda\rho}^{3/2}(p) = \frac{1}{10}(\mathcal{P}_{\mu}\mathcal{P}_{\lambda}\mathcal{P}_{\nu\rho} + \mathcal{P}_{\mu}\mathcal{P}_{\rho}\mathcal{P}_{\nu\lambda} + \mathcal{P}_{\nu}\mathcal{P}_{\lambda}\mathcal{P}_{\mu\rho} + \mathcal{P}_{\nu}\mathcal{P}_{\rho}\mathcal{P}_{\mu\lambda}) - \frac{2}{15}\mathcal{P}_{\mu\nu}\mathcal{P}_{\lambda\rho},$$

$$\mathcal{P}_{21,\mu\nu;\lambda\rho}^{3/2}(p) = \frac{1}{2\sqrt{5}p^2}[p_{\lambda}(\mathcal{P}_{\mu}\mathcal{P}_{\nu\rho} + \mathcal{P}_{\nu}\mathcal{P}_{\mu\rho}) + p_{\rho}(\mathcal{P}_{\mu}\mathcal{P}_{\nu\lambda} + \mathcal{P}_{\nu}\mathcal{P}_{\mu\lambda})]\not{p} - \frac{1}{3\sqrt{5}p^2}\mathcal{P}_{\mu\nu}\mathcal{R}_{\lambda\rho}\not{p} = -\mathcal{P}_{21,\lambda\rho;\mu\nu}^{3/2}(p), \quad (\text{A2})$$

$$\mathcal{P}_{11,\mu\nu;\lambda\rho}^{1/2}(p) = \mathcal{Q}_{\mu\nu}\mathcal{Q}_{\lambda\rho}, \quad \mathcal{P}_{22,\mu\nu;\lambda\rho}^{1/2}(p) = \frac{1}{3}\mathcal{P}_{\mu\nu}\mathcal{P}_{\lambda\rho}, \quad \mathcal{P}_{33,\mu\nu;\lambda\rho}^{1/2}(p) = \frac{1}{6p^2}\mathcal{R}_{\mu\nu}\mathcal{R}_{\lambda\rho},$$

$$\mathcal{P}_{21,\mu\nu;\lambda\rho}^{1/2}(p) = \frac{1}{\sqrt{3}}\mathcal{P}_{\mu\nu}\mathcal{Q}_{\lambda\rho} = \mathcal{P}_{12,\lambda\rho;\mu\nu}^{1/2}(p), \quad \mathcal{P}_{31,\mu\nu;\lambda\rho}^{1/2}(p) = \frac{1}{\sqrt{6}p^2}\mathcal{R}_{\mu\nu}\mathcal{Q}_{\lambda\rho}\not{p} = -\mathcal{P}_{13,\lambda\rho;\mu\nu}^{1/2}(p),$$

$$\mathcal{P}_{23,\mu\nu;\lambda\rho}^{1/2}(p) = -\frac{1}{3\sqrt{2}p^2}\mathcal{P}_{\mu\nu}\mathcal{R}_{\lambda\rho}\not{p} = -\mathcal{P}_{32,\lambda\rho;\mu\nu}^{1/2}(p), \quad (\text{A3})$$

with

$$\mathcal{P}_{\mu\nu}(p) = g_{\mu\nu} - \frac{1}{p^2}p_{\mu}p_{\nu}, \quad \mathcal{P}_{\mu}(p) = \gamma^{\nu}\mathcal{P}_{\mu\nu}(p) = \gamma_{\mu} - \frac{\not{p}}{p^2}p_{\mu}, \quad \mathcal{Q}_{\mu\nu}(p) = \frac{1}{p^2}p_{\mu}p_{\nu},$$

$$\mathcal{R}_{\mu\nu}(p) = p_{\mu}\mathcal{P}_{\nu} + \mathcal{P}_{\mu}p_{\nu} = (\gamma_{\mu}p_{\nu} + \gamma_{\nu}p_{\mu}) - \frac{2}{p^2}\not{p}p_{\mu}p_{\nu}. \quad (\text{A4})$$

The projection operators project the spin-5/2 field $\psi_{\mu\nu}$ onto the (physical) spin-5/2 component and the (unphysical) spin-3/2 and spin-1/2 components, respectively. The following orthogonality relations apply to these operators [7]:

$$g^{\sigma\sigma'}g^{\tau\tau'}\mathcal{P}_{i\ell,\mu\nu;\sigma\tau}^J(p)\mathcal{P}_{kj,\sigma'\tau';\lambda\rho}^{J'}(p) = \delta_{JJ'}\delta_{ik}\mathcal{P}_{ij,\mu\nu;\lambda\rho}^J(p). \quad (\text{A5})$$

APPENDIX B: THE SPIN-(n + 1/2) PROJECTION OPERATOR

The k th term in expression (42) for the spin-($n + 1/2$) projection operator reads

$$\frac{n+1}{2n+3}\frac{1}{(n+1)!^2}\gamma^{\mu_1}\left(\sum_{P(\mu)}\sum_{P(\nu)}A_k^{n+1}\underbrace{\mathcal{P}_{\mu_1\mu_2}\mathcal{P}_{\nu_1\nu_2}\cdots\mathcal{P}_{\mu_{2k-1}\mu_{2k}}\mathcal{P}_{\nu_{2k-1}\nu_{2k}}}_{4^k k!^2}\underbrace{\prod_{i=2k+1}^{n+1}\mathcal{P}_{\mu_i\nu_i}}_{(n-2k+1)!}\right)\gamma^{\nu_1}. \quad (\text{B1})$$

The braces indicate how many times the relevant factor can be transformed into itself by applying permutations of the Lorentz indices, which are contained in the double sum. From now on, the factor $\frac{n+1}{2n+3}\frac{1}{(n+1)!^2}$ and the double sum are dropped for reasons of simplicity. By explicitly carrying out the contractions with the Dirac matrices, five different terms are obtained, namely,

$$A_k^{n+1}\mathcal{P}_{\mu_2}\mathcal{P}_{\nu_2}\underbrace{\mathcal{P}_{\mu_3\mu_4}\mathcal{P}_{\nu_3\nu_4}\cdots\mathcal{P}_{\mu_{2k-1}\mu_{2k}}\mathcal{P}_{\nu_{2k-1}\nu_{2k}}}_{4^{k-1}(k-1)!^2}\underbrace{\prod_{i=2k+1}^{n+1}\mathcal{P}_{\mu_i\nu_i}}_{(n-2k+1)!}, \quad (\text{B2})$$

$$A_k^{n+1}\underbrace{\mathcal{P}_{\mu_2}\mathcal{P}_{\mu_3}\mathcal{P}_{\nu_2\nu_3}\mathcal{P}_{\mu_4\mu_5}\mathcal{P}_{\nu_4\nu_5}\cdots\mathcal{P}_{\mu_{2k}\mu_{2k+1}}\mathcal{P}_{\nu_{2k}\nu_{2k+1}}}_{4^k k!(k-1)!}\underbrace{\prod_{i=2k+2}^{n+1}\mathcal{P}_{\mu_i\nu_i}}_{(n-2k)!}, \quad (\text{B3})$$

VRANCX, DE CRUZ, RYCKEBUSCH, AND VANCRAEYVELD

PHYSICAL REVIEW C **84**, 045201 (2011)

$$A_k^{n+1} \underbrace{\mathcal{P}_{\mu_2\mu_3} \mathcal{P}_{\nu_2} \mathcal{P}_{\nu_3} \mathcal{P}_{\mu_4\mu_5} \mathcal{P}_{\nu_4\nu_5} \cdots \mathcal{P}_{\mu_{2k}\mu_{2k+1}} \mathcal{P}_{\nu_{2k}\nu_{2k+1}}}_{4^k k!(k-1)!} \underbrace{\prod_{i=2k+2}^{n+1} \mathcal{P}_{\mu_i\nu_i}}_{(n-2k)!}, \quad (\text{B4})$$

$$A_k^{n+1} (\gamma^{\mu_1} \mathcal{P}_{\mu_1\nu_1} \gamma^{\nu_1}) \underbrace{\mathcal{P}_{\mu_2\mu_3} \mathcal{P}_{\nu_2\nu_3} \cdots \mathcal{P}_{\mu_{2k}\mu_{2k+1}} \mathcal{P}_{\nu_{2k}\nu_{2k+1}}}_{4^k k!^2} \underbrace{\prod_{i=2k+2}^{n+1} \mathcal{P}_{\mu_i\nu_i}}_{(n-2k)!}, \quad (\text{B5})$$

$$A_k^{n+1} \mathcal{P}_{\nu_2} \mathcal{P}_{\mu_2} \underbrace{\mathcal{P}_{\mu_3\mu_4} \mathcal{P}_{\nu_3\nu_4} \cdots \mathcal{P}_{\mu_{2k+1}\mu_{2k+2}} \mathcal{P}_{\nu_{2k+1}\nu_{2k+2}}}_{4^k k!^2} \underbrace{\prod_{i=2k+3}^{n+1} \mathcal{P}_{\mu_i\nu_i}}_{(n-2k-1)!}. \quad (\text{B6})$$

Note that only expressions (B5) and (B6) have a $k = 0$ term. All of these terms have to be multiplied with a factor that accounts for the modified number of permutations that can be performed to transform the relevant term into itself. These factors read

$$(\text{B2}) \rightarrow \frac{4^k k!^2 (n-2k+1)!}{4^{k-1} (k-1)!^2 (n-2k+1)!} = 4k^2, \quad (\text{B7})$$

$$(\text{B3}) \rightarrow \frac{4^k k!^2 (n-2k+1)!}{4^k k!(k-1)!(n-2k)!} = k(n-2k+1), \quad (\text{B8})$$

$$(\text{B4}) \rightarrow \frac{4^k k!^2 (n-2k+1)!}{4^k k!(k-1)!(n-2k)!} = k(n-2k+1), \quad (\text{B9})$$

$$(\text{B5}) \rightarrow \frac{4^k k!^2 (n-2k+1)!}{4^k k!^2 (n-2k)!} = n-2k+1, \quad (\text{B10})$$

$$(\text{B6}) \rightarrow \frac{4^k k!^2 (n-2k+1)!}{4^k k!^2 (n-2k-1)!} = (n-2k+1)(n-2k). \quad (\text{B11})$$

By renaming the Lorentz indices and by using the following properties:

$$\begin{aligned} \mathcal{P}_\mu \mathcal{P}_\nu &= -\mathcal{P}_\nu \mathcal{P}_\mu + 2\mathcal{P}_{\mu\nu}, \\ \gamma^\mu \mathcal{P}_{\mu\nu} \gamma^\nu &= 3, \end{aligned} \quad (\text{B12})$$

expressions (B2)–(B6) can be transformed into

$$(\text{B2}) \rightarrow 4(k+1)^2 A_k^{n+1} \mathcal{P}_{\mu_1} \mathcal{P}_{\nu_1} \mathcal{P}_{\mu_2\mu_3} \mathcal{P}_{\nu_2\nu_3} \cdots \mathcal{P}_{\mu_{2k}\mu_{2k+1}} \mathcal{P}_{\nu_{2k}\nu_{2k+1}} \prod_{i=2k+2}^n \mathcal{P}_{\mu_i\nu_i}, \quad (\text{B13})$$

$$(\text{B3}) \rightarrow 2k(n-2k+1) A_k^{n+1} \times \mathcal{P}_{\mu_1\mu_2} \mathcal{P}_{\nu_1\nu_2} \cdots \mathcal{P}_{\mu_{2k-1}\mu_{2k}} \mathcal{P}_{\nu_{2k-1}\nu_{2k}} \prod_{i=2k+1}^n \mathcal{P}_{\mu_i\nu_i}, \quad (\text{B14})$$

$$(\text{B4}) \rightarrow 2k(n-2k+1) A_k^{n+1} \times \mathcal{P}_{\mu_1\mu_2} \mathcal{P}_{\nu_1\nu_2} \cdots \mathcal{P}_{\mu_{2k-1}\mu_{2k}} \mathcal{P}_{\nu_{2k-1}\nu_{2k}} \prod_{i=2k+1}^n \mathcal{P}_{\mu_i\nu_i}, \quad (\text{B15})$$

$$(\text{B5}) \rightarrow 3(n-2k+1) A_k^{n+1} \times \mathcal{P}_{\mu_1\mu_2} \mathcal{P}_{\nu_1\nu_2} \cdots \mathcal{P}_{\mu_{2k-1}\mu_{2k}} \mathcal{P}_{\nu_{2k-1}\nu_{2k}} \prod_{i=2k+1}^n \mathcal{P}_{\mu_i\nu_i}, \quad (\text{B16})$$

$$(\text{B6}) \rightarrow -(n-2k+1)(n-2k) \times A_k^{n+1} \mathcal{P}_{\mu_1} \mathcal{P}_{\nu_1} \mathcal{P}_{\mu_2\mu_3} \mathcal{P}_{\nu_2\nu_3} \cdots \mathcal{P}_{\mu_{2k}\mu_{2k+1}} \mathcal{P}_{\nu_{2k}\nu_{2k+1}} \times \prod_{i=2k+2}^n \mathcal{P}_{\mu_i\nu_i} + 2(n-2k+1)(n-2k) \times A_k^{n+1} \mathcal{P}_{\mu_1\nu_1} \mathcal{P}_{\mu_2\mu_3} \mathcal{P}_{\nu_2\nu_3} \cdots \mathcal{P}_{\mu_{2k}\mu_{2k+1}} \mathcal{P}_{\nu_{2k}\nu_{2k+1}} \times \prod_{i=2k+2}^n \mathcal{P}_{\mu_i\nu_i}. \quad (\text{B17})$$

Here, the substitution $k \rightarrow k+1$ was made for expression (B13), and the $k = 0$ term was added for expressions (B14) and (B15) since they are proportional to k . In this way, all expressions obtain a $k = 0$ term. Note that the second term of expression (B17) can be rewritten as

$$2(n-2k+1)(n-2k) A_k^{n+1} \times \mathcal{P}_{\mu_1\nu_1} \mathcal{P}_{\mu_2\mu_3} \mathcal{P}_{\nu_2\nu_3} \cdots \mathcal{P}_{\mu_{2k}\mu_{2k+1}} \mathcal{P}_{\nu_{2k}\nu_{2k+1}} \prod_{i=2k+2}^n \mathcal{P}_{\mu_i\nu_i} = 2(n-2k+1)(n-2k) A_k^{n+1} \mathcal{P}_{\mu_1\mu_2} \mathcal{P}_{\nu_1\nu_2} \cdots \mathcal{P}_{\mu_{2k-1}\mu_{2k}} \mathcal{P}_{\nu_{2k-1}\nu_{2k}} \prod_{i=2k+1}^{n-1} \mathcal{P}_{\mu_i\nu_i}, \quad (\text{B18})$$

$$\times \mathcal{P}_{\mu_1\mu_2} \mathcal{P}_{\nu_1\nu_2} \cdots \mathcal{P}_{\mu_{2k-1}\mu_{2k}} \mathcal{P}_{\nu_{2k-1}\nu_{2k}} \prod_{i=2k+1}^n \mathcal{P}_{\mu_i\nu_i}, \quad (\text{B19})$$

The transition from expression (B18) to (B19) is valid since both expressions are equal for odd n ; and for even n , the $k = \frac{n}{2}$ term, i.e., the last one, vanishes due to the prefactor $(n-2k)$. Next, the factor $\frac{n+1}{2n+3} \frac{1}{(n+1)!^2}$ and the double sum are

introduced again. The sum of expressions (B14)–(B16) and (B19) equals

$$\sum_{P(\mu)} \sum_{P(\nu)} \sum_{k=0}^{k_{\max,1}} \mathcal{A}_k^n \mathcal{P}_{\mu_1 \mu_2} \mathcal{P}_{\nu_1 \nu_2} \cdots \mathcal{P}_{\mu_{2k+1} \mu_{2k+2}} \mathcal{P}_{\nu_{2k+1} \nu_{2k+2}} \prod_{i=2k+3}^n \mathcal{P}_{\mu_i \nu_i}. \quad (\text{B20})$$

The coefficients \mathcal{A}_k^n can be calculated as

$$\begin{aligned} \mathcal{A}_k^n &= \frac{n+1}{2n+3} \frac{1}{(n+1)!^2} [3(n-2k+1) + 4k(n-2k+1) \\ &\quad + 2(n-2k+1)(n-2k)] A_k^{n+1}, \\ &= \frac{(n-2k+1)}{(n+1)!n!} A_k^{n+1}. \end{aligned} \quad (\text{B21})$$

From the definition of the coefficients A_k^n , i.e., Eq. (46), the expression for \mathcal{A}_k^n can be further

reduced to

$$\begin{aligned} \mathcal{A}_k^n &= \frac{(n-2k+1)}{(n+1)!n!} \left(\frac{1}{(-2)^k} \frac{(n+1)!}{k!(n-2k+1)!} \frac{(2n-2k+1)!!}{(2n+1)!!} \right), \\ &= \frac{1}{(-2)^k} \frac{1}{n!k!(n-2k)!} \frac{(2n-2k+1)!!}{(2n+1)!!}. \end{aligned} \quad (\text{B22})$$

For even values of n , one has $k_{\max,1} = \frac{n}{2}$. For odd values of n , this becomes $k_{\max,1} = \frac{n-1}{2}$.

Finally, the sum of expression (B13) and the first term of expression (B17) equal

$$\sum_{P(\mu)} \sum_{P(\nu)} \mathcal{P}_{\mu_1} \mathcal{P}_{\nu_1} \sum_{k=0}^{k_{\max,2}} \mathcal{B}_k^n \mathcal{P}_{\mu_2 \mu_3} \mathcal{P}_{\nu_2 \nu_3} \cdots \mathcal{P}_{\mu_{2k} \mu_{2k+1}} \mathcal{P}_{\nu_{2k} \nu_{2k+1}} \prod_{i=2k+2}^n \mathcal{P}_{\mu_i \nu_i}. \quad (\text{B23})$$

The coefficients \mathcal{B}_k^n are then given by

$$\begin{aligned} \mathcal{B}_k^n &= \frac{n+1}{2n+3} \frac{1}{(n+1)!^2} [4(k+1)^2 A_{k+1}^{n+1} - (n-2k+1)(n-2k) A_k^{n+1}], \\ &= \frac{n+1}{2n+3} \frac{1}{(n+1)!^2} \left(4(k+1)^2 \frac{1}{(-2)^{k+1}} \frac{(n+1)!}{(k+1)!(n-2k-1)!} \frac{(2n-2k-1)!!}{(2n+1)!!} \right. \\ &\quad \left. - (n-2k+1)(n-2k) \frac{1}{(-2)^k} \frac{(n+1)!}{k!(n-2k+1)!} \frac{(2n-2k+1)!!}{(2n+1)!!} \right), \\ &= -\frac{1}{(-2)^k} \frac{1}{n!k!(n-2k-1)!} \frac{(2n-2k-1)!!}{(2n+1)!!}. \end{aligned} \quad (\text{B24})$$

For even values of n , one has $k_{\max,1} = \frac{n-2}{2}$. For odd values of n , this becomes $k_{\max,1} = \frac{n-1}{2}$.

APPENDIX C: THE MODIFIED DECAY WIDTH FOR THE MULTI-DIPOLE-GAUSS FORM FACTOR

The expression for the total cross section of Eq. (74) is proportional to the following factor:

$$\sigma(s) \propto [(s - m_R^2)^2 + m_R^2 \tilde{\Gamma}_R^2]^{-2J_R}, \quad (\text{C1})$$

which stems from the squared multi-dipole-Gauss form factor and the squared spin- J_R propagator denominator. The values of s , which correspond to the half maximum of this factor are the solutions to the equation,

$$[(s - m_R^2)^2 + m_R^2 \tilde{\Gamma}_R^2]^{2J_R} = 2(m_R^2 \tilde{\Gamma}_R^2)^{2J_R}. \quad (\text{C2})$$

These are found as

$$s_{\pm} = m_R^2 \left(1 \pm \frac{\tilde{\Gamma}_R}{m_R} \sqrt{2^{1/(2J_R)} - 1} \right). \quad (\text{C3})$$

The FWHM is then calculated as

$$\begin{aligned} (\text{FWHM})_R &= \sqrt{s_+} - \sqrt{s_-} \\ &= m_R \left(\sqrt{1 + \frac{\tilde{\Gamma}_R}{m_R} \sqrt{2^{1/(2J_R)} - 1}} \right. \\ &\quad \left. - \sqrt{1 - \frac{\tilde{\Gamma}_R}{m_R} \sqrt{2^{1/(2J_R)} - 1}} \right). \end{aligned} \quad (\text{C4})$$

If $\tilde{\Gamma}_R$ is defined as

$$\tilde{\Gamma}_R(J_R) = \frac{\Gamma_R}{\sqrt{2^{1/(2J_R)} - 1}}, \quad (\text{C5})$$

then

$$(\text{FWHM})_R \approx \Gamma_R, \quad (\text{C6})$$

for $\Gamma_R \ll m_R$, which is the desired result.

VRANCX, DE CRUZ, RYCKEBUSCH, AND VANCRAEYVELD

PHYSICAL REVIEW C **84**, 045201 (2011)

- [1] W. Rarita and J. Schwinger, *Phys. Rev.* **60**, 61 (1941).
- [2] V. Pascalutsa and R. Timmermans, *Phys. Rev. C* **60**, 042201 (1999).
- [3] K. Johnson and E. C. G. Sudarshan, *Ann. Phys.* **13**, 126 (1961).
- [4] G. Velo and D. Zwanziger, *Phys. Rev.* **186**, 1337 (1969); **188**, 2218 (1969).
- [5] V. Pascalutsa, *Phys. Rev. D* **58**, 096002 (1998).
- [6] V. Shklyar, H. Lenske, and U. Mosel, *Phys. Rev. C* **82**, 015203 (2010).
- [7] F. A. Berends, J. W. van Holten, P. van Nieuwenhuizen, and B. De Wit, *Nucl. Phys. B* **154**, 261 (1979).
- [8] M. Benmerrouche, R. M. Davidson, and N. C. Mukhopadhyay, *Phys. Rev. C* **39**, 2339 (1989).
- [9] S.-Z. Huang, P.-F. Zhang, T.-N. Ruan, Y.-C. Zhu, and Z.-P. Zheng, *Eur. Phys. J. C* **42**, 375 (2005).
- [10] S. Weinberg, *Phys. Rev. B* **133**, 1318 (1964).
- [11] V. Shklyar, G. Penner, and U. Mosel, *Eur. Phys. J. A* **21**, 445 (2004).
- [12] R. E. Behrends and C. Fronsdal, *Phys. Rev.* **106**, 345 (1957).
- [13] S. Janssen, J. Ryckebusch, D. Debruyne, and T. Van Cauteren, *Phys. Rev. C* **65**, 015201 (2001).
- [14] K. Nakamura, *J. Phys. G* **37**, 075021 (2010).
- [15] E. Klempt and J.-M. Richard, *Rev. Mod. Phys.* **82**, 1095 (2010).
- [16] S. Janssen, J. Ryckebusch, W. Van Nespen, D. Debruyne, and T. Van Cauteren, *Eur. Phys. J. A* **11**, 105 (2001).
- [17] M. Benmerrouche, N. C. Mukhopadhyay, and J. F. Zhang, *Phys. Rev. D* **51**, 3237 (1995).
- [18] B. C. Pearce and B. K. Jennings, *Nucl. Phys. A* **528**, 655 (1991).
- [19] T. Corthals, J. Ryckebusch, and T. Van Cauteren, *Phys. Rev. C* **73**, 045207 (2006).

The Regge-plus-resonance-2011 model

Background and outline

The consistent-interaction formalism, developed in the previous chapter, allows for an improved description of spin-3/2 resonances and the inclusion of higher-spin resonances in the RPR framework. The nucleon-resonance spectrum features only one reported state with a spin higher than 5/2 in the $m_R \lesssim 2$ GeV region, being the ‘resonance region’ of the RPR model, namely the $F_{17}(1990)$ which is a spin-7/2 resonance [1]. This state is still unconfirmed, however. For the time being, it therefore suffices to consider nucleon resonances with spin 1/2, 3/2, and 5/2.

The transition operator becomes more complicated with increasing spin of the propagating fermion. This, for example, became apparent for consistent interactions in the previous chapter. As the number of off-shell parameters also grows with the spin (see Ref. [35], for example), it is therefore an enormous computational advantage to employ the consistent-interaction formalism, where a single interaction Lagrangian is characterized by a single parameter. For pseudoscalar-meson photo-production, this comes down to two effective parameters for each high-spin resonance, being the two electromagnetic coupling constants (g_1 and g_2 in Eqs. (3.68)) multiplied with the strong coupling constant (g_0 in Eq. (3.67)), and one effective parameter for each spin-1/2 resonance ($G_{MBR}G_{\gamma RN}^m$ in Eq. (2.56)).

The RPR model is implemented by the StrangeCalc software [36], which was developed by the “Theoretical Nuclear Physics and Statistical Physics” research group at Ghent University over a decade ago. Until early 2011, the transition operators of Sec. 2.3.5 were encoded “implicitly” in StrangeCalc, meaning that the matrix operations and tensor contractions had to be executed during runtime. For each individual calculation at some kinematics, these operations had to be repeated all over again. Not surprisingly, this was very time consuming. The extension of the RPR model to spin-5/2 resonances required a more time-efficient strategy, given the growing complexity of the transition operators with the spin of the resonance.

The number of matrix operations and tensor contractions constitutes the most time-consuming aspect of the old implementation of StrangeCalc. A more efficient strategy consists of expanding

the transition operators in a set of basis amplitudes. In the new implementation of StrangeCalc, the following basis set is employed [23]

$$\begin{aligned}
\zeta_1^\mu &= \gamma_5 \gamma_\nu (q^\nu \gamma^\mu - q^\mu \gamma^\nu), \\
\zeta_2^\mu &= 2\gamma_5 q_\nu (p'^\nu p^\mu - p'^\mu p^\nu), \\
\zeta_3^\mu &= \gamma_5 q_\nu (p^\nu \gamma^\mu - p^\mu \gamma^\nu), \\
\zeta_4^\mu &= \gamma_5 q_\nu (p'^\nu \gamma^\mu - p'^\mu \gamma^\nu), \\
\zeta_5^\mu &= -\gamma_5 q_\nu (q^\nu p'^\mu - q^\mu p'^\nu), \\
\zeta_6^\mu &= \gamma_5 q_\nu (q^\nu \gamma^\mu - q^\mu \gamma^\nu),
\end{aligned}$$

with q^μ , p^μ , and p'^μ being the center-of-mass four-momenta defined in Eq. (2.1). Note that $q_\mu \zeta_i^\mu = 0$ and that only four basis amplitudes are relevant in photoproduction, since $\epsilon_\mu^\lambda \zeta_{5,6}^\mu = 0$ for $Q^2 = 0$. The transition operator $T_{D_i}^\mu$ for each diagram D_i can hence be expanded as

$$T_{D_i}^\mu = \sum_{j=1}^6 (c_{D_i})_j \zeta_j^\mu, \quad (4.1)$$

with $(c_{D_i})_j$ being the expansion coefficients of diagram D_i . This implies that the total transition operator $T^\mu = \sum_i T_{D_i}^\mu$ can be expressed as

$$T^\mu = \sum_{j=1}^6 c_j \zeta_j^\mu, \quad (4.2)$$

with $c_j = \sum_i (c_{D_i})_j$. Since the full matrix structure is contained in the amplitudes ζ_i^μ , the expansion coefficients are scalar functions of the kinematics.

For each specific transition operator in StrangeCalc, the expansion coefficients/functions were determined using the Mathematica software [37]. These functions become more complicated with increasing spin of the intermediate particle. Calculating the transition operator with the new implementation of StrangeCalc is far more efficient compared to the old one. Indeed, in order to calculate the total transition operator, the matrix basis amplitudes have to be determined only once at certain kinematics. In addition, the evaluation of the scalar coefficients/functions at runtime is much faster than applying algebraic operations on the matrix and tensor objects of StrangeCalc. For example, the evaluation of the s -channel spin-3/2 and spin-5/2 transition operators is about 3.5 and 53 times faster, respectively. For an optimization procedure, the required computation time is even further reduced. Indeed, when varying the fit parameters, only the expansion functions have to be recalculated. The basis amplitudes for each data point only have to be determined once and can be used throughout the whole optimization procedure. In Ref. [23], it is shown that for a single spin-5/2 resonance exchange, the required optimization time is reduced by a factor of more than 300.

In this chapter, the most recent RPR model for $p(\gamma^{(*)}, K^+) \Lambda$, coined ‘‘RPR-2011’’, will be briefly discussed, as well as how its specific resonance content was selected. The realization of this model is both the result of the improved RPR framework, which accounts for the exchange of spin-5/2 resonances and employs a consistent interaction theory for high-spin resonances, as well as the ‘‘upgraded’’ implementation of StrangeCalc. More information on the development of RPR-2011 can be found in Refs. [21–23].

Available online at www.sciencedirect.com

SciVerse ScienceDirect

Nuclear Physics A 914 (2013) 74–78

www.elsevier.com/locate/nucphysa

The $p(\gamma, K^+)\Lambda$ reaction: Consistent high-spin interactions and Bayesian inference of its resonance content

T. Vrancx*, L. De Cruz, J. Ryckebusch, P. Vancraeyveld

Department of Physics and Astronomy, Ghent University, Proeftuinstraat 86, B-9000 Gent, Belgium

Received 29 November 2012; accepted 10 December 2012

Available online 13 December 2012

Abstract

A Bayesian analysis of the world's $p(\gamma, K^+)\Lambda$ data is presented. We adopt a Regge-plus-resonance framework featuring consistent interactions for nucleon resonances up to spin $J = 5/2$. The power of the momentum dependence of the consistent interaction structure rises with the spin of the resonance. This leads to unphysical structures in the energy dependence of the computed cross sections when the short-distance physics is cut off with standard hadronic form factors. A plausible, spin-dependent modification of the hadronic form factor is proposed which suppresses the unphysical artifacts. Next, we evaluate all possible combinations of 11 candidate resonances. The best model is selected from the 2048 model variants by calculating the Bayesian evidence values against the world's $p(\gamma, K^+)\Lambda$ data. From the proposed selection of 11 resonances, we find that the following nucleon resonances have the highest probability of contributing to the reaction: $S_{11}(1535)$, $S_{11}(1650)$, $F_{15}(1680)$, $P_{13}(1720)$, $D_{13}(1900)$, $P_{13}(1900)$, $P_{11}(1900)$, and $F_{15}(2000)$.

© 2012 Elsevier B.V. All rights reserved.

Keywords: Kaon production; Regge phenomenology; Baryon resonances; Bayesian inference; Consistent interactions

1. Introduction

The Regge-plus-resonance (RPR) framework provides a hybrid model that conjoins an iso-bar description of nucleon exchanges in the s channel and the exchange of Regge trajectories

* Corresponding author.
E-mail address: tom.vrancx@ugent.be (T. Vrancx).

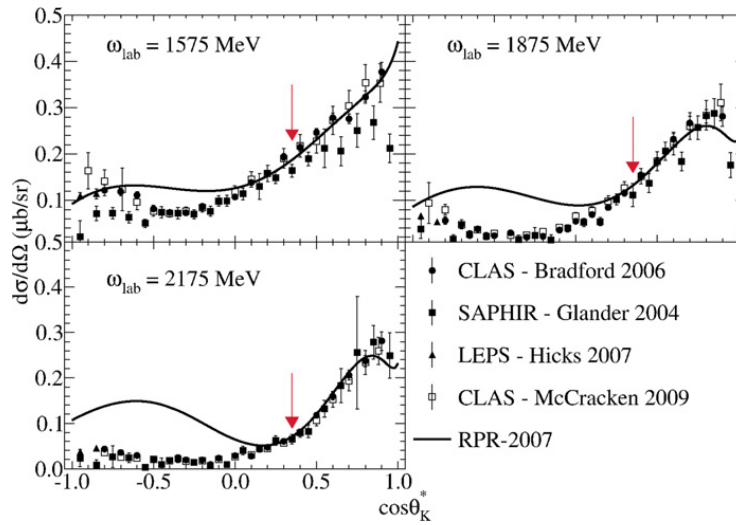


Fig. 1. RPR-2007 prediction and experimental data for the $p(\gamma, K^+)\Lambda$ differential cross section at photon lab energies of 1575, 1875, and 2175 MeV. The RPR-2007 model is optimized against the $\cos\theta_K^* > 0.35$ data, which is indicated by the arrows. More details about the calculations and the data can be found in Ref. [3].

in the background channel. The members of a Regge trajectory share identical internal quantum numbers, such as strangeness and isospin, but have different total spins. More specifically, the spins and the squared masses of the Regge trajectory members are linearly related [1]. As the $p(\gamma, K^+)\Lambda$ reaction is dominated by background contributions at forward kaon scattering angles, only t channel Regge trajectories are introduced in the RPR model. The featuring Regge families of the RPR model are the $K^+(494)$ and $K^{*+}(892)$ trajectories. By replacing the Feynman propagators of the $K^+(494)$ and $K^{*+}(892)$ diagrams with the corresponding Regge propagators, the Reggeized background amplitude is obtained.

In the s channel of the RPR model, individual nucleon resonances are exchanged. These nucleon resonances have half-integral spins and are modeled by effective Rarita–Schwinger (R-S) fields.¹ The finite lifetime of a resonance is incorporated in the RPR model by replacing the real pole of the Feynman propagator, i.e. $s - m_R^2$, with the imaginary pole $s - m_R^2 + im_R\Gamma_R$. Here m_R and Γ_R represent the mass and the decay width of the resonance, respectively. In order to ensure that the resonance contributions vanish in the high- s limit, a phenomenological hadronic form factor (HFF) is introduced. Such a form factor essentially “cuts off” the s channel amplitude beyond a certain energy scale.

2. Consistent interactions: RPR-2007 versus RPR-2011

In Ref. [2] a model was introduced that is now dubbed “RPR-2007”. In this model, only spin-1/2 and spin-3/2 nucleon resonances are included. While spin-1/2 interactions are straightforward to deal with, spin-3/2 (in fact, spin $J \geq 3/2$ in general) couplings are more difficult to treat. The tensor-spinor representation of the R-S formalism inevitably invokes additional components for the R-S fields. These degrees of freedom are unphysical and are attributed to additional spin-1/2, 3/2, \dots , $J - 1$ components, next to the physical components of the spin- J R-S field.

¹ The spin-1/2 R-S field is the Dirac field. Only fields with a spin $J \geq 3/2$ will be referred to as R-S fields.

It is clear that these unphysical degrees of freedom should be eliminated from the transition amplitude in order to have reaction observables that are physically meaningful.

In RPR-2007 so-called “contact-invariant” interaction Lagrangians are used to characterize the spin-3/2 couplings [2]. These Lagrangians contain one (two) “off-shell” parameter(s) for the strong (electromagnetic) vertex. There are hence three off-shell parameters for each amplitude that models a spin-3/2 resonance exchange. The HFF that is used in RPR-2007 is of the Gaussian form and has a common cutoff energy for all of the resonant amplitudes. The coupling constants, off-shell parameters, and the cutoff energy of the RPR-2007 model were optimized against the available, forward-angle experimental data at that time. The following resonance content was found for RPR-2007: $S_{11}(1650)$, $P_{11}(1710)$, $P_{13}(1720)$, $P_{13}(1900)$ and the missing resonance $D_{13}(1900)$. Fig. 1 shows the RPR-2007 prediction for the $p(\gamma, K^+)\Lambda$ differential cross section at three different photon energies in the lab frame. At forward kaon angles RPR-2007 is fully consistent with the data. At backward kaon angles, however, the model deviates significantly from the data. Moreover, an artificial bump is present and the situation worsens with increasing photon lab energy or, equivalently, increasing s . The observed elevation between the data and the RPR-2007 predictions can, to minor extent, be attributed to the fact that only $\cos\theta_K^* > 0.35$ data were considered when optimizing the RPR-2007 parameters. The main cause, however, of the unphysical bumps at $\cos\theta_K^* < 0$ is the adopted inconsistent interaction Lagrangians for the spin-3/2 vertices. As mentioned earlier, these Lagrangians contain one or two off-shell parameters. Now, these parameters allow for physical couplings to the unphysical components of the spin-3/2 R-S field. Hence, they give rise to unphysical structures in the predicted observables, which cannot be eliminated for any combination of the values of the off-shell parameters. What is more, the off-shell parameters are actually fitted to the data and, consequently, so are the artificial structures. Clearly this is a peculiar situation and it has to be put right.

In Ref. [4], a formalism was developed in which the interaction of R-S fields with fundamental fields can be described in a consistent way. The consistent interaction Lagrangians are invariant under the so-called “unconstrained R-S gauge” and it was proven that the unphysical components of the R-S field decouple from the transition amplitude for this type of interactions. Moreover, the gauge-invariant Lagrangians do not contain any additional parameters, apart from the usual coupling constants. In Ref. [4] a novel, spin-dependent HFF was developed as well, dubbed the “multidipole-Gauss” HFF. This HFF is able to regularize the amplitudes involving consistently interacting R-S fields, something that is not feasible with the standard Gaussian HFF. The combination of consistent high-spin interactions and the accompanying multidipole-Gauss HFF, constitutes the foundations of a new RPR model, i.e. RPR-2011.

3. Bayesian inference of the RPR-2011 resonance content

When it comes to specifying the set of nucleon resonances that has the most important contribution to the $p(\gamma, K^+)\Lambda$ reaction, one faces a lack of consensus between the various analyses for the reaction at hand. This disagreement becomes clear by inspecting Table I of Ref. [5]. The difficulty in determining the resonance contributions lies in the observed dominance of background (i.e. t channel) reactions in the $p(\gamma, K^+)\Lambda$ process.

The challenge for the newly developed RPR model is to determine the most probable model variant M (read: the most probable set of resonances) given the $p(\gamma, K^+)\Lambda$ data $\{d_k\}$ of the last decade. The standard χ^2 distribution for the RPR model variant space is only capable of specifying the set of resonances that offers the best description of the data $\{d_k\}$. However, the χ^2 distribution does not punish for the expansion of the set of resonances, i.e. the addition of extra

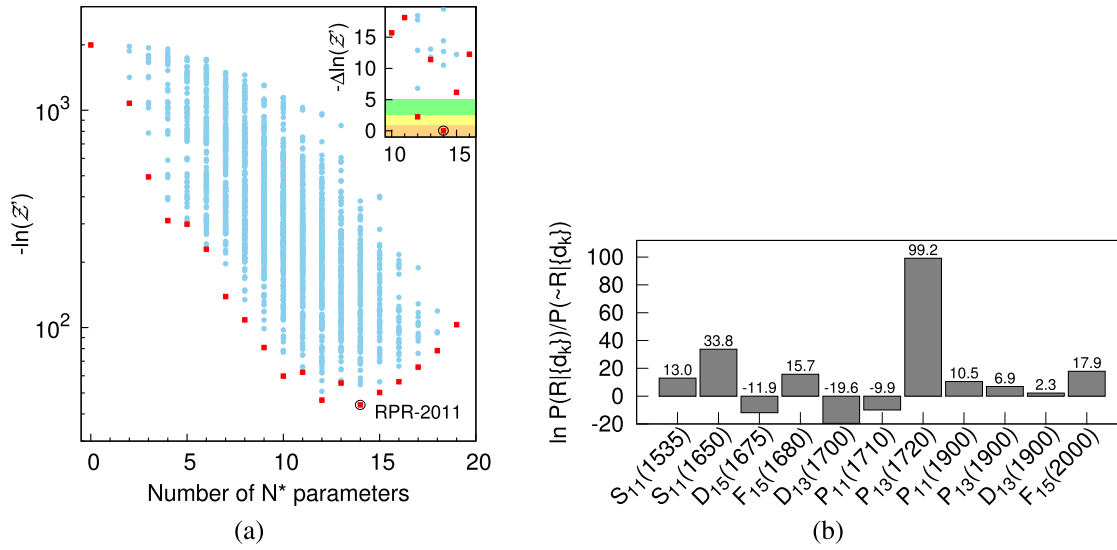


Fig. 2. (a) The evidence values for the 2048 RPR model variants (blue circles) as a function of the number of nucleon resonance parameters. The most probable model for a fixed number of parameters is indicated with a red square. Top right inset: evidence ratios relative to RPR-2011 for the models with the highest corrected evidence. The color coding refers to Jeffreys' scale: barely worth mentioning (orange), significant (yellow), strong to very strong (green) and decisive (white). More details can be found in Ref. [5]. (b) The relative resonance probabilities for each of the 11 considered resonances. More details can be found in Ref. [3]. (For interpretation of the references to color in this figure legend, the reader is referred to the web version of this article.)

model parameters. In fact, the absolute minimum of the χ^2 hypersurface is most likely relocated, in general, by increasing the dimension of the model parameter space. Therefore, a model with a “large” number of contributing resonances is not a probable model.

Bayesian inference offers a quantitative way of selecting the most probable model amongst its possible variants. The Bayesian evidence \mathcal{Z} for a specific set of resonances is defined as the probability of the data $\{d_k\}$, given the model variant M , and can be expressed as

$$\mathcal{Z} = P(\{d_k\}|M) = \int P(\{d_k\}, \alpha_M|M) d\alpha_M, \quad (1)$$

with α_M being the model's parameters. The integrand of the right-hand side of Eq. (1) is the product of the likelihood function $\mathcal{L}(\alpha_M) = P(\{d_k\}|\alpha_M, M)$ and the prior distribution $\pi(\alpha_M) = P(\alpha_M|M)$. The prior distribution for the model's parameters α_M is chosen to be a uniform distribution. Now, consider the two model variants M_A and M_B . The probabilities for both models are given by $P(\{d_k\}|M_A)$ and $P(\{d_k\}|M_B)$. By using Bayes' theorem, the probability ratio $P(\{d_k\}|M_A)/P(\{d_k\}|M_B)$ can be calculated as

$$\frac{P(M_A|\{d_k\})}{P(M_B|\{d_k\})} = \frac{P(\{d_k\}|M_A) P(M_A)}{P(\{d_k\}|M_B) P(M_B)} = \frac{\mathcal{Z}_A P(M_A)}{\mathcal{Z}_B P(M_B)}. \quad (2)$$

Since there is no prior preference for any of the two model variants, $P(M_A) = P(M_B)$ and the probability ratio reduces to the evidence ratio. The most probable model is therefore the model with the highest evidence. Due to the non-Gaussian and correlated nature of the systematic errors of $\{d_k\}$, the Bayesian evidence is underestimated. In Ref. [5] an approximate expression can be found for the corresponding corrected evidence, i.e. \mathcal{Z}' .

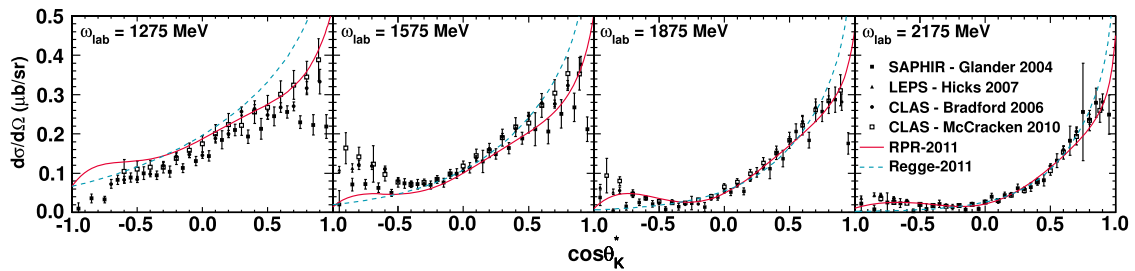


Fig. 3. RPR-2011 prediction and experimental data for the $p(\gamma, K^+)\Lambda$ differential cross section at photon lab energies of 1275, 1575, 1875, and 2175 MeV. More details about the calculations and the data can be found in Ref. [5].

For the Bayesian analysis of the RPR-2011 model, 11 candidate resonances up to spin-5/2 are considered. So next to the consistent couplings, RPR-2011 differs from RPR-2007 in the inclusion of spin-5/2 resonances. The candidate resonances are: $S_{11}(1535)$, $S_{11}(1650)$, $D_{15}(1675)$, $F_{15}(1680)$, $D_{13}(1700)$, $P_{11}(1710)$, and $P_{13}(1720)$ (established resonances), $P_{13}(1900)$ and $F_{15}(2000)$ (less-established resonances), and $D_{13}(1900)$ and $P_{11}(1900)$ (“missing” resonances). Now, each of the $2^{11} = 2048$ model variants were optimized against $\{d_k\}$ (6148 data points to date) and the corresponding \mathcal{Z}' value was calculated. The result is shown in Fig. 2(a). The model variant with the highest evidence is indicated as “RPR-2011”. The resonances that are not included in RPR-2011 are $D_{15}(1675)$, $D_{13}(1700)$, and $P_{11}(1710)$. The best RPR model variant, i.e. the one that includes all of the 11 candidate resonances, is hence not the most probable model. The individual probability ratio for each of the candidate resonances is shown in Fig. 2(b). A positive ratio indicates that it is more probable that the resonance contributes to the reaction $p(\gamma, K^+)\Lambda$ than that it does not. Vice versa, a negative ratio implies that the possibility that the resonance contributes to the reaction is not supported by the data. There are only 3 resonances that have a negative probability ratio, which are exactly those that are not part of the resonance set of RPR-2011.

In Fig. 3 the RPR-2011 prediction for the $p(\gamma, K^+)\Lambda$ differential cross section is shown at four different photon lab energies. It is seen that the bumps at $\cos\theta_K^* < 0$ (see Fig. 1) are no longer present and that RPR-2011 offers a good description of the data for the whole range of kaon scattering angles.

Acknowledgements

This work is supported by the Research Council of Ghent University and the Flemish Research Foundation (FWO Vlaanderen).

References

- [1] T. Corthals, J. Ryckebusch, T. Van Cauteren, Phys. Rev. C 73 (2006) 045207, arXiv:nucl-th/0510056.
- [2] T. Corthals, Ph.D. thesis, Ghent University, 2007, <http://inwpent5.ugent.be/papers/phdtamara.pdf>.
- [3] L. De Cruz, J. Ryckebusch, T. Vrancx, P. Vancraeyveld, Phys. Rev. C 86 (2012) 015212, arXiv:1205.2195 [nucl-th].
- [4] T. Vrancx, L. De Cruz, J. Ryckebusch, P. Vancraeyveld, Phys. Rev. C 84 (2011) 045201, arXiv:1105.2688 [nucl-th].
- [5] L. De Cruz, T. Vrancx, P. Vancraeyveld, J. Ryckebusch, Phys. Rev. Lett. 108 (2012) 182002, arXiv:1111.6511 [nucl-th].

Incompleteness of complete $N(\gamma, M)B$ data sets

Background and outline

In Sec. 2.2.1, it was pointed out that the $N(\gamma, M)B$ observables can be expressed in terms of the matrix elements $\mathcal{M}_{\lambda_N, \lambda_B}^\lambda$, also called the “reaction amplitudes”. These amplitudes are complex scalar functions of the kinematics of the reaction. Since the photon (λ), nucleon (λ_N), and baryon (λ_B) each have two polarization states, eight different amplitudes can be distinguished. As a result of angular momentum conservation, however, only four of these are independent. The specific spin-quantization axes employed for the initial- and final-state particles involved in the $N(\gamma, M)B$ reaction, determines the representation of the reaction amplitudes.

The four complex amplitudes can be expressed by four moduli and four phases, which are real functions of the kinematic variables. As quantum-mechanical observables are invariant under a global phase shift, only the relative phases are of importance. This implies that for a specific kinematic setting, pseudoscalar-meson photoproduction is fully quantified by seven real numbers, being the four moduli and three relative phases. From expression (2.11) it appears that polarization observables are only dependent of the moduli of the reaction amplitudes. This, however, is generally not the case. Indeed, upon using the definition of the $\mathcal{M}_{\lambda_N, \lambda_B}^\lambda$ in Eq. (2.9), the following expression is obtained for A :

$$A = \frac{\sum_{\{\lambda_i=0\}} |\epsilon_x^\lambda J_{\lambda_N, \lambda_B}^x + \epsilon_y^\lambda J_{\lambda_N, \lambda_B}^y|^2 - \sum_{\{\lambda'_i=0\}} |\epsilon_x^{\lambda'} J_{\lambda'_N, \lambda'_B}^x + \epsilon_y^{\lambda'} J_{\lambda'_N, \lambda'_B}^y|^2}{\sum_{\{\lambda_i=0\}} |\epsilon_x^\lambda J_{\lambda_N, \lambda_B}^x + \epsilon_y^\lambda J_{\lambda_N, \lambda_B}^y|^2 + \sum_{\{\lambda'_i=0\}} |\epsilon_x^{\lambda'} J_{\lambda'_N, \lambda'_B}^x + \epsilon_y^{\lambda'} J_{\lambda'_N, \lambda'_B}^y|^2}.$$

Here, the ‘ x ’ and ‘ y ’ denote the corresponding Lorentz components of the quantities in question. For the photon-polarization four-vector these are not to be confused with the linear polarization indices

(see Table 2.1). From this definition of A , it is seen that, once the photon polarization is fixed, the polarization observables are in general non-linear functions of the moduli and relative phases of the reaction amplitudes. Provided the four moduli and three (independent) relative phases are known at certain kinematics, the corresponding differential cross section and all the polarization observables can be determined.

Pseudoscalar-meson photoproduction is characterized by sixteen different observables, which in their turn can be expressed in terms of only seven variables. If these variables can be determined from experiment, they would constitute the ultimate test bed for $N(\gamma, M)B$ models as all of the possible ‘information’ on the reaction is contained in them. Given the non-linearity in their mutual relations, it can be inferred that extracting the variables from a measured set of observables is not a trivial task. A set containing the minimum number of observables, required to obtain the seven variables is known as a “complete set of observables”.

In theory, complete sets can be solved exactly to yield the four generating moduli and three relative phases. When experimentally determined, however, such a set becomes the subject of experimental uncertainty and it can be anticipated that this will have an impact on the extraction of the variables. In this chapter, it will be quantified how experimental error affects the potential of theoretical complete sets. To that end, simulated data for the $p(\gamma, K^+)\Lambda$ reaction will be analyzed. The simulated data will be provided by the RPR-2011 model of the previous chapter, which constitutes a realistic model for $K^+\Lambda$ photoproduction. For the first time, the reaction-amplitude moduli of a real data set (GRAAL data for $\{\Sigma, T, P\}$ [38]) will be extracted and compared to the corresponding predictions from RPR-2011.

PHYSICAL REVIEW C **87**, 055205 (2013)**Incompleteness of complete pseudoscalar-meson photoproduction**Tom Vrancx,^{*} Jan Ryckebusch,[†] Tom Van Cuyck, and Pieter Vancraeyveld*Department of Physics and Astronomy, Ghent University, Proeftuinstraat 86, B-9000 Gent, Belgium*

(Received 14 March 2013; published 28 May 2013)

Background: A complete set is a minimum set of observables which allows one to determine the underlying reaction amplitudes unambiguously. Pseudoscalar-meson photoproduction from the nucleon is characterized by four such amplitudes and complete sets involve single- and double-polarization observables.

Purpose: Identify complete sets of observables and study how measurements with finite error bars impact their potential to determine the reaction amplitudes unambiguously.

Method: The authors provide arguments to employ the transversity representation in order to determine the amplitudes in pseudoscalar-meson photoproduction. It is studied whether the amplitudes in the transversity basis for the $\gamma p \rightarrow K^+ \Lambda$ reaction can be estimated without ambiguity. To this end, data from the GRAAL collaboration and simulations from a realistic model are analyzed.

Results: It is illustrated that the moduli of normalized transversity amplitudes can be determined from precise single-polarization data. Starting from simulations with achievable experimental resolution, it is quite likely to obtain imaginary solutions for the relative phases of the amplitudes. Also the real solutions face a discrete phase ambiguity which makes it impossible to obtain a statistically significant solution for the relative phases at realistic experimental conditions.

Conclusions: Single polarization observables are effective in determining the moduli of the amplitudes in a transversity basis. Determining the relative phases of the amplitudes from double-polarization observables is far less evident. The availability of a complete set of observables does not allow one to unambiguously determine the reaction amplitudes with statistical significance.

DOI: [10.1103/PhysRevC.87.055205](https://doi.org/10.1103/PhysRevC.87.055205)

PACS number(s): 11.80.Cr, 13.60.Le, 24.10.-i, 25.20.Lj

I. INTRODUCTION

Pseudoscalar-meson photoproduction from the nucleon continues to be an invaluable source of information about the operation of quantum chromodynamics (QCD) in the nonperturbative regime [1–5]. Various classes of models, like constituent-quark approaches, have been developed to understand the structure and dynamics of hadrons in the low-energy regime of QCD. Experimental determination of the reaction amplitudes represents the most stringent test of those models and may open up a new chapter in the understanding of the energy eigenvalues and decay properties of hadron states.

Quantum mechanics dictates that measurable quantities can be expressed as bilinear combinations of complex amplitudes. Pseudoscalar meson photoproduction involves only two kinematical degrees of freedom, for example the energy of the incident photon and the scattering angle of the pseudoscalar meson. Since the (real) photon, the target, and the recoiling baryon have two spin degrees of freedom, eight possible amplitudes can be constructed. Due to angular momentum conservation, and depending on the adopted representation, half of these amplitudes either vanish identically or can be expressed in terms of the other four amplitudes. This leaves one with a set of four independent amplitudes. These amplitudes are complex functions (of the two kinematical variables) and therefore eight real functions are to be distinguished: four *moduli* and four *phases*. As quantum states are determined up to a constant

phase factor, only the relative phases of the amplitudes can be extracted. This means that pseudoscalar photoproduction can be quantified in terms of seven real-valued functions of the two kinematical variables. Equivalently, at fixed kinematics seven real values suffice to determine all observables.

A set containing a minimum number of observables from which, at fixed kinematics, the seven real values can be determined unambiguously is referred to as a *complete set*. In a seminal paper dating back to 1975, Barker, Donnachie, and Storrow argued that a complete set requires nine observables of a specific type [6]. In 1996, this was contested by Keaton and Workman [7] and by Wen-Tai Chiang and Tabakin [8]. The latter proved that eight well-chosen observables suffice to unambiguously determine the four moduli and three independent relative phases.

In theory, a complete set of eight observables suffices to retrieve the generating seven variables. The need for an additional observable (a set of eight equations involving only seven variables) to uniquely determine the relative phases is a reflection of the fact that the latter are linked to the observables through nonlinear equations. A set of seven well-chosen observables generally yields multiple solutions for the phases. Therefore, an extra observable is required to mark the correct solution. In reality, however, observables have a finite precision and deviate from the exact values. This compromises the solution of the phase ambiguity [9]. It then remains a question whether a set of eight observables is still sufficient to reach a situation of complete knowledge about the amplitudes.

Thanks to recent technological advances in producing high-quality polarized beams and in developing polarized nucleon targets [10], it becomes possible to measure a

^{*}Tom.Vrancx@UGent.be[†]Jan.Ryckebusch@UGent.be

sufficiently large amount of single- and double-polarization observables in pion and kaon photoproduction. As a result, a status of complete quantum mechanical information of pseudoscalar meson photoproduction comes within reach. The self-analyzing character of the Λ is an enormous asset for achieving truly complete measurements for $\gamma p \rightarrow K^+ \Lambda$ and experimental efforts are underway [2]. For example, the CLAS collaboration at Jefferson Lab has many $\gamma p \rightarrow K^+ \Lambda$ polarization data in the pipeline.

It should be stressed that in the quality and quantity of the experimental results, there is some kind of hierarchy. Indeed, double-polarization data is most often outnumbered by single-polarization results, which in their turn are outnumbered by the size of the differential cross-section database. In view of this, the transversity representation of the amplitudes is a very promising one. Indeed, in this basis the single-polarization observables are linked to the squared moduli of the amplitudes by means of linear equations. Accordingly, the transversity basis occupies a central position in this work.

The outline of the remainder of this paper is as follows. In Sec. II, the transversity amplitudes are introduced and all possible observables for pseudoscalar meson photoproduction are expressed in this basis. In Sec. III, Wen-Tai Chiang and Tabakin's formalism for solving complete sets is briefly reviewed. This formalism is solid in the exact case. When experimental uncertainty is involved, however, a consistency issue for a unique determination of the phases arises. A method to resolve this inconsistency is proposed. As a test of this method, in Sec. IV it is applied to simulations from a realistic model for the $\gamma p \rightarrow K^+ \Lambda$ reaction. The conclusions are summarized in Sec. V. In the Appendix, both the helicity and the CGLN expansions of the observables are considered, and a connection to the transversity basis is established.

II. OBSERVABLES FOR PSEUDOSCALAR MESON PRODUCTION

A. Reaction amplitudes

The convention is adopted that the xz plane coincides with the reaction plane and that the positive z axis is along the direction of the photon's three-momentum. The two independent kinematic variables that will be considered throughout this work are the total energy of the reaction, or *invariant mass*, W , and the *scattering angle* of the pseudoscalar meson in the center-of-mass frame, $\theta_{c.m.}$. As mentioned in Sec. I, pseudoscalar-meson photoproduction can be quantified by four complex reaction amplitudes $\mathcal{M}_i(W, \cos \theta_{c.m.})$ ($i = 1, 2, 3, 4$). The unpolarized differential cross section, for example, is given by

$$\frac{d\sigma(W, \cos \theta_{c.m.})}{d\Omega} = \varrho \sum_{i=1}^4 |\mathcal{M}_i(W, \cos \theta_{c.m.})|^2, \quad (1)$$

where ϱ is a kinematic factor. There are various equivalent representations for the \mathcal{M}_i , all of which have a distinct kinematic factor ϱ . The representation is determined by the choices made with regard to the quantization axis of the

involved particles with a nonvanishing spin: the nucleon target, the incoming photon, and the recoiling baryon.

The Dirac spinors for a particle with rest mass m , four-momentum $p^\mu = (E, \vec{p})$, and a spin vector with polar angles (θ, ϕ) are defined as

$$u_\pm(p^\mu, \theta, \phi) = \frac{1}{\sqrt{2m(E+m)}} \left[(E+m)I_2 \right] \vec{\sigma} \cdot \vec{p} s_\pm(\theta, \phi), \quad (2)$$

following the Björken-Drell convention [11]. Here I_2 represents the 2×2 identity matrix and $\vec{\sigma} = (\sigma_x, \sigma_y, \sigma_z)$ is the Pauli vector. Further, the Pauli spinors $s_+(\theta, \phi)$ ("spin up") and $s_-(\theta, \phi)$ ("spin down") are given by

$$s_+(\theta, \phi) = \begin{pmatrix} \cos \frac{\theta}{2} \\ e^{i\phi} \sin \frac{\theta}{2} \end{pmatrix}, \quad (3)$$

$$s_-(\theta, \phi) = \begin{pmatrix} -e^{-i\phi} \sin \frac{\theta}{2} \\ \cos \frac{\theta}{2} \end{pmatrix}.$$

The following shorthand notations are introduced:

$$|\pm\rangle_x = u_\pm(p^\mu, \frac{\pi}{2}, 0),$$

$$|\pm\rangle_y = u_\pm(p^\mu, \frac{\pi}{2}, \frac{\pi}{2}), \quad (4)$$

$$|\pm\rangle_z = u_\pm(p^\mu, 0, 0).$$

Using Eq. (2) it can readily be verified that the $|\pm\rangle_x$ and $|\pm\rangle_z$ can be expressed in terms of the $|\pm\rangle_y$ as follows:

$$|\pm\rangle_x = \frac{1 \mp i}{2} (|- \rangle_y \pm |+ \rangle_y), \quad (5)$$

$$|\pm\rangle_z = \frac{1}{\sqrt{2}} (|\pm \rangle_y - i |\mp \rangle_y).$$

The $\mathcal{M}_i(W, \cos \theta_{c.m.})$ are the amplitudes of the operator $\epsilon_\lambda^\mu J_\mu$ for a fixed polarization of the initial- and final-state particles. The ϵ_λ^μ is the photon's polarization four-vector and J^μ the transition current operator. The photon beam polarizations denoted by " $\mathcal{B} = x$ " ($+\vec{e}_x$ direction) and " $\mathcal{B} = y$ " ($+\vec{e}_y$ direction) correspond with

$$\epsilon_x^\mu = (0, 1, 0, 0),$$

$$\epsilon_y^\mu = (0, 0, 1, 0), \quad (6)$$

and give rise to the following currents:

$$J_x = \epsilon_x^\mu J_\mu,$$

$$J_y = \epsilon_y^\mu J_\mu. \quad (7)$$

The photon beam polarizations denoted by " $\mathcal{B} = \pm\pi/4$ " [oblique polarization, $\epsilon_{\pm\pi/4}^\mu = \frac{1}{\sqrt{2}}(0, 1, \pm 1, 0)$] and " $\mathcal{B} = \pm$ " [circular polarization, $\epsilon_\pm^\mu = \frac{1}{\sqrt{2}}(0, 1, \pm i, 0)$] correspond with

$$J_{\pm\pi/4} = -\frac{1}{\sqrt{2}}(J_x \pm J_y), \quad (8)$$

$$J_\pm = -\frac{1}{\sqrt{2}}(J_x \pm i J_y). \quad (9)$$

B. Observables in the transversity basis

The so-called *transversity amplitudes* b_i express the \mathcal{M}_i in terms of the spinors $|\pm\rangle_y$ (quantization axis perpendicular to

the reaction plane) and the linear photon polarizations J_x and J_y , i.e.,

$$\begin{aligned} b_1 &= {}_y\langle +|J_y|+\rangle_y, & b_2 &= {}_y\langle -|J_y|-\rangle_y, \\ b_3 &= {}_y\langle +|J_x|-\rangle_y, & b_4 &= {}_y\langle -|J_x|+\rangle_y. \end{aligned} \quad (10)$$

In these definitions, the bra (ket) refers to the recoil (target). The differential cross section for a given beam \mathcal{B} , target \mathcal{T} , and recoil polarization \mathcal{R} is denoted as

$$\zeta^{(\mathcal{B}, \mathcal{T}, \mathcal{R})} = \frac{d\sigma^{(\mathcal{B}, \mathcal{T}, \mathcal{R})}}{d\Omega}. \quad (11)$$

An unpolarized state is denoted by “0.” For example, $\mathcal{T} = 0$ denotes an unpolarized target and in computing the cross section (11) for $\mathcal{T} = 0$, an averaging over both target polarizations is implicitly assumed.

An asymmetry A can generally be expressed as

$$A = \frac{\zeta^{(\mathcal{B}_1, \mathcal{T}_1, \mathcal{R}_1)} - \zeta^{(\mathcal{B}_2, \mathcal{T}_2, \mathcal{R}_2)}}{\zeta^{(\mathcal{B}_1, \mathcal{T}_1, \mathcal{R}_1)} + \zeta^{(\mathcal{B}_2, \mathcal{T}_2, \mathcal{R}_2)}}. \quad (12)$$

A *single* asymmetry comprises one polarized and two unpolarized states. Hence, there are three possible single-polarization observables, namely the beam asymmetry Σ ($\mathcal{B} \neq 0$), the target asymmetry T ($\mathcal{T} \neq 0$), and the recoil asymmetry P ($\mathcal{R} \neq 0$). The explicit definitions of these three single asymmetries can be found in Table I. A *double* asymmetry, involves two polarized and one unpolarized state. There are three types of double asymmetries: the target-recoil asymmetries ($\mathcal{B}_1 = \mathcal{B}_2 = 0$), the beam-recoil asymmetries ($\mathcal{T}_1 = \mathcal{T}_2 = 0$), and the beam-target asymmetries ($\mathcal{R}_1 = \mathcal{R}_2 = 0$). The definitions for the various double asymmetries are contained in Table I.

The aim of the current section is to represent the single and double asymmetries in the transversity basis. As representative examples, the transversity expansions of the single asymmetry Σ and of the double asymmetry C_x are derived. The beam

asymmetry Σ is defined as

$$\Sigma = \frac{\zeta^{(y, 0, 0)} - \zeta^{(x, 0, 0)}}{\zeta^{(y, 0, 0)} + \zeta^{(x, 0, 0)}}. \quad (13)$$

Using

$$\begin{aligned} \zeta^{(y, 0, 0)} &= \frac{1}{2}(\zeta^{-(y, +y, +y)} + \zeta^{-(y, +y, -y)} \\ &\quad + \zeta^{-(y, -y, +y)} + \zeta^{-(y, -y, -y)}), \\ &= \frac{\varrho}{2} \left(\underbrace{|{}_y\langle +|J_y|+\rangle_y|^2}_{=b_1} + \underbrace{|{}_y\langle -|J_y|+\rangle_y|^2}_{=0} \right. \\ &\quad \left. + \underbrace{|{}_y\langle +|J_y|-\rangle_y|^2}_{=0} + \underbrace{|{}_y\langle -|J_y|-\rangle_y|^2}_{=b_2} \right), \\ &= \frac{\varrho}{2}(|b_1|^2 + |b_2|^2), \end{aligned} \quad (14)$$

and

$$\begin{aligned} \zeta^{(x, 0, 0)} &= \frac{1}{2}(\zeta^{-(x, +y, +y)} + \zeta^{-(x, +y, -y)} \\ &\quad + \zeta^{-(x, -y, +y)} + \zeta^{-(x, -y, -y)}), \\ &= \frac{\varrho}{2} \left(\underbrace{|{}_y\langle +|J_x|+\rangle_y|^2}_{=0} + \underbrace{|{}_y\langle -|J_x|+\rangle_y|^2}_{=b_4} \right. \\ &\quad \left. + \underbrace{|{}_y\langle +|J_x|-\rangle_y|^2}_{=b_3} + \underbrace{|{}_y\langle -|J_x|-\rangle_y|^2}_{=0} \right), \\ &= \frac{\varrho}{2}(|b_3|^2 + |b_4|^2), \end{aligned} \quad (15)$$

TABLE I. The expressions for the single and double asymmetries in the normalized transversity basis. Both the expressions obtained in this work and those found in the literature [13] are listed. The convention for the beam-target asymmetry E is adopted from Ref. [12] instead of Ref. [13].

	$(\mathcal{B}_1, \mathcal{T}_1, \mathcal{R}_1)$	$(\mathcal{B}_2, \mathcal{T}_2, \mathcal{R}_2)$	Transversity representation	
			This work	Literature [13]
Σ	$(y, 0, 0)$	$(x, 0, 0)$		$r_1^2 + r_2^2 - r_3^2 - r_4^2$
T	$(0, +y, 0)$	$(0, -y, 0)$		$r_1^2 - r_2^2 - r_3^2 + r_4^2$
P	$(0, 0, +y)$	$(0, 0, -y)$		$r_1^2 - r_2^2 + r_3^2 - r_4^2$
C_x	$(+, 0, +x)$	$(+, 0, -x)$	$-2\text{Im}(a_1 a_4^* + a_2 a_3^*)$	$-2\text{Im}(a_1 a_4^* - a_2 a_3^*)$
C_z	$(+, 0, +z)$	$(+, 0, -z)$	$+2\text{Re}(a_1 a_4^* - a_2 a_3^*)$	$+2\text{Re}(a_1 a_4^* + a_2 a_3^*)$
O_x	$(+\frac{\pi}{4}, 0, +x)$	$(+\frac{\pi}{4}, 0, -x)$	$+2\text{Re}(a_1 a_4^* + a_2 a_3^*)$	$+2\text{Re}(a_1 a_4^* - a_2 a_3^*)$
O_z	$(+\frac{\pi}{4}, 0, +z)$	$(+\frac{\pi}{4}, 0, -z)$	$+2\text{Im}(a_1 a_4^* - a_2 a_3^*)$	$+2\text{Im}(a_1 a_4^* + a_2 a_3^*)$
E	$(+, -z, 0)$	$(+, +z, 0)$	$+2\text{Re}(a_1 a_3^* - a_2 a_4^*)$	$-2\text{Re}(a_1 a_3^* + a_2 a_4^*)$
F	$(+, +x, 0)$	$(+, -x, 0)$	$-2\text{Im}(a_1 a_3^* + a_2 a_4^*)$	$+2\text{Im}(a_1 a_3^* - a_2 a_4^*)$
G	$(+\frac{\pi}{4}, +z, 0)$	$(+\frac{\pi}{4}, -z, 0)$	$-2\text{Im}(a_1 a_3^* - a_2 a_4^*)$	$+2\text{Im}(a_1 a_3^* + a_2 a_4^*)$
H	$(+\frac{\pi}{4}, +x, 0)$	$(+\frac{\pi}{4}, -x, 0)$	$+2\text{Re}(a_1 a_3^* + a_2 a_4^*)$	$-2\text{Re}(a_1 a_3^* - a_2 a_4^*)$
T_x	$(0, +x, +x)$	$(0, +x, -x)$	$+2\text{Re}(a_1 a_2^* + a_3 a_4^*)$	$+2\text{Re}(a_1 a_2^* - a_3 a_4^*)$
T_z	$(0, +x, +z)$	$(0, +x, -z)$	$+2\text{Im}(a_1 a_2^* + a_3 a_4^*)$	$+2\text{Im}(a_1 a_2^* - a_3 a_4^*)$
L_x	$(0, +z, +x)$	$(0, +z, -x)$	$-2\text{Im}(a_1 a_2^* - a_3 a_4^*)$	$-2\text{Im}(a_1 a_2^* + a_3 a_4^*)$
L_z	$(0, +z, +z)$	$(0, +z, -z)$	$+2\text{Re}(a_1 a_2^* - a_3 a_4^*)$	$+2\text{Re}(a_1 a_2^* + a_3 a_4^*)$

one obtains

$$\Sigma = \frac{|b_1|^2 + |b_2|^2 - |b_3|^2 - |b_4|^2}{|b_1|^2 + |b_2|^2 + |b_3|^2 + |b_4|^2}. \quad (16)$$

At this point the *normalized* transversity amplitudes a_i

$$a_i = \frac{b_i}{\sqrt{|b_1|^2 + |b_2|^2 + |b_3|^2 + |b_4|^2}} \quad (17)$$

are introduced. Upon using the notation $r_i = |a_i|$, the normalization condition of the a_i reads

$$r_1^2 + r_2^2 + r_3^2 + r_4^2 = 1, \quad (18)$$

which means that there are only three independent moduli or six real values to be determined. For the b_i , this is respectively four and seven. The $|b_i|$ can be obtained from the r_i , combined with the magnitude of the unpolarized differential cross section. Using the r_i , the beam asymmetry Σ can be expressed as

$$\Sigma = r_1^2 + r_2^2 - r_3^2 - r_4^2. \quad (19)$$

Similar calculations as those for Σ yield the expressions for T and P , contained in Table I.

Next, the beam-recoil asymmetry C_x

$$C_x = \frac{\zeta^{(+,0,+x)} - \zeta^{(+,0,-x)}}{\zeta^{(+,0,+x)} + \zeta^{(+,0,-x)}} \quad (20)$$

is considered. The first term in the numerator can be expressed as

$$\begin{aligned} \zeta^{(+,0,+x)} &= \frac{1}{2}(\zeta^{(+,+y,+x)} + \zeta^{(+,-y,+x)}), \\ &= \frac{\rho}{2}(|x\langle +|J_+|+\rangle_y|^2 + |x\langle +|J_+|-\rangle_y|^2). \end{aligned} \quad (21)$$

Using Eq. (9), one obtains

$$\begin{aligned} \zeta^{(+,0,+x)} &= \frac{\rho}{4}(|x\langle +|J_x|+\rangle_y + i_x\langle +|J_y|+\rangle_y|^2 \\ &\quad + |x\langle +|J_x|-\rangle_y + i_x\langle +|J_y|-\rangle_y|^2). \end{aligned} \quad (22)$$

Then Eq. (5) is employed to transform the $x\langle +|$ spinors into $y\langle \pm|$ spinors, i.e.,

$$\begin{aligned} \zeta^{(+,0,+x)} &= \frac{\rho}{8} \left(\underbrace{|y\langle +|J_x|+\rangle_y}_{=0} + \underbrace{|y\langle -|J_x|+\rangle_y}_{=b_4} \right. \\ &\quad + i \underbrace{|y\langle +|J_y|+\rangle_y}_{=b_1} + i \underbrace{|y\langle -|J_y|+\rangle_y}_{=0} \\ &\quad + \underbrace{|y\langle +|J_x|-\rangle_y}_{=b_3} + \underbrace{|y\langle -|J_x|-\rangle_y}_{=0} \\ &\quad \left. + i \underbrace{|y\langle +|J_y|-\rangle_y}_{=0} + i \underbrace{|y\langle -|J_y|-\rangle_y}_{=b_2} \right)^2, \\ &= \frac{\rho}{8} (|ib_1 + b_4|^2 + |ib_2 + b_3|^2). \end{aligned} \quad (23)$$

An analogous calculation for $\zeta^{(+,0,-x)}$ yields

$$\zeta^{(+,0,-x)} = \frac{\rho}{8} (|ib_1 - b_4|^2 + |ib_2 - b_3|^2). \quad (24)$$

Inserting expressions (23) and (24) in the definition (20) leads to

$$\begin{aligned} C_x &= \frac{i(b_1 b_4^* - b_1^* b_4 + b_2 b_3^* - b_2^* b_3)}{|b_1|^2 + |b_2|^2 + |b_3|^2 + |b_4|^2}, \\ &= -2\text{Im}(a_1 a_4^* + a_2 a_3^*). \end{aligned} \quad (25)$$

Analogous derivations for the remaining beam-recoil (C_z, O_x, O_x), the beam-target (E, F, G, H), and the target-recoil asymmetries (T_x, T_z, L_x, L_z) yield the expressions listed in Table I.

As it is unfrequently used in the field, the transversity representation for the observables is not contained in the extensive recent review by Sandorfi *et al.* [12]. However, when it comes to extracting the invariant amplitudes from complete measurements, it will turn out that the transversity representation is highly beneficial. This will be the subject of Sec. IV B. The transversity expressions for the double asymmetries obtained in this work, are not consistent with those listed in literature [6,9,13].

By inspecting Table I it is clear that the substitution $a_3 \rightarrow -a_3$ makes the expressions derived in this work consistent with those contained in Ref. [13]. To the knowledge of the authors, the expressions for the asymmetries in the transversity basis were first published by Barker, Donnachie, and Storror in 1975 [6]. Slightly different expressions are contained in a 1990 paper by Adelseck and Saghai [13]. However, explicit derivations are not contained in either article. In the Appendix, the asymmetries are expanded in the helicity and the CGLN basis. The helicity representation is presented in Table VIII and is consistent with the one obtained by Fasano *et al.* [14]. On the other hand, the CGLN expansion was found to coincide with the one calculated by Sandorfi *et al.* [12]. Interestingly enough, both the helicity and CGLN representations were derived from the transversity expressions obtained in this work. Starting from the transversity expressions listed in the last column of Table I the helicity and CGLN expansions available in the literature are not retrieved.

III. INFERRING THE TRANSVERSITY AMPLITUDES FROM THE ASYMMETRIES

A. The moduli

In Sec. II B the notation $r_i = |a_i|$ was introduced. Hence, the (normalized) transversity amplitudes can be expressed as

$$a_j = r_j e^{i\alpha_j}. \quad (26)$$

Here α_j represents the phase of the transversity amplitude a_j . From the expressions for Σ , T , and P in Table I and from the normalization condition (18), one can readily solve for the moduli of the amplitudes in terms of the single asymmetries to obtain

$$\begin{aligned} r_1 &= \frac{1}{2}\sqrt{1 + \Sigma + T + P}, & r_2 &= \frac{1}{2}\sqrt{1 + \Sigma - T - P}, \\ r_3 &= \frac{1}{2}\sqrt{1 - \Sigma - T + P}, & r_4 &= \frac{1}{2}\sqrt{1 - \Sigma + T - P}. \end{aligned} \quad (27)$$

TABLE II. Correspondence between the independent (δ_i) and nonindependent (Δ_{ij}) phases for the reference phase α_4 and the independent ($\delta_i^{\alpha_k}$) and nonindependent ($\Delta_{ij} = \delta_i^{\alpha_k} - \delta_j^{\alpha_k} = \alpha_i - \alpha_j$) phases for the reference phase α_k ($k = 1, 2, 3$).

α_4	δ_1	δ_2	δ_3	Δ_{12}	Δ_{13}	Δ_{23}
α_1	$-\delta_4^{\alpha_1}$	Δ_{24}	Δ_{34}	$-\delta_2^{\alpha_1}$	$-\delta_3^{\alpha_1}$	Δ_{23}
α_2	Δ_{14}	$-\delta_4^{\alpha_2}$	Δ_{34}	$\delta_1^{\alpha_2}$	Δ_{13}	$-\delta_3^{\alpha_2}$
α_3	Δ_{14}	Δ_{24}	$-\delta_4^{\alpha_3}$	Δ_{12}	$\delta_1^{\alpha_3}$	$\delta_2^{\alpha_3}$

Hence, a measurement of Σ , T , and P at fixed kinematics ($W, \cos \theta_{c.m.}$) yields the moduli of the transversity amplitudes r_i .

In Sec. II B, it was mentioned that only three of the four moduli are independent. Any of the four combinations of three independent moduli can be chosen without violating generality. As will be explained in Sec. IV C 2, however, it is not beneficial to eliminate one of the moduli.

B. The relative phases

1. Independent and nonindependent relative phases

From the double asymmetries one can extract the relative phases $\alpha_{ij} = \alpha_i - \alpha_j$, given that the moduli r_i are known. There are six possible combinations for the relative phases, namely $\alpha_{12}, \alpha_{13}, \alpha_{14}, \alpha_{23}, \alpha_{24}$, and α_{34} , all of which can be extracted from the double asymmetries (see Table I). However, only three of these are independent variables; the remaining three can be expressed as linear combinations of the three independent relative phases. For example, with α_4 as the reference phase, ($\alpha_{14}, \alpha_{24}, \alpha_{34}$) are the independent phases, and ($\alpha_{12}, \alpha_{13}, \alpha_{23}$) are the nonindependent ones

$$\alpha_{12} = \alpha_{14} - \alpha_{24}, \quad \alpha_{13} = \alpha_{14} - \alpha_{34}, \quad \alpha_{23} = \alpha_{24} - \alpha_{34}. \quad (28)$$

Alternatively, one can express the phases relative to α_1, α_2 , or α_3 . From now on, α_4 will serve as the reference phase and the independent phases are denoted as $\delta_i = \alpha_i - \alpha_4$ ($i = 1, 2, 3$). The nonindependent phases are labeled as $\Delta_{ij} = \delta_i - \delta_j$ ($i \neq j$). Table II shows the correspondence between the independent and the nonindependent phases for the four distinct reference phases.

2. Complete sets

In Ref. [8], Wen-Tai Chiang and Tabakin proved that a specific set of four double asymmetries is sufficient to extract two of the independent phases, δ_i and δ_j , and two of the nonindependent phases, Δ_{ik} and Δ_{jk} ($i \neq j \neq k$). The remaining independent phase δ_k can be constructed as $\delta_k = \delta_i - \Delta_{ik}$ or $\delta_k = \delta_j - \Delta_{jk}$. Hence, a *complete set*, consisting of three single and four double asymmetries, determines the four moduli and the three independent relative phases of the transversity amplitudes a_i .

The collection of complete sets, which is listed in Tables III–VIII of Ref. [8], can be divided into two categories.

An example of a complete set of the first kind is $\{C_x, O_x, E, F\}$ (the single asymmetries Σ, T , and P are implicitly assumed to be included as they are a vital part of any complete set in the transversity basis). From Table I one obtains

$$\begin{aligned} r_1 r_4 \sin \delta_1 + r_2 r_3 \sin \Delta_{23} &= -\frac{C_x}{2}, \\ r_1 r_4 \cos \delta_1 + r_2 r_3 \cos \Delta_{23} &= \frac{O_x}{2}, \end{aligned} \quad (29)$$

and

$$\begin{aligned} r_1 r_3 \cos \Delta_{13} - r_2 r_4 \cos \delta_2 &= \frac{E}{2}, \\ r_1 r_3 \sin \Delta_{13} + r_2 r_4 \sin \delta_2 &= -\frac{F}{2}. \end{aligned} \quad (30)$$

Since Eq. (29) contains both a sine and a cosine of the unknowns, there are generally two solutions for $\{\delta_1, \Delta_{23}\}$. The same reasoning applies to E and F , and, hence, there are four possible solutions for $\{\delta_1, \delta_2, \Delta_{13}, \Delta_{23}\}$. Yet only one of these solutions will satisfy the (trivial) relation

$$\delta_1 + \Delta_{23} - \delta_2 - \Delta_{13} = 0, \quad (31)$$

and that specific solution is the actual solution.

If, for example, one replaces F with H in Eq. (30), a complete set of the second kind is obtained. Table I yields

$$r_1 r_3 \cos \Delta_{13} + r_2 r_4 \cos \delta_2 = \frac{H}{2}. \quad (32)$$

Since $\{E, H\}$ contain only the cosine of the unknowns, there are four possible solutions for $\{\delta_2, \Delta_{13}\}$. Hence, an eightfold ambiguity for $\{\delta_1, \delta_2, \Delta_{13}, \Delta_{23}\}$ emerges. Only one of the solutions, however, obeys the constraint (31). Similarly, the complete set $\{C_x, O_x, F, G\}$ is subject to an eightfold phase ambiguity.

C. Introducing experimental error

As indicated in Sec. III B 2, a complete set provides access to two independent and two nonindependent phases, i.e., the set $\{\delta_i, \delta_j, \Delta_{ik}, \Delta_{jk}\}$ ($i \neq j \neq k$). There are two ways to calculate the third independent phase δ_k : $\delta_k = \delta_i - \Delta_{ik}$ or $\delta_k = \delta_j - \Delta_{jk}$. For infinite experimental resolution both expressions for δ_k are equivalent. When experimental error is introduced, the estimated values $\{\widehat{\delta}_i, \widehat{\delta}_j, \widehat{\Delta}_{ik}, \widehat{\Delta}_{jk}\}$ deviate from their actual values $\{\delta_i, \delta_j, \Delta_{ik}, \Delta_{jk}\}$ (estimators are marked with a “ $\widehat{}$ ”) and the two expressions for $\widehat{\delta}_k$ yield a different result in general. Since there is no prior preference, an equal weight can be assigned to both estimators,

$$\widehat{\delta}_k = \frac{1}{2}(\widehat{\delta}_i - \widehat{\Delta}_{ik}) + \frac{1}{2}(\widehat{\delta}_j - \widehat{\Delta}_{jk}), \quad (33)$$

thereby resolving the $\widehat{\delta}_k$ ambiguity. However, this is not the only problem that emerges from introducing experimental error. Consider, again, the complete set $\{C_x, O_x, E, F\}$ of Eqs. (29) and (30). For this set of observables the δ_i read

$$\begin{cases} \widehat{\delta}_1, \\ \widehat{\delta}_2, \\ \widehat{\delta}_3 = \frac{1}{2}(\widehat{\delta}_1 - \widehat{\Delta}_{13}) + \frac{1}{2}(\widehat{\delta}_2 - \widehat{\Delta}_{23}). \end{cases} \quad (34)$$

Suppose that, for example, α_1 was assigned as the reference phase, instead of α_4 . Then $\{C_x, O_x, E, F\}$ provides access to $\{\widehat{\delta}_3^{\alpha_1}, \widehat{\delta}_4^{\alpha_1}, \widehat{\Delta}_{23}, \widehat{\Delta}_{24}\}$, as can be inferred from Table II. The corresponding independent set of phases reads

$$\begin{cases} \widehat{\delta}_2^{\alpha_1} = \frac{1}{2}(\widehat{\delta}_3^{\alpha_1} + \widehat{\Delta}_{23}) + \frac{1}{2}(\widehat{\delta}_4^{\alpha_1} + \widehat{\Delta}_{24}), \\ \widehat{\delta}_3^{\alpha_1}, \\ \widehat{\delta}_4^{\alpha_1}. \end{cases} \quad (35)$$

From (35) one can estimate the δ_i through $\{\widehat{\delta}_1' = -\widehat{\delta}_4^{\alpha_1}, \widehat{\delta}_2' = \widehat{\delta}_2^{\alpha_1} - \widehat{\delta}_4^{\alpha_1}, \widehat{\delta}_3' = \widehat{\delta}_3^{\alpha_1} - \widehat{\delta}_4^{\alpha_1}\}$ and Table II. This yields

$$\begin{cases} \widehat{\delta}_1' = \widehat{\delta}_1, \\ \widehat{\delta}_2' = \frac{1}{2}\widehat{\delta}_2 + \frac{1}{2}(\widehat{\delta}_1 + \widehat{\Delta}_{23} - \widehat{\Delta}_{13}), \\ \widehat{\delta}_3' = \widehat{\delta}_1 - \widehat{\Delta}_{13}. \end{cases} \quad (36)$$

The set (36) is not consistent with the set (34). Indeed, the estimates for the independent phases (there are four possible sets) depends on the choice of reference phase.

One would like to have a consistent set of estimators for the independent phases $\delta_i^{\alpha_j}$ ($i \neq j$) and $\delta_i^{\alpha_i} \equiv \delta_i$ ($i = 1, 2, 3$). The notation $\widetilde{\delta}_i^{\alpha_j}$ is adopted for the consistent estimators. The aforementioned reference-phase ambiguity can be resolved by imposing that

$$\widetilde{\delta}_i^{\alpha_j} = \widetilde{\delta}_i^{\alpha_k} - \widetilde{\delta}_j^{\alpha_k}. \quad (37)$$

Since this requirement is linear in the independent phases, the consistent estimators are also linear in $\{\widehat{\delta}_i^{\alpha_l}, \widehat{\delta}_j^{\alpha_l}, \widehat{\Delta}_{ik}, \widehat{\Delta}_{jk}\}$ ($i \neq j \neq k \neq l$). The most general expression for a consistent set of estimated phases reads

$$\begin{cases} \widetilde{\delta}_i^{\alpha_l} = c_1 \widehat{\delta}_i^{\alpha_l} + (1 - c_1)(\widehat{\delta}_j^{\alpha_l} + \widehat{\Delta}_{ik} - \widehat{\Delta}_{jk}), \\ \widetilde{\delta}_j^{\alpha_l} = c_1 \widehat{\delta}_j^{\alpha_l} + (1 - c_1)(\widehat{\delta}_i^{\alpha_l} + \widehat{\Delta}_{jk} - \widehat{\Delta}_{ik}), \\ \widetilde{\delta}_k^{\alpha_l} = c_2(\widehat{\delta}_i^{\alpha_l} - \widehat{\Delta}_{ik}) + (1 - c_2)(\widehat{\delta}_j^{\alpha_l} - \widehat{\Delta}_{jk}). \end{cases} \quad (38)$$

Here three constraints have been imposed. First, the $\widetilde{\delta}_{\{i,j,k\}}^{\alpha_l}$ should yield the exact set $\delta_{\{i,j,k\}}^{\alpha_l}$ for vanishing experimental error bars. Second, the expressions for $\widetilde{\delta}_i^{\alpha_j}$ and $\widetilde{\delta}_j^{\alpha_i}$ should be equal for $i \leftrightarrow j$. This leaves one with two unknowns c_1 and c_2 . Third, c_1 and c_2 cannot depend on α_j , which is implied by Eq. (37). By applying Eq. (37) on expressions (38) and by using Table II, one readily finds that $c_1 = \frac{3}{4}$ and $c_2 = \frac{1}{2}$. Therefore, the consistent set of estimators for the phases reads

$$\begin{cases} \widetilde{\delta}_i^{\alpha_j} = \frac{3}{4}\widehat{\delta}_i^{\alpha_j} + \frac{1}{4}(\widehat{\delta}_j^{\alpha_j} + \widehat{\Delta}_{ik} - \widehat{\Delta}_{jk}), \\ \widetilde{\delta}_j^{\alpha_i} = \frac{3}{4}\widehat{\delta}_j^{\alpha_i} + \frac{1}{4}(\widehat{\delta}_i^{\alpha_i} + \widehat{\Delta}_{jk} - \widehat{\Delta}_{ik}), \\ \widetilde{\delta}_k^{\alpha_l} = \frac{1}{2}(\widehat{\delta}_i^{\alpha_l} - \widehat{\Delta}_{ik}) + \frac{1}{2}(\widehat{\delta}_j^{\alpha_l} - \widehat{\Delta}_{jk}). \end{cases} \quad (39)$$

The estimates $\widetilde{\delta}_i$'s ($i = 1, 2, 3$) for the independent phases are now insensitive to the choices made with regard to the reference phase.

IV. RESULTS

A. The angular and energy dependence of the transversity amplitudes

A complete measurement comprises a minimal set of asymmetries from which the accessible parameters of the

normalized transversity amplitudes a_i can be estimated. These parameters include three independent moduli r_i and three independent relative phases δ_i . In Sec. III, it was shown how the moduli can be obtained from the single asymmetries and how a set of three independent phases can be estimated in a consistent way from a complete measurement which also involves double asymmetries.

Figures 1 and 2 show the ($W, \cos \theta_{\text{c.m.}}$) dependence of the r_i and the δ_i for the $\gamma p \rightarrow K^+ \Lambda$ reaction as predicted by a realistic model, namely the latest version of the Reggeplus-Resonance (RPR) model, i.e., RPR-2011 [15–17]. This model has a Reggeized t -channel background and includes a total of 8 s -channel resonances, namely $S_{11}(1535)$, $S_{11}(1650)$, $F_{15}(1680)$, $P_{13}(1720)$, $P_{11}(1900)$, $P_{13}(1900)$, $D_{13}(1900)$, and $F_{15}(2000)$. The most apparent feature of the RPR-2011 predictions for the moduli and phases are the strong variations with energy W at backward scattering angles, due to s -channel resonances. The smooth energy dependence of the moduli and phases at very forward scattering angles reflects the important t -channel background contributions of $\gamma p \rightarrow K^+ \Lambda$. At forward kaon angles, where most of the strength resides, the RPR-2011 model predicts a dominant role for r_2 .

B. The merits of the transversity basis

In Sec. III, it was shown how the transversity amplitudes can be inferred from a complete set of measured observables. The first and essential step comprised the determination of the moduli from the three single asymmetries. Indeed, as became clear, the extraction of the δ_i requires prior knowledge about the moduli r_i . Luckily enough, single asymmetries are more easily obtained experimentally than double asymmetries. Consequently, the single asymmetries database generally have better statistics compared to double polarization observables. The published database for, e.g., $\gamma p \rightarrow K^+ \Lambda$ includes 2260 single asymmetries (Σ : 178, T : 69, P : 2013), in contrast to only 456 double asymmetries (C_x : 162, C_z : 162, O_x : 66, O_z : 66) [17]. The beam-recoil asymmetries $\{O_x, O_z\}$ are related to $\{O_x, O_z\}$ through Eq. (A9). In the transversity representation the parameters that are most easily extracted from the data, namely the moduli, are related to that class of asymmetries that are more readily measured, namely the single asymmetries. This is not the case for the helicity basis, where the moduli are related to the set of double asymmetries $\{C_{z'}, E, L_{z'}\}$. It is important to stress that determining invariant amplitudes at some kinematical point requires knowledge of a complete set at the same kinematics. To date, however, there is not a single pseudoscalar photoproduction reaction for which a complete data set has been published.

For the $\gamma p \rightarrow K^+ \Lambda$ reaction, the GRAAL collaboration has measured $\{\Sigma, T, P\}$ at 66 kinematical points [18,19]. These data cover $1.65 \lesssim W \lesssim 1.91$ GeV (bins of $\Delta W \approx 50$ MeV) and $-0.81 \lesssim \cos \theta_{\text{c.m.}} \lesssim 0.86$ (bins of $\Delta \cos \theta_{\text{c.m.}} \approx 0.3$) and can be used to estimate the moduli r_i through Eqs. (27). Figure 3 shows these extracted moduli at three $\cos \theta_{\text{c.m.}}$ intervals (33 of the 66 kinematical points for which data is available) along with the corresponding predictions from RPR-2011. It is observed that at a few kinematical points,

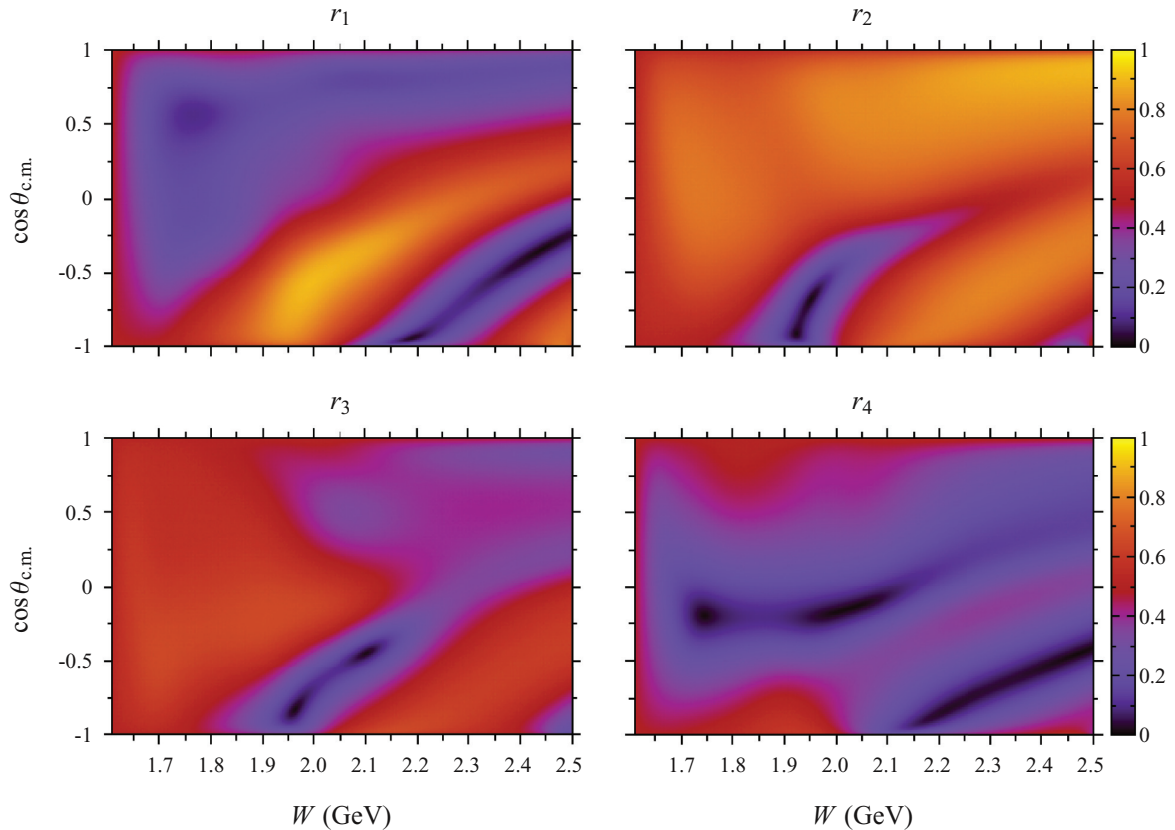


FIG. 1. (Color online) The energy and angular dependence of the moduli r_i of the normalized transversity amplitudes for the $\gamma p \rightarrow K^+ \Lambda$ reaction. The calculations are performed with the RPR-2011 model ($\Delta W \approx 2.38$ MeV, $\Delta \cos \theta_{c.m.} \approx 8.33 \times 10^{-3}$).

some of the \hat{r}_i cannot be extracted from the data. This occurs whenever the measured set $\{\Sigma, T, P\}$ deviates too strongly from the “exact” set so one or more arguments of the square roots (27) become negative. For the GRAAL data, only 17 of the $66 \times 4 = 264 \hat{r}_i$ values are imaginary ($r_1: 12, r_2: 3, r_4: 2$). Overall, the RPR-2011 model offers a fair description of the energy and angular dependence of the extracted \hat{r}_i except for the \hat{r}_2 and \hat{r}_4 at $0.808 \lesssim \cos \theta_{c.m.} \lesssim 0.861$.

Obviously, the GRAAL bin width of $\Delta W \approx 50$ MeV suffices to map the energy dependence of the r_i . The most extensive $\gamma p \rightarrow K^+ \Lambda$ data set to date is due to the CLAS collaboration at Jefferson Lab [20]. The data cover $1.62 \leq W \leq 2.84$ GeV (bins of $\Delta W = 10$ MeV) and $-0.85 \leq \cos \theta_{c.m.} \leq 0.95$ (bins of $\Delta \cos \theta_{c.m.} = 0.1$) and include data for $\frac{d\sigma}{d\Omega}$ and the recoil polarization P .

In addition to $\{\Sigma, T, P\}$, GRAAL provides data for $\{O_{x'}, O_{z'}\}$ at the same kinematical points. Since a complete set of asymmetries is required to extract the δ_i , these beam-recoil data cannot be employed in order to gain additional information about the transversity amplitudes.

As is seen from Table VIII, the GRAAL data for $\{\Sigma, T, P, O_{x'}, O_{z'}\}$ cannot be used to extract the moduli of the helicity amplitudes. The latter would require experimental data for $\{C_{z'}, E, L_{z'}\}$ at the same kinematics, which is not available to this day. Clearly, given the current status of the

experimental $\gamma p \rightarrow K^+ \Lambda$ program, the transversity representation offers the best perspectives to learn about the reaction amplitudes.

The extracted information about the energy and angular dependence of the amplitudes $r_i(W, \cos \theta_{c.m.})$ of Fig. 3 is complementary to what could be obtained about the partial waves in a so-called truncated partial wave analysis (TPWA) [21–23]. In TPWA one aims at extracting information about the energy dependence of the partial waves from the experimental data. The partial waves serve as expansion parameters for the angular dependence of the observables. The amount of partial waves which can be included (usually denoted by l_{\max}) in the fits, depends on the quality and quantity of the measured $\cos \theta_{c.m.}$ dependence of the observables. It is anticipated that in a reaction channel like $\gamma p \rightarrow K^+ \Lambda$ with substantial background contributions, l_{\max} cannot be truncated to small values. In the TPWA approach the underlying dynamics is parameterized in terms of functions which depend on W , whereas in an amplitude analysis as presented here, one attempts to map the full $(W, \cos \theta_{c.m.})$ dependence. In the forthcoming section, it will be shown that the availability of complete sets of eight observables with realistic error bars at given $(W, \cos \theta_{c.m.})$ does not guarantee that one can retrieve the underlying transversity amplitudes. In a recent analysis of $\gamma N \rightarrow \pi N$ simulated data [21] it was shown that the

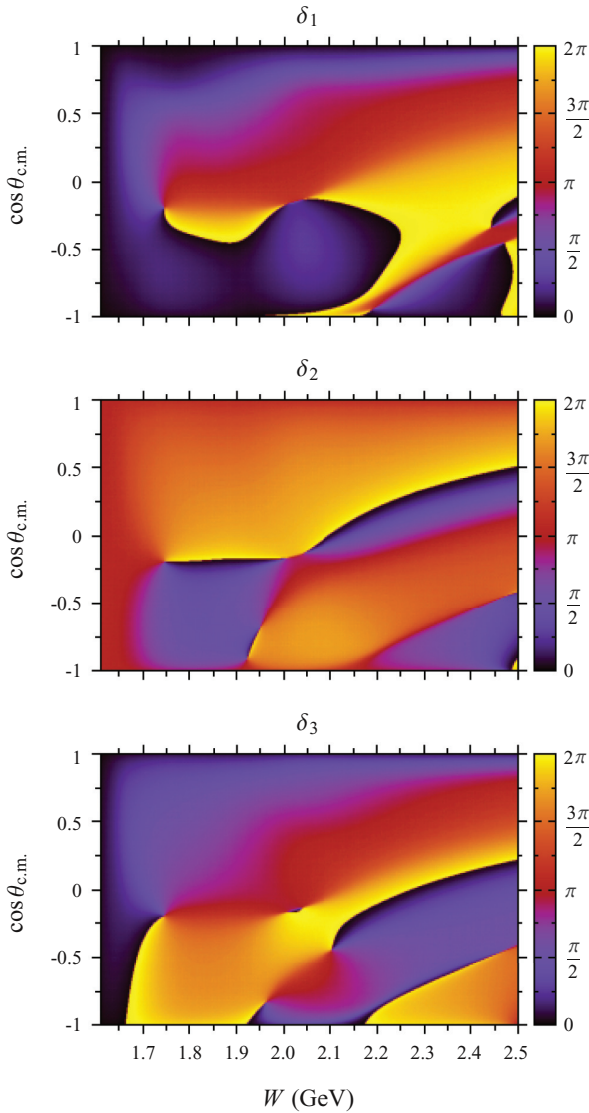


FIG. 2. (Color online) The energy and angular dependence of the independent phases δ_i of the normalized transversity amplitudes of the $\gamma p \rightarrow K^+ \Lambda$ reaction. The calculations are performed with the RPR-2011 model ($\Delta W \approx 1.43$ MeV, $\Delta \cos \theta_{c.m.} = 5 \times 10^{-3}$).

availability of the $\cos \theta_{c.m.}$ dependence of six observables at given W yields unique partial-wave solutions.

C. Extracting the transversity amplitudes from RPR-2011 simulations

In this section the completeness of complete sets is investigated. The analysis is performed for the representative complete set $\{C_x, O_x, E, F\}$ of the first kind. The goal is to determine the moduli \hat{r}_i and the consistent independent phases $\tilde{\delta}_i$ of the transversity amplitudes from simulated observables with finite experimental resolution generated with the RPR-2011 model. It is investigated to what extent the

retrieved amplitudes comply with the input amplitudes from the simulations.

1. Strategy

A measured asymmetry is simulated by generating a fixed number of events from a Gaussian distribution. The mean of this distribution is the RPR-2011 prediction for a certain value of W and $\cos \theta_{c.m.}$. The standard deviation is a specific experimental resolution σ_{exp} . The mean and standard deviation of the generated events determine the value and the error of the simulated data point. If the error of the simulated data point is smaller than the specified σ_{exp} , the former is rejected.

From a simulated set $\{C_x, O_x, E, F\}$, one can obtain the \hat{r}_i and the $\tilde{\delta}_i$ by means of Eqs. (27) and (39). In order to estimate the error on the \hat{r}_i and the $\tilde{\delta}_i$, standard error propagation is applied. Since seven asymmetries are required to estimate the six parameters of the normalized transversity amplitudes, the correlation between the asymmetries has to be taken into account on estimating errors. The squared error of a certain function f of the asymmetries is calculated as

$$\sigma^2(f) = \sum_i \left(\frac{\partial f}{\partial A_i} \right)^2 \sigma^2(A_i) + \sum_{\substack{i,j \\ i \neq j}} \frac{\partial f}{\partial A_i} \frac{\partial f}{\partial A_j} \sigma(A_i, A_j), \quad (40)$$

with $A_i, A_j \in \{\Sigma, T, P, C_x, O_x, E, F\}$ and $\sigma(A_i, A_j)$ the covariance between A_i and A_j .

2. Analysis

As indicated in Sec. IV B, the extraction of the \hat{r}_i from a measured set of single asymmetries through Eqs. (27) is rather straightforward. In some isolated situations at least one of the retrieved \hat{r}_i became imaginary. The moduli estimates, however, are required to extract the relevant phases from a complete set, as is seen from Eqs. (29), (30), and (32). Consequently, an imaginary estimate for one of the moduli results in imaginary estimates for the phases, no matter the achieved precision of the double-asymmetry observables. Through the normalization condition (18) only three of the four moduli are independent. One imaginary modulus estimate, be it an independent or a nonindependent one, is sufficient to jeopardize the phase analysis. For this reason, the four moduli are treated on equal grounds and a selection of a set of three independent moduli has been avoided all along.

Estimating the δ_i is far less straightforward than estimating the r_i . Table III lists two simulated measurements of the complete set $\{C_x, O_x, E, F\}$ at $W = 1700$ MeV and $\cos \theta_{c.m.} = -0.5$, performed at an input resolution of $\sigma_{\text{exp}} = 0.05$. The mean value and standard deviation of the asymmetries were calculated from a sample of 50 events. On inspecting Table III, both simulations are seen to be qualitatively equivalent. This is also reflected by the accurate moduli estimates from both simulations, which are listed in Table IV. In Sec. III B2 it was mentioned that four distinct solutions for $\{\delta_1, \delta_2, \Delta_{13}, \Delta_{23}\}$ exist for the concerned complete set. Only one satisfies the

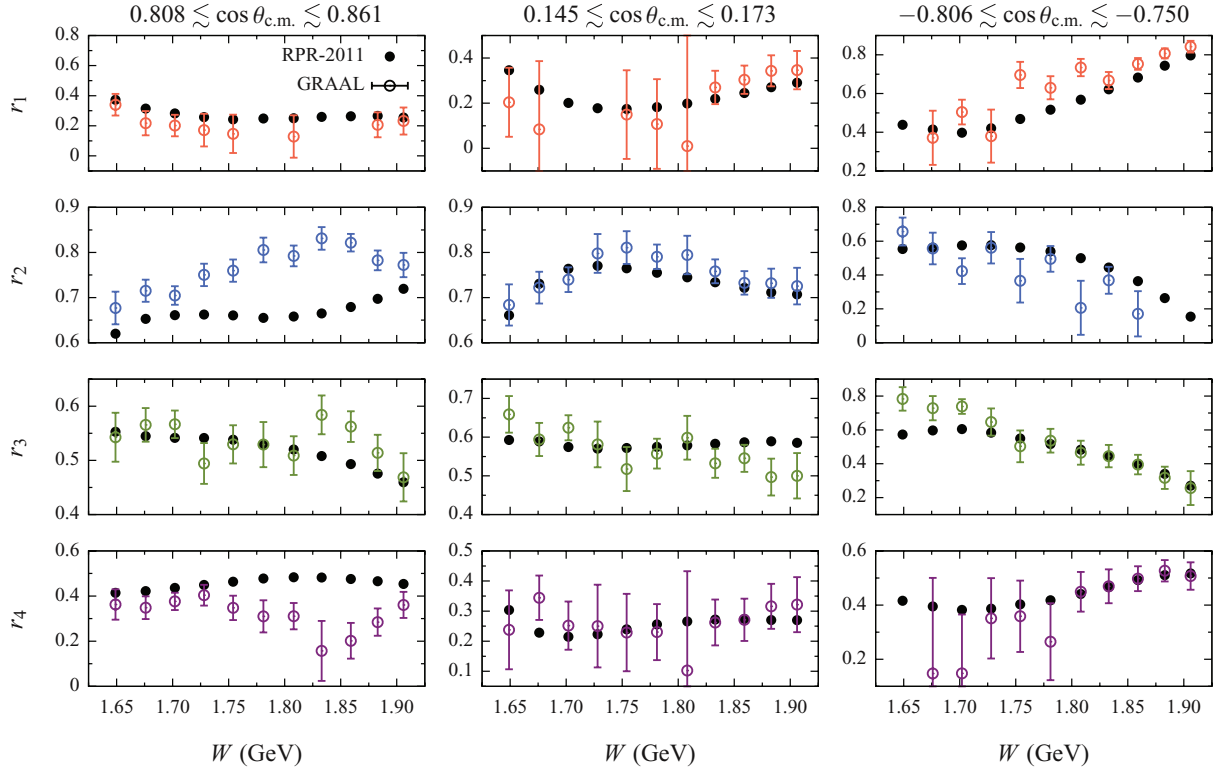


FIG. 3. (Color online) The energy dependence of the moduli r_i of the normalized transversity amplitudes for the $\gamma p \rightarrow K^+\Lambda$ reaction. The data are extracted from the GRAAL results for the single-polarization observables reported in Refs. [18,19]. The dots are the bin-centered RPR-2011 predictions.

constraint (31) in the exact case, though. When experimental error is involved, however, none of the four solutions satisfies the constraint. In Table V, the outcome of constraint (31) is listed for each of the four solutions to both data sets. As the constraint is a sum of phases and its evaluation in the exact case yields a zero value, the mean values listed in Table V were rotated to $]-\pi, +\pi]$. The table also lists by how many standard deviations (denoted by n_σ) the mean deviates from zero. The solution with the lowest n_σ has the highest likelihood. In principle, a solution can be excluded if it is statistically insignificant, commonly quantified by a small confidence interval $\text{CI} = 1 - \text{erf}(n_\sigma/\sqrt{2})$. From the CI values of data set

TABLE III. The model's values and two simulated data sets for the complete set $\{C_x, O_x, E, F\}$ at $W = 1700$ MeV and $\cos \theta_{c.m.} = -0.5$ with $\sigma_{\text{exp}} = 0.05$.

Model	Simulation A	Simulation B	
Σ	0.0489	0.0543 ± 0.0519	0.0458 ± 0.0533
T	-0.6843	-0.6905 ± 0.0511	-0.6685 ± 0.0524
P	0.0056	0.0111 ± 0.0552	0.0892 ± 0.0555
C_x	-0.4808	-0.4809 ± 0.0515	-0.4728 ± 0.0588
O_x	-0.5989	-0.5971 ± 0.0519	-0.6149 ± 0.0567
E	0.5672	0.5655 ± 0.0505	0.5695 ± 0.0564
F	-0.4525	-0.4411 ± 0.0519	-0.4486 ± 0.0503

B it follows that solution 3 and solution 4 can be excluded with significance. For data set A, these solutions are also the least significant ones. Of the two remaining solutions, data set A predicts that solution 1 is the real solution (99.4% CI). According to data set B, however, solution 2 is the most likely one, though with a smaller confidence interval (79.9% CI). This example illustrates that ambiguities remain for (theoretically) complete sets when experimental uncertainties are taken into account.

In Table VI, the model's phases are compared with the corresponding estimates from solution 1 of data set A and solution 2 of data set B. From this table, it is seen that solution 1 is the actual solution. This finding could have been anticipated by comparing CI values (99.4% versus 79.9%). However, a real experiment only yields a single data set at a certain kinematical

TABLE IV. The model's values for the \hat{r}_i at $W = 1700$ MeV and $\cos \theta_{c.m.} = -0.5$ and the corresponding estimates from data set A and data set B.

Model	Simulation A	Simulation B	
\hat{r}_1	0.304	0.306 ± 0.037	0.311 ± 0.037
\hat{r}_2	0.657	0.658 ± 0.017	0.653 ± 0.018
\hat{r}_3	0.640	0.642 ± 0.018	0.639 ± 0.018
\hat{r}_4	0.256	0.248 ± 0.046	0.263 ± 0.044

TABLE V. The constraint of Eq. (31) for the four $\{\delta_1, \delta_2, \Delta_{13}, \Delta_{23}\}$ solutions extracted from the simulated data listed in Table III. The number of standard deviations, by which the constraint differs from zero, is denoted by n_σ . The CI are the confidence intervals corresponding with the n_σ .

Solution	Simulation A		
	Constraint	n_σ	CI (%)
1	0.029 ± 3.866	0.007	99.4
2	-0.200 ± 3.316	0.060	95.2
3	-2.513 ± 3.316	0.758	44.9
4	-2.741 ± 3.865	0.709	47.8
Solution	Simulation B		
	Constraint	n_σ	CI (%)
1	0.592 ± 1.261	0.467	63.8
2	-0.229 ± 0.898	0.255	79.9
3	-2.393 ± 0.903	2.651	0.8
4	3.069 ± 1.264	2.428	1.5

point. If an experiment were to yield data set A, one could not exclude solutions 3 and 4 with significance and one could only conclude that solution 1 is most likely the real solution with 99.4% CI. If data set B were the result of a real experiment, then solutions 3 and 4 could be excluded with significance and one could state that solution 2 is most likely the actual solution with a CI value of only 79.9%, though. The confidence interval on the constraint (31) is the only parameter able to distinguish

TABLE VI. The model's values for the $\tilde{\delta}_i$ at $W = 1700$ MeV and $\cos\theta_{c.m.} = -0.5$, along with the estimates resulting from the most significant solution of data set A (solution 1) and data set B (solution 2).

	Model	Simulation A	Simulation B
$\tilde{\delta}_1$	0.487	0.424 ± 0.801	0.704 ± 0.478
$\tilde{\delta}_2$	2.458	2.424 ± 0.992	2.637 ± 0.348
$\tilde{\delta}_3$	6.106	6.090 ± 0.235	3.046 ± 0.234

among the four solutions. In some cases, however, the solution with the highest CI does not deliver the correct solution for the phases.

In the beginning of this section, it was argued that an imaginary estimate for the \hat{r}_i leads to imaginary $\tilde{\delta}_i$. Even with real \hat{r}_i , however, it cannot be excluded that imaginary $\tilde{\delta}_i$ are retrieved. Indeed, from Eqs. (29) and (30) the phases are determined by solving a quadratic equation in the sine or cosine of the phase. For certain combinations of the measured double asymmetries the discriminant of this quadratic equation becomes negative. In such a case, the particular data set can solely be used to estimate the moduli. In what follows, the authors wish to quantify the insolubility of a complete set, i.e., how frequently it occurs that imaginary or incorrect solutions are obtained for the transversity amplitudes.

Figure 4 shows the insolubility of the transversity amplitudes as a function of the input experimental resolution

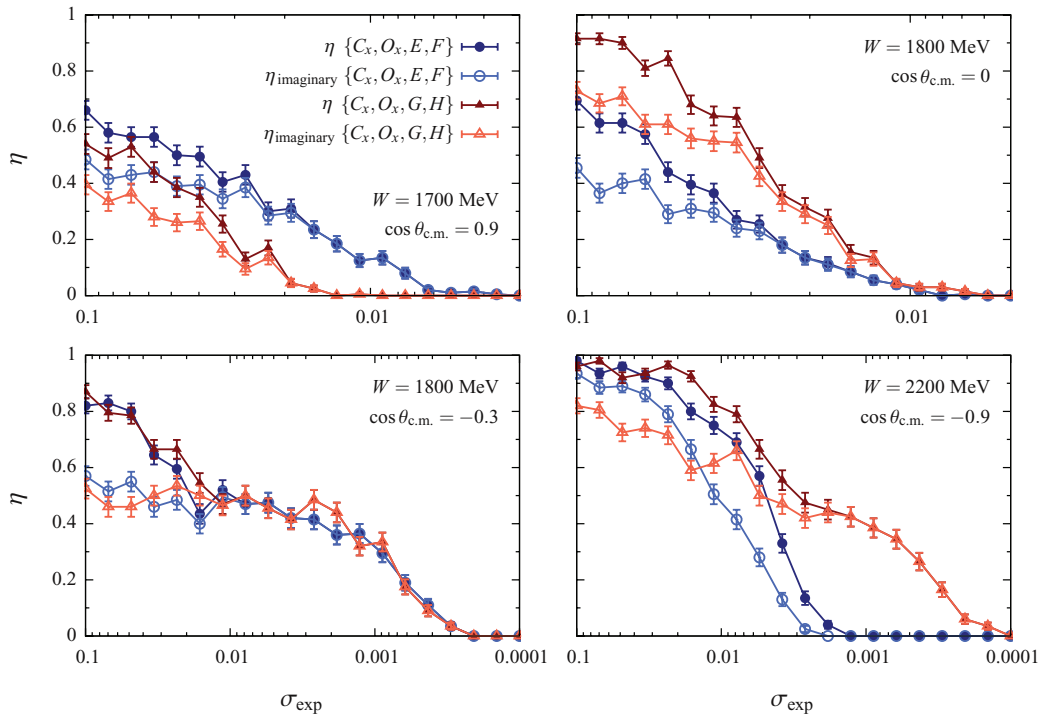


FIG. 4. (Color online) The insolubility of the transversity amplitudes at four different kinematical points. The circles and triangles are simulated data generated from the complete sets $\{C_x, O_x, E, F\}$ and $\{C_x, O_x, G, H\}$. The filled and unfilled symbols correspond with $\eta = \eta_{\text{imaginary}} + \eta_{\text{incorrect}}$ and $\eta_{\text{imaginary}}$.

σ_{exp} . Simulations for the complete sets $\{C_x, O_x, E, F\}$ and $\{C_x, O_x, G, H\}$ are analyzed at four different kinematics. Each point in Fig. 4 results from an ensemble of 200 simulated data sets constructed from samples of 50 events for each of the asymmetries. The insolvability η is the fraction of unsuccessful simulated data sets. The η is defined as the sum of the fraction of (two or four) imaginary solutions ($\eta_{\text{imaginary}}$) and the fraction of incorrect solutions ($\eta_{\text{incorrect}}$). An incorrect solution is a solution with the highest CI value that does not correspond with the model's value in the limit $\sigma_{\text{exp}} \rightarrow 0$. The insolvability η is binomially distributed and, hence, the corresponding error is calculated as

$$\sigma(\eta) = \sqrt{\frac{\eta(1-\eta)}{N}}, \quad (41)$$

where N represents the number of simulated data sets. It is seen that the insolvability decreases with decreasing σ_{exp} , as is expected. Further, the $\eta_{\text{imaginary}}$ has the largest contribution and $\eta_{\text{incorrect}}$ vanishes more rapidly with σ_{exp} than $\eta_{\text{imaginary}}$. In some situations, the insolvability only vanishes for very challenging experimental resolutions, and it is seen that this behavior depends on the complete set in question.

Figure 5 shows the $\{C_x, O_x, E, F\}$ insolvabilities η and $\eta_{\text{incorrect}}$ as a function of W and $\cos \theta_{\text{c.m.}}$ for $\sigma_{\text{exp}} = 0.1$ and $\sigma_{\text{exp}} = 0.01$. For each of the $375 \times 241 = 90375$ kinematical points, 1000 simulated data sets were generated (from samples of 50 events for all asymmetries) from which the average

$\eta_{\text{imaginary}}$ and $\eta_{\text{incorrect}}$ are calculated. It is seen that for $\sigma_{\text{exp}} = 0.1$ the insolvability can become quite substantial ($0.7 \lesssim \eta \lesssim 0.9$) for some regions in the $(W, \cos \theta_{\text{c.m.}})$ space. In other regions of the phase space the insolvability vanishes. For $\sigma_{\text{exp}} = 0.1$, $\eta_{\text{imaginary}}$ has the largest contribution to η . In Fig. 5, the effect of improving the experimental resolution by an order of magnitude is clearly visible. Indeed, both the $\eta_{\text{imaginary}}$ and $\eta_{\text{incorrect}}$ surfaces are significantly reduced. The overall insolvability, however, still occupies a fair fraction of the phase space. It is also striking that the regions for $|\cos \theta_{\text{c.m.}}| \approx 1$ and/or W approaching the threshold are highly insoluble, for both $\sigma_{\text{exp}} = 0.1$ and $\sigma_{\text{exp}} = 0.01$.

Figure 6 presents a sample extraction analysis of the transversity amplitudes for both $\sigma_{\text{exp}} = 0.1$ and $\sigma_{\text{exp}} = 0.01$. At each of the $125 \times 81 = 10125$ kinematical points a single simulated data set was generated and subsequently analyzed. The samples represent how the result of a measurement of the $(W, \cos \theta_{\text{c.m.}})$ dependence of the asymmetries might look. For $\sigma_{\text{exp}} = 0.1$, a large fraction of the kinematical phase space suffers from imaginary or incorrect solutions. Increasing the resolution to $\sigma_{\text{exp}} = 0.01$ substantially improves the situation. For $\sigma_{\text{exp}} = 0.1$, the fraction of incorrect solutions is rather small and for $\sigma_{\text{exp}} = 0.01$ their contribution is almost negligible.

Though having the smaller contribution to the insolvability, incorrect solutions are spurious and, therefore, should be eliminated, if possible. Incorrect solutions arise from simply

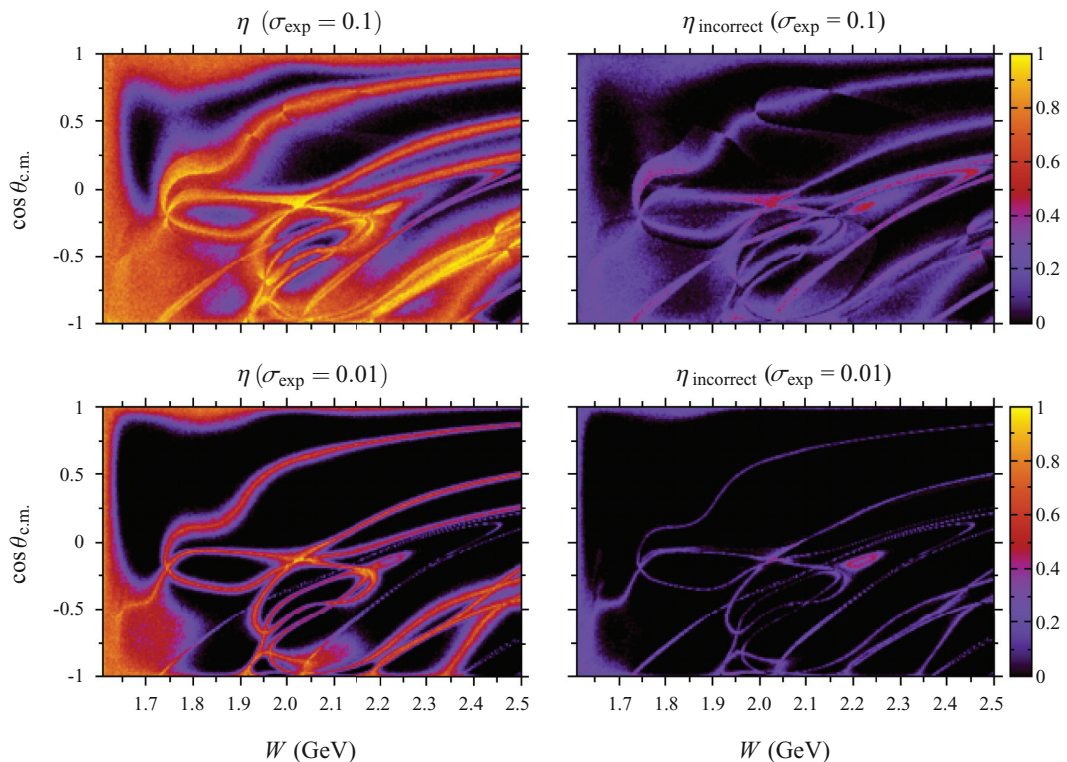


FIG. 5. (Color online) The $\{C_x, O_x, E, F\}$ insolvabilities $\eta = \eta_{\text{imaginary}} + \eta_{\text{incorrect}}$ and $\eta_{\text{incorrect}}$ as a function of W and $\cos \theta_{\text{c.m.}}$ for two values of the input experimental resolution ($\sigma_{\text{exp}} = 0.1$ and $\sigma_{\text{exp}} = 0.01$).

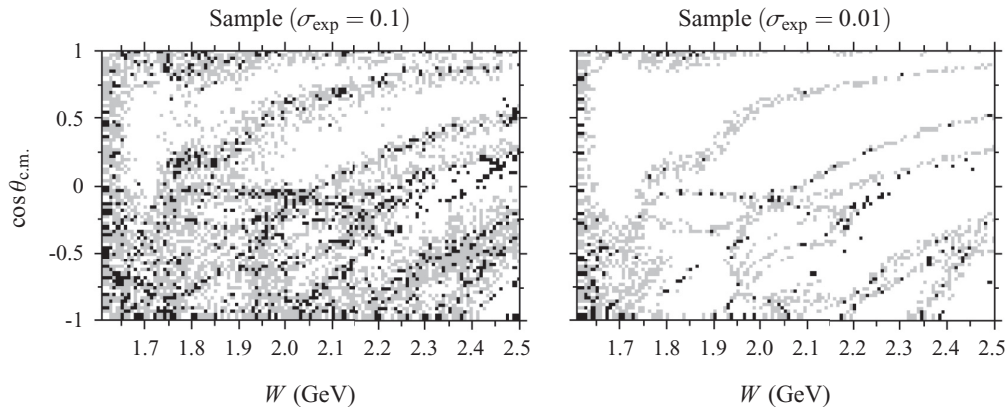


FIG. 6. Two random samples of the individual events that give rise to the left plots shown in Fig. 5. The gray, black, and white dots correspond with imaginary moduli and/or phases, incorrect phases, and correct phases.

marking the solution with the highest CI value as the correct solution. Such a procedure, however, does not stand on statistically solid grounds. A more conservative approach would consist of imposing a tolerance level on the CI values. This would mean that the solution with the highest CI value is accepted as the correct solution only if its confidence interval is greater than or equals the tolerance level. Imposing a tolerance level would not come without a cost, however. The downside of this “filtering” procedure would be a substantial increase in the overall insolvability. Indeed, all of the correct solutions that do not pass the tolerance level would also be rejected and, therefore, lead to an increase in the insolvability. Nevertheless, the question remains whether such a tolerance requirement can really suppress the fraction of incorrect solutions entirely?

In Table VII, the mean confidence intervals are listed for both 1000 correct and 1000 incorrect solutions at random kinematical points. While the “correct” $\overline{\text{CI}}$ values are higher than the “incorrect” ones, for each σ_{exp} value listed, the difference between both is not at all substantial. Moreover, it is seen that a fair fraction of the incorrect solutions have a confidence interval of at least 95%. As there is a significant overlap between the “correct” and “incorrect” $\overline{\text{CI}}$ values, the entire elimination of the incorrect solutions would require a confidence level so high that nearly all of the correct solutions would get rejected as well, thereby resulting in a practically 100% insolvability. Even lowering the confidence level so as to remove the bulk of the incorrect solutions would equally wipe

TABLE VII. The mean confidence intervals $\overline{\text{CI}}$ for 1000 correct and 1000 incorrect solutions at random kinematical points ($W < 2500$ MeV and $\cos \theta_{c.m.} \in [-1, 1]$).

σ_{exp}	$\overline{\text{CI}}$ (%)	
	Correct	Incorrect
0.1	$93.0^{+4.4}_{-8.3}$	$91.8^{+5.4}_{-11.0}$
0.01	$91.5^{+5.3}_{-9.1}$	$88.1^{+7.9}_{-18.2}$
0.001	$91.7^{+5.0}_{-8.5}$	$84.9^{+10.0}_{-22.6}$

out the majority of the correct solutions and hence substantially increase the insolvability.

Therefore, the spurious incorrect solutions can never really be identified, at least not at achievable experimental resolutions. It was shown in the above analysis that even when the confidence interval of a solution is significantly high, it is simply not possible to state whether the solution in question is a correct or an incorrect one. This is in stark contrast with the observation that for a considerable experimental resolution the fraction of incorrect solutions is nearly negligible.

V. CONCLUSIONS

In this paper, the issue of extracting complete information about reaction amplitudes from pseudoscalar-meson photoproduction data is addressed. The merits of employing the transversity basis (for finite experimental resolution) have been highlighted. Indeed, linear equations connect the moduli of the amplitudes to single-polarization observables. Nonlinear equations connect the relative phases of the amplitudes to double-polarization observables, which are less readily available.

The observables of pseudoscalar-meson photoproduction have been expanded in the transversity basis. An inconsistency with the existing literature is discovered. An independent test of the derived expressions is presented. By rotating the obtained transversity expressions to both the helicity and the CGLN basis, expressions from literature are retrieved. Therefore, convincing evidence has been provided that the derived transversity expansion for the observables is correct.

The extraction of the moduli r_i of the normalized transversity amplitudes is a rather straightforward procedure. The authors have performed this analysis for the $\gamma p \rightarrow K^+ \Lambda$ reaction with sets of $\{\Sigma, T, P\}$ data from the GRAAL collaboration. These data cover the range $1.65 \lesssim W \lesssim 1.91$ GeV. For the moduli, imaginary solutions can be obtained at some isolated kinematics due to finite experimental resolution. In the performed analysis of the GRAAL data, less

than 6.5% of the extracted \hat{r}_i are complex. On improving the experimental resolution, the fraction of complex \hat{r}_i can be reduced. It is found that the $(W, \cos \theta_{c.m.})$ dependence of the extracted \hat{r}_i can be nicely reproduced by the RPR-2011 model.

The formalism of Wen-Tai Chiang and Tabakin for solving complete sets has been extended so as to provide consistent estimates for the independent relative phases for data with finite error bars. As a check of this formalism, it was applied to Monte Carlo simulations of the complete set $\{C_x, O_x, E, F\}$ for the reaction $\gamma p \rightarrow K^+ \Lambda$. The simulations are generated with the RPR-2011 model.

Estimating the independent phases is far more challenging than determining the moduli. In order to quantify the phase-related issues, the insolvability of the transversity amplitudes has been introduced. The insolvability is a measure for the fraction of complete measurements which does not result in a successful determination of the transversity amplitudes. The insolvability receives contributions from both imaginary and incorrect solutions. It was observed that the fraction of imaginary solutions is much larger for the phases than for the moduli. However, the amount of imaginary solutions can be reduced by increasing the experimental resolution. The ‘‘incorrect’’ component of the insolvability is much more troublesome. It originates from a discrete phase ambiguity that cannot be resolved for finite uncertainties of the asymmetries. Although this component is not the dominant one and decreases for increasing experimental resolution, it was found that at achievable experimental conditions it is impossible to discriminate between correct and incorrect solutions for the phases with statistical significance.

It remains to be investigated whether the measurement of an additional double asymmetry, or multiple ones, could help in resolving the phase ambiguities for realistic experimental resolutions.

ACKNOWLEDGMENTS

This work is supported by the Research Council of Ghent University and the Flemish Research Foundation (FWO Vlaanderen).

APPENDIX: OTHER REPRESENTATIONS OF THE ASYMMETRIES

1. Helicity representation

The helicity amplitudes $H_1, H_2, H_3,$ and H_4 are defined as

$$\begin{aligned} H_1 &= {}_R\langle +|J_+|- \rangle_T, & H_2 &= {}_R\langle +|J_+|+ \rangle_T, \\ H_3 &= {}_R\langle -|J_+|- \rangle_T, & H_4 &= {}_R\langle -|J_+|+ \rangle_T. \end{aligned} \quad (\text{A1})$$

Here, $|\pm\rangle_T$ and $|\pm\rangle_R$ represent the target and recoil helicity eigenstates, respectively, and J_+ is defined in Eq. (9). As the target (recoil) momentum \vec{p}_T (\vec{p}_R) is directed along the negative z axis (z' axis), it follows that

$$\begin{aligned} |\pm\rangle_T &= |\pm\rangle_{-z} = u_{\pm}(p_T, \pi, 0), \\ |\pm\rangle_R &= |\pm\rangle_{-z'} = u_{\pm}(p_R, \pi - \theta_{c.m.}, \pi). \end{aligned} \quad (\text{A2})$$

From Eqs. (2), (3), (4), and (A2) one deduces the following relations:

$$\begin{aligned} |\pm\rangle_T &= \mp \frac{1}{\sqrt{2}}(i|\pm\rangle_y - |\mp\rangle_y), \\ |\pm\rangle_R &= \pm \frac{1}{\sqrt{2}}(ie^{\mp i\theta_{c.m.}/2}|\pm\rangle_y - e^{\pm i\theta_{c.m.}/2}|\mp\rangle_y), \end{aligned} \quad (\text{A3})$$

and in combination with the definition of J_- in Eq. (9), one can readily show that the following properties hold:

$$\begin{aligned} H_1 &= {}_R\langle +|J_+|- \rangle_T = +{}_R\langle -|J_-|+ \rangle_T, \\ H_2 &= {}_R\langle +|J_+|+ \rangle_T = -{}_R\langle -|J_-|- \rangle_T, \\ H_3 &= {}_R\langle -|J_+|- \rangle_T = -{}_R\langle +|J_-|+ \rangle_T, \\ H_4 &= {}_R\langle -|J_+|+ \rangle_T = +{}_R\langle +|J_-|- \rangle_T. \end{aligned} \quad (\text{A4})$$

From Eqs. (10), (9), (A1), and (A3), one then obtains

$$H_i = \frac{1}{\sqrt{2}}U_{ij}b_j, \quad (\text{A5})$$

with U a unitary matrix ($U^\dagger U = U U^\dagger = 1$)

$$U = \frac{e^{i\theta_{c.m.}/2}}{2} \begin{pmatrix} 1 & -e^{-i\theta_{c.m.}} & -1 & -e^{-i\theta_{c.m.}} \\ i & ie^{-i\theta_{c.m.}} & i & -ie^{-i\theta_{c.m.}} \\ i & ie^{-i\theta_{c.m.}} & -i & ie^{-i\theta_{c.m.}} \\ -1 & e^{-i\theta_{c.m.}} & -1 & -e^{-i\theta_{c.m.}} \end{pmatrix}. \quad (\text{A6})$$

The ‘‘normalized’’ helicity amplitudes h_i

$$h_i = \frac{\sqrt{2}H_i}{\sqrt{|H_1|^2 + |H_2|^2 + |H_3|^2 + |H_4|^2}} \quad (\text{A7})$$

can be written in terms of the normalized transversity amplitudes a_i of Eq. (17)

$$a_i = \frac{1}{\sqrt{2}}(U^\dagger)_{ij}h_j = \frac{1}{\sqrt{2}}U_{ji}^*h_j, \quad (\text{A8})$$

whereby use is made of the unitarity of U . From the above relations and the expressions of Table I, one obtains the helicity representation (Table VIII) of the polarization observables. The $\{A_{x'}, A_{z'}\}$ ($A \in \{C, O, T, L\}$) are related to the $\{A_x, A_z\}$ through

$$\begin{pmatrix} A_{x'} \\ A_{z'} \end{pmatrix} = \begin{pmatrix} \cos \theta_{c.m.} & -\sin \theta_{c.m.} \\ \sin \theta_{c.m.} & \cos \theta_{c.m.} \end{pmatrix} \begin{pmatrix} A_x \\ A_z \end{pmatrix}. \quad (\text{A9})$$

The expressions of Table VIII coincide with those in Ref. [14].

2. CGLN representation

The Chew-Goldberger-Low-Nambu (CGLN) amplitudes F_i are, for example, defined in Eq. (8) of Ref. [12]. In what follows a connection is established between the the CGLN and the transversity amplitudes, as this might be useful for future analyses. From the definition of the Dirac spinor (2), the reduced CGLN amplitudes $f_i = \sqrt{\rho_0}F_i$ can be related to the a_i of Eq. (17). Here, ρ_0 is the density-of-states factor, defined in Eq. (5) of Ref. [12]. The following relation holds

$$f_i = V_{ij}a_j, \quad (\text{A10})$$

TABLE VIII. The expressions for the single and double asymmetries in the normalized helicity basis.

	Helicity representation
Σ	$-\text{Re}(h_1 h_4^* - h_2 h_3^*)$
T	$-\text{Im}(h_1 h_2^* + h_3 h_4^*)$
P	$-\text{Im}(h_1 h_3^* + h_2 h_4^*)$
$C_{x'}$	$-\text{Re}(h_1 h_3^* + h_2 h_4^*)$
$C_{z'}$	$-\frac{1}{2}(h_1 ^2 + h_2 ^2 - h_3 ^2 - h_4 ^2)$
$O_{x'}$	$+\text{Im}(h_1 h_2^* - h_3 h_4^*)$
$O_{z'}$	$-\text{Im}(h_1 h_4^* - h_2 h_3^*)$
E	$-\frac{1}{2}(h_1 ^2 - h_2 ^2 + h_3 ^2 - h_4 ^2)$
F	$-\text{Re}(h_1 h_2^* + h_3 h_4^*)$
G	$+\text{Im}(h_1 h_4^* + h_2 h_3^*)$
H	$+\text{Im}(h_1 h_3^* - h_2 h_4^*)$
$T_{x'}$	$+\text{Re}(h_1 h_4^* + h_2 h_3^*)$
$T_{z'}$	$+\text{Re}(h_1 h_2^* - h_3 h_4^*)$
$L_{x'}$	$-\text{Re}(h_1 h_3^* - h_2 h_4^*)$
$L_{z'}$	$-\frac{1}{2}(h_1 ^2 - h_2 ^2 - h_3 ^2 + h_4 ^2)$

with V a nonunitary matrix, given by

$$V = -\frac{i}{\sin^2 \theta_{c.m.}} \begin{pmatrix} i e^{i\theta_{c.m.}} & i e^{-i\theta_{c.m.}} & 0 & 0 \\ i \sin \theta_{c.m.} & i \sin \theta_{c.m.} & 0 & 0 \\ -e^{i\theta_{c.m.}} & e^{-i\theta_{c.m.}} & e^{i\theta_{c.m.}} & e^{-i\theta_{c.m.}} \\ 1 & -1 & -1 & -1 \end{pmatrix}. \quad (\text{A11})$$

This means that the CGLN basis is not orthogonal. By substituting $a_i = (V^{-1})_{ij} f_j$ in Table I with

$$V^{-1} = \frac{i}{2} \begin{pmatrix} -1 & e^{-i\theta_{c.m.}} & 0 & 0 \\ 1 & -e^{i\theta_{c.m.}} & 0 & 0 \\ -1 & e^{-i\theta_{c.m.}} & -i \sin \theta_{c.m.} & -i e^{-i\theta_{c.m.}} \sin \theta_{c.m.} \\ -1 & e^{i\theta_{c.m.}} & i \sin \theta_{c.m.} & i e^{i\theta_{c.m.}} \sin \theta_{c.m.} \end{pmatrix}, \quad (\text{A12})$$

one retrieves the CGLN expansion of the asymmetries as is listed in Eqs. (58b–p) of Ref. [12].

As $V \propto \sin^{-2} \theta_{c.m.}$, it is divergent at $\cos \theta_{c.m.} = \pm 1$. In these two cases, the CGLN amplitudes cannot be expressed in terms of the transversity ones. Conversely, for $\cos \theta_{c.m.} = \pm 1$ the a_i can be expanded in the f_i basis, though. By substituting $\cos \theta_{c.m.} = \pm 1$ in $a_i = (V^{-1})_{ij} f_j$, it is found that

$$a_1 = -a_2 = a_3 = a_4 = -\frac{i}{2}(f_1 \mp f_2). \quad (\text{A13})$$

The normalization condition (18) then leads to $|a_i| = \frac{1}{2}$ for $\cos \theta_{c.m.} = \pm 1$. As a consequence, by invoking Table I, all the single and double asymmetries can be quantified at these two extreme angles. At $\cos \theta_{c.m.} = \pm 1$ one has that $C_z = E = 1$ and $L_z = -1$, while all other asymmetries vanish. This result holds for any possible value of W . It is quite remarkable that this interesting general result can be derived by altering the representation of the amplitudes.

- [1] E. Pasyuk, *EPJ Web Conf.* **37**, 06013 (2012).
[2] F. J. Klein (CLAS Collaboration), *AIP Conf. Proc.* **1432**, 51 (2012).
[3] A. D'Angelo *et al.*, *AIP Conf. Proc.* **1432**, 56 (2012).
[4] H.-J. Arends, *AIP Conf. Proc.* **1432**, 142 (2012).
[5] F. Klein, *AIP Conf. Proc.* **1432**, 150 (2012).
[6] I. S. Barker, A. Donnachie, and J. K. Storrow, *Nucl. Phys. B* **95**, 347 (1975).
[7] G. Keaton and R. Workman, *Phys. Rev. C* **53**, 1434 (1996).
[8] Wen-Tai Chiang and F. Tabakin, *Phys. Rev. C* **55**, 2054 (1997).
[9] D. G. Ireland, *Phys. Rev. C* **82**, 025204 (2010).
[10] S. Hoblit *et al.*, *Phys. Rev. Lett.* **102**, 172002 (2009).
[11] J. D. Bjorken and S. D. Drell, *Relativistic Quantum Mechanics* (McGraw-Hill, New York, 1964).
[12] A. M. Sandorfi, S. Hoblit, H. Kamano, and T.-S. H. Lee, *J. Phys.* **38**, 053001 (2011).
[13] R. A. Adelseck and B. Saghai, *Phys. Rev. C* **42**, 108 (1990).
[14] C. G. Fasano, F. Tabakin, and B. Saghai, *Phys. Rev. C* **46**, 2430 (1992).
[15] T. Corthals, J. Ryckebusch, and T. Van Cauteren, *Phys. Rev. C* **73**, 045207 (2006).
[16] L. De Cruz, T. Vranx, P. Vancraeyveld, and J. Ryckebusch, *Phys. Rev. Lett.* **108**, 182002 (2012).
[17] L. De Cruz, J. Ryckebusch, T. Vranx, and P. Vancraeyveld, *Phys. Rev. C* **86**, 015212 (2012).
[18] A. Lleres *et al.* (GRAAL Collaboration), *Eur. Phys. J. A* **31**, 79 (2007).
[19] A. Lleres *et al.* (GRAAL Collaboration), *Eur. Phys. J. A* **39**, 149 (2009).
[20] M. E. McCracken *et al.* (CLAS Collaboration), *Phys. Rev. C* **81**, 025201 (2010).
[21] R. L. Workman, M. W. Paris, W. J. Briscoe, L. Tiator, S. Schumann, M. Ostrick, and S. S. Kamalov, *Eur. Phys. J. A* **47**, 143 (2011).
[22] L. Tiator, *AIP Conf. Proc.* **1432**, 162 (2012).
[23] L. Tiator, arXiv:1211.3927.

Charged-pion electroproduction above the resonance region

Background and outline

So far, the photoproduction of pseudoscalar mesons has been considered, in particular the $p(\gamma, K^+)\Lambda$ reaction. Now the subject turns to electroinduced reactions, with incident photons of finite virtuality Q^2 . More specifically, the electroproduction of charged pions off the nucleon will be studied, i.e. the $p(\gamma^*, \pi^+)n$ and $n(\gamma^*, \pi^-)p$ reactions, above the resonance region. In the spirit of the RPR formalism, electromagnetic pseudoscalar-meson production can be modeled with t -channel Regge amplitudes at high energies. Indeed, for increasing invariant mass, the resonance contributions become less and less significant. Hence, if one aims at modeling the trans-resonance region of $N(\gamma^{(*)}, M)B$ reactions, it is a good approximation to only account for a background amplitude in the t channel.

The extension of a certain photoproduction model to the corresponding electroproduction model, requires the introduction of the appropriate transition form factors at the electromagnetic vertices of the tree-channel diagrams. For the $N(\gamma^*, \pi^\pm)N'$ reactions considered here, the t channel demands the $F_{\gamma\pi\pi}(Q^2)$ and $F_{\gamma\pi^*\pi}(Q^2)$ electromagnetic form factors. Here, π^* denotes the charged-pion resonances ($\gamma\pi \rightarrow \pi^*$) that constitute the first materializations of the corresponding Regge trajectories, included in the background amplitude. In addition, the proton electric transition form factor $F_p^e(Q^2)$ is required in the gauge-fixing s - and u -channel diagrams, respectively for π^+n and π^-p electroproduction (see Eqs. (2.52) and (2.53)).

In Ref. [27], Kaskulov and Mosel model the $N(\gamma^*, \pi^\pm)N'$ reactions above the resonance region through the exchange of three Regge trajectories in the t channel: the degenerate $\pi(140)/b_1(1235)$ (pseudoscalar) and $\rho(770)/a_1(1320)$ (vector) trajectories, which are shown in Fig. 2.3, along with the non-degenerate $a_1(1360)$ (axial-vector) trajectory. It is shown that when adopting the appropriate electromagnetic form factors in the t channel and the well-established proton electric form factor in the gauge-fixing s - and u -channel diagrams, the three-trajectory background model fails to reproduce the experimentally observed magnitude of the transverse response σ_T , and the signs of the

interference structure functions σ_{LT} and σ_{TT} (see Eq. (2.17) for the definition of these observables).

In order to explain the discrepancy between theory and experiment, Kaskulov and Mosel propose a mechanism through which resonances have a residual effect on the gauge-fixing amplitudes. They argue that such resonance effects can be justified since the intermediate proton in these channels is highly off-shell above the resonance region. In the Kaskulov-Mosel (KM) model, a modified proton electromagnetic transition form factor is adopted. It accounts for the residual resonance effects and is therefore different from the standard proton electric form factor $F_p^e(Q^2)$. This model successfully explains the experimentally observed separated structure functions in high-energy π^+n and π^-p electroproduction.

Although the KM formalism reproduces the trends in the high-energy $N(\gamma^*, \pi^\pm)N'$ data, it features two theoretical inadequacies regarding the employed prescriptions for the pion and proton electromagnetic transition form factors. In this chapter, the shortcomings of the KM model will be addressed and an appropriate alternate model will be proposed for $N(\gamma^*, \pi^\pm)N'$ above the resonance region. The new model will be compared to the available high-energy $N(\gamma^*, \pi^\pm)N'$ data and its predictions will be presented for the planned $F\pi$ experiment with the 12 GeV upgrade at JLab [39].

PHYSICAL REVIEW C **89**, 025203 (2014)

Charged-pion electroproduction above the resonance region

Tom Vrancx* and Jan Ryckebusch†

Department of Physics and Astronomy, Ghent University, Proeftuinstraat 86, B-9000 Gent, Belgium

(Received 30 October 2013; published 24 February 2014)

Background: Above the nucleon resonance region, the $N(e, e'\pi^\pm)N'$ data cannot be explained by conventional hadronic models. For example, the observed magnitude of the transverse cross section is significantly underestimated in a framework with Reggeized background amplitudes.

Purpose: Develop a phenomenological framework for the $N(e, e'\pi^\pm)N'$ reaction at high invariant mass W and deep photon virtuality Q^2 .

Method: Building on the work of Kaskulov and Mosel [Phys. Rev. C **81**, 045202 (2010)], a gauged pion-exchange current is introduced with a running cutoff energy for the proton electromagnetic transition form factor. A new transition form factor is proposed. It respects the correct on-shell limit, has a simple physical interpretation, and reduces the number of free parameters by one.

Results: A study of the W dependence of the $N(e, e'\pi^\pm)N'$ lends support for the newly proposed transition form factor. In addition, an improved description of the separated and unseparated cross sections at $-t \lesssim 0.5 \text{ GeV}^2$ is obtained. The predictions overshoot the measured unseparated cross sections for $-t > 0.5 \text{ GeV}^2$. Introducing a strong hadronic form factor in the Reggeized background amplitudes brings the calculations considerably closer to the high $-t$ data.

Conclusions: Hadronic models corrected for resonance-parton duality describe the separated pion electroproduction cross sections above the resonance region reasonably well at low $-t$. In order to validate the applicability of these models at high $-t$, separated cross sections are needed. These are expected to provide a more profound insight into the relevant reaction mechanisms.

DOI: [10.1103/PhysRevC.89.025203](https://doi.org/10.1103/PhysRevC.89.025203)

PACS number(s): 13.60.Le, 13.75.Gx, 13.85.-t, 24.10.-i

I. INTRODUCTION

The charged-pion electroproduction reaction $N(e, e'\pi^\pm)N'$ at high energies and deep photon virtuality is a topic of great theoretical and experimental interest. At high invariant masses, the reaction process is no longer dominated by individual resonances and background contributions prevail in all observables. By increasing the photon virtuality, the electromagnetic charge distribution of the nucleon can be mapped to more and more detail. The hadronic $N(e, e'\pi^\pm)N'$ phenomenology, however, is pushed to its limits in this deep-inelastic regime and is facing complications as partonic degrees of freedom start to overshadow hadronic ones.

The question of which mechanisms exactly contribute to the deeply virtual $N(e, e'\pi^\pm)N'$ reaction above the resonance region is a yet-unresolved issue which has been around for a few decades [1–3]. The hadronic $N(e, e'\pi^\pm)N'$ models fail to reproduce the observed magnitude of the transverse (T) and the signs of the interference (TT and LT) cross sections in the deep-virtuality, high-energy regime [4]. In Refs. [5,6], Kaskulov *et al.* proposed a model which explains the observed features of the transverse cross section. This model is of a hybrid nature: the hadronic background contributions, which dominate at low photon virtuality, are complemented with direct interactions of virtual photons with partons, followed by quark fragmentation into the final nucleon-pion state.

The framework developed in Refs. [5,6] deals with the $N(e, e'\pi^\pm)N'$ reaction at the cross-section level. In Ref. [7],

Kaskulov and Mosel propose a hadronic model which is able to explain the deep-inelastic $N(e, e'\pi^\pm)N'$ observables at the amplitude level. This model accounts for the residual effects of nucleon resonances in the proton electromagnetic transition form factor. In this approach, nucleon resonances are treated as dual to partons and so the terminology of “resonance-parton (R-P) contributions” may be used on occasion. The predictions of the Kaskulov–Mosel (KM) model can be brought in good agreement with the data. However, the electromagnetic form factor for the proton employed in this model is considerably harder than the measured proton Dirac form factor.

In this work, it is shown that the KM model falls short of providing a reasonable description of the data when the employed proton electromagnetic form factor is softened to make it compatible with the Dirac form. An alternative R-P transition form factor is proposed that is both simple and intuitive and features the accepted cutoff energy scale for the proton electromagnetic form factor. After replacing the transition form factor of the KM model with the newly proposed one, an even better description of the deep-inelastic $N(e, e'\pi^\pm)N'$ data is obtained.

The outline of this work is as follows: In Sec. II, the KM model will be reviewed and discussed. In Sec. III, the R-P transition form factor of the KM model will be addressed and an alternative parametrization will be presented. The comparison of the models with the available deep-inelastic data is the subject of Sec. IV. Here, the model predictions are also given for the planned $F\pi$ experiment at the 12 GeV upgrade at Jefferson Lab (JLab) [8], and for the recently published CEBAF Large Acceptance Spectrometer (CLAS) $p(e, e'\pi^+)n$

*Tom.Vrancx@UGent.be

†Jan.Ryckebusch@UGent.be

TOM VRANCX AND JAN RYCKEBUSCH

PHYSICAL REVIEW C **89**, 025203 (2014)

data in the deep pion momentum transfer regime [9]. Finally, the conclusions will be listed in Sec. V.

II. KASKULOV-MOSEL MODEL

A. Gauged pion exchange

The main component of the KM model is the gauged pion-exchange current. For the $p(e, e' \pi^+)n$ and the $n(e, e' \pi^-)p$ reaction, these currents read

$$\begin{aligned} J_{m,m'}^\mu(Q^2, s, t) &= i\sqrt{2}g_{\pi NN}\bar{u}_{m'}(p')\gamma_5\left(\mathcal{F}_{\gamma\pi\pi}(Q^2, t, s)\frac{(2k' - q)^\mu}{t - m_\pi^2}\right. \\ &\quad \left.+ \mathcal{F}_p(Q^2, s, t)\frac{\not{p} + \not{q} + m_p}{s - m_p^2}\gamma^\mu\right)u_m(p), \end{aligned} \quad (1)$$

and

$$\begin{aligned} J_{m,m'}^\mu(Q^2, u, t) &= -i\sqrt{2}g_{\pi NN}\bar{u}_{m'}(p')\left(\mathcal{F}_{\gamma\pi\pi}(Q^2, t, s)\frac{(2k' - q)^\mu}{t - m_\pi^2}\right. \\ &\quad \left.- \mathcal{F}_p(Q^2, u, t)\gamma^\mu\frac{\not{p}' - \not{q} + m_p}{u - m_p^2}\right)\gamma_5 u_m(p), \end{aligned} \quad (2)$$

in the Lorentz gauge, where $q \cdot \epsilon = 0$ [7]. Here, p and q are the four-momenta of the incoming nucleon and virtual photon, k' and p' are the four-momenta of the outgoing pion and nucleon, and ϵ is the photon polarization four-vector. These kinematics are defined in the laboratory frame. The photon virtuality is defined as $Q^2 = -q^2$, and the Mandelstam variables are given by $t = (k' - q)^2$, $s = W^2 = (p + q)^2$, and $u = (p' - q)^2$. The spin indices of the incoming and outgoing nucleon are denoted by m and m' . Furthermore, $g_{\pi NN}$ is the pion-nucleon coupling constant and is fixed at $g_{\pi NN} = 13.4$ in the KM model. The $\mathcal{F}_{\gamma\pi\pi}(Q^2, t, s)$ and $\mathcal{F}_p(Q^2, s, t)$ (where “ s ” is interchangeably used for s and u) represent the transition form factors of the intermediate pion and proton. The pion-exchange currents, as defined in Eqs. (1) and (2), are gauge-invariant: $q \cdot J_{m,m'} = 0$.

The separated cross sections $d\sigma_{\{L,T,TT,LT\}}/dt$ are defined as in Eqs. (A1–A4) of Ref. [7]. Throughout this work, “ $\sigma_{\{U,L,T,TT,LT\}}$ ” will often be used as a shorthand notation for $d\sigma_{\{U,L,T,TT,LT\}}/dt$ or $d\sigma_{\{U,L,T,TT,LT\}}/d\Omega_\pi$. Here, σ_U denotes the unseparated cross section and is given by

$$\sigma_U = \sigma_T + \varepsilon\sigma_L, \quad (3)$$

with ε being the ratio of longitudinal to transverse polarization of the virtual photon [Eq. (8) of Ref. [7]].

The pion transition form factor $\mathcal{F}_{\gamma\pi\pi}(Q^2, t, s)$ is defined as

$$\mathcal{F}_{\gamma\pi\pi}(Q^2, t, s) = F_{\gamma\pi\pi}(Q^2)\mathcal{P}_\pi(t, s)(t - m_\pi^2), \quad (4)$$

with $\mathcal{P}_\pi(t, s)$ being the degenerate $\pi(140)/b_1(1235)$ -Regge propagator:

$$\mathcal{P}_\pi(t, s) = -\alpha'_\pi \varphi_\pi(t) \Gamma(-\alpha_\pi(t)) (\alpha'_\pi s)^{\alpha_\pi(t)}. \quad (5)$$

Here,

$$\alpha_\pi(t) = \alpha'_\pi(t - m_\pi^2), \quad (6)$$

is the corresponding Regge trajectory with $\alpha'_\pi = 0.74 \text{ GeV}^{-2}$. The Regge phase $\varphi_\pi(t)$ is given by

$$\varphi_\pi(t) = \begin{cases} e^{-i\pi\alpha_\pi(t)}, & p(e, e' \pi^+)n \\ 1, & n(e, e' \pi^-)p. \end{cases} \quad (7)$$

For the pion transition form factor $F_{\gamma\pi\pi}(Q^2)$ a monopole parametrization is used:

$$F_{\gamma\pi\pi}(Q^2) = \left(1 + \frac{Q^2}{\Lambda_{\gamma\pi\pi}^2}\right)^{-1}, \quad (8)$$

with $\Lambda_{\gamma\pi\pi}$ being the pion cutoff energy. In order for the currents $J_{m,m'}^\mu$ to remain gauge-invariant, the transition form factors must coincide at the real-photon point:

$$\mathcal{F}_{\gamma\pi\pi}(Q^2 = 0, t, s) = \mathcal{F}_p(Q^2 = 0, s, t), \quad (9)$$

which implies that the proton transition form factor must be proportional to the pion-Regge propagator:

$$\mathcal{F}_p(Q^2, s, t) = F_p(Q^2, s)\mathcal{P}_\pi(t, s)(t - m_\pi^2). \quad (10)$$

In the KM model an additional antishrinkage effect in $\mathcal{F}_p(Q^2, s, t)$ is taken into account. More specifically, the slope of the $\pi(140)/b_1(1235)$ -Regge trajectory in the Regge propagator of Eq. (10) is altered as follows:

$$\alpha'_\pi \rightarrow \alpha'_\pi(Q^2, s) = \frac{\alpha'_\pi}{1 + a\frac{Q^2}{s}}, \quad (11)$$

with $a > 0$. The incorporation of this antishrinkage effect does not violate gauge invariance because

$$\alpha'_\pi(Q^2 = 0, s) = \alpha'_\pi. \quad (12)$$

B. Nucleon resonances

In Ref. [7], it is argued that assigning the proton Dirac form factor to $F_p(Q^2, s)$ might be too naive, because the intermediate proton becomes highly off shell. A transition form factor which accounts for the effects of the virtual proton fluctuating into resonances was proposed:

$$F_p(Q^2, s) = \frac{\lim_{\varepsilon \rightarrow 0^+} \int_{m_p^2}^{\infty} ds_i \frac{s_i^{-\beta}}{s - s_i + i\varepsilon} (1 + \xi \frac{Q^2}{s_i})^{-2}}{\lim_{\varepsilon \rightarrow 0^+} \int_{m_p^2}^{\infty} ds_i \frac{s_i^{-\beta}}{s - s_i + i\varepsilon}}. \quad (13)$$

The above integral is the continuation of an infinite sum running over all the proton resonances with squared mass s_i . The factor $s_i^{-\beta}$, with $\beta \geq 1$ being a fit parameter, accounts for the electromagnetic and the strong proton-resonance coupling strengths, and the density of resonance states. The factor

$$F_{r_i}(Q^2, s_i) = \left(1 + \xi \frac{Q^2}{s_i}\right)^{-2}, \quad (14)$$

is a dipole parametrization for the electromagnetic form factor of the resonance r_i . Here, ξ is a common average cutoff parameter. In the s channel the singularity at $s_i = s + i\varepsilon$ generates an imaginary part for the proton transition form factor, which is absent in the u channel where the singularity resides in the unphysical region.

C. Additional Regge exchanges and model parameters

The KM model features two additional Regge exchanges: the vector $\rho(770)/a_1(1320)$ and the axial-vector $a_1(1260)$ trajectories. The exchange currents and accompanying parameters for these amplitudes are listed in Sec. V and Table I of Ref. [7].

In the KM model, the parameters (a, β, ξ) introduced in Eqs. (11) and (13) adopt the values

$$a = 2.4, \quad \beta = 3, \quad \xi = 0.4, \quad (15)$$

and the following prescription for the pion cutoff energy $\Lambda_{\gamma\pi\pi}$ is employed (see last paragraph of Sec. IV of Ref. [7]):

$$\Lambda_{\gamma\pi\pi} \simeq \begin{cases} 775 \text{ MeV}, & Q^2 < 0.4 \text{ GeV}^2 \\ 630 \text{ MeV}, & 0.6 < Q^2 < 1.5 \text{ GeV}^2 \\ 680 \text{ MeV}, & \text{“deep } (Q^2, W) \text{ region.”} \end{cases} \quad (16)$$

III. TRANSITION FORM FACTOR

A. On-shell limit of Kaskulov–Mosel transition form factor

The transition form factor $F_p(Q^2, s)$ essentially quantifies the R-P contributions to the electromagnetic coupling strength of the intermediate proton in the gauged pion-exchange diagram. The tree-level Feynman diagram of this process is depicted in Fig. 1 for the s channel. The R-P transition form factor of Eq. (13) was developed independently from the $N(e, e'\pi^\pm)N'$ reaction and could find application in any reaction which has a virtual photon coupling between an on-shell and an off-shell proton.

In the limit $s \rightarrow m_p^2$, the proton remains on its mass shell and the process depicted in Fig. 1 describes elastic electron-proton scattering. As a consequence, one expects that $F_p(Q^2, s)$ reduces to the Dirac form factor $F_p^{\text{Dirac}}(Q^2)$:

$$\lim_{s \rightarrow m_p^2} F_p(Q^2, s) = F_p^{\text{Dirac}}(Q^2), \quad (17)$$

which can be approximated by a dipole form factor (especially at low Q^2):

$$F_p^{\text{Dirac}}(Q^2) \simeq \left(1 + \frac{Q^2}{\Lambda_{\gamma pp}^2}\right)^{-2}, \quad (18)$$

with $\Lambda_{\gamma pp} = 840$ MeV. As becomes apparent from Fig. 2, the transition form factor of Eq. (13) does not satisfy this constraint and corresponds with a form factor which is considerably

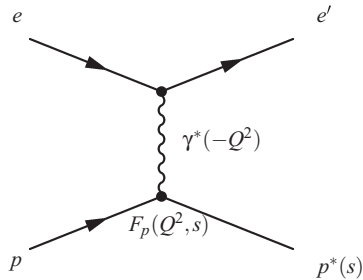


FIG. 1. Feynman diagram of a virtual photon exciting an incoming proton to the s channel.

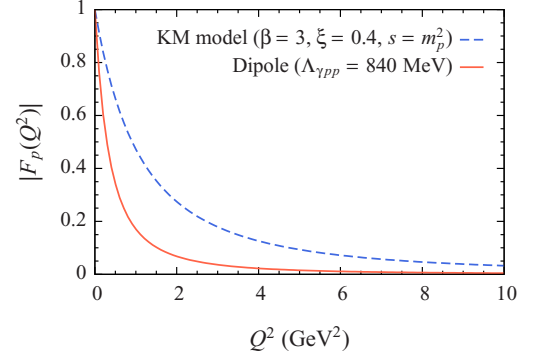


FIG. 2. (Color online) The modulus of the R-P transition form factor of the KM model in the limit $s \rightarrow m_p^2$ (dashed lines) and of the proton dipole form factor (full line).

harder than $F_p^{\text{Dirac}}(Q^2)$. In that respect, it should be mentioned that the KM framework was developed based on duality arguments, which are only meaningful at higher invariant masses.

The transition form factor of Eq. (13) is composed of a smooth, infinite distribution of resonance form factors $F_{r_i}(Q^2, s_i)$, which are defined in Eq. (14). The ground state “ r_0 ” of those resonances is the proton ($s_0 = m_p^2$). This implies that the form factor for the proton, adopted in the KM model, reads

$$F_{r_0}(Q^2, s_0) = \left(1 + \xi \frac{Q^2}{m_p^2}\right)^{-2}. \quad (19)$$

It can be shown that $\lim_{s \rightarrow m_p^2} F_p(Q^2, s) = F_{r_0}(Q^2, s_0)$, as expected intuitively. Hence, the proton cutoff energy used in the KM model amounts to

$$\Lambda_{\gamma pp} \rightarrow \frac{m_p}{\sqrt{\xi}} \simeq 1484 \text{ MeV}, \quad (20)$$

which is considerably larger than 840 MeV. In order to impose the $s \rightarrow m_p^2$ limit of Eq. (17) to the KM transition form factor a value

$$\xi = \frac{m_p^2}{\Lambda_{\gamma pp}^2} \simeq 1.248 \quad (21)$$

is required. The KM model with $\xi = 1.248$ and β the only remaining free parameter, will be dubbed the “constrained Kaskulov–Mosel” or “cKM” model.

B. Alternate transition form factor

Apart from not respecting the constraint (17), the KM prescription (13) for the proton transition form factor has a complex functional dependence on its variables and parameters. Consider the following phenomenological s -dependent transition form factor:

$$F_p(Q^2, s) = \left(1 + \frac{Q^2}{\Lambda_{\gamma pp^*(s)}^2}\right)^{-2}, \quad (22)$$

which is of the dipole form and has an s -dependent cutoff energy $\Lambda_{\gamma pp^*}(s)$. On-shell consistency requires that

$$\Lambda_{\gamma pp^*}(m_p^2) = \Lambda_{\gamma pp}. \quad (23)$$

From the observed magnitude of σ_T at high energies, it is conceived that an s -channel cutoff energy much larger than $\Lambda_{\gamma pp}$ is required. For the transition form factor (22), this implies that $\Lambda_{\gamma pp^*}(s)$ should grow with s . Assuming that $\Lambda_{\gamma pp^*}(s \rightarrow \infty)$ approaches a constant value Λ_∞ , the lowest-order (with respect to s^{-1}) ansatz for the cutoff energy reads

$$\Lambda_{\gamma pp^*}(s) = \Lambda_{\gamma pp} + (\Lambda_\infty - \Lambda_{\gamma pp}) \left(1 - \frac{m_p^2}{s}\right), \quad (24)$$

for $s \geq m_p^2$. For $u \leq m_p^2$, the symmetrization of the above expression (for $s \geq m_p^2$) about m_p^2 will be employed:

$$\Lambda_{\gamma pp^*}(u) = \Lambda_{\gamma pp} + (\Lambda_\infty - \Lambda_{\gamma pp}) \left(1 - \frac{m_p^2}{2m_p^2 - u}\right). \quad (25)$$

The form factor of Eq. (22) has a very intuitive (Q^2, s) dependence: an exponential charge distribution is assigned to the proton and the charge radius asymptotically decreases with increasing virtuality.

C. Pion coupling strengths

In the KM model, a (Q^2, s)-dependent parametrization (16) for the pion cutoff energy $\Lambda_{\gamma\pi\pi}$ is employed. This parametrization is discontinuous with respect to Q^2 and s . In the new model, a constant pion cutoff energy will be adopted which is the average of the upper and intermediate values used in the KM model (respectively 680 and 630 MeV):

$$\Lambda_{\gamma\pi\pi} = 655 \text{ MeV}. \quad (26)$$

In analogy with the off-shell proton case, a t -dependent pion cutoff energy could be adopted which amounts to the vector-meson dominance value of $\Lambda_{\gamma\pi\pi} = m_{\rho(770)} \simeq 775.5$ MeV for $t = m_\pi^2$. However, as the available data only covers a small range of $-t$ values ($-t \lesssim 0.5 \text{ GeV}^2$), a constant pion cutoff energy can be used. Note that as the t -channel pion exchange is replaced by the exchange of a pion-Regge trajectory, the relationship to the on-shell pion form factor might be lost and $\Lambda_{\gamma\pi\pi}$ should be interpreted as an effective transition cutoff energy.

The “exact” value of the pion-nucleon coupling $g_{\pi NN}$ is a matter of debate in the literature. Reported values vary from $g_{\pi NN} \simeq 13.0$ – 13.5 [10–13]. As mentioned, the value $g_{\pi NN} = 13.4$ is used in the KM model. However, a better agreement with the available $N(e, e'\pi^\pm)N'$ data can be obtained with $g_{\pi NN} = 13.0$ and this value will be used in the new model. The new model will now be dubbed the “Vrancx–Ryckebusch” or “VR” model.

IV. RESULTS

A. Proton cutoff energy

The VR model features only one parameter (Λ_∞) for the proton transition form factor, instead of two (β and ξ) for the KM model. Before determining the value of the asymptotic proton cutoff energy Λ_∞ , the experimental energy dependence of the proton cutoff energy will be investigated. To that end, the cutoff energy $\Lambda_{\gamma pp^*}$ of the dipole transition form factor (22) is fit to each set of observables (σ_U , σ_L , σ_T , σ_{TT} , and/or σ_{LT}) at a fixed invariant mass W and varying Q^2 and/or t values. The data employed are from CEA [14], Cornell [15,16], DESY [17–19], and JLab [4,20–22].

In Fig. 3, the fitted proton cutoff energies $\Lambda_{\gamma pp^*}$ are shown as a function of W . There is clear evidence that the high-energy data require a proton cutoff energy much larger than

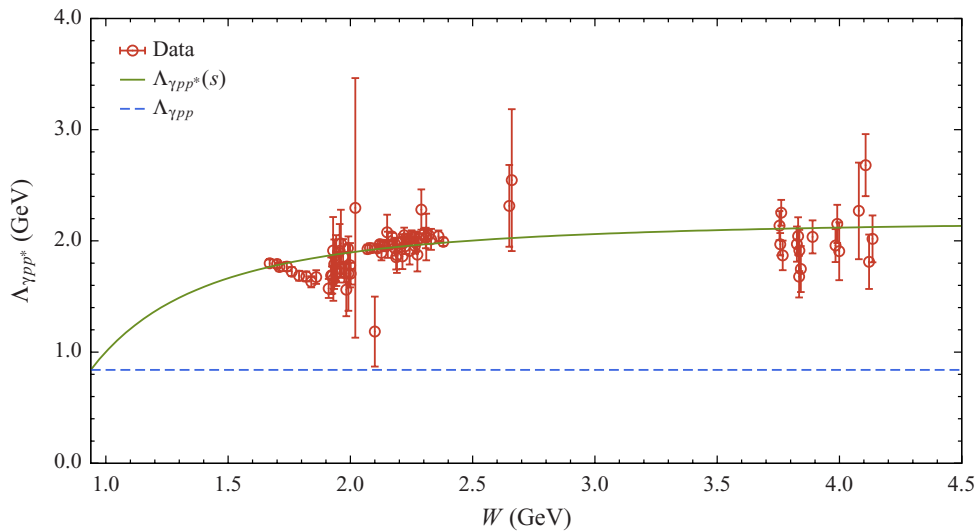


FIG. 3. (Color online) The fitted proton cutoff energy as a function of W . The “data” are the cutoff values extracted from fitting the VR model (with $g_{\pi NN} = 13.0$, $\Lambda_{\gamma\pi\pi} = 655$ MeV, and $a = 2.4$) to sets of experimental observables (see text). The full line corresponds with the s -dependent proton cutoff energy of Eq. (24) for $\Lambda_\infty = 2194$ MeV. The dashed line shows $\Lambda_{\gamma pp} = 840$ MeV.

TABLE I. Comparison of the χ^2_{NDF} values for the available $p(e, e'\pi^+)n$ and $n(e, e'\pi^-)p$ DIS data between the KM, cKM, and VR models.

	Observable(s)	W (GeV)	Q^2 (GeV ²)		χ^2_{NDF}		
					KM	cKM	VR
CEA	σ_{LT}	2.02–2.31	0.354–0.426	[14]	0.71	2.79	0.52
	$\sigma_{\text{TT}}, \sigma_{\text{LT}}$	2.15	0.176–0.188	[14]	0.78	1.35	0.99
Cornell	$\sigma_{\text{U}}, \sigma_{\text{TT}}, \sigma_{\text{LT}}$	2.66	1.20	[15]	0.96	1.20	1.56
	$\sigma_{\text{L}}, \sigma_{\text{T}}$	2.15–2.65	1.19–3.32	[16]	2.31	2.06	1.87
DESY	$\sigma_{\text{L}}, \sigma_{\text{T}}, \sigma_{\text{TT}}, \sigma_{\text{LT}}$	2.10	0.35	[17]	1.69	0.95	3.27
	$\sigma_{\text{U}}, \sigma_{\text{TT}}, \sigma_{\text{LT}}$ (p)	2.19	0.70–1.35	[18]	3.18	6.61	2.77
	(n)				2.22	1.55	1.74
	$\sigma_{\text{L}}, \sigma_{\text{T}}, \sigma_{\text{TT}}, \sigma_{\text{LT}}$	2.19	0.70	[18]	2.59	3.06	3.24
	σ_{U}	3.768–4.121	1.37–5.44	[19]	4.37	74.5	3.59
JLab	$\sigma_{\text{L}}, \sigma_{\text{T}}, \sigma_{\text{TT}}, \sigma_{\text{LT}}$	1.911–2.001	0.526–1.702	[20]	8.11	7.95	6.03
	$\sigma_{\text{L}}, \sigma_{\text{T}}, \sigma_{\text{TT}}, \sigma_{\text{LT}}$	2.153–2.308	1.416–2.703	[4]	4.84	31.8	3.96
	$\sigma_{\text{L}}, \sigma_{\text{T}}, \sigma_{\text{TT}}, \sigma_{\text{LT}}$	2.21–2.22	2.15–3.91	[21]	3.37	14.1	3.29
	σ_{U}	1.70–2.38	0.92–4.98	[22]	4.48	5.10	3.70
	$A_{\text{LU}}^{\sin\phi_\pi}$	2.0	1.5	[23]	0.43	9.08	0.96
			Total		3.97	11.0	3.35

$\Lambda_{\gamma pp} = 840$ MeV. The fitted cutoff energies rise slowly with the energy in the region $W \simeq 1.7$ –2.4 GeV and tend to reach a certain asymptotic value. The “experimental” cutoff energies can be well described by the function $\Lambda_{\gamma pp^*}(s)$ of Eq. (24). Optimizing this function against the extracted cutoff energies yields

$$\Lambda_\infty = 2194 \pm 13 \text{ MeV}, \quad (27)$$

with $\chi^2_{\text{NDF}} = 1.97$ for 84 degrees of freedom. This value is about 2.6 times larger than the on-shell proton cutoff energy. In the VR model, Λ_∞ is fixed to the value of Eq. (27).

B. Low $-t$ regime

At low momentum transfer in the t -channel, the final pion is produced at low scattering angles. In this regime, the exchanged pion-Regge trajectory is close to its first materialization (the pion), which results in a dominant longitudinal and a small transverse contribution to the differential cross section. Experimentally, however, it is observed that in the deep-inelastic-scattering (DIS) regime the differential cross

section receives a sizable contribution from the transverse component. In the current framework, this transverse strength is provided by contributions from resonances or partons to the s - or u -channel gauge-fixing terms of Eqs. (1) and (2).

In Table I, the χ^2_{NDF} values for the available $p(e, e'\pi^+)n$ and $n(e, e'\pi^-)p$ DIS data are listed for the KM, cKM, and VR models. For the cKM model, the value $\beta = 1$ was found to be in best agreement with the data. The cKM model provides a far worse description of the data ($\chi^2_{\text{NDF}} = 11.0$) than the KM model ($\chi^2_{\text{NDF}} = 3.97$). Hence, the KM framework cannot provide a fair description of the data once the correct on-shell limit of the proton electromagnetic transition form factor is imposed.

The VR model can be conceived as a real competitor for the KM model. Despite the fact that it features one additional parameter, the KM model does not provide the best agreement with the data. The VR model, which employs an intuitive prescription for the proton transition form factor, a fixed value for $\Lambda_{\gamma\pi\pi}$, and only one parameter, performs better ($\chi^2_{\text{NDF}} = 3.35$). In Figs. 4 through 6, the predictions of the KM, cKM,

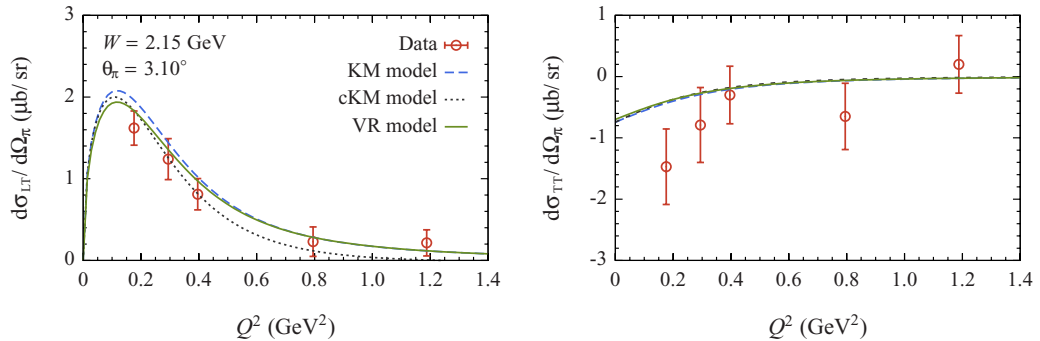


FIG. 4. (Color online) The Q^2 dependence of the interference cross sections $d\sigma_{\text{LT}}/d\Omega_\pi$ and $d\sigma_{\text{TT}}/d\Omega_\pi$ of the $p(e, e'\pi^+)n$ reaction at forward scattering ($\theta_\pi = 3.10^\circ$) and $W = 2.15$ GeV. The dashed curves, the dotted (dark gray), and the full curves are the predictions of the KM, the cKM, and the VR model. The data are from Ref. [14] (CEA).

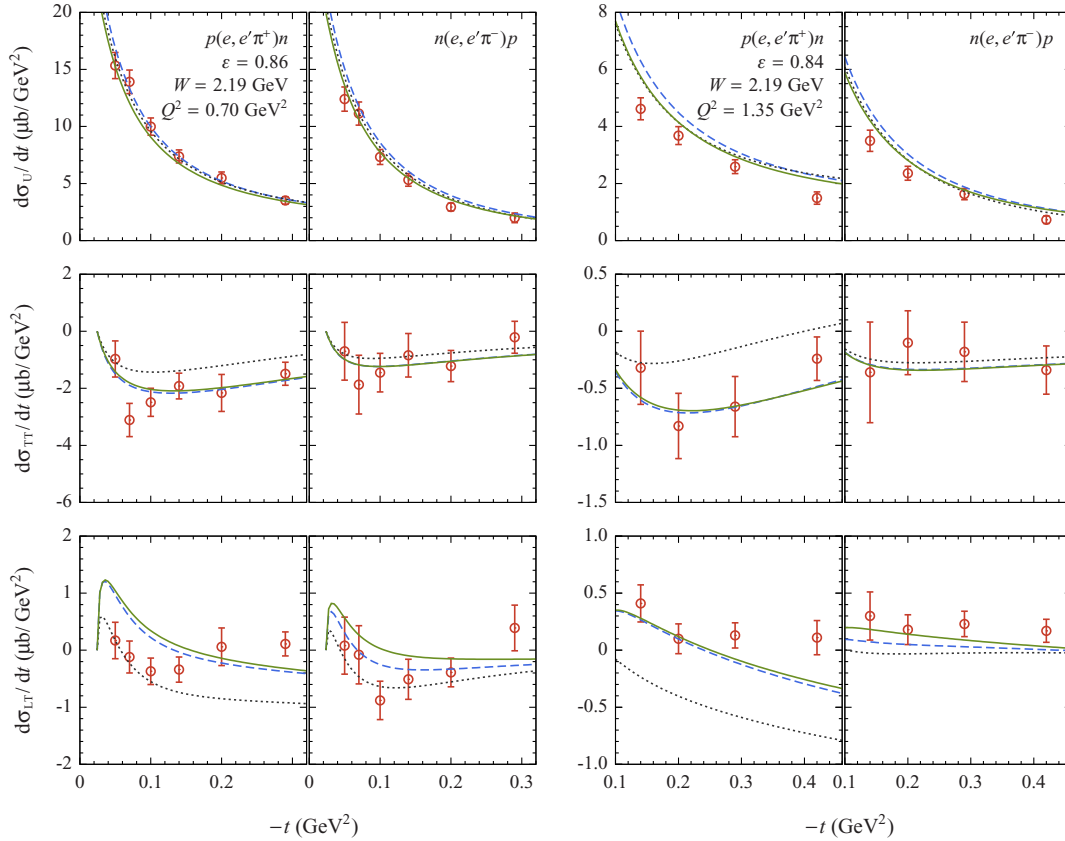


FIG. 5. (Color online) The $-t$ dependence of the unseparated and interference cross sections $d\sigma_U/dt$, and $d\sigma_{TT}/dt$ and $d\sigma_{LT}/dt$ of the $p(e, e'\pi^+)n$ and $n(e, e'\pi^-)p$ reactions at two different (W, Q^2, ε) values. Curve notations of Fig. 4 are used. The data are from Ref. [18] (DESY).

and VR models are compared with the experimental DIS data at low $-t$. It is seen that the cKM model offers the worst description of the data and that the predictions of the KM and the VR model are comparably good. The latter provides a slightly better description, though.

In Ref. [7], predictions for the planned $F\pi$ experiment at JLab's 12 GeV upgrade [8] are provided. These are shown for two (W, Q^2) bins in Fig. 7, together with the corresponding VR predictions. It appears that both models are qualitatively equivalent at these kinematics. There is, however, a quantitative difference between the models, which can become quite substantial in some kinematic regions. For example, at $W = 3.28$ GeV, $Q^2 = 4.50$ GeV², and $t = -1.98$ GeV² the KM and VR $n(e, e'\pi^-)p$ predictions for $d\sigma_{LT}/dt$ differ by about 25%.

C. High $-t$ regime

Earlier this year, the CLAS Collaboration at Jefferson Lab published new DIS data for the $p(e, e'\pi^+)n$ reaction [9]. These data cover $-t$ values up to 4.8 GeV² and allow the study of the reaction in the deep pion momentum transfer regime. In Fig. 8, the model predictions are compared with the deep $(Q^2, W, -t)$ CLAS data. It is seen that all three models dramatically overshoot the $-t \gtrsim 1$ GeV² data; the

corresponding χ_{NDF}^2 values are 3.9×10^4 (KM), 3.1×10^4 (cKM), and 3.3×10^4 (VR). The data show a much faster falloff with $-t$ compared with the theoretical curves.

The situation can be remedied to some extent by introducing a form factor in the strong vertex of the t -channel Regge amplitudes. Such a strong hadronic form factor accounts for the finite size of the interacting hadrons at the vertex and, in essence, suppresses the πNN coupling at high momentum transfers. A possible parametrization for the hadronic form factor is a monopole:

$$F_{m_t}(t) = \left(1 + \frac{m_t^2 - t}{\Lambda_{m_t}^2}\right)^{-1}, \quad (28)$$

where $m_t \in \{m_\pi, m_\rho, m_{a_1}\}$ is the “ground-state” mass of the exchanged Regge trajectory and Λ_{m_t} is the corresponding strong cutoff energy. The finite size of a certain vertex can be accounted for by introducing a running coupling strength. At the πNN vertex, for example, this implies that the strong coupling constant $g_{\pi NN}$ acquires a t dependence:

$$g_{\pi NN}(t) = g_{\pi NN} F_{m_t}(t). \quad (29)$$

By construction, one has $F_{m_t}(m_t^2) = 1$. Note that the gauge-fixing s -channel term of the pion-exchange current (1) is also

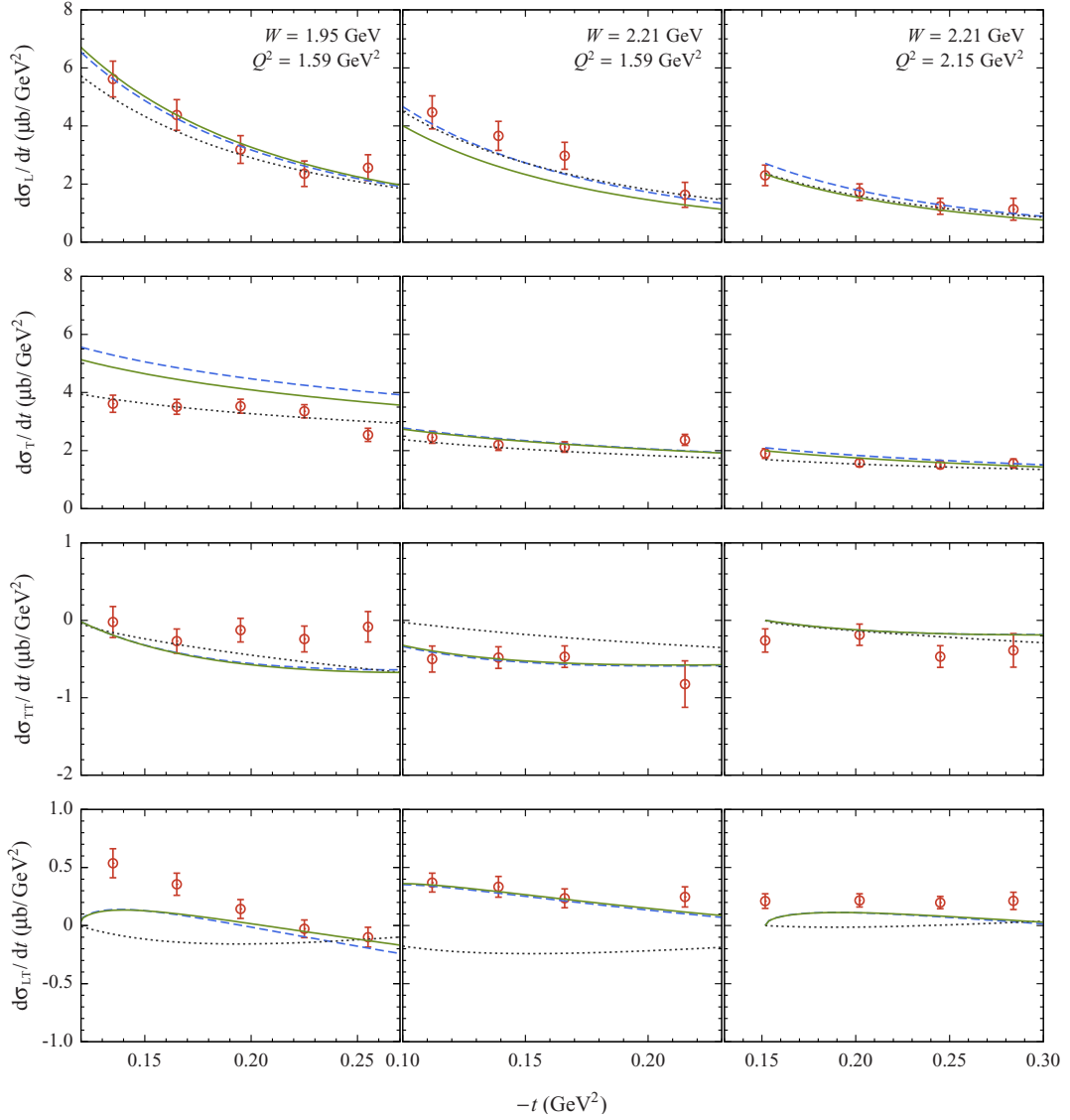


FIG. 6. (Color online) The $-t$ dependence of the longitudinal σ_L , transverse σ_T , and interference cross sections σ_{TT} of the $p(e,e'\pi^+)n$ reaction at three different (W, Q^2) values. The (W, Q^2) values listed are the average values; the curves were calculated for the (W, Q^2) values corresponding with the first $-t$ bin. Curve notations of Fig. 4 are used. The data are from the F π -1 [20] (left), F π -2 [4] (center), and π -CT [21] (right) experiments at JLab.

affected by the strong hadronic form factor, as this term is proportional to $g_{\pi NN}$.

After introducing a coupling of the type (29) with $\Lambda_{m_t} = 0.8$ GeV, the VR model provides a reasonable description of the data. Indeed, the dash-dotted curves in Fig. 8 correspond with a $\chi^2_{\text{NDF}} = 16.3$, which is about 2000 times smaller than the χ^2_{NDF} value obtained with $F_{m_t}(t) = 1$. The incorporation of the strong hadronic form factor deteriorates the agreement with the DIS data at low $-t$: the χ^2_{NDF} value of 3.35 (see Table I) is increased to 21.9 due to the inclusion of $F_{m_t}(t)$.

In Ref. [9], it is shown that the predictions of the Laget model [24] are in fair agreement with the observed unseparated cross sections at high $-t$. Contrary to the KM framework, the

Laget model does not consider off-shell effects in the proton electromagnetic transition form factor due to resonances or partons. The Laget model features Reggeized π and ρ meson exchanges in the t channel, complemented with the exchange of a nucleon Regge trajectory in the u channel [25]. The pion cutoff energy $\Lambda_{\gamma\pi\pi}$ is assigned a phenomenological t dependence, which is vital for explaining the observed behavior of $d\sigma_U/dt$ for $0.5 \lesssim -t \lesssim 5$ GeV 2 in the Laget model.

In the current framework, the addition of a nucleon Regge trajectory in the u channel and/or the inclusion of a t -dependent pion cutoff energy does not considerably improve the description of the high $-t$ data (compared to taking into

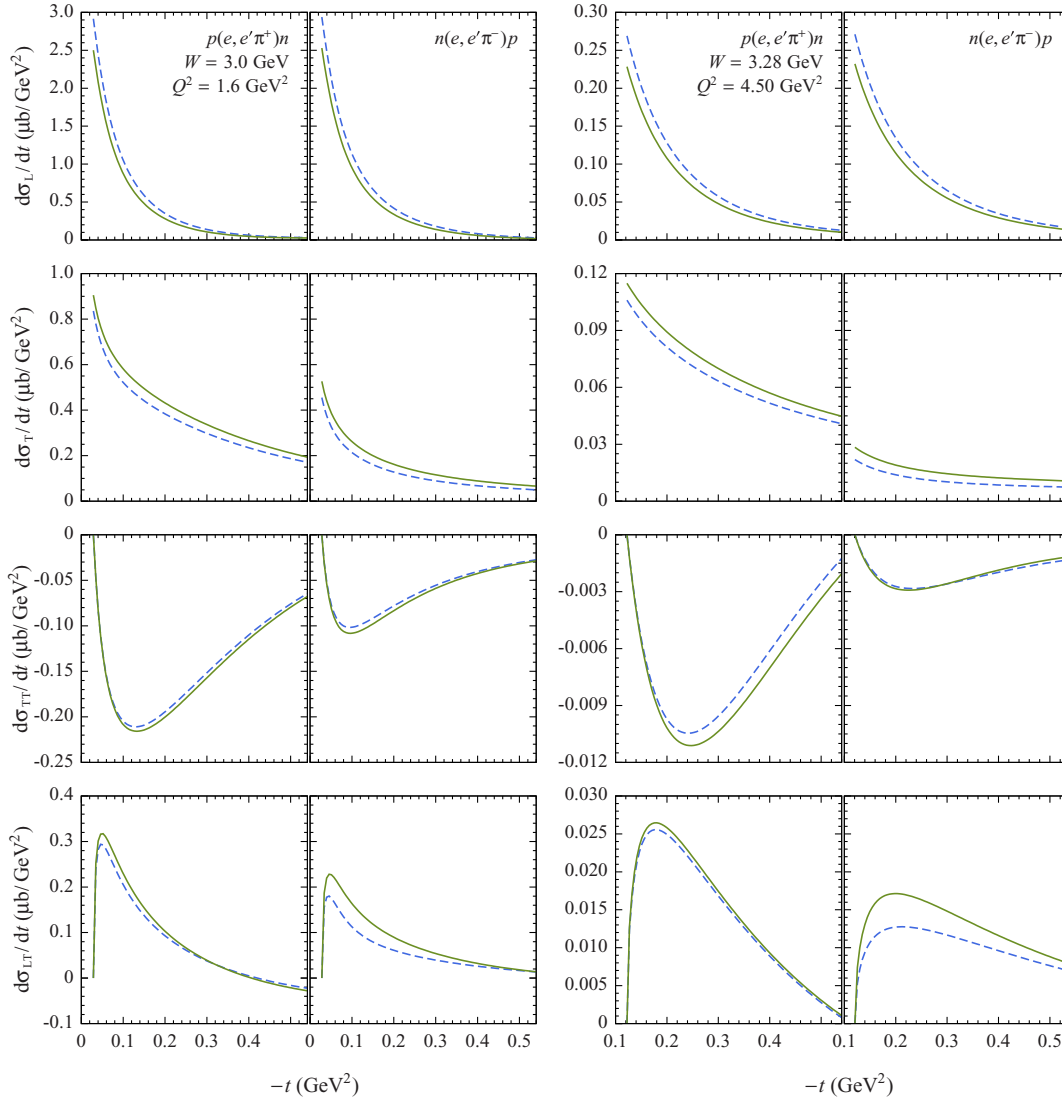


FIG. 7. (Color online) The $-t$ dependence of the separated cross sections $d\sigma_L/dt$, $d\sigma_T/dt$, $d\sigma_{TT}/dt$, and $d\sigma_{LT}/dt$ of the $p(e, e'\pi^+)n$ and $n(e, e'\pi^-)p$ reactions at two different (W, Q^2) values. Curve notations of Fig. 4 are used. These are predictions for the F π experiment planned for the 12 GeV upgrade at JLab.

account a strong hadronic form factor only, which is also included in the Laget model). For now, it is not clear how, in the current framework, the low $-t$ regime, which does not require a strong hadronic form factor, can be smoothly conjoined with the high $-t$ regime, where $F_m(t)$ is essential to capture the observed t dependence of σ_U . The corresponding interference cross sections σ_{TT} and σ_{LT} are the subject of an ongoing analysis by the CLAS Collaboration [9] and is expected to provide new constraints for the models at high $-t$.

V. CONCLUSION AND OUTLOOK

In this work, a phenomenological model for the $N(e, e'\pi^\pm)N'$ reaction in the deep-inelastic regime was presented. The model builds on the Kaskulov–Mosel model,

which includes three Reggeized background amplitudes in the t channel and takes into account the residual effects of resonances or partons, which are encoded in the proton electromagnetic transition form factor.

It was pointed out that the KM transition form factor, which is derived from duality arguments, does not respect the expected limit for $s \rightarrow m_p^2$ by construction. Another suboptimal feature of the KM model is that it uses a discontinuous functional form for the pion cutoff energy. A modified model was proposed, dubbed the “VR” model, which resolves both issues. In this model the pion cutoff energy is kept fixed and an intuitive functional dependence for the proton transition form factor was introduced, which respects the physical $s \rightarrow m_p^2$ constraints. The VR model has one parameter; the KM model has two. Nevertheless, the VR model offers a somewhat better

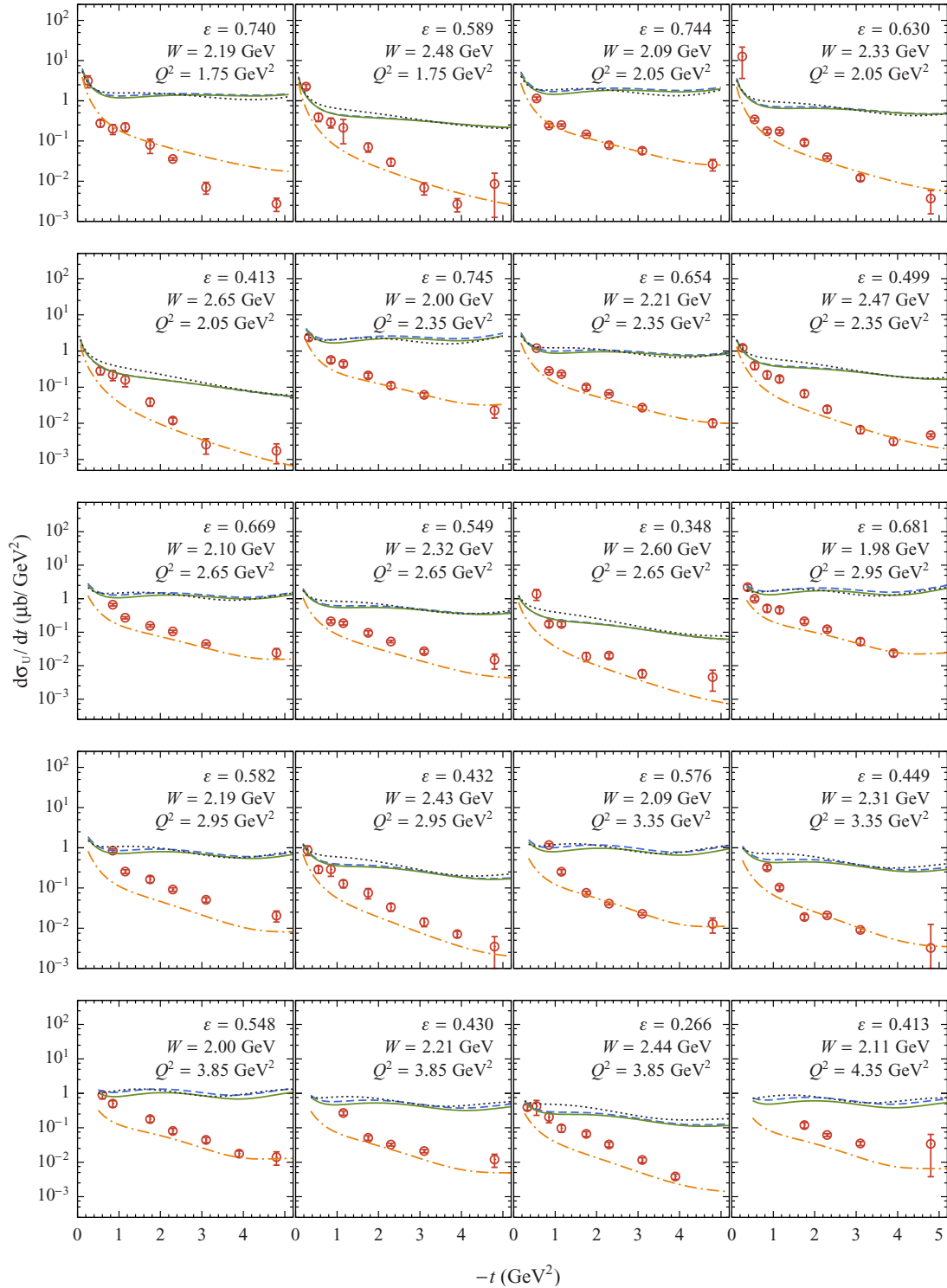


FIG. 8. (Color online) The $-t$ dependence of the unseparated cross section $d\sigma_U/dt$ of the $p(e,e'\pi^+)n$ reaction at twenty (W, Q^2, ε) combinations. The dash-dotted curves correspond to the prediction of the VR model with the inclusion of the strong hadronic form factor $F_{m_i}(t)$ of Eq. (28) with $\Lambda_{m_i} = 0.8 \text{ GeV}$; for the other curves the notation of Fig. 4 is used. The data are from Ref. [9].

TOM VRANCX AND JAN RYCKEBUSCH

PHYSICAL REVIEW C **89**, 025203 (2014)

description of the low $-tN(e,e'\pi^\pm)N'$ data than the KM model. It was shown that imposing the correct $s \rightarrow m_p^2$ behavior in the KM prescription for the proton electromagnetic transition form factor, does not result in a fair description of the data.

The VR predictions for the planned $F\pi$ experiment at JLab were provided and compared to those of the KM model. The models were also tested against the recent unseparated $p(e,e'\pi^+)n$ data which extend to pion momentum transfers of 4.8 GeV^2 , corresponding with the deep $-t$ regime. The VR and KM models fail miserably to describe the observed t dependence of the cross sections. For the VR model, it was shown that the introduction of a strong hadronic form factor in the πNN vertex dramatically improves the agreement with

the high $-t$ data, but at the same time results in a deteriorated description of the low $-t$ data. At this moment it is unclear how the low and the high $-t$ regimes can be smoothly matched. It can be expected that the availability of separated cross sections at high $-t$ will shed new light on this issue.

ACKNOWLEDGMENTS

This work is supported by the Research Council of Ghent University and the Flemish Research Foundation (FWO Vlaanderen). The authors would like to thank Dipangar Dutta, Tanja Horn, Garth Huber, and Igor Strakovsky for providing most of the relevant data, and Murat Kaskulov for his help with the implementation of the KM model.

-
- [1] O. Nachtmann, *Nucl. Phys. B* **115**, 61 (1976).
 - [2] P. D. B. Collins and T. D. B. Wilkie, *Z. Phys. C: Part. Fields* **7**, 357 (1981).
 - [3] A. Faessler, T. Gutsche, V. E. Lyubovitskij, and I. T. Obukhovskiy, *Phys. Rev. C* **76**, 025213 (2007).
 - [4] H. P. Blok *et al.*, *Phys. Rev. C* **78**, 045202 (2008).
 - [5] M. M. Kaskulov, K. Gallmeister, and U. Mosel, *Phys. Rev. D* **78**, 114022 (2008).
 - [6] M. M. Kaskulov and U. Mosel, *Phys. Rev. C* **80**, 028202 (2009).
 - [7] M. M. Kaskulov and U. Mosel, *Phys. Rev. C* **81**, 045202 (2010).
 - [8] G. M. Huber *et al.*, JLab PAC **30**, PR12-06-101 (2006).
 - [9] K. Park *et al.*, *Eur. Phys. J. A* **49**, 16 (2013).
 - [10] W. R. Gibbs, L. Ai, and W. B. Kaufmann, *Phys. Rev. C* **57**, 784 (1998).
 - [11] M. C. M. Rentmeester, R. G. E. Timmermans, J. L. Friar, and J. J. de Swart, *Phys. Rev. Lett.* **82**, 4992 (1999).
 - [12] T. E. O. Ericson, B. Loiseau, and A. W. Thomas, *Nucl. Phys. A* **663**, 541c (2000).
 - [13] M. M. Pavan, R. A. Arndt, I. I. Strakovsky, and R. L. Workman, *Phys. Scr.* **T87**, 65 (2000).
 - [14] C. N. Brown, C. R. Canizares, W. E. Cooper, A. M. Eisner, G. J. Feldmann, C. A. Lichtenstein, L. Litt, W. Loceretz, V. B. Montana, and F. M. Pipkin, *Phys. Rev. D* **8**, 92 (1973).
 - [15] C. J. Bebek *et al.*, *Phys. Rev. D* **9**, 1229 (1974).
 - [16] C. J. Bebek *et al.*, *Phys. Rev. Lett.* **37**, 1326 (1976).
 - [17] H. Ackermann, T. Azemoon, W. Gabriel, H. D. Mertiens, H. D. Reich, G. Specht, F. Janata, and D. Schmidt, *Nucl. Phys. B* **137**, 294 (1978).
 - [18] P. Brauel, T. Canzler, D. Cords, R. Felst, G. Grindhammer, M. Helm, W. D. Kollmann, H. Krehbiel, and M. Schadlich, *Z. Phys. C: Part. Fields* **3**, 101 (1979).
 - [19] A. Airapetian *et al.*, *Phys. Lett. B* **659**, 486 (2008).
 - [20] V. Tadevosyan *et al.*, *Phys. Rev. C* **75**, 055205 (2007).
 - [21] T. Horn *et al.*, *Phys. Rev. C* **78**, 058201 (2008).
 - [22] X. Qian *et al.*, *Phys. Rev. C* **81**, 055209 (2010).
 - [23] H. Avakian *et al.*, *AIP Conf. Proc.* **698**, 612 (2004).
 - [24] J. M. Laget, *Phys. Rev. D* **70**, 054023 (2004).
 - [25] J. M. Laget, *Phys. Lett. B* **489**, 313 (2000).

$K^+ \Lambda$ electroproduction above the resonance region

Background and outline

In the previous chapter, a model was developed for the description of charged-pion electroproduction above the resonance region. This model was dubbed the “VR model” and builds on the framework set up by Kaskulov and Mosel in Ref. [27]. The main component of the VR model is the electromagnetic transition form factor for the proton in the gauge-fixing channel, which accounts for the residual effects of nucleon resonances (or parton effects, equivalently). This form factor is of the dipole form (see Eq. (2.26)) and features a transition cutoff energy that increases asymptotically with increasing virtuality (s or $-u$) of the intermediate proton. The VR model is capable of reproducing the separated and unseparated high-energy $N(\gamma^*, \pi^\pm)N'$ data at $-t \lesssim 0.5 \text{ GeV}^2$.

The resonance-parton effects are essential in the VR model in order to explain the observed trends in the high-energy $N(\gamma^*, \pi^\pm)N'$ data at low $-t$. Since these contributions are manifest through the proton electromagnetic transition form factor, it can be argued that the resonance-parton effects are more ‘universal’ and should also affect other reactions where a virtual photon interacts with an on-shell and an off-shell proton. Following the lines of Chapters 3, 4, and 5, where $p(\gamma, K^+)\Lambda$ played a central or supporting role, the most obvious example of such a reaction is $K^+\Lambda$ electroproduction.

From the ‘universal’ character of the proton electromagnetic transition form factor, it can be inferred that above the resonance region a larger than expected transverse response σ_T could also be observed in $K^+\Lambda$ electroproduction. To this day, there is no high-energy σ_T data available for $p(\gamma^*, K^+)\Lambda$ to test this hypothesis directly. It can only be tested indirectly through the few unseparated $\sigma_U = \sigma_T + \epsilon\sigma_L$ data that are available at the kinematics of interest. With the 12 GeV upgrade at JLab, however, an experiment has been planned which aims at obtaining the L-T-separated structure functions above the resonance region in $K^+\Lambda$ electroproduction [40]. From the available high-energy data for $p(\gamma^*, K^+)\Lambda$, it has already been established that a prototypical Regge model underestimates the observed magnitude of σ_U and that a kaon cutoff energy $\Lambda_{\gamma KK}$ is required

that is significantly larger than the one obtained from elastic eK scattering [41]. Within the VR framework, this discrepancy could be explained by the absence of resonance-parton contributions to the proton electromagnetic transition form factor.

In this chapter, the VR model for $K^+\Lambda$ electroproduction above the resonance region will be developed, following the spirit of the previous chapter, which covered the corresponding charged-pion case. First, an improved background model for $K^+\Lambda$ photoproduction will be constructed which, on its turn, will serve as the basis of the VR framework for the corresponding electroproduction reaction. The resulting model will be compared to the available high-energy $p(\gamma^*, K^+)\Lambda$ data at low $-t$, and predictions will be presented for the upcoming L-T-separation experiment at JLab.

$K^+\Lambda$ electroproduction above the resonance region

Tom Vrancx,^{*} Jan Ryckebusch,[†] and Jannes Nys[‡]
Department of Physics and Astronomy,
Ghent University, Proeftuinstraat 86, B-9000 Gent, Belgium
 (Dated: May 27, 2014)

Background: In π^+n and π^-p electroproduction, conventional models cannot satisfactorily explain the data above the resonance region, in particular the transverse cross section. Although no high-energy L - T -separated cross-section data is available to date, a similar scenario can be inferred for $K^+\Lambda$ electroproduction.

Purpose: Develop a phenomenological model for the $p(\gamma^*, K^+)\Lambda$ reaction at forward angles and high-energies. Propose a universal framework for interpreting charged-kaon and charged-pion electroproduction above the resonance region.

Method: Guided by the recent model for charged-pion electroproduction, developed by the authors, a framework for $K^+\Lambda$ electroproduction at high energies and forward angles is constructed. To this end, a Reggeized background model for $K^+\Lambda$ photoproduction is first developed. This model is used as a starting base to set up an electroproduction framework.

Results: The few available data of the unseparated $p(\gamma^*, K^+)\Lambda$ cross section are well explained by the model. Predictions for the L - T -separation experiment planned with the 12 GeV upgrade at Jefferson Lab are given. The newly-proposed framework predicts an increased magnitude for the transverse structure function, similar to the situation in charged-pion electroproduction.

Conclusions: Within a hadronic framework featuring Reggeized background amplitudes, s -channel resonance-parton effects can explain the observed magnitude of the unseparated $p(\gamma^*, K^+)\Lambda$ cross section at high energies and forward angles. Thereby, no hardening of the kaon electromagnetic form factor is required.

PACS numbers: 13.40.Gp, 13.60.Le, 24.10.-i, 25.30.Rw

I. INTRODUCTION

Above the resonance region, the transverse cross section σ_T measured in charged-pion electroproduction is significantly larger than predicted by regular hadronic models [1]. In Ref. [2], Kaskulov and Mosel proposed a framework explaining this observation. In the Kaskulov-Mosel formalism, the missing transverse strength is provided by the residual effects of nucleon resonances in the gauge-fixing s (or u) channel.

It is argued that such contributions become more important for increasing intermediate-proton and photon virtualities. Indeed, above the resonance region the proton is highly off-shell and the contributions from more massive intermediate states increase in importance. With growing intermediate-proton virtuality, also the hardening of the resonance electromagnetic transition can be anticipated to play an increasingly important role. This results in a dual viewpoint in which the residual effects can be interpreted as originating from the partonic picture of hadrons.

The resonance-parton (R-P) contributions are effectively implemented by means of an electromagnetic (EM) transition form factor for the proton in the s channel. In Ref. [3], a new version of this form factor was proposed which has a simple physical interpretation and respects the correct on-shell limit. The resulting model was dubbed the ‘‘Vrancx-Ryckebusch’’ (VR) model and offers an explanation for the high-energy, forward-angle π^+n and π^-p electroproduction data, thereby covering a wide range of invariant masses ($2 \text{ GeV} \lesssim W \lesssim 4 \text{ GeV}$) and photon virtualities ($0.2 \text{ GeV}^2 \lesssim Q^2 \lesssim 5 \text{ GeV}^2$).

From the observations in the pion case, along with SU(3) symmetry considerations, one may infer that an increased transverse response might also occur in charged-kaon electroproduction. Within the VR framework, this can be anticipated from the employed strategy of introducing an effective EM transition form factor for the proton in the s channel, accounting for the R-P contributions.

To this day, no σ_T data is available for high-energy $K^+\Lambda$ electroproduction and it is to be awaited if its magnitude is larger than expected. In this regard it is worth noting that the measured $p(\gamma^*, K^+)\Lambda$ unseparated cross section σ_U at high energies can be reproduced by the Vanderhaeghen-Guidal-Laget (VGL) model [4–7] after introducing an effective kaon EM form factor. The kaon EM cutoff energy employed in the VGL model is significantly increased compared to the value extracted from elastic eK scattering. This may hint at an anomalously large transverse contribution to the unseparated cross section. After completing the 12 GeV upgrade at Jefferson Lab (JLab), one plans to measure the first $p(\gamma^*, K^+)\Lambda$ separated structure functions σ_L and σ_T at high energies [8].

Following the strategy employed in charged-pion electroproduction [3], the VR model for high-energy forward-angle $K^+\Lambda$ electroproduction will be developed. In Sec. II, the transition currents are discussed. These will be used in Sec. III to construct an improved model for high-energy, forward-angle $K^+\Lambda$ photoproduction. Starting from this photoproduction model, the VR model will be derived in Sec. IV. There, predictions will be presented for the above-mentioned experiment planned at JLab [8]. In Sec. V, the conclusions of this work will be given.

^{*} Tom.Vrancx@UGent.be

[†] Jan.Ryckebusch@UGent.be

[‡] Jannes.Nys@UGent.be

II. TRANSITION CURRENTS

In complete analogy to the pion case [3], the adopted current for the gauged pseudoscalar-kaon exchange in $p(\gamma^*, K^+)\Lambda$ is given by

$$(J_K)_{\lambda_p, \lambda_\Lambda}^\mu(s, t, Q^2) = i g_{K\Lambda p} \bar{u}_{\lambda_\Lambda}(p') \gamma_5 \left(F_{\gamma KK}(Q^2) \mathcal{P}_K(t, s) (2k' - q)^\mu + F_p(Q^2, s) \mathcal{P}'_K(t, s, Q^2) \frac{t - m_K^2}{s - m_p^2} (\not{p} + \not{q} + m_p) \gamma^\mu \right) u_{\lambda_p}(p). \quad (1)$$

Here, p , q , k' , and p' are the four-momenta of the nucleon, of the virtual photon, of the kaon, and of the hyperon in the center-of-mass frame.¹ The Mandelstam variables (s, t, u) are defined in the standard way. The proton and Λ polarizations are denoted by λ_p and λ_Λ , and the strong $K\Lambda p$ coupling constant by $g_{K\Lambda p}$. Note the absence of the $SU(2)$ $\sqrt{2}$ factor in J_K , compared to the pion-exchange current of Ref. [3]. The employed expression for the kaon-Regge propagator $\mathcal{P}_K(t, s)$ reads

$$\mathcal{P}_K(t, s) = -\alpha'_K \varphi(\alpha_K(t)) \Gamma(-\alpha_K(t)) \left(\frac{s}{s_0} \right)^{\alpha_K(t)}. \quad (2)$$

Following the convention of the VGL [4–7] and the Regge-plus-Resonance (RPR) [9–12] models, the “mass scale” s_0 is fixed to $s_0 = 1 \text{ GeV}^2$. In Ref. [3], the convention $s_0 = 1/\alpha'$ is adopted. The model assumptions with regard to the Regge trajectories $\alpha(t)$ and Regge phases $\varphi(\alpha(t))$, will be discussed in Sec. III A. The EM form factors $F_{\gamma KK}(Q^2)$ and $F_p(Q^2, s)$, and the modified kaon-Regge propagator $\mathcal{P}'_K(t, s, Q^2)$ will be discussed in Sec. IV A. At this point, it suffices to note that at vanishing photon virtuality ($Q^2 = 0$) it holds that $F_{\gamma KK}(Q^2 = 0) = F_p(Q^2 = 0, s) = 1$ and $\mathcal{P}'_K(t, s, Q^2 = 0) \equiv \mathcal{P}_K(t, s)$.

The expressions for the vector ($V, J^P = 1^-$) and axial-vector ($A, J^P = 1^+$) transition currents J_{K_V} and J_{K_A} are adopted from Ref. [2] and read

$$(J_{K_V})_{\lambda_p, \lambda_\Lambda}^\mu(s, t, Q^2) = G_{\gamma K_V K} G_{K_V \Lambda p} F_{\gamma K_V K}(Q^2) \mathcal{P}_{K_V}(t, s) \varepsilon^{\mu\nu\sigma\tau} q_\nu k_\sigma \times \bar{u}_{\lambda_\Lambda}(p') \left((1 + \kappa_{K_V \Lambda p}) \gamma_\tau - \frac{\kappa_{K_V \Lambda p}}{2m_p} (p + p')_\tau \right) u_{\lambda_p}(p), \quad (3)$$

and

$$(J_{K_A})_{\lambda_p, \lambda_\Lambda}^\mu(s, t, Q^2) = -i G_{\gamma K_A K} G_{K_A \Lambda p} F_{\gamma K_A K}(Q^2) \mathcal{P}_{K_A}(t, s) (k^\mu q^\nu - q^\sigma k_\sigma g^{\mu\nu}) \times \bar{u}_{\lambda_\Lambda}(p') \left((1 + \kappa_{K_A \Lambda p}) \gamma_\nu - \frac{\kappa_{K_A \Lambda p}}{2m_p} (p + p')_\nu \right) \gamma_5 u_{\lambda_p}(p). \quad (4)$$

Note that the $\sqrt{2}$ factor was dropped again, and that a minus sign missing in Ref. [2], was added to the right-hand side of Eq. (4). The EM coupling constant is represented by $G_{\gamma K_V K}$, and the standard vector and anomalous tensor coupling constants by $G_{K_V \Lambda p}$ and $\kappa_{K_V \Lambda p}$. The vector and axial-vector Regge propagators have the same functional dependence and are given by

$$\mathcal{P}_{K_V A}(t, s) = -\alpha'_{K_V A} \varphi(\alpha_{K_V A}(t) - 1) \Gamma(1 - \alpha_{K_V A}(t)) \left(\frac{s}{s_0} \right)^{\alpha_{K_V A}(t) - 1}. \quad (5)$$

The EM transition form factors $F_{\gamma K_V A K}(Q^2)$ will be discussed in Sec. IV A. As for the form factors $F_{\gamma KK}(Q^2)$ and $F_p(Q^2, s)$ in Eq. (1), it holds that $F_{\gamma K_V A K}(0) = 1$.

III. HIGH-ENERGY $K^+\Lambda$ PHOTOPRODUCTION

A. A third Regge trajectory

In the kaon sector, the two most important Regge trajectories are the $K(494)$ (pseudoscalar) and $K^*(892)$ (vector) trajectories [13]. These can be parametrized as [9]

$$\alpha_K(t) = \alpha'_K (t - m_K^2), \quad (6)$$

$$\alpha_{K^*}(t) = 1 + \alpha'_{K^*} (t - m_{K^*}^2), \quad (7)$$

with $\alpha'_K = 0.70 \text{ GeV}^{-2}$ and $\alpha'_{K^*} = 0.85 \text{ GeV}^{-2}$. Both the VGL and the RPR model feature these two trajectories and have established that they are essential for the description of $K^+\Lambda$ photo- and electroproduction.

In Refs. [11, 12], the Regge background for the $p(\gamma, K^+)\Lambda$ reaction was determined from the recent differential cross section and recoil polarization data by the CEBAF Large Acceptance Spectrometer (CLAS) Collaboration [16].² More specifically, a Bayesian analysis was performed for the high-energy ($W > 2.6 \text{ GeV}$) and forward-angle ($\cos \theta_K^* > 0.35$) part of these CLAS data (262 data points) to determine the Regge model variant with the highest evidence. Here, $W = \sqrt{s}$ is the invariant mass and θ_K^* the kaon scattering angle in the center-of-mass frame. It was found that the best model, dubbed “Regge-2011”, features rotating phases for both the K and K^* trajectories. For this model, a $\chi^2_{\text{NDF}} = 3.15$ is obtained for the description of the high-energy and forward-angle $p(\gamma, K^+)\Lambda$ CLAS data [11, 12]. As there is definitely room for improvement, the possibility is exploited of introducing a third Regge trajectory contributing to the $p(\gamma^*, K^+)\Lambda$ reaction. In this regard, two candidates are considered: the $K_1(1400)$ (axial-vector) and the $K^*(1410)$ (vector) trajectory [13]. These are parametrized as [14, 15]

$$\alpha_{K_1(1400)}(t) = 1 + \alpha'_{K_1(1400)} (t - m_{K_1(1400)}^2), \quad (8)$$

¹ In Ref. [3], these four-momenta are also defined in the center-of-mass frame and not in the laboratory frame, as mentioned.

² In Table IV of Ref. [12], an overview is given of the available $p(\gamma, K^+)\Lambda$ data.

TABLE I. Coupling constants and corresponding χ^2_{NDF} values of the three-trajectory Regge model variants featuring a K , a K^* and a $K_1(1400)$ trajectory. Results are listed for a rotating K trajectory and all phase combinations for the K^* and K_1 . For the sake of reference also the results of the two-trajectory Regge-2011 model are shown. The models were optimized against the high energy ($W > 2.6$ GeV) and forward-angle ($\cos \theta_K^* > 0.35$) CLAS data for the $p(\gamma, K^+) \Lambda$ differential cross section and recoil polarization (262 data points) [16].

Model	$\{\varphi_K, \varphi_{K^*}, \varphi_{K_1(1400)}\}$	$g_{K\Lambda p}$	$G_{\gamma K^* K} G_{K^* \Lambda p}$ (GeV $^{-1}$)	$\kappa_{K^* \Lambda p}$	$G_{\gamma K_1(1400) K} G_{K_1(1400) \Lambda p}$ (GeV $^{-1}$)	$\kappa_{K_1(1400) \Lambda p}$	χ^2_{NDF}
Ia	{R, C, C}	-12.2	-0.29	50	32.3	-1.35	17.1
IIa	{R, R, C}	-13.2	-9.84	1.51	16.5	-0.86	2.58
IIIa	{R, C, R}	-10.8	-0.44	50	28.0	-1.74	13.6
IVa	{R, R, R}	-12.6	-10.5	1.38	7.48	-0.19	2.99
Regge-2011	{R, R, -}	-12.9	-10.8	1.77	-	-	3.15

 TABLE II. As in Table I, but for the model based on a third $K^*(1410)$ trajectory instead of a $K_1(1400)$ trajectory.

Model	$\{\varphi_K, \varphi_{K^*}, \varphi_{K^*(1410)}\}$	$g_{K\Lambda p}$	$G_{\gamma K^* K} G_{K^* \Lambda p}$ (GeV $^{-1}$)	$\kappa_{K^* \Lambda p}$	$G_{\gamma K^*(1410) K} G_{K^*(1410) \Lambda p}$ (GeV $^{-1}$)	$\kappa_{K^*(1410) \Lambda p}$	χ^2_{NDF}
Ib	{R, C, C}	-13.2	-0.01	0.03	41.6	-0.53	6.33
IIb	{R, R, C}	-13.2	-6.79	1.04	32.7	0.70	1.06
IIIb	{R, C, R}	-12.4	-0.23	50	49.3	-0.46	4.91
IVb	{R, R, R}	-14.2	-19.4	0.68	-54.4	-0.55	2.04
Regge-2011	{R, R, -}	-12.9	-10.8	1.77	-	-	3.15

$$\alpha_{K^*(1410)}(t) = 1 + \alpha'_{K^*(1410)}(t - m_{K^*(1410)}^2), \quad (9)$$

with $\alpha'_{K_1(1400)} = 0.75$ GeV $^{-2}$ and $\alpha'_{K^*(1410)} = 0.83$ GeV $^{-2}$. All the trajectories considered here are degenerate. This means that the corresponding Regge phases can either be constant (C) or be rotating (R):

$$\varphi(\alpha(t)) = \begin{cases} 1 & C, \\ e^{-i\pi\alpha(t)} & R. \end{cases} \quad (10)$$

B. Parameter constraints

Since the phases of the Regge trajectories considered here can be either constant or rotating, there are 8 possible variants for each three-trajectory model. These models, however, are all restricted to some extent as the K and K^* coupling constants must meet certain constraints, based on symmetry arguments. The strong coupling $g_{K\Lambda p}$ can be inferred from the strong pion-nucleon coupling $g_{\pi NN}$ by means of SU(3) symmetry:

$$g_{K\Lambda p} = -\frac{1}{\sqrt{3}}(3 - 2\alpha_D)g_{\pi NN}, \quad (11)$$

with $\alpha_D = 0.644$ the experimentally determined SU(3) symmetric coupling fraction. By allowing a 20% breaking of SU(3) symmetry and taking into account the uncertainty on the pion-nucleon coupling, i.e. $g_{\pi NN} \approx 13.0$ – 13.5 [3], the following limits on $g_{K\Lambda p}$ emerge:

$$-16.0 \leq g_{K\Lambda p} \leq -10.3. \quad (12)$$

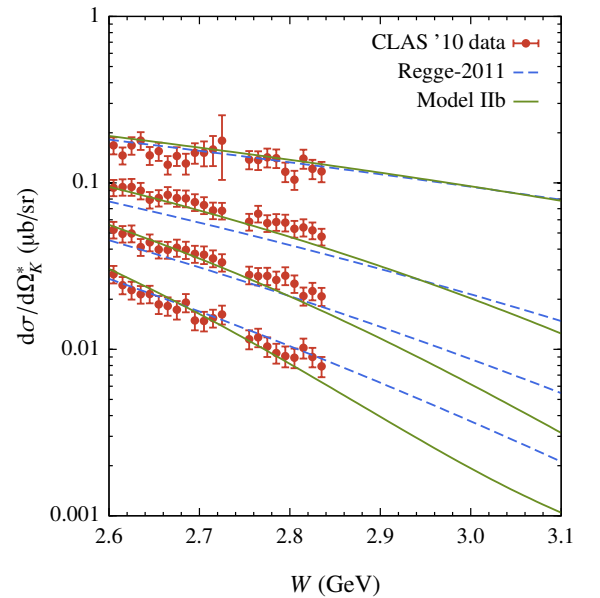
The EM coupling constant $G_{\gamma K^* K}$ can be estimated from the decay width of $K^* \rightarrow K\gamma$ [4]:

$$\Gamma_{K^* \rightarrow K\gamma} = \frac{\alpha_e G_{\gamma K^* K}^2}{24 m_{K^*}^3} (m_{K^*}^2 - m_K^2)^3, \quad (13)$$

with α_e the fine-structure constant. From the experimentally determined value $\Gamma_{K^* \rightarrow K\gamma} = 50 \pm 5$ keV [13] one obtains

$$G_{\gamma K^* K} = 0.834 \pm 0.042 \text{ GeV}^{-1}. \quad (14)$$

Also the strong vector and tensor couplings $G_{K^* \Lambda p}$ and $\kappa_{K^* \Lambda p}$ can be related to $G_{\rho NN}$ and $\kappa_{\rho NN}$ through SU(3) symmetry. However, following the arguments given in Ref. [4], only the


 FIG. 1. (Color online) The W dependence of the $p(\gamma, K^+) \Lambda$ unpolarized differential cross section for (from bottom to top) $\cos \theta_K^* = 0.50, 0.60, 0.70, 0.86$ – 0.87 . Predictions from the Regge-2011 model and model IIB are shown. The data are from Ref. [16].

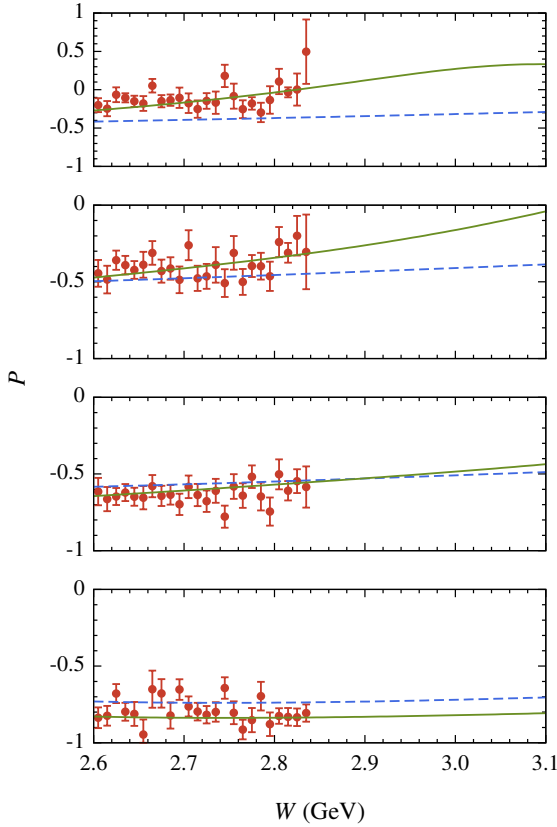


FIG. 2. (Color online) The W dependence of the $p(\gamma, K^+)\Lambda$ recoil polarization P for (from bottom to top) $\cos\theta_K^* = 0.50, 0.60, 0.70, 0.86\text{--}0.87$. Predictions from the Regge-2011 model and model IIb are shown. Curve notations of Fig. 1 are used. The data are from Ref. [16].

predicted signs for the vector and tensor couplings will be respected:

$$G_{K^*\Lambda p} < 0, \quad \kappa_{K^*\Lambda p} > 0. \quad (15)$$

Due to the lack of relevant experimental information, no constraints are imposed on the $K_1(1400)$ and $K^*(1410)$ coupling constants.

C. Results

Tables I and II list the best-fit parameters of the three-trajectory model variants. The coupling constants are optimized against the high-energy and forward-angle CLAS data and respect the constraints of Eqs. (12) and (15). Only the models featuring a rotating K trajectory are listed, as those with a constant K trajectory are not compatible with the data. Indeed, a constant phase for the K trajectory leads to $\chi_{\text{NDF}}^2 = 32.5\text{--}35.2$ for the $K_1(1400)$ model variants, and to $\chi_{\text{NDF}}^2 = 17.2\text{--}34.1$ for the $K^*(1410)$ model variants.

The models with a rotating K and constant K^* phase are systematically in poorest agreement with the data. In fact, these models yield coupling constants approaching the maximum values allowed during the optimization process: models Ia, IIIa, and IIIb yield $\kappa_{K^*\Lambda p} = 50$, and model Ib yields $G_{\gamma K^* K} G_{K^*\Lambda p} = -0.01 \text{ GeV}^{-1}$. This implies that the analyzed CLAS data exclude a constant K^* phase given the constraints of Eq. (15).

Amongst the models with a rotating K^* phase, those with a $K^*(1410)$ (vector) trajectory perform better than those with an $K_1(1400)$ (axial-vector) trajectory. Model IIb clearly stands out from the rest and is in excellent agreement with the data ($\chi_{\text{NDF}}^2 = 1.06$). This model features a constant $K^*(1410)$ and rotating K and K^* trajectories. Note that the value $g_{K\Lambda p} = -13.2$ for this model coincides with the predicted SU(3) value, given the uncertainty on $g_{\pi NN}$. This is also the case for the Regge-2011 model. The employed CLAS data, along with the corresponding predictions of the Regge-2011 model and model IIb, are shown in Figs. 1 and 2 for four $\cos\theta_K^*$ bins. Model IIb constitutes the basis for the VR model, which will be discussed in the forthcoming section.

IV. HIGH-ENERGY $K^+\Lambda$ ELECTROPRODUCTION

A. Form factors

As the $Q^2 = 0$ limit of the proposed $p(\gamma^*, K^+)\Lambda$ model has been established, the Q^2 -dependent quantities in the transition

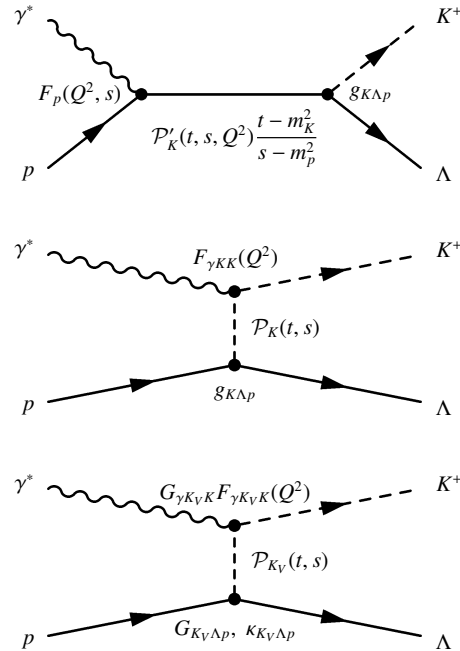


FIG. 3. The gauge-fixing s -channel diagram and the Reggeized pseudoscalar and vector t -channel diagrams that constitute the VR model for $K^+\Lambda$ electroproduction above the resonance region.

current operators of Eqs. (1) and (3) can now be examined. Pursuing the analogy to the VR model for pion electroproduction, an antishrinkage effect is introduced in the s -channel gauge-fixing term of the kaon transition current (1). To this end, the Regge propagator $\mathcal{P}'_K(t, s, Q^2)$ in Eq. (1) is defined as in Eq. (2), but with an altered Regge slope:

$$\alpha'_K \rightarrow \alpha'_K(Q^2, s) = \frac{\alpha'_K}{1 + a \frac{Q^2}{s}}. \quad (16)$$

Here, a is the corresponding dimensionless slope parameter, which has yet to be determined. Figure 3 depicts the s - and t -channel diagrams which constitute the VR model for $p(\gamma^*, K^+)\Lambda$.

A monopole form is adopted for the elastic kaon EM form factor $F_{\gamma KK}(Q^2)$ in of Eq. (1) with a kaon cutoff energy $\Lambda_{\gamma KK}$:

$$F_{\gamma KK}(Q^2) = \left(1 + \frac{Q^2}{\Lambda_{\gamma KK}^2}\right)^{-1}. \quad (17)$$

As the root-mean-square charge radius of the K is experimentally determined as [13]

$$\sqrt{\langle r_K^2 \rangle} = 0.560 \pm 0.031 \text{ fm}, \quad (18)$$

the corresponding monopole cutoff energy is

$$\Lambda_{\gamma KK} = \sqrt{\frac{6}{\langle r_K^2 \rangle}} = 863 \pm 48 \text{ MeV}. \quad (19)$$

In the vector-meson dominance (VMD) model, the kaon EM form factor receives contributions from primarily the ρ , ω , and ϕ mesons [17]:

$$F_{\gamma KK}^{\text{VMD}}(Q^2) = \frac{1}{N} \sum_{v=\rho,\omega,\phi} \frac{g_{vKK}}{f_v} \frac{1}{1 + Q^2/m_v^2}, \quad (20)$$

with $N = \sum_{v=\rho,\omega,\phi} \frac{g_{vKK}}{f_v}$ a normalization constant. Assuming an exact SU(3) flavor symmetry, the EM and strong ω and ϕ coupling constants can be related to those of the ρ :

$$\begin{aligned} f_\omega &= 3f_\rho, & g_{\omega KK} &= g_{\rho KK}, \\ f_\phi &= -\frac{3}{\sqrt{2}}f_\rho, & g_{\phi KK} &= -\sqrt{2}g_{\rho KK}. \end{aligned} \quad (21)$$

From these SU(3) coefficients and the masses of the ρ , ω , and ϕ mesons [13], the VMD monopole cutoff energy for the K is calculated as

$$\Lambda_{\gamma KK}^{\text{VMD}} = \left(-\frac{dF_{\gamma KK}^{\text{VMD}}(Q^2)}{dQ^2} \Big|_{Q^2=0} \right)^{-1/2} \simeq 838 \text{ MeV}, \quad (22)$$

which is consistent with the experimental value of Eq. (19).

The form factors $F_{\gamma K_V K}(Q^2)$ in Eq. (3) describe the EM transitions of the vector-kaon trajectories to the outgoing pseudoscalar kaon. For these form factors a monopole form (17) is also adopted. No data is available for the cutoff energies $\Lambda_{\gamma K^* K}$ and $\Lambda_{\gamma K^*(1410) K}$, however, so one has to rely on

the corresponding VMD predictions. The VMD description requires the following replacement in expression (20):

$$g_{vKK} \rightarrow G_{vK_V K}. \quad (23)$$

As the K_V are nothing but orbitally excited states of the K , the same SU(3) constraints (21) apply to the strong coupling constants $G_{vK_V K}$:

$$\begin{aligned} G_{\omega K_V K} &= G_{\rho K_V K}, \\ G_{\phi K_V K} &= -\sqrt{2}G_{\rho K_V K}. \end{aligned} \quad (24)$$

Therefore, the K^* and $K^*(1410)$ EM transition form factors in the VMD model are identical and equal to $F_{\gamma KK}^{\text{VMD}}(Q^2)$. Consequently, the value of Eq. (22) will be used for the corresponding cutoff energies:

$$\Lambda_{\gamma K_V K} = 838 \text{ MeV}. \quad (25)$$

Note that the above reasoning also applies to axial-vector kaons.

The form factor $F_p(Q^2, s)$ in Eq. (1) describes the EM transition of an on-shell to an off-shell proton with squared four-momentum s , induced by a virtual photon. In the VR model for pion electroproduction, $F_p(Q^2, s)$ is a dipole [3]:

$$F_p(Q^2, s) = \left(1 + \frac{Q^2}{\Lambda_{\gamma pp^*}^2(s)}\right)^{-2}, \quad (26)$$

with an s -dependent cutoff energy ($s \geq m_p^2$)

$$\Lambda_{\gamma pp^*}(s) = \Lambda_{\gamma pp} + (\Lambda_\infty - \Lambda_{\gamma pp}) \left(1 - \frac{m_p^2}{s}\right). \quad (27)$$

Here, $\Lambda_{\gamma pp} = 840 \text{ MeV}$ is the on-shell proton EM cutoff energy. The asymptotic, off-shell proton cutoff energy was determined as $\Lambda_\infty = 2194 \text{ MeV}$ [3].

B. Results

The value of a in Eq. (16) is the only parameter left in the VR model and is fitted to the scarce high-energy, forward-angle $p(\gamma^*, K^+)\Lambda$ data. In order to tune the VR model for pion electroproduction, data with $-t \lesssim 0.5 \text{ GeV}^2$ was used [3]. As few $p(\gamma^*, K^+)\Lambda$ data are available that cover the high-energy region, this range will be extended to $-t < 1 \text{ GeV}^2$. For the same reason the minimum W value will be decreased from 2.6 GeV (Sec. III) to 2.5 GeV. There are 25 published data points that meet these kinematic restrictions: 9 data points measured at Cornell in the seventies [18–20] and 16 recent data points from CLAS [21]. Most of the $p(\gamma^*, K^+)\Lambda$ data are available at $W < 2.5 \text{ GeV}$, recent examples of which can be found in Refs. [22–26]. For the 25 high-energy and forward-angle data points, the optimum value for the slope parameter is found to be

$$a = 2.43. \quad (28)$$

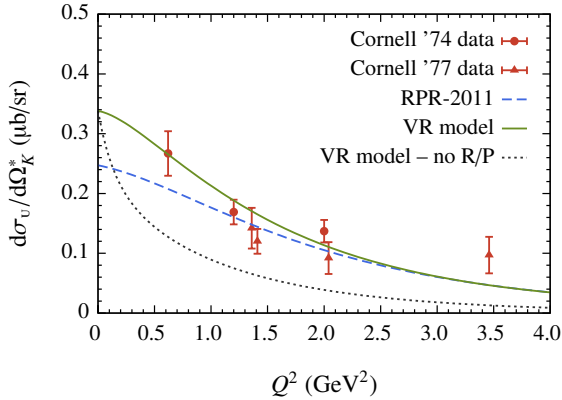


FIG. 4. (Color online) The Q^2 dependence of the $p(\gamma^*, K^+)\Lambda$ unseparated cross section $d\sigma_v/d\Omega_K^*$. Predictions from the RPR model, the VR model, and the VR model without R-P contributions ($\Lambda_\infty = \Lambda_{\gamma pp}$ and $a = 0$) are shown for $W = 2.70$ GeV, $\cos\theta_K^* = 0.98$, and $\varepsilon = 0.86$, which are the averaged kinematics for the different datasets [18, 19].

Remarkably, this value coincides with the one obtained in the pion case [3]. With $\chi_{\text{NDF}}^2 = 2.93$, the resulting VR model provides a fair description of the considered $p(\gamma^*, K^+)\Lambda$ data. A word of caution is in order, given the scarcity of the data and the fact that they cover a rather limited W range.

Figures 4 and 5 show 23 of the 25 employed data points, along with the corresponding predictions of the VR and RPR-2011 models. The RPR-2011 model is a prototypical example of a single-channel model, designed to describe the $p(\gamma^*, K^+)\Lambda$ reaction both in and beyond the resonance region [11, 12]. It yields $\chi_{\text{NDF}}^2 = 3.58$ for the high-energy $p(\gamma^*, K^+)\Lambda$ data considered. In addition to the t -channel Regge-2011 background discussed in Sec. III A, RPR-2011 features the exchange of the nucleon resonances $S_{11}(1535)$, $S_{11}(1650)$, $F_{15}(1680)$, $P_{13}(1720)$, $D_{13}(1900)$, $P_{13}(1900)$, $P_{11}(1900)$, and $F_{15}(2000)$, in the s channel. For $W \gtrsim 2$ GeV, the effects of these resonances is rather modest.

The VR model is in good agreement with the 19 σ_v data points. For $Q^2 \lesssim 2$ GeV², the VR model predicts larger σ_v cross sections than Regge-2011. Both models predict a similar σ_v for $3 \lesssim Q^2 \lesssim 4$ GeV², but have different $Q^2 \rightarrow \infty$ limits. Fig. 5 contains the available data for the separated cross sections at $W > 2.5$ GeV. The biggest difference between the VR and RPR-2011 models is observed for the σ_{tr} and σ_{tr^*} . The largest deviations between theory and data are found for the σ_{tr} and σ_{tr^*} . The quantity and quality of the data, however, does not allow one to draw any definite conclusions.

From Figs. 4 and 5, one can easily see that in the VR model the anomalously large σ_v can be attributed to the R-P effects. An appealing feature of this approach is that $F_p(Q^2, s)$ can account for both the pion [3] and the kaon data at high energies and forward angles. It is worth mentioning that the RPR-2011 model does not adopt a proton EM transition form factor, i.e. $F_p^{\text{RPR}}(Q^2, s) = 1$. As a competing explanation for the observed trends in the Q^2 evolution of the data, a hard form factor is in-

roduced at the K and K^* EM vertices of the RPR-2011 model:

$$\Lambda_{\gamma KK}^{\text{RPR}} = \Lambda_{\gamma K^* K}^{\text{RPR}} = 1.3 \text{ GeV}. \quad (29)$$

For the K , this is a considerably larger cutoff energy than the measured value of Eq. (19) and considerably increases the longitudinal and transverse responses of the computed $p(\gamma^*, K^+)\Lambda$ cross sections. In a similar vein, the VGL model adopts [6]

$$\Lambda_{\gamma KK}^{\text{VGL}} = \Lambda_{\gamma K^* K}^{\text{VGL}} \simeq 1.2 \text{ GeV}. \quad (30)$$

Guidal *et al.* argue that for the K this could be attributed to the fact that the pole in the kaon propagator $(t - m_K^2)^{-1}$ is

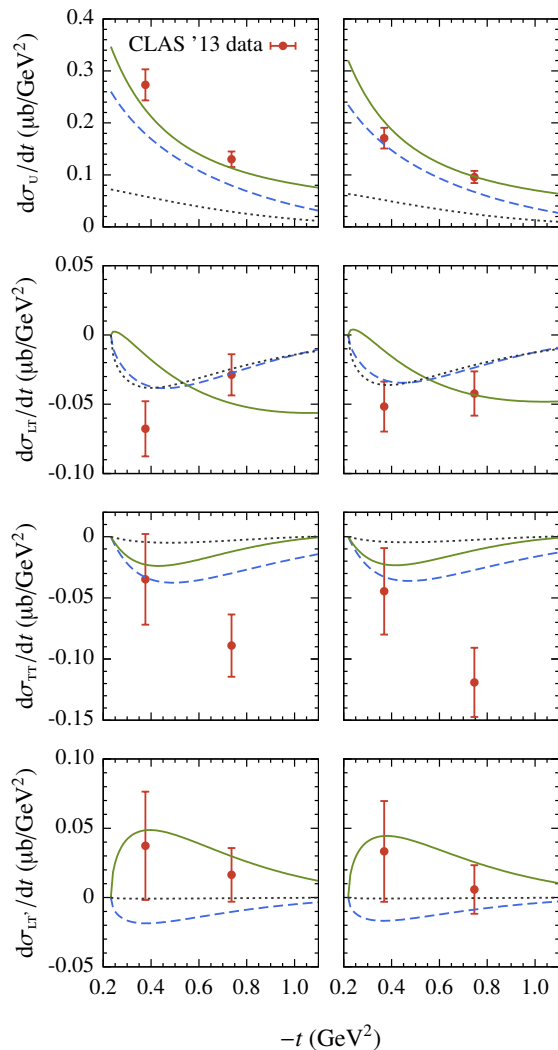


FIG. 5. (Color online) The $-t$ dependence of the $p(\gamma^*, K^+)\Lambda$ unseparated cross section $d\sigma_v/dt$ and the separated cross sections $d\sigma_{\text{tr}}/dt$, $d\sigma_{\text{tr}^*}/dt$, and $d\sigma_{\text{tr}^*}/dt$ at $E_e = 5.499$ GeV and $Q^2 = 1.80$ GeV² for $W = 2.525$ GeV (left) and $W = 2.575$ GeV (right). Curve notations of Fig. 4 are used. The data are from Ref. [21].

further from the physical region, compared to the pion case $(t - m_\pi^2)^{-1}$. Hence, the high $\Lambda_{\gamma KK}$ value would be representative for the whole kaon-Regge trajectory, rather than for the physical kaon.

Figures 6 and 7 show the VR and RPR-2011 predictions for the $p(\gamma^*, K^+)\Lambda$ L-T-separation experiment planned for the 12 GeV upgrade at JLab [8]. From both figures it is clear that the VR model predicts both substantially smaller longitudinal and larger transverse cross sections than the RPR-2011 model. For the σ_L this can be mainly attributed to the adopted values of $\Lambda_{\gamma KK}$ and to a smaller extent of $\Lambda_{\gamma K^*K}$. In particular at small $-t$, where t -channel K exchange is dominant, the magnitude of σ_L is very sensitive to the value of $\Lambda_{\gamma KK}$. On the

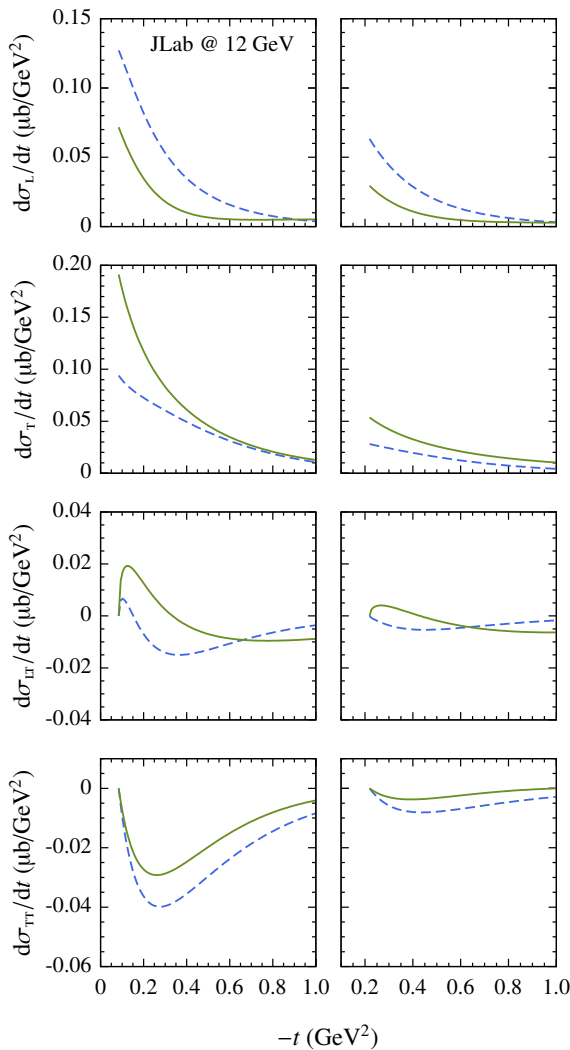


FIG. 6. (Color online) The $-t$ dependence of the separated $p(\gamma^*, K^+)\Lambda$ cross sections $d\sigma_L/dt$, $d\sigma_T/dt$, $d\sigma_{TT}/dt$, and $d\sigma_{LT}/dt$ at $t = t_{\min}$ for $x_B = 0.25$ (left) and $x_B = 0.40$ (right), with x_B being the Bjorken scaling variable. For the shown Q^2 ranges, one has $2.45 \text{ GeV} \lesssim W \lesssim 3.46 \text{ GeV}$ and $0.21 \text{ GeV}^2 \lesssim -t \lesssim 0.25 \text{ GeV}^2$ for $x_B = 0.25$, and $2.32 \text{ GeV} \lesssim W \lesssim 3.14 \text{ GeV}$ and $0.50 \text{ GeV}^2 \lesssim -t \lesssim 0.53 \text{ GeV}^2$ for $x_B = 0.40$. Curve notations of Fig. 4 are used. These are predictions for the planned $p(\gamma^*, K^+)\Lambda$ L-T-separation experiment [8].

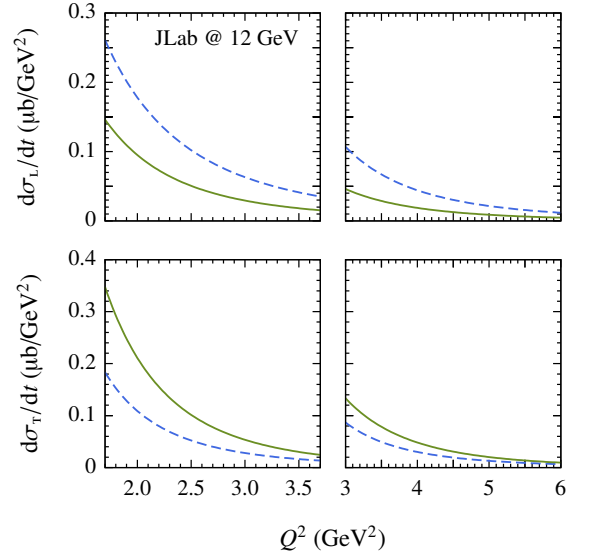


FIG. 7. (Color online) The Q^2 dependence of the separated $p(\gamma^*, K^+)\Lambda$ cross sections $d\sigma_L/dt$, $d\sigma_T/dt$, $d\sigma_{TT}/dt$, and $d\sigma_{LT}/dt$ at $t = t_{\min}$ for $x_B = 0.25$ (left) and $x_B = 0.40$ (right), with x_B being the Bjorken scaling variable. For the shown Q^2 ranges, one has $2.45 \text{ GeV} \lesssim W \lesssim 3.46 \text{ GeV}$ and $0.21 \text{ GeV}^2 \lesssim -t \lesssim 0.25 \text{ GeV}^2$ for $x_B = 0.25$, and $2.32 \text{ GeV} \lesssim W \lesssim 3.14 \text{ GeV}$ and $0.50 \text{ GeV}^2 \lesssim -t \lesssim 0.53 \text{ GeV}^2$ for $x_B = 0.40$. Curve notations of Fig. 4 are used. These are predictions for the planned $p(\gamma^*, K^+)\Lambda$ L-T-separation experiment of Ref. [8].

other hand, the larger transverse response in the VR model can be attributed to the R-P contributions in the gauge-fixing s channel. This is a key element of the VR framework and is not present in the RPR-2011 and the VGL model.

In π^+n electroproduction, hadronic models like the VGL model cannot account for the anomalously large σ_T above the resonance region [1]. A similar scenario is expected in high-energy $K^+\Lambda$ electroproduction. Indeed, when adopting the experimental value of Eq. (19) for $\Lambda_{\gamma KK}$, the VGL model, for example, significantly underpredicts the unseparated Cornell data shown in Fig. 4. Also the VR model without R-P effects substantially underpredicts these data (Figs. 4 and 5). Given that $\sigma_U = \sigma_T + \epsilon\sigma_L$ and that $\Lambda_{\gamma KK}$ predominantly influences σ_L at forward scattering, the much larger kaon cutoff energy required by the VGL model might actually be a compensation for an increased transverse response which remains unrevealed in σ_U . In this respect, the VR framework constitutes a promising approach as it inherently accounts for a larger σ_T and already successfully explains the separated structure functions, measured in high-energy pion electroproduction [3].

The JLab L-T-separation experiment for high-energy $K^+\Lambda$ electroproduction is expected to settle the magnitude of the σ_T response. In addition, the measurement of σ_L at small $-t$ will provide access to the value of $\Lambda_{\gamma KK}$ in off-shell circumstances. Another experiment is planned with the 12 GeV upgrade at JLab. The CLAS Collaboration intends to obtain the interference structure functions σ_{LT} , σ_{TT} , and $\sigma_{LT'}$ for Q^2 and

W values up to 12 GeV² and 3 GeV [27]. These data will also constitute an important test bed for the VR model as the proposed kinematics cover the trans-resonance region.

V. CONCLUSION AND OUTLOOK

Building on the VR model for charged-pion electroproduction, the VR model for the $p(\gamma^*, K^+)\Lambda$ reaction above the resonance region and forward angles ($-t < 1$ GeV²) was introduced. This model uses a three-trajectory Regge model for the photoproduction reaction as a starting base. The model features one pseudoscalar- and two vector-kaon Regge trajectories in the t channel. It provides an excellent description of the high-energy ($W > 2.6$ GeV), forward-angle ($\cos\theta_K^* > 0.35$) cross section and recoil polarization $p(\gamma, K^+)\Lambda$ data from the CLAS Collaboration. Turning to finite photon virtualities, a key feature of the VR model for $p(\gamma^*, K^+)\Lambda$ is to introduce a proton EM transition form factor, accounting for the contributions of resonances-partons connected to the highly off-shell proton in the gauge-fixing s -channel. The same proton transition form factor is assumed in both π^+n and $K^+\Lambda$ electroproduction. The magnitude of the antishrinkage effect in the s -channel is the sole parameter of the VR model and was optimized against the scarce $p(\gamma^*, K^+)\Lambda$ data. Remarkably, its optimized value coincides with the one obtained in pion electroproduction, for which far more data is available.

After introducing the R-P contributions, a good theory-experiment agreement is achieved for the 19 unseparated $p(\gamma^*, K^+)\Lambda$ cross-section data σ_U for $W > 2.5$ GeV and $-t \lesssim 1$ GeV². To date, only six data points are available for the interference structure functions. Due to limited statistics, the situation is rather inconclusive for those. An alternate explanation of the anomalous magnitude of the measured σ_U is that the kaon electromagnetic form factor in t -channel $p(\gamma^*, K^+)\Lambda$ is substantially harder than in elastic eK scattering.

Predictions are provided for the upcoming L-T-separation experiment at JLab. This experiment will provide the first data for the $p(\gamma^*, K^+)\Lambda$ longitudinal and transverse responses above the resonance region. It is expected that the forward-scattering σ_L data will map the kaon electromagnetic form factor in $K^+\Lambda$ electroproduction. The σ_T data, on the other hand, will reveal the importance of additional model features, like the role of resonance-parton effects. In high-energy pion electroproduction these provide a natural explanation for the observed magnitude of the transverse response. It is to be awaited whether or not this is the case in kaon electroproduction.

ACKNOWLEDGMENTS

This work is supported by the Research Council of Ghent University and the Flemish Research Foundation (FWO Vlaanderen). The authors would like to thank Daniel Carman and Viktor Mokeev for providing the recent $K^+\Lambda$ electroproduction data from the CLAS Collaboration and for useful

discussions.

Appendix: Observables

1. Photoproduction

The laboratory frame coordinate system is defined as

$$\mathbf{z} = \frac{\mathbf{q}}{|\mathbf{q}|}, \quad \mathbf{y} = \frac{\mathbf{q} \times \mathbf{k}'}{|\mathbf{q} \times \mathbf{k}'|}, \quad \mathbf{x} = \mathbf{y} \times \mathbf{z}, \quad (\text{A.1})$$

where \mathbf{q} and \mathbf{k}' are the three-momenta of the photon and outgoing kaon. The hadronic matrix elements $M_{\lambda_p, \lambda_\Lambda}^\lambda$ are defined as

$$M_{\lambda_p, \lambda_\Lambda}^\lambda = \epsilon_\mu^\lambda J_{\lambda_p, \lambda_\Lambda}^\mu, \quad (\text{A.2})$$

with $J_{\lambda_p, \lambda_\Lambda}^\mu$ being the transition current of the $p(\gamma^{(*)}, K^+)\Lambda$ reaction and ϵ_μ^λ the covariant polarization four-vector of the $\gamma^{(*)}$. For the observables covered in this work, it suffices to consider circularly polarized photons:

$$\epsilon_\mu^\pm = \frac{1}{\sqrt{2}}(0, \pm 1, i, 0). \quad (\text{A.3})$$

The unpolarized $p(\gamma, K^+)\Lambda$ differential cross section is calculated as

$$\frac{d\sigma}{d\Omega_K^*} = \frac{\alpha_e m_p m_\Lambda |\mathbf{k}^*|}{16\pi W (s - m_p^2)} \sum_{\lambda, \lambda_p, \lambda_\Lambda} |M_{\lambda_p, \lambda_\Lambda}^\lambda|^2, \quad (\text{A.4})$$

where

$$|\mathbf{k}^*| = \sqrt{\frac{(s + m_K^2 - m_\Lambda^2)^2}{4s} - m_K^2}, \quad (\text{A.5})$$

is the size of the three-momentum of the outgoing kaon in the center-of-mass frame. In terms of the hadronic matrix elements, the recoil polarization P reads

$$P = \frac{\sum_{\lambda, \lambda_p} (|M_{\lambda_p, \lambda_\Lambda}^{\lambda=+y}|^2 - |M_{\lambda_p, \lambda_\Lambda}^{\lambda=-y}|^2)}{\sum_{\lambda, \lambda_p, \lambda_\Lambda} |M_{\lambda_p, \lambda_\Lambda}^\lambda|^2}. \quad (\text{A.6})$$

2. Electroproduction

In electroproduction, the photon is virtual and a longitudinal polarization is allowed:

$$\epsilon_\mu^0 = \frac{1}{\sqrt{Q^2}}(\sqrt{v^2 + Q^2}, 0, 0, -v), \quad (\text{A.7})$$

with $v = E_e - E_{e'}$ being the energy difference between the initial and final electrons, e and e' . The unseparated differential cross section reads

$$\frac{d\sigma_U}{dt} = \frac{d\sigma_T}{dt} + \varepsilon \frac{d\sigma_L}{dt}, \quad (\text{A.8})$$

with ε given by

$$\varepsilon = \frac{4E_e E_{e'} - Q^2}{2(E_e^2 + E_{e'}^2) + Q^2}. \quad (\text{A.9})$$

The longitudinal and transverse structure functions are calculated as

$$\begin{aligned} \frac{d\sigma_L}{dt} &= 2\eta H_{0,0}, \\ \frac{d\sigma_T}{dt} &= \eta(H_{+,+} + H_{-,-}), \end{aligned} \quad (\text{A.10})$$

where

$$H_{\lambda,\lambda'} = \sum_{\lambda_p, \lambda_\Lambda} M_{\lambda_p, \lambda_\Lambda}^\lambda (M_{\lambda_p, \lambda_\Lambda}^{\lambda'})^*. \quad (\text{A.11})$$

The normalization factor η reads

$$\eta = \frac{\alpha_e m_p m_\Lambda}{4W(s - m_p^2) |q^*|}, \quad (\text{A.12})$$

with

$$|q^*| = \sqrt{\frac{(m_p^2 - s + Q^2)^2}{4s} + Q^2}, \quad (\text{A.13})$$

being the size of the photon's three-momentum in the center-of-mass frame. The interference structure functions for the longitudinal and transverse components of the virtual photon polarization can be expressed as

$$\begin{aligned} \frac{d\sigma_{LT}}{dt} &= -\eta(H_{+,0} + H_{0,+} - H_{0,-} - H_{-,0}), \\ \frac{d\sigma_{TT}}{dt} &= -\eta(H_{+,-} + H_{-,+}), \\ \frac{d\sigma_{LT'}}{dt} &= -\eta(H_{+,0} - H_{0,+} + H_{0,-} - H_{-,0}). \end{aligned} \quad (\text{A.14})$$

Finally, the transformation from dt to $d\Omega_K^*$ can be accomplished by employing the relation

$$\frac{d\Omega_K^*}{dt} = \frac{\pi}{|q^*| |k'^*|}. \quad (\text{A.15})$$

Note that, strictly speaking, the differential “ dt ” in Eqs. (A.8), (A.10), (A.14) and (A.15) should read “ $-dt$ ”. It is a conventional, however, to write “ dt ” in the expressions for the differential cross sections.

-
- [1] H. P. Blok *et al.*, *Phys. Rev. C* **78**, 045202 (2008).
[2] M. M. Kaskulov and U. Mosel, *Phys. Rev. C* **81**, 045202 (2010).
[3] T. Vranx and J. Ryckebusch, *Phys. Rev. C* **89**, 025203 (2014).
[4] M. Guidal, J. M. Laget, and M. Vanderhaeghen, *Nucl. Phys. A* **627**, 645 (1997).
[5] M. Vanderhaeghen, M. Guidal, and J. M. Laget, *Phys. Rev. C* **57**, 1454 (1998).
[6] M. Guidal, J. M. Laget, and M. Vanderhaeghen, *Phys. Rev. C* **61**, 025204 (2000).
[7] M. Guidal, J. M. Laget, and M. Vanderhaeghen, *Phys. Rev. C* **68**, 058201 (2003).
[8] T. Horn *et al.*, JLab PAC 34, PR12-09-011 (2009).
[9] T. Corthals, J. Ryckebusch, and T. Van Cauteren, *Phys. Rev. C* **73**, 045207 (2006).
[10] T. Corthals, T. Van Cauteren, P. Van Craeyveld, J. Ryckebusch, and D. G. Ireland, *Phys. Lett. B* **656**, 186 (2007).
[11] L. De Cruz, T. Vranx, P. Vancraeyveld, and J. Ryckebusch, *Phys. Rev. Lett.* **108**, 182002 (2012).
[12] L. De Cruz, J. Ryckebusch, T. Vranx, and P. Vancraeyveld, *Phys. Rev. C* **86**, 015212 (2012).
[13] J. Beringer *et al.* [Particle Data Group Collaboration], *Phys. Rev. D* **86**, 010001 (2012).
[14] T. Corthals, D. G. Ireland, T. Van Cauteren, and J. Ryckebusch, *Phys. Rev. C* **75**, 045204 (2007).
[15] P. Vancraeyveld, *Ph. D. thesis*, Ghent University (2011).
[16] M. E. McCracken *et al.* [CLAS Collaboration], *Phys. Rev. C* **81**, 025201 (2010).
[17] S. A. Ivashyn and A. Y. Korchin, *Eur. Phys. J. C* **49**, 697 (2007).
[18] C. J. Bebek *et al.*, *Phys. Rev. Lett.* **32**, 21 (1974).
[19] C. J. Bebek, C. N. Brown, P. Bucksbaum, M. Herzlinger, S. D. Holmes, C. A. Lichtenstein, F. M. Pipkin, S. W. Raither, and L. K. Sisterson, *Phys. Rev. D* **15**, 594 (1977).
[20] C. J. Bebek, A. Browman, C. N. Brown, K. M. Hanson, R. V. Kline, D. Larson, F. M. Pipkin, S. W. Raither, A. Silverman, and L. K. Sisterson, *Phys. Rev. D* **15**, 3082 (1977).
[21] D. S. Carman *et al.* [CLAS Collaboration], *Phys. Rev. C* **87**, 025204 (2013).
[22] R. M. Moring *et al.* [E93018 Collaboration], *Phys. Rev. C* **67**, 055205 (2003).
[23] P. Ambrozewicz *et al.* [CLAS Collaboration], *Phys. Rev. C* **75**, 045203 (2007).
[24] R. Nasseripour *et al.* [CLAS Collaboration], *Phys. Rev. C* **77**, 065208 (2008).
[25] D. S. Carman *et al.* [CLAS Collaboration], *Phys. Rev. C* **79**, 065205 (2009).
[26] M. Coman *et al.* [Jefferson Lab Hall A Collaboration], *Phys. Rev. C* **81**, 052201 (2010).
[27] D. S. Carman, R. Gothe, and V. Mokeev [CLAS Collaboration], Private communication.

Conclusions

The Regge-plus-resonance approach

The RPR framework for electromagnetic pseudoscalar-meson production was discussed in detail in Chapter 2. It treats hadrons as the effective degrees of freedom and combines a background amplitude in the t channel with individual resonance exchanges in the s channel. The t -channel background is effectively modeled through the exchange of Regge trajectories. A Regge trajectory connects a family of particles with identical quantum numbers through a spin-mass relation. Employing the Regge phenomenology in the background amplitude strongly reduces the number of background diagrams and hence model parameters, and ensures a proper high-energy limit without the need to include hadronic form factors.

By construction, a model developed within the RPR framework has a wide applicability range in terms of invariant mass, as it accounts for the dominant components in both the resonance (low-energy) and the background (higher-energy) region. In the resonance region, the background is supplemented with contributions from a limited set of individual resonances, allowing to model the resonant features observed in the data. At higher energies, the effect of individual resonances becomes increasingly less important and background contributions start to prevail. The latter are modeled by Regge amplitudes, which lead to a ‘natural damping’ of the cross section in the high-energy regime. The RPR formalism has exclusively been applied to electromagnetic kaon-hyperon production off the proton, but it can in principle be used to model a wide variety of $N(\gamma^{(*)}, M)B$ reactions.

Consistent interactions

In Chapter 3, a consistent interaction theory was developed for high-spin fermions that are off-shell. It was proven that imposing the RS gauge symmetry on the relevant interaction Lagrangians leads to the decoupling of the unphysical, lower-spin components of the high-spin fermion propagator.

The most general expression for the explicitly gauge-invariant spin- $(n + 1/2)$ RS field was derived, from which consistent interaction theories can be constructed.

The developed theory is of particular interest for the description of high-spin fermion exchanges within a hadrodynamical framework. It was shown that the application of consistent interactions in isobar models gives rise to unphysical structures in the computed cross sections if the reaction is cut off by conventional hadronic form factors. This behavior is caused by the consistent interaction structure featuring a growing power dependence on the four-momentum carried by the off-shell fermion with its spin, and the inability of conventional form factors to counterbalance this increasing momentum dependence. An alternate hadronic form factor was proposed, namely the “multi-dipole-Gauss” one, which suppresses the observed unphysical behavior of the computed observables. The combination of gauge-invariant interaction Lagrangians with the multi-dipole-Gauss hadronic form factor, allows for a fully consistent description of off-shell fermions with arbitrary spin in isobar models.

The RPR-2011 model

The developed framework for the description of consistent high-spin interactions, was used in Chapter 4 to replace the inconsistent spin-3/2 interactions of the RPR model for $p(\gamma, K^+)\Lambda$ with consistent ones and to include the exchange of spin-5/2 nucleon resonances in the s channel. The resulting RPR framework is very economical with regard to the number of parameters. One coupling constant is required for the pseudoscalar Regge trajectory in the t channel and for each spin-1/2 resonance in the s channel. Two coupling constants are required for each vector and axial-vector Regge trajectories in the t channel and for each resonance with a spin of 3/2 or higher in the s channel. There is one additional parameter in the RPR framework, namely the multi-dipole-Gauss cutoff energy, which is common for all resonances in the s channel.

Through Bayesian inference, which constitutes a statistical method to determine the most likely of model variants (instead of best-performing, as with the χ^2 method), the resonance content for the improved RPR framework was determined from the world’s $p(\gamma, K^+)\Lambda$ data. From an initial set of selected resonances, the combination with the highest Bayesian evidence was determined from the available $p(\gamma, K^+)\Lambda$ data. The resulting RPR-2011 model features the nucleon resonances $S_{11}(1535)$, $S_{11}(1650)$, $F_{15}(1680)$, $P_{13}(1720)$, $D_{13}(1900)$, $P_{13}(1900)$, $P_{11}(1900)$, and $F_{15}(2000)$ in the s channel, and rotating K (pseudoscalar) and K^* (vector) Regge trajectories in the t channel. The RPR-2011 model provides a fair description of the variety of measured $p(\gamma, K^+)\Lambda$ observables, which cover a broad kinematic range. The model can also be employed as a strong predictive tool for future $p(\gamma, K^+)\Lambda$ data.

Complete sets of observables

In Chapter 5, the issue of extracting the four reaction amplitudes from complete sets of observables in pseudoscalar-meson photoproduction was addressed. It was argued that, given the availability and resolution of single- and double-polarization data, it is most advantageous to employ the transversity basis for the reaction amplitudes. Upon expanding the reaction amplitudes of pseudoscalar-meson photoproduction in the transversity basis, an alleged inconsistency in the literature was discovered.

The extraction of the amplitude moduli is a rather straightforward procedure. This was shown for the $p(\gamma, K^+)\Lambda$ reaction with single-polarization data from the GRAAL collaboration. In some cases, however, one or more of the moduli cannot be extracted as the limited experimental resolution leads to imaginary solutions. The extracted GRAAL moduli, can be fairly reproduced by the RPR-2011 model, which was developed in Chapter 4.

In the transversity basis, the extraction of the relative phases of the amplitudes is much more complicated compared to the moduli. As no experimental data is available for a complete set of

observables in pseudoscalar-meson photoproduction, simulated data generated from the RPR-2011 model for $p(\gamma, K^+)\Lambda$ was analyzed. It was found that when the relative phases can be extracted, i.e. when no imaginary solutions are obtained, the most likely solution to the set of phases (of the four or eight possible solutions) is not always the ‘correct’ one. For achievable experimental resolutions, it was shown that these ‘incorrect’ solutions do not allow one to determine the reaction amplitudes from a complete data set unambiguously.

Deep-inelastic π^+n and π^-p electroproduction

Chapter 6 dealt with charged-pion electroproduction off the nucleon, above the resonance region. Following the approach of Kaskulov and Mosel, the proton electromagnetic transition form factor in the gauge-fixing s channel was altered so as to account for the residual effects of resonances, or equivalently partons, due to the high virtuality of the considered proton. The proposed “VR model” employs a transition form factor that respects the on-shell limit for the s -channel proton, and uses a continuous electromagnetic form factor for the charged-pion in the t channel. Both issues are not addressed in the KM model. The proposed proton electromagnetic transition form factor is of the dipole form and features a cutoff energy that depends on the four-momentum carried by the off-shell proton. The high-energy behavior of this cutoff energy was determined from data.

Despite having an additional fit parameter, the KM model offers a less satisfying description of the available data at low $-t$, compared to the VR model. From the most recent CLAS data for $p(e, e'\pi^+)n$, it appeared that neither the VR model, nor the KM model, is capable of explaining the observed magnitude of the unseparated cross section at medium and high $-t$ values. In the light of the $F\pi$ experiment planned with the 12 GeV upgrade at JLab, predictions from the VR model were presented and compared to those of the KM model.

Deep-inelastic $K^+\Lambda$ electroproduction

In Chapter 7, the model of Chapter 6 was applied to the deep-inelastic regime of $p(e, e'K^+)\Lambda$ at low $-t$. The VR model for $K^+\Lambda$ electroproduction uses a new photoproduction model as a starting base. The new $p(\gamma, K^+)\Lambda$ model features three Regge trajectories, namely a rotating K (pseudoscalar), a rotating K^* (vector), and a constant $K^*(1410)$ (vector) trajectory, and is in excellent agreement with the most recent high-energy and forward-angle cross section and recoil polarization data from the CLAS Collaboration.

Upon employing the kaon cutoff energy value as obtained from elastic eK scattering, the observed magnitude of the available high-energy, forward-angle unseparated cross-section data is well explained by the VR model. This correspondence is attributed to the resonance-parton contributions, without which the VR model underestimates the unseparated data by a factor of about two. In conventional $K^+\Lambda$ electroproduction models, like the Vanderhaeghen-Guidal-Laget model, the kaon cutoff energy is dramatically increased so as to explain the magnitude of the unseparated data. Keeping in mind that the unseparated cross section features both the longitudinal and transverse components, it is worth noting that the resonance-parton contributions mainly affect the transverse response, whereas the value of the kaon cutoff energy primarily alters the magnitude of the longitudinal structure function at forward angles.

In high-energy, forward-scattering charged-pion electroproduction, the observed magnitude of the longitudinal cross section is consistent with a pion cutoff energy value that is roughly equal to the one obtained from elastic scattering. In order to explain the corresponding transverse cross-section data, additional model features are required, like the resonance-parton contributions in the VR model. The same situation is expected for high-energy $K^+\Lambda$ electroproduction at forward angles. With the 12 GeV upgrade at JLab, the scheduled longitudinal-transverse-separation experiment for

$p(e, e' K^+) \Lambda$ is expected to clarify this issue. For this experiment, predictions from the VR model were given. A larger transverse and a smaller longitudinal response was observed than would be the case if an increased kaon cutoff energy and no resonance-parton contributions were to be used.

Appendix

Conventions

In this work, Roman lowercase letters are used to denote spatial indices, e.g. $i = 1, 2, 3$ (equivalently $i = x, y, z$), and Greek letters to denote Lorentz indices, e.g. $\mu = 0, 1, 2, 3$ (equivalently $\mu = t, x, y, z$), unless stated otherwise. A bold font weight is used to represent three-vectors, e.g. $\mathbf{v} = (v^1, v^2, v^3)$. The notations ‘ v^μ ’ and ‘ v_μ ’ are used for contravariant and covariant four-vectors, respectively, and are defined as

$$v^\mu = (v^0, \mathbf{v}) \quad \text{and} \quad v_\mu = (v_0, -\mathbf{v}),$$

with $v^0 = v_0$ being the time and \mathbf{v} the spatial component of the four-vector in question. For example, the four-gradient is given by $\partial^\mu = (\frac{\partial}{\partial t}, \nabla)$. Contravariant and covariant indices are related through the Minkowski metric $g^{\mu\nu}$, for which the adopted convention is $g^{\mu\nu} = \text{diag}(1, -1, -1, -1)$, in matrix notation. When applicable, the Einstein notation is implied, as for example in $v^\mu = g^{\mu\nu}v_\nu$. Further, natural units are assumed in this work, i.e. $\hbar = c = \varepsilon_0 = 1$.

Dirac algebra

The adopted representation for the Dirac or gamma matrices γ^μ is the Dirac representation, which reads

$$\gamma^0 = \begin{pmatrix} I_2 & 0 \\ 0 & -I_2 \end{pmatrix}, \quad \gamma^i = \begin{pmatrix} 0 & \sigma^i \\ -\sigma^i & 0 \end{pmatrix},$$

with I_2 representing the 2×2 identity matrix and σ^i being the Pauli matrices, which are defined as

$$\sigma^1 = \begin{pmatrix} 0 & 1 \\ 1 & 0 \end{pmatrix}, \quad \sigma^2 = \begin{pmatrix} 0 & -i \\ i & 0 \end{pmatrix}, \quad \sigma^3 = \begin{pmatrix} 1 & 0 \\ 0 & -1 \end{pmatrix}.$$

The anticommutator of the gamma matrices can be expressed as

$$\{\gamma^\mu, \gamma^\nu\} = 2g^{\mu\nu}.$$

The corresponding commutator is found in the definition of $\sigma^{\mu\nu}$:

$$\sigma^{\mu\nu} = \frac{i}{2}[\gamma^\mu, \gamma^\nu] = i(g^{\mu\nu} - \gamma^\nu\gamma^\mu).$$

The Hermitian conjugates of the gamma matrices read

$$(\gamma^0)^\dagger = \gamma^0, \quad \text{and} \quad (\gamma^i)^\dagger = \gamma^0\gamma^i\gamma^0 = -\gamma^i.$$

The Feynman slash notation for a four-vector p^μ is defined as $\not{p} = \gamma_\mu p^\mu$. The fifth gamma matrix $\gamma^5 = \gamma_5$ is defined as

$$\gamma^5 = i\gamma^0\gamma^1\gamma^2\gamma^3 = \begin{pmatrix} 0 & I_2 \\ I_2 & 0 \end{pmatrix}.$$

This matrix is Hermitian and anticommutes with the regular gamma matrices:

$$\begin{aligned} (\gamma^5)^\dagger &= \gamma^5, \\ \{\gamma^5, \gamma^\mu\} &= 0. \end{aligned}$$

The totally antisymmetric Levi-Civita tensor $\varepsilon^{\mu\nu\sigma\tau}$ is defined as +1 if $(\mu\nu\sigma\tau)$ is an even permutation of (0123), as -1 if $(\mu\nu\sigma\tau)$ is an odd permutation of (0123), and as 0 if at least two indices are equal. This tensor can be expressed as

$$\varepsilon^{\mu\nu\sigma\tau} = \gamma^5 \left(\frac{i}{2} \{\sigma^{\mu\nu}, \sigma^{\sigma\tau}\} + g^{\mu\sigma} \sigma^{\nu\tau} - g^{\mu\tau} \sigma^{\nu\sigma} \right).$$

Dirac spinors

The Dirac spinor u_λ for a spin-1/2 particle with rest mass m , total energy E , four-momentum $p^\mu = (E, \mathbf{p})$, and polarization λ satisfies the Dirac equation:

$$(\not{p} - m)u_\lambda = 0.$$

The adopted convention for the definition of the Dirac spinors is the Bjorken-Drell one [42]:

$$u_\lambda(p^\mu) = \frac{1}{\sqrt{2m(E+m)}} \begin{pmatrix} (E+m)I_2 \\ \boldsymbol{\sigma} \cdot \mathbf{p} \end{pmatrix} s_\lambda,$$

with $\boldsymbol{\sigma} = (\sigma^1, \sigma^2, \sigma^3)$ being the Pauli vector. The polarization λ is defined with respect to the quantization axis $\mathbf{n} = (\sin\theta \cos\phi, \sin\theta \sin\phi, \cos\theta)$, with polar and azimuthal angles θ and ϕ . It can either be $\lambda = +\mathbf{n}$ ("spin up") or $\lambda = -\mathbf{n}$ ("spin down"). The corresponding Pauli spinors are given by

$$s_{+\mathbf{n}} = \begin{pmatrix} \cos \frac{\theta}{2} \\ e^{i\phi} \sin \frac{\theta}{2} \end{pmatrix} \quad \text{and} \quad s_{-\mathbf{n}} = \begin{pmatrix} -e^{-i\phi} \sin \frac{\theta}{2} \\ \cos \frac{\theta}{2} \end{pmatrix}.$$

The conjugate Dirac spinor is defined as $\bar{u}_\lambda = u_\lambda^\dagger \gamma^0$, and is orthonormal to the regular spinors:

$$\bar{u}_\lambda u_{\lambda'} = \delta_{\lambda\lambda'}.$$

Summary

Introduction

Of all the visible mass in the universe, more than 99.9% can be associated with the protons and neutrons populating the atomic nuclei, collectively called “nucleons”. According to the masses of their quark constituents, nucleons should be about 100 times less massive than observed. This mass difference is caused by the antiscreening effect of the strong interaction, which binds the quarks in hadrons. This is in stark contrast with electromagnetically bound systems, for which the binding leads to a decrease in the total mass of the system.

At a more fundamental level, the antiscreening effect of the strong interaction is caused by the mutual interaction of the strong force carriers, i.e. the gluons. Because of this, the quantum field theory of the strong interaction cannot be treated perturbatively at low energies, which prevents a direct quantification of most of the properties of hadrons, such as their masses and resonance spectra for example. In order to model elastic and inelastic reactions involving hadrons, such as electromagnetic pseudoscalar-meson production, it is more effective to treat the hadrons as the relevant degrees of freedom, rather than the quarks. This is the main concept of quantum hadrodynamics. In electromagnetic pseudoscalar-meson production, an incident photon or electron interacts with a target nucleon, resulting in a pseudoscalar-meson-baryon pair in the final state. The photoinduced case is known as “photoproduction”, the electroinduced one as “electroproduction”.

The Regge-plus-resonance framework for electromagnetic pseudoscalar-meson production

The Regge-plus-resonance (RPR) formalism provides a tree-level, or “isobar”, framework for modeling the electromagnetic production of pseudoscalar mesons. It combines the description of intermediate nucleon resonance states, generated by the photo- or electroinduced excitation of the nucleon, with the exchange of so-called “Regge trajectories” in the background amplitude. A Regge trajectory connects a family of particles with identical quantum numbers through a spin-mass relation.

Employing the Regge phenomenology in the background amplitude strongly reduces the number of background diagrams and hence model parameters, and ensures a proper high-energy limit without the need to include hadronic form factors.

The RPR formalism accounts for the dominant components in both the resonance (low-energy) and the background (higher-energy) region and can hence be applied within a wide range of invariant masses. In the resonance region, the background is supplemented with contributions from a limited set of individual resonances, allowing to model the resonant features observed in the data. At higher energies, the $p(\gamma, K^+)\Lambda$ data indicates a decreasing effect of individual resonance mechanisms and background contributions start to prevail. The latter are modeled by Regge amplitudes, which lead to a ‘natural damping’ of the cross section in the high-energy regime.

The RPR formalism has exclusively been applied to electromagnetic kaon-hyperon production off the nucleon, but it can in principle be used to model a wide variety of electromagnetic pseudoscalar-meson production reactions. The development of the first RPR model, dubbed “RPR-2007”, was the subject of the Ph. D. thesis of T. Corthals, a former member of the “Theoretical Nuclear Physics and Statistical Physics” group at Ghent University. The RPR-2007 model for electromagnetic $K^+\Lambda$ production off the proton, features the nucleon resonances $S_{11}(1650)$, $P_{11}(1710)$, $P_{13}(1720)$, $D_{13}(1900)$, and $P_{13}(1900)$, combined with rotating K (pseudoscalar) and K^* (vector) Regge trajectories in the background amplitude. It offers a good description of the forward-scattering $p(\gamma, K^+)\Lambda$ data, against which it was optimized. At increasing kaon-scattering angles, the correspondence between RPR-2007 predictions and the data worsens. This can be partly attributed to the restriction to forward-scattering data in the optimization procedure, but mainly to the absence of nucleon resonances with a spin higher than $3/2$ and to the inconsistent description of the spin- $3/2$ interactions.

Consistent interactions for off-shell fermions with arbitrary spin

The interactions of off-shell fermions with a spin higher than $1/2$, play a crucial role in the quantum-hydrodynamical description of baryon resonances in hadronic reactions. High-spin fermion fields are commonly modeled using the Rarita-Schwinger theory. Rarita-Schwinger fields, however, involve unphysical degrees of freedom, which are associated with their inevitable lower-spin content. If left untreated, these unphysical contributions enter the interaction, leading to spurious behavior in the computed observables.

It was shown that upon imposing the invariance of the interaction under the so-called “unconstrained Rarita-Schwinger gauge”, the lower-spin content of the high-spin fermion propagator is decoupled, leading to a consistent description of the interaction. From the gauge symmetry, the most general consistent interaction structure for high-spin fermions was developed.

It was found that for a consistent interaction, the power of the momentum dependence rises with the spin of the fermion field. This leads to unphysical structures in the energy dependence of the computed tree-level observables, such as the cross section, when the short-distance physics is cut off with standard hadronic form factors. A new, spin-dependent, hadronic form factor was proposed, dubbed the “multi-dipole-Gauss” form factor, that suppresses the unphysical artifacts and consequently leads to a fully consistent description of the interaction.

The RPR-2011 model for electromagnetic $K^+\Lambda$ production off the proton

The devised theory for consistent high-spin interactions enabled a major update of the RPR formalism. More specifically, the inconsistent spin- $3/2$ interactions were replaced with consistent ones and intermediate spin- $5/2$ states can be described. The ‘upgraded’ RPR framework is very economical with regard to the number of parameters: the K Regge trajectory and spin- $1/2$ resonances require

only one coupling constant each, whereas the K^* Regge trajectory and each resonance with a spin higher than 1/2 requires only two coupling constants. There is one additional parameter in the RPR framework, namely the multi-dipole-Gauss cutoff energy, which is common for all resonances.

Using the upgraded and extended RPR formalism, a new model for $p(\gamma, K^+)\Lambda$ was developed. The specific resonance content of this model was obtained through a Bayesian analysis of the 2048 model variants that can be constructed from all the combinations of a preselected set of 11 nucleon resonances. The model variant with the highest Bayesian evidence, dubbed “RPR-2011”, was found to contain the nucleon resonances $S_{11}(1535)$, $S_{11}(1650)$, $F_{15}(1680)$, $P_{13}(1720)$, $D_{13}(1900)$, $P_{13}(1900)$, $P_{11}(1900)$, and $F_{15}(2000)$. In analogy to the RPR-2007 model, the RPR-2011 model also features a rotating K and a rotating K^* Regge trajectory in the background amplitude. The RPR-2011 model provides a fair description of the world’s $p(\gamma, K^+)\Lambda$ data, which cover a broad kinematic range.

The incompleteness of complete data sets in pseudoscalar-meson photoproduction

A complete set is a minimum set of observables from which the underlying reaction amplitudes can be determined unambiguously. Pseudoscalar-meson photoproduction from the nucleon is characterized by four such amplitudes. Given the quality and quantity of available single- and double-polarization data, it is most advantageous to express the amplitudes in the so-called “transversity basis”. In the transversity representation, the moduli of the normalized amplitudes can be determined from the three single-polarization observables and the relative phases from a well-chosen set of four double-polarization observables, provided that all the required observables are known to infinite precision.

In reality, observables are subject to experimental error. It is therefore not guaranteed that the reaction amplitudes can be extracted from a complete set of measured observables. Using the GRAAL data for the three $p(\gamma, K^+)\Lambda$ single asymmetries, it was shown that the moduli of the normalized transversity amplitudes can be readily extracted. In some of the kinematic points, however, imaginary solutions were obtained due to the finite experimental resolution. The moduli extracted from the GRAAL data, are fairly well reproduced by the RPR-2011 model.

Extracting the relative phases of the amplitudes from a complete set of finite-precision observables, is far more challenging. As no complete data sets are available in pseudoscalar-meson photoproduction, the phase-extraction analysis was performed using simulated $p(\gamma, K^+)\Lambda$ data, generated from the RPR-2011 model. It was shown to be quite likely to obtain imaginary solutions for the relative phases. When this is not the case, it was seen that the most likely solution to the set of phases (of the four or eight possible solutions) is not always the ‘correct’ one. It was pointed out that for achievable experimental resolutions, these ‘incorrect’ solutions do not allow one to determine the reaction amplitudes from a complete data set with statistical significance.

The VR model for deep-inelastic π^+n and π^-p electroproduction

Above the nucleon resonance region, the charged-pion electroproduction data cannot be explained by conventional hadronic models. The observed magnitude of the transverse cross section, for example, is significantly underestimated in a framework with Reggeized background amplitudes. Building on the work of Kaskulov and Mosel, a three-trajectory Regge model is introduced with an altered proton electromagnetic transition form factor in the gauged pion-exchange current. This form factor accounts for the residual effects of nucleon resonances, or equivalently partons, due to the high virtuality of the intermediate proton.

The proposed “Vrancx-Ryckebusch model” (VR model) employs a dipole form for the proton electromagnetic transition form factor with a cutoff energy that depends on the four-momentum carried by the exchanged proton. The high-energy behavior of this cutoff energy was determined

from data. The proton electromagnetic transition form factor of the VR model respects the on-shell limit for the exchanged proton and uses a continuous electromagnetic form factor for the intermediate pion in the background amplitude. Both these issues are not addressed in the Kaskulov-Mosel (KM) model.

Although the KM model has an additional fit parameter, the VR model offers a more satisfying description of the available high-energy data at forward scattering. In the light of the $F\pi$ experiment planned with the 12 GeV upgrade at JLab, predictions from the VR model were presented and compared to those of the KM model. From the most recent CLAS data for $p(e, e'\pi^+)n$, it appeared that the VR and KM model are both unable to explain the observed magnitude of the unseparated cross section in the non-forward-scattering regime. Introducing a strong hadronic form factor in the background amplitude, brings the model predictions considerably closer to the data. For now, it is unclear how the forward- and non-forward-scattering regimes can be smoothly matched within the VR framework. The upcoming separation of the concerned CLAS data into longitudinal and transverse components might elucidate this issue.

The VR model for deep-inelastic $K^+\Lambda$ electroproduction

The resonance-parton contributions are essential in the VR model in order to explain the deep-inelastic charged-pion electroproduction data at forward scattering. Since these effects are manifest through the proton electromagnetic transition form factor, it can be argued that they should also affect other reactions where a virtual photon interacts with an on-shell and an off-shell proton. The most prominent example of such a reaction, within the context of this work, is $K^+\Lambda$ electroproduction.

The VR framework was applied to forward-scattering $K^+\Lambda$ electroproduction above the resonance region. It is based on a newly developed photoproduction model that features three Regge trajectories, namely a rotating K and K^* trajectory, analogous to the RPR-2011 model, and a constant $K^*(1410)$ (vector) trajectory. The three-trajectory photoproduction model is in excellent agreement with the most recent high-energy and forward-angle cross section and recoil polarization data from the CLAS Collaboration, against which it was optimized.

The magnitude of the available unseparated $p(e, e'K^+)\Lambda$ cross-section data at high energies and forward scattering is well explained by the VR model, when the kaon cutoff energy is set to the value obtained from elastic eK scattering. It should be noted that without the resonance-parton contributions, the VR model underestimates the unseparated data by a factor of about two. In conventional $K^+\Lambda$ electroproduction models, like the Vanderhaeghen-Guidal-Laget model, the kaon cutoff energy is dramatically increased so as to explain the magnitude of the unseparated data. As the unseparated cross section features both the longitudinal and transverse components, it is worth noting that the resonance-parton contributions mainly affect the transverse response, whereas the value of the kaon cutoff energy primarily alters the magnitude of the longitudinal structure function at forward angles.

In deep-inelastic charged-pion electroproduction, the longitudinal cross section data at forward scattering can be explained by using the elastic pion cutoff energy value. The explanation of the corresponding transverse cross-section data requires additional model features, like the resonance-parton contributions in the VR model. For $K^+\Lambda$ electroproduction a similar situation is expected. The upcoming longitudinal-transverse-separation experiment for $p(e, e'K^+)\Lambda$, with the 12 GeV upgrade at JLab, is anticipated to clarify this issue. The predictions presented for this experiment, showed that the VR model features significantly larger transverse and smaller longitudinal responses. This behavior can be attributed to the introduction of resonance-parton contributions.

Samenvatting

Introductie

Meer dan 99.9% van al de zichtbare massa in het universum kan toegeschreven worden aan de protonen en neutronen van atoomkernen, gezamenlijk “nucleonen” genoemd. Op basis van de quarkmassa's zouden nucleonen ongeveer 100 keer minder massief moeten zijn dan experimenteel waargenomen wordt. Dit massaverschil wordt veroorzaakt door het anti-afschermingseffect van de sterke interactie, dewelke de quarks onderling bindt in hadronen. Dit staat in sterk contrast met de elektromagnetische wisselwerking, waar de bindingsenergie juist leidt tot een afname van de totale massa van het systeem.

Op een meer fundamenteel niveau, wordt het anti-afschermingseffect van de sterke wisselwerking veroorzaakt door de wederzijdse interacties van de gluonen, die de sterke kracht mediëren. Hierdoor kan de kwantumveldentheorie van de sterke interactie niet perturbatief behandeld worden bij lage energieën, hetgeen een rechtstreekse kwantificatie van de belangrijkste eigenschappen van hadronen, zoals hun massa's en resonantiespectra, onmogelijk maakt. Voor het modelleren van elastische en inelastische hadronische reacties, zoals elektromagnetische productie van pseudoscalaire mesonen, is het daarom doeltreffender om de hadronen zelf als de relevante vrijheidsgraden te beschouwen, en niet de quarks. Dit is het concept van de kwantumhadrodynamica. In elektromagnetische productie van pseudoscalaire mesonen, interageert een inkomend foton (fotoproductie) of elektron (elektroproductie) met een nucleon om zo een pseudoscalair meson en een baryon te vormen in de finale toestand.

Het Regge-plus-resonantieformalisme voor elektromagnetische productie van pseudoscalaire mesonen

Het Regge-plus-resonantieformalisme (RPR-formalisme) biedt een uniek ‘tree-level’-, of ‘isobar’-, raamwerk waarbinnen elektromagnetische productie van pseudoscalaire mesonen kan gemodelleerd worden. Het combineert de beschrijving van intermediaire nucleonresonantietoestanden, gegenereerd

door de foto- of elektro-excitatie van het nucleon, met de uitwisseling van zogenaamde “Regge-trajecten” in de achtergrondamplitude. Een Regge-traject verbindt een familie van deeltjes met identieke kwantumgetallen via een spin-massarelatie. Het toepassen van de Reggefenomenologie in de achtergrondamplitude heeft meerdere voordelen, zoals bijvoorbeeld het reduceren van het aantal achtergronddiagrammen en dus het aantal modelparameters.

Het RPR-formalisme houdt rekening met de dominante componenten in zowel het resonantie- (lage energie) als het achtergrondgebied (hogere energie) en is dus toepasbaar voor een breed bereik aan invariante massa’s. In het resonantiegebied wordt de achtergrond vergezeld door bijdragen van een beperkt aantal individuele resonanties, hetgeen de modellering toelaat van resonante kenmerken die waargenomen worden in de data. Bij hogere energieën wordt het effect van de individuele resonanties steeds minder belangrijk en nemen de achtergrondbijdragen de bovenhand. Deze laatste worden gemodelleerd door Regge-amplitudes, die zorgen voor een ‘natuurlijke demping’ van de werkzame doorsnede in het hoge-energiegebied.

Het RPR-formalisme werd voorlopig enkel nog maar toegepast op elektromagnetische kaon-hyperonproductie aan het nucleon, maar kan in principe gebruikt worden voor het modelleren van een hele variëteit aan gelijkaardige reacties. De ontwikkeling van het eerste RPR-model, “RPR-2007” genaamd, was het onderwerp van de doctoraatsthesis van T. Corthals, een voormalig lid van de onderzoeksgroep “Theoretical Nuclear Physics and Statistical Physics” aan de Universiteit Gent. Het RPR-2007-model voor elektromagnetische $K^+\Lambda$ -productie aan het proton bevat de nucleonresonanties $S_{11}(1650)$, $P_{11}(1710)$, $P_{13}(1720)$, $D_{13}(1900)$, en $P_{13}(1900)$, gecombineerd met roterende K - (pseudoscalair) en K^* - (vector) Regge-trajecten in de achtergrondamplitude. Het biedt een goede beschrijving van de $p(\gamma, K^+)\Lambda$ -data bij voorwaartse verstrooiing, dewelke gebruikt werden in de optimalisatieprocedure. Voor toenemende kaon-verstrooiingshoeken wordt de overeenkomst tussen RPR-2007 en de data slechter. Dit kan ten dele gewijd worden aan het beperken van de optimalisatiedata tot voorwaartse verstrooiing, maar voornamelijk aan de afwezigheid van nucleonresonanties met een spin hoger dan $3/2$ en de inconsistente beschrijving van de betrokken spin- $3/2$ -interacties.

Consistente interacties voor off-shell fermionen met arbitraire spin

De interacties van off-shell fermionen met arbitraire spin (hoger dan $1/2$) spelen een cruciale rol in de kwantumhadrodynamische beschrijving van baryonresonanties met hoge spin in hadronische reacties. Fermionvelden met hoge spin worden gewoonlijk gemodelleerd a.d.h.v. de Rarita-Schwingertheorie. Rarita-Schwinger-velden worden geplaagd door onfysische vrijheidsgraden, die geassocieerd zijn met hun onvermijdbare lagere-spininhoud. Indien onbehandeld, worden deze onfysische componenten opgenomen in de interactie, hetgeen navenant onfysische structuren kan teweegbrengen in de modelvoorspellingen van waarneembare grootheden.

Er werd aangetoond dat de lagere-spincomponenten van de fermionpropagator ontkoppelen indien de interactie de zogenaamde “niet-beperkte Rarita-Schwinger-ijksymmetrie” vertoont, hetgeen als dusdanig leidt tot een consistente beschrijving van de interactie. Aan de hand van deze ijksymmetrie werd de meest algemene consistente-interactiestructuur voor hoge-spinfermionen ontwikkeld.

Het blijkt dat voor een consistente interactie de macht van de momentumaafhankelijkheid toeneemt met de spin van het fermionveld. Dit leidt tot onfysische structuren in de energie-afhankelijkheid van de berekende tree-level-observabelen, zoals de werkzame doorsnede, wanneer de kortefstandsphysica gesupprimeerd wordt door standaard hadronische vormfactoren. Er werd een nieuwe, spinafhankelijke, hadronische vormfactor gesuggereerd, “multi-dipool-Gauss-vormfactor” genaamd, die de onfysische artefacten onderdrukt en bijgevolg aanleiding geeft tot een volledig consistente beschrijving van de interactie.

Het RPR-2011-model voor elektromagnetische $K^+\Lambda$ -productie aan het proton

De ontwikkelde theorie voor consistente hoge-spininteracties werd toegepast op het RPR-formalisme. Meer specifiek, werden de inconsistente spin-3/2-interacties vervangen door consistente interacties en het formalisme werd uitgebreid zodat intermediaire spin-5/2-toestanden nu kunnen beschreven worden. Het verbeterde RPR-raamwerk is heel zuinig wat betreft het aantal parameters: het K -Regge-traject en spin-1/2-resonanties worden elk beschreven door slechts één koppelingsconstante, terwijl het K^* -Regge-traject en elke hoge-spinresonantie beschreven wordt door twee koppelingsconstanten. Er is één bijkomende parameter in het nieuwe RPR-formalisme, namelijk de cutoff-energie van de multi-dipool-Gauss-vormfactor, waarvoor dezelfde waarde aangenomen wordt voor iedere individuele resonantie.

Binnen het verbeterde en uitgebreide RPR-raamwerk werd een nieuw model voor $p(\gamma, K^+)\Lambda$ ontwikkeld. The specifieke resonantie-inhoud van dit model werd bepaald a.d.h.v. een Bayesiaanse analyse van de 2048 modelvarianten die ontstaan uit alle mogelijke combinaties van resonanties uit een voorgeselecteerde set van 11 nucleonresonanties. Het model met de hoogste Bayesiaanse waarschijnlijkheid, “RPR-2011” genaamd, bevat de resonanties $S_{11}(1535)$, $S_{11}(1650)$, $F_{15}(1680)$, $P_{13}(1720)$, $D_{13}(1900)$, $P_{13}(1900)$, $P_{11}(1900)$, en $F_{15}(2000)$. Naar analogie met het RPR-2007-model, wordt de achtergrondamplitude van het RPR-2011-model tevens beschreven door een roterende K - en een roterend K^* -Regge-traject. Het RPR-2011-model biedt een degelijke beschrijving van alle beschikbare $p(\gamma, K^+)\Lambda$ -data, dewelke een uitgestrekt gebied aan kinematica beslaat.

De incompleetheid van complete datasets in fotoproductie van pseudoscalaire mesonen

Een complete set is een minimale set van observabelen, waaruit de onderliggende reactie-amplitudes ondubbelzinnig kunnen bepaald worden. Fotoproductie van pseudoscalaire mesonen aan het nucleon wordt gekenmerkt door vier zulke amplitudes. Gebaseerd op de kwaliteit en kwantiteit van de beschikbare enkelvoudig- en dubbel-gepolariseerde data, is het het meest voordelig om deze amplitudes uit te drukken in de zogenaamde “transversiteitsbasis”. In deze representatie kunnen de moduli van de genormaliseerde amplitudes bepaald worden uit de drie enkelvoudig-gepolariseerde observabelen en de corresponderende faseverschillen uit een welbepaalde set van vier dubbel-gepolariseerde observabelen, gegeven dat alle vereiste observabelen gekend zijn met oneindig nauwkeurige precisie.

In realiteit zijn observabelen echter onderhevig aan experimentele onzekerheid. Het is daarom niet gegarandeerd dat de reactie-amplitudes geëxtraheerd kunnen worden van een complete set van gemeten observabelen. Aan de hand van de GRAAL-data voor de drie enkelvoudig-gepolariseerde $p(\gamma, K^+)\Lambda$ -asymmetrieën, werd er aangetoond dat de moduli van de genormaliseerde transversiteit-samplitudes met gemak bepaald kunnen worden. In sommige van de kinematische punten echter, werden imaginaire oplossingen bekomen door de eindige experimentele resolutie. De moduli die konden bepaald worden uit de GRAAL-data, bleken goed beschreven te worden door het RPR-2011-model.

Het bepalen van de faseverschillen van de amplitudes uit een complete set van eindig nauwkeurige observabelen, is een veel moeilijkere opgave. Aangezien er tot op heden nog geen complete datasets voorhanden zijn in fotoproductiereacties van pseudoscalaire mesonen, werd de fase-extractie-analyse uitgevoerd a.d.h.v. gesimuleerde $p(\gamma, K^+)\Lambda$ -data, gegenereerd via het RPR-2011-model. Er werd aangetoond dat het relatief waarschijnlijk is dat imaginaire oplossingen voor de faseverschillen bekomen worden. Wanneer dit niet het geval is, bleek dat de meest waarschijnlijke oplossing voor de set van faseverschillen (van de vier of acht mogelijke oplossingen) niet altijd de ‘juiste’ oplossing is. Er werd aangegeven dat voor haalbare experimentele resoluties, deze ‘onjuiste’ oplossingen

het niet toelaten om de reactie-amplitudes ondubbelzinnig te bepalen uit een complete dataset met statistische significantie.

Het VR-model voor diep-inelastische π^+n - en π^-p -elektroproductie

Boven het resonantiegebied kan de $\pi^\pm N'$ -elektroproductiedata niet verklaard worden door gebruikelijke hadronische modellen. De geobserveerde magnitude van de transversale werkzame doorsnede, bij wijze van voorbeeld, wordt significant onderschat binnen een raamwerk opgebouwd uit Regge-trajecten in de achtergrondamplitude. Voortbouwend op het werk van Kaskulov en Mosel, wordt een drie-traject Regge-model geïntroduceerd met een gewijzigde elektromagnetische transitievormfactor voor het proton in de geijkte pion-uitwisselingsstroom. Deze vormfactor brengt de residuele effecten van nucleonresonanties, of equivalent partonen, in rekening als gevolg van de hoge virtualiteit van het intermediaire proton.

In het voorgestelde “Vrancx-Ryckebusch-model” (VR-model), wordt een dipoolvorm gebruikt voor de elektromagnetische transitievormfactor voor het proton met een cutoff-energie die functie is van het viermomentum van het uitgewisselde proton. Het hoge-energiegedrag voor deze cutoff-energie werd bepaald uit de relevante data. De proton-transitievormfactor van het VR-model respecteert de verwachte on-shell-limiet voor het intermediaire proton en gebruikt een continue elektromagnetische vormfactor voor het intermediaire pion in de achtergrondamplitude. Beide deze elementen zijn niet aanwezig in het Kaskulov-Mosel-model (KM-model).

Hoewel het KM-model een extra optimalisatieparameter heeft, levert het VR-model een meer bevredigende beschrijving van de beschikbare hoge-energieedata voor voorwaartse verstrooiing. In het kader van het $F\pi$ -experiment dat gepland is voor de 12-GeV-upgrade in JLab, werden voorspellingen gepresenteerd van het VR-model en vergeleken met die van het KM-model. Uit de meest recente CLAS-data voor $p(e, e'\pi^+)n$ bleek dat noch het VR-model, noch het KM-model, de geobserveerde magnitude kunnen verklaren van de niet-gesepareerde werkzame doorsnede bij niet-voorwaartse verstrooiing. Door het introduceren van een sterke hadronische vormfactor in de achtergrondamplitude, konden de modelvoorspellingen aanzienlijk dichter bij de data gebracht worden. Voorlopig is het echter nog onduidelijk hoe het voorwaartse- en niet-voorwaartse-verstrooiingsgebied geünificeerd kunnen worden binnen het VR-raamwerk. De geplande separatie van de beschouwde CLAS-data naar longitudinale en transversale componenten zou deze kwestie mogelijks kunnen opklaren.

Het VR-model voor diep-inelastische $K^+\Lambda$ -elektroproductie

De resonantie-partonbijdragen zijn van essentieel belang in het VR-model om de diep-inelastische $\pi^\pm N'$ -elektroproductiedata te verklaren bij voorwaartse verstrooiing. Aangezien deze effecten zich binnen het VR-raamwerk manifesteren via de proton-transitievormfactor, zouden ze ook van belang moeten zijn in andere reacties waar een virtueel foton interageert met een on-shell en off-shell proton. Het meest vooraanstaande voorbeeld, binnen de context van dit werk, is $K^+\Lambda$ -elektroproductie.

Het VR-raamwerk werd toegepast op $K^+\Lambda$ -elektroproductie boven het resonantiegebied, bij voorwaartse verstrooiing. Het is gebaseerd op een nieuw ontwikkeld fotoproductiemodel met drie Regge-trajecten in de achtergrondamplitude, zijnde een K - en K^* -traject met roterende Regge-fases, analoog aan het RPR-2011-model, en een $K^*(1410)$ -traject (vectortraject) met constante Regge-fase. Het drie-traject fotoproductiemodel biedt een uitstekende beschrijving van de meest recente hoge-energieedata van de CLAS-collaboratie bij voorwaartse verstrooiing voor de werkzame doorsnede en recoil-polarizatie, waaraan het geoptimaliseerd werd.

De magnitude van de beschikbare niet-gesepareerde werkzame-doorsnededata voor $p(e, e'K^+)\Lambda$ bij hoge energieën en voorwaartse verstrooiing wordt goed verklaard door het VR-model, indien voor de cutoff-energie van het kaon de corresponderende waarde verkregen uit elastische eK -verstrooiing

gebruikt wordt. Er moet vermeld dat zonder de resonantie-partonbijdragen, de voorspellingen van het betreffende VR-model voor de niet-gesepareerde data amper half zo groot zijn. In conventionele $K^+\Lambda$ -elektroproductiemodellen, zoals bijvoorbeeld het Vanderhaeghen-Guidal-Laget-model, wordt de magnitude van de niet-gesepareerde data verklaard door een significant verhoogde waarde voor de cutoff-energie van het kaon; dit in tegenstelling tot de resonantie-partonbijdragen in het VR-raamwerk. Aangezien de niet-gesepareerde werkzame doorsnede zowel de longitudinale als de transversale component bevat, is het nodig te vermelden dat de resonantie-partonbijdragen voornamelijk de transversale respons beïnvloeden, terwijl de cutoff-energie voor het kaon hoofdzakelijk verantwoordelijk is voor de grootte van de longitudinale structuurfunctie bij voorwaartse verstrooiing.

In diep-inelastische $\pi^\pm N'$ -elektroproductie kan de longitudinale werkzame-doorsnededata bij voorwaartse verstrooiing verklaard worden door gebruik te maken van de ‘elastische’ waarde voor de cutoff-energie van het pion. De verklaring van de transversale werkzame-doorsnededata vereist bijkomende ‘modelingrediënten’, zoals de resonantie-partonbijdragen in het VR-model. Voor $K^+\Lambda$ -elektroproductie wordt een gelijkaardige situatie verwacht. Het geplande experiment voor de separatie van de $p(e, e'K^+)\Lambda$ -werkzame-doorsnede naar de longitudinale en transversale componenten, voor de 12-GeV-upgrade in JLab, wordt verwacht duidelijkheid te scheppen in deze kwestie. De voorspellingen voor dit experiment toonden aan dat het VR-model een significant grotere transversale en kleinere longitudinale respons kent dan wat het geval zou zijn wanneer de cutoff-energie voor het kaon naar de vereiste waarde verhoogd zou worden, in de afwezigheid van resonantie-partonbijdragen.

Bibliography

- [1] J. Beringer *et al.* [Particle Data Group],
[Phys. Rev. D **86**, 010001 \(2012\)](#).
- [2] K. G. Wilson,
[Phys. Rev. D **10**, 2445 \(1974\)](#).
- [3] J. Bulava *et al.* [Hadron Spectrum Collaboration],
[J. Phys. Conf. Ser. **180**, 012067 \(2009\)](#).
- [4] S. Dürr *et al.* [Budapest-Marseille-Wuppertal Collaboration],
[Science **322**, 1224 \(2008\)](#).
- [5] R. G. Edwards, J. J. Dudek, D. G. Richards, and S. J. Wallace,
[Phys. Rev. D **84**, 074508 \(2011\)](#).
- [6] S. Capstick and W. Roberts,
[Prog. Part. Nucl. Phys. **45**, S241 \(2000\)](#).
- [7] U. Loring, B. C. Metsch, and H. R. Petry,
[Eur. Phys. J. A **10**, 395 \(2001\)](#).
- [8] M. Anselmino, E. Predazzi, S. Ekelin, S. Fredriksson, and D. B. Lichtenberg,
[Rev. Mod. Phys. **65**, 1199 \(1993\)](#).
- [9] J. Ferretti, A. Vassallo, and E. Santopinto,
[Phys. Rev. C **83**, 065204 \(2011\)](#).
- [10] E. Santopinto,
[Phys. Rev. C **72**, 022201 \(2005\)](#).
- [11] S. Janssen, J. Ryckebusch, W. Van Nespén, D. Debruyne, and T. Van Cauteren,
[Eur. Phys. J. A **11**, 105 \(2001\)](#).

- [12] S. Janssen, J. Ryckebusch, D. Debruyne, and T. Van Cauteren, *Phys. Rev. C* **65**, 015201 (2002).
- [13] S. Janssen, *Ph. D. thesis, Ghent University* (2002).
- [14] S. Janssen, J. Ryckebusch, and T. Van Cauteren, *Phys. Rev. C* **67**, 052201 (2003).
- [15] S. Janssen, D. G. Ireland, and J. Ryckebusch, *Phys. Lett. B* **562**, 51 (2003).
- [16] D. G. Ireland, S. Janssen, and J. Ryckebusch, *Nucl. Phys. A* **740**, 147 (2004).
- [17] T. Corthals, J. Ryckebusch, and T. Van Cauteren, *Phys. Rev. C* **73**, 045207 (2006).
- [18] T. Corthals, T. Van Cauteren, P. Van Craeyveld, J. Ryckebusch, and D. G. Ireland, *Phys. Lett. B* **656**, 186 (2007).
- [19] T. Corthals, *Ph. D. thesis, Ghent University* (2007).
- [20] L. De Cruz, D. G. Ireland, P. Vancraeyveld, and J. Ryckebusch, *Phys. Lett. B* **694**, 33 (2010).
- [21] L. De Cruz, T. Vrancx, P. Vancraeyveld, and J. Ryckebusch, *Phys. Rev. Lett.* **108**, 182002 (2012).
- [22] L. De Cruz, J. Ryckebusch, T. Vrancx, and P. Vancraeyveld, *Phys. Rev. C* **86**, 015212 (2012).
- [23] L. De Cruz, *Ph. D. thesis, Ghent University* (2011).
- [24] T. Corthals, D. G. Ireland, T. Van Cauteren, and J. Ryckebusch, *Phys. Rev. C* **75**, 045204 (2007).
- [25] P. Vancraeyveld, *Ph. D. thesis, Ghent University* (2011).
- [26] P. Vancraeyveld, L. De Cruz, J. Ryckebusch, and T. Van Cauteren, *Phys. Lett. B* **681**, 428 (2009).
- [27] M. M. Kaskulov and U. Mosel, *Phys. Rev. C* **81**, 045202 (2010).
- [28] A. M. Sandorfi, S. Hoblit, H. Kamano, and T.-S. H. Lee, *J. Phys.* **38**, 053001 (2011).
- [29] R. A. Adelseck and B. Saghai, *Phys. Rev. C* **42**, 108 (1990).
- [30] R. A. Arndt, W. J. Briscoe, I. I. Strakovsky, and R. L. Workman, *Phys. Rev. C* **74**, 045205 (2006).

- [31] A. V. Anisovich, R. Beck, E. Klempt, V. A. Nikonov, A. V. Sarantsev, and U. Thoma, *Eur. Phys. J. A* **48**, 15 (2012).
- [32] S. Capstick and W. Roberts, *Phys. Rev. D* **49**, 4570 (1994).
- [33] R. Bradford *et al.* [CLAS Collaboration], *Phys. Rev. C* **73**, 035202 (2006).
- [34] W. Rarita and J. Schwinger, *Phys. Rev.* **60**, 61 (1941).
- [35] V. Shklyar, G. Penner, and U. Mosel, *Eur. Phys. J. A* **21**, 445 (2004).
- [36] T. Corthals, L. De Cruz, D. G. Ireland, S. Janssen, P. Vancraeyveld, J. Ryckebusch, and T. Vrancx, *StrangeCalc* (2014).
- [37] Wolfram Research, *Mathematica 7* (2008).
- [38] A. Lleres *et al.* [GRAAL Collaboration], *Eur. Phys. J. A* **39**, 149 (2009).
- [39] G. M. Huber *et al.*, *JLab PAC 30*, PR12-06-101 (2006).
- [40] T. Horn *et al.*, *JLab PAC 34*, PR12-09-011 (2009).
- [41] M. Guidal, J. M. Laget, and M. Vanderhaeghen, *Phys. Rev. C* **61**, 025204 (2000).
- [42] J. D. Bjorken and S. D. Drell, *Relativistic Quantum Mechanics*, McGraw-Hill Education (1998).

Publications

Journal articles – A1

As first author

- T. Vrancx, J. Ryckebusch, and J. Nys,
“ $K^+\Lambda$ electroproduction above the resonance region”,
[Phys. Rev. C](#), in press (2014).
- T. Vrancx and J. Ryckebusch,
“Charged-pion electroproduction above the resonance region”,
[Phys. Rev. C](#) **89**, 025203 (2014).
- T. Vrancx, J. Ryckebusch, T. Van Cuyck, and P. Vancraeyveld,
“Incompleteness of complete pseudoscalar-meson photoproduction”,
[Phys. Rev. C](#) **87**, 055205 (2013).
- T. Vrancx, L. De Cruz, J. Ryckebusch, and P. Vancraeyveld,
“The $p(\gamma, K^+)\Lambda$ reaction: Consistent high-spin interactions and Bayesian inference of its resonance content”,
11th International Conference on Hypernuclear and Strange Particle Physics,
1–5 Oct. 2012, Barcelona, Spain,
[Nucl. Phys. A](#) **914**, 74 (2013).
- T. Vrancx, L. De Cruz, J. Ryckebusch, and P. Vancraeyveld,
“Consistent interactions for high-spin fermion fields”,
[Phys. Rev. C](#) **84**, 045201 (2011).

As co-author

- J. Nys, T. Vrancx, and J. Ryckebusch,
“Amplitude extraction in pseudoscalar-meson photoproduction: towards a situation of complete information”,
[J. Phys. G](#), submitted (2014).
- P. Vancraeyveld, L. De Cruz, J. Ryckebusch, and T. Vrancx,
“Kaon photoproduction from the deuteron in a Regge-plus-resonance approach”,
[Nucl. Phys. A](#) **897**, 42 (2013).
- L. De Cruz, J. Ryckebusch, T. Vrancx, and P. Vancraeyveld,
“A Bayesian analysis of kaon photoproduction with the Regge-plus-resonance model”,
[Phys. Rev. C](#) **86**, 015212 (2012).
- L. De Cruz, T. Vrancx, P. Vancraeyveld, and J. Ryckebusch,
“Bayesian inference of the resonance content of $p(\gamma, K^+)\Lambda$ ”,
[Phys. Rev. Lett.](#) **108**, 182002 (2012).

Conference papers – C1

As first author

- T. Vrancx, J. Ryckebusch, and J. Nys,
“Complete sets of observables in pseudoscalar-meson photoproduction”,
13th International Conference on Meson-Nucleon Physics and the Structure of the Nucleon,
30 Sept. – 4 Oct. 2013, Rome, Italy,
[EPJ Web Conf.](#), in press (2014).
- T. Vrancx, L. De Cruz, J. Ryckebusch, and P. Vancraeyveld,
“Consistent interactions for high-spin baryons”,
8th International Workshop on the Physics of Excited Nucleons,
17–20 May 2011, Newport News (Virginia), USA,
[AIP Conf. Proc.](#) **1432**, 361 (2012).

As co-author

- J. Ryckebusch and T. Vrancx,
“Incompleteness of complete kaon photoproduction”,
9th International Workshop on the Physics of Excited Nucleons,
27–30 May 2013, Valencia, Spain,
[Int. J. Mod. Phys. Conf. Ser.](#) **26**, 1460097 (2014).
- J. Ryckebusch, L. De Cruz, T. Vrancx, and P. Vancraeyveld,
“Bayesian inference of the missing resonances in $K^+\Lambda$ photoproduction”,
11th Conference on the Intersections of Particle and Nuclear Physics,
29 May – 2 June 2012, St. Petersburg, Florida, USA,
[AIP Conf. Proc.](#) **1560**, 442 (2013).
- P. Vancraeyveld, L. De Cruz, J. Ryckebusch, and T. Vrancx,
“Bayesian inference of the resonance content of $p(\gamma, K^+)\Lambda$ ”,
12th International Workshop on Meson Production, Properties and Interaction,
31 May – 5 June 2012, Cracow, Poland,
[EPJ Web Conf.](#) **37**, 08001 (2012).

- J. Ryckebusch, L. De Cruz, P. Vancraeyveld, and T. Vrancx,
“*The Regge-plus-resonance model for kaon production on the proton and the neutron*”,
8th International Workshop on the Physics of Excited Nucleons,
17–20 May 2011, Newport News (Virginia), USA,
[AIP Conf. Proc. 1432, 357 \(2012\)](#).

Nomenclature

c.m.	center-of-mass frame
$\gamma^{(*)}$	real (virtual) photon
SU(n)	special unitary group of degree n
B	baryon with $J^P = (1/2)^+$
M	pseudoscalar meson
M_A	axial-vector meson
M_V	vector meson
N	nucleon
LT	longitudinal-transverse
L	longitudinal
TT	transverse-transverse
T	transverse
CEBAF	Continuous Electron Beam Accelerator Facility
CLAS	CEBAF Large Acceptance Spectrometer
GRAAL	Grenoble Anneau Accélérateur Laser
JLab	Thomas Jefferson National Accelerator Facility
KM	Kaskulov-Mosel

QCD	quantum chromodynamics
RPP	Review of Particle Physics
RPR	Regge-plus-resonance
RS	Rarita-Schwinger
VR	Vrancx-Ryckebusch